Degradation-aware optimal control of grid-connected lithium-ion batteries

Jorn Reniers

Department of Engineering Science

University of Oxford

This dissertation is submitted for the degree of

Doctor of Philosophy

St Cross College March 2020

VITO

Declaration

I, Jorn Reniers, hereby declare that except where specific reference is made to the work of others, the contents of this dissertation are original and have not been submitted in whole or in part for consideration for any other degree or qualification in this, or any other university. This dissertation is my own work and contains nothing which is the outcome of work done in collaboration with others, except as specified in the text and Acknowledgements. Parts of the work have been presented at conferences and published in journal papers; these are specified in the text and referenced accordingly.

Jorn Reniers
March 2020

Acknowledgements

First and foremost, I want to thank my supervisor professor David Howey for his advise and help during my PhD. His patience and feedback motivated me to keep on searching for more. Also Grietus Mulder was a great support with his huge experience and practical tips.

This work would not have been possible without the input from VITO. Both the funding and advise were invaluable. I would therefore like to express my gratitude to the full team at VITO for helping with my experiments and setting up a full battery test rig. In Oxford, the discussions with professor Sina Ober-Blöbaum about the optimisation techniques are greatly appreciated. I am also grateful for the collaboration with researchers at TU Munich.

This work would not have been possible without my friends in Oxford. The ‘old’ Holder team was most welcoming when I arrived and provided a much-needed relaxed atmosphere to settle in. The ‘new’ Holder team has kept this up with great banter and laughs. In the wider research group, I have made many new friends during the numerous pub trips. Also at St Cross College I have met many wonderful people who added a truly international perspective to Oxford, while the Oxford Belgo-Luxembourgish Society relieved the homesickness with numerous real beers and waffles. Although I still do not like getting up early, Wolfson College Boat Club has made the mornings more bearable by being a fantastic bunch of friends even in the worst British weather. I should thank Damien for his two-year advertising campaign to get me into rowing in the first place.

Finally, I would like to thank my parents and siblings for their support throughout the years. You turned ‘coming back to Belgium’ into ‘coming home’, however long I had been abroad.

Abstract

With the accelerating deployment of intermittent renewable energy sources, the need for balancing on the power system is ever increasing. Even though lithium-ion (Li-ion) batteries are not yet cost-competitive with other solutions for most applications, the number of grid-connected Li-ion batteries is expected to increase sharply in the coming years.

Due to the sunk costs of the upfront investment, understanding the lifetime of a battery is crucial for the business case. Nevertheless, predicting the lifetime of a battery is not straightforward. Many degradation mechanisms reduce the total energy which can be stored in a battery, thus decreasing its lifetime. This thesis begins with an extensive literature review into the causes of this battery degradation, both qualitatively and quantitatively. Various physics-based degradation models are combined into one flexible battery degradation model which is used to study which mechanisms cause degradation under which operating conditions.

The model is then carefully formulated for optimisation in a power system application. While a battery makes revenue from trading power on the day-ahead market, it degrades. The physics-based model is used to optimise the usage profile of the battery, determining when to buy power (charging the battery) and when to sell (discharging the battery), in order to maximise revenue while minimising degradation. These optimal profiles are compared to profiles which are obtained using state-of-the-art economic optimisation models.

Finally, Li-ion batteries were cycled with different usage profiles in an experimental validation. The battery degradation was measured monthly, while the revenue each battery could make was also tracked. It is shown that the usage profiles determined by the physics-based model outperform the profiles from conventional optimisation models. The revenue can be increased by 17% while at the same time decreasing the degradation by 31%. This implies that such physics-based models can increase the revenue and the lifetime of grid-connected batteries, increasing the net profit by over 300%.

Publications

Part of the work presented in this thesis has been published in a number of articles. The results from the optimisation with the three different battery models (see sections 4.1 to 4.4) have been presented in [2]. This did not yet include the simulation with the generalised degradation model, nor the experimental results.

Chapter 2 is a rewritten version of a paper in the Journal of the Electrochemical Society [5]. A software code, which implements a large range of degradation models from literature alongside the single-particle model, has been published as open-access code on GitHub [6]. The mathematical foundations for the implementation of the single-particle model using Chebyshev spectral methods were developed by Adrien Bizeray, as detailed in sections 3.2 and 3.3.

Together with Dr. Leong Gan, I wrote a conference paper on a hybrid flow battery and lithium-ion battery system [1]. I developed and implemented the algorithm to optimally divide the total power demand between both batteries considering a simple model for losses and degradation, while Dr. Gan implemented high-accuracy models for the entire micro-grid and a rule-based control system. This work is not presented in this thesis.

The work for a conference paper in collaboration with researchers from TU Munich [3], and follow-up journal paper [4], was mostly done by members from the Jossen group (Michael Schimpe, Holger Hesse, Volkan Kumtepeli, etc.). My contribution is limited to discussing the ideas, implementation and results, as well as writing sections of the introduction / literature review.

[1] L. K. Gan, J. M. Reniers, and D. A. Howey, “A hybrid vanadium redox/lithium-ion energy storage system for off-grid renewable power,” *2017 IEEE Energy Conversion Congress and Exposition (ECCE)*, pp. 1016–1023. IEEE, Oct. 2017.

[2] J. M. Reniers, G. Mulder, S. Ober-Blöbaum, and D. A. Howey, “Improving optimal control of grid-connected lithium-ion batteries through more accurate battery and degradation modelling,” *Journal of Power Sources*, vol. 379, 2018.

[3] M. Schimpe, C. N. Truong, M. Naumann, A. Jossen, H. C. Hesse, J. M. Reniers, and D. A. Howey, “Marginal Costs of Battery System Operation in Energy Arbitrage Based on Energy Losses and Cell Degradation,” *2018 IEEE International Conference on Environment and Electrical Engineering and 2018 IEEE Industrial and Commercial Power Systems Europe (EEEIC / I&CPS Europe)*, pp. 1–5. IEEE, Jun. 2018.

[4] H. C. Hesse, V. Kumtepeli, M. Schimpe, J M Reniers, D. A. Howey, A. Tripathi, Y. Wang, and A. Jossen, “Ageing and Efficiency Aware Battery Dispatch for Arbitrage Markets Using Mixed Integer Linear Programming,” *Energies*, vol. 12, no. 6:999, Mar. 2019.

[5] J. M. Reniers, G. Mulder, and D. A. Howey, “Review and performance comparison of mechanical-chemical degradation models for lithium-ion batteries,” *Journal of The Electrochemical Society*, vol. 166, no. 14, pp. A3189–A3200, Sep. 2019.

[6] D. A. Howey and J. M. Reniers, “Slide, a simulator for lithium-ion degradation,” Oxford, 2019. [Online]. Available:https://github.com/davidhowey/SLIDE

Table of contents

List of figures

List of tables

Nomenclature

Roman Symbols

A	Total geometric surface area, m^2
a	Specific electrode surface area, $\mathrm{m}^2\ \mathrm{m}^{-3}$
$\bar{A}$	Matrix in the discretised state-space model for the diffusion PDE, [-]
$\mathbf{b}$	Array in the discretised state-space model for the diffusion PDE, [-]
c	Lithium concentration, $\mathrm{mol\ m}^{-3}$
$\bar{C}$	Matrix in the discretised state-space model for the diffusion PDE, [-]
$\bar{c}$	Chebyshev interpolant for the lithium concentration, $\mathrm{mol\ m}^{-3}$
C_p	Heat capacity of the cell, $\mathrm{J\ kg}^{-1}\ \mathrm{K}^{-1}$
C_p^{ecm}	Parallel capacitance in the ECM, F
c_s	Solvent concentration, $\mathrm{mol\ m}^{-3}$
D	Diffusion constant, $\mathrm{m}^2\ \mathrm{s}^{-1}$
$\mathbf{d}$	Array in the discretised state-space model for the diffusion PDE, [-]
$D_c^{(p)}$	Chebyshev differentiation matrix of order p, [-]

E_D	Activation energy for the Arrhenius relationship for the diffusion constant, J mol^{-1}
E_{en}	Energy capacity of the battery, MWh
E_k	Activation energy for the Arrhenius relationship for the rate constant, J mol^{-1}
E_{ch}^{lost}	Lost charge capacity, Ah
E_{en}^{lost}	Lost energy capacity, MWh
F	Faraday's constant, C mol^{-1}
f	Function which calculates the time derivatives of the state
f_1	Nonlinear function of voltage and temperature in the degradation model of the ECM
f_2	Nonlinear function of voltage and depth of discharge in the degradation model of the ECM
g	Function which calculates the voltage
h	Convective heat transfer coefficient, W m^{-2} K^{-1}
I	Total current, A
i	Current density, A m^{-2}
i_0	Exchange current density, A m^{-2}
I_r^{ecm}	Current through the parallel resistance in the ECM, A
j	Molar flux, mol m^{-2} s^{-1}
k	Rate constant, m$^{4-3\alpha}$ s^{-1} mol$^{\alpha-1}$
L	Lithium lost, Ah

M	Molecular weight, kg mol^{-1}
m	Slope of the Wöhler curve, [-]
N	Cycle number, [-]
n	Number of electrons involved in the reaction, [-]
N_1	Number of time steps in the optimisation, [-]
N_2	Number of time steps in the time integration, [-]
N_c	Number of Chebyshev nodes, [-]
N^{m}	Number of optimisation time steps at which the time horizon moves forward, [-]
P	Power, MW
Q	State of charge, [-]
$\bar{Q}$	Matrix with the eigenvectors of the diffusion PDE, [-]
R	Radius of a particle, m
r	Radial coordinate, m
R_{dc}	DC resistance of the cell, Ω
r_{dc}	Specific DC resistance, Ω m^2
R_g	Ideal gas constant, J mol^{-1} K^{-1}
R_p^{ecm}	Parallel resistance in the ECM, Ω
R_s^{ecm}	Series resistance in the ECM, Ω
$\mathbf{s}$	Array with the state variables

S	Function which integrates the state-space model over one optimisation time step
T	Temperature, K
T_k	Chebyshev basis functions, [-]
U	Open-circuit potential, V
u	Transformed lithium concentration, m mol m^{-3}
V	Voltage, V
$\mathbf{W}$	Array with the optimisation variables
x	Lithium fraction, [-]
$\bar{x}$	Coordinate in the computational Chebyshev domain, [-1, 1]
x_j	Chebyshev spatial nodes, [-]
Y	Young's modulus, Pa
$\hat{y}_k$	Chebyshev coefficients, mol m^{-3}
z	Lithium concentration in the eigenspace of the transformed concentration u, m mol m^{-3}

Greek Symbols

α	Transfer coefficient, [-]
β	Fitting parameter
Γ	Constraint function of the optimisation problem
Δt	Time step, s

Δt_1	Time step in the optimisation, s
Δt_2	Time step in the time integration, s
ε	Volume fraction of active material, [-]
ζ	Dummy integration variable, m
η	Overpotential, V
$\bar{\Lambda}$	Matrix with the eigenvalues of the discrete diffusion PDE
λ	Price of electricity, € MWh^{-1}
ν	Poisson's ratio, [-]
Π	Objective function giving the profit, €
ρ	Density, kg m^{-3}
σ_h	Hydrostatic stress, Pa
σ_r	Radial stress, Pa
σ_t	Tangential stress, Pa
σ_{yield}	Yield strength, Pa
τ	Thickness, m
Φ	Revenue, €
Ψ	Degradation cost, €
Ω	Partial molar volume, $\mathrm{m}^3\ \mathrm{mol}^{-1}$

Superscripts

end	refers to the value of the property at the end of a period
max	refers to the maximum value of the property
mean	refers to the mean value of the property over a period
min	refers to the minimum value of the property
ref	refers to the value of the property at reference conditions
RMS	refers to the root-mean-squared value of the property over the period
T	refers to the transposed matrix

Subscripts

batt	refers to the entire battery or cell
cr	refers to the cracks on the surface
diss	refers to the dissolution reaction of the electrode
el	refers to the electrolyte
env	refers to the environment
i	$i \in \{p, n\}$ refers to the positive or negative electrode respectively
l	refers to the lower limit
n	refers to the negative electrode
P	refers to the optimisation maximising profit, i.e. maximising revenue while minimising degradation
p	refers to the positive electrode

pl	refers to the lithium plating reaction
R	refers to the optimisation maximising revenue and ignoring degradation
sei	refers to the SEI layer
u	refers to the upper limit

Acronyms / Abbreviations

BM	bucket model
BMS	battery management system
CC	constant current (dis)charge
CV	constant voltage (dis)charge
ECM	equivalent-circuit model
EMS	energy management system
FEC	full equivalent cycles
LAM	loss of active material
LFP	$\mathrm{LiFePO_4}$
LLI	Loss of lithium inventory
LMO	$\mathrm{LiMn_2O_4}$
MPC	model-predictive control
MTTB	market-trading test bench, a realistic implementation of the battery control algorithm
NMC	$\mathrm{LiNiMnCoO_2}$

OCV	open-circuit voltage
ODE	ordinary differential equation
P2D	pseudo-two-dimensional
PDE	partial differential equation
SEI	solid-electrolyte-interphase
SoC	state of charge
SPMe	single-particle model with electrolyte dynamics
SPM	single-particle model

Chapter 1

Introduction

This chapter gives a brief introduction to the main concepts of this work. Section 1.1 gives the background for grid-connected batteries and the economic environment in which they are operating. Section 1.2 explains how a grid-connected lithium-ion battery is made up of many small cells, and the operating principles of one such cell. Section 1.3 describes qualitatively how the performance of batteries decreases as they age, a process called 'battery degradation'. Finally section 1.4 shows the data which was used to parametrise the models in this work.

1.1 Storage for electricity grids

At all times, the electrical power generated on a network must equal the total consumption. Because the latter varies with time, flexible generation units which can modulate their output power are needed. Different types of generation technologies exist, each with their own dynamic limitations.

Storage can be used to support the system in the balancing of production and demand. Traditionally, this is done in pumped hydro plants, which pump water up and down over a height differential. In 2015, there was about 125 GW to 150 GW capacity installed globally (about 50 GW of which is located in Europe), mostly in large-scale systems of several hundreds of MW [1, 2].

1.1.1 Electricity markets

Power systems in many regions of the world have been liberalised. In the European Union, the successive energy directives have created competitive markets in which private companies trade electricity. Some markets are purely commercial exchanges between traders, producers or consumers at various scales and time horizons.

Other grid services require coordination by a central organisation, which is the ‘transmission system operator’. Examples of such services are the various types of reserves (to cover for unexpected outages), frequency control, black start capability, power quality services, etc. Depending on the country, there might be full-scale markets, open tender procedures or an over-the-counter procurement.

As a result, there are a large number of applications in which grid storage can be used. Comprehensive overviews for Europe are given in [1, 3–6], and for the US in [7–9]. Depending on who owns and operates the storage unit and where it is located, a different classification might apply. Because one physical action (e.g. discharging the battery) can create value for different market actors, a storage unit can deliver many applications ‘at once’. There are different names for this feature: application stacking, application synergies, multi-purpose use, multi-service use, etc. [5, 10–14]. This also covers the situation in which one storage unit is used for different applications at different points in time.

However, all applications come down to a time-varying price signal and a set of market rules. The price can be the market clearing price (which is not known *a priori*), or a contractually agreed price. Depending on the application, the time resolution of the market operation and consequently of the price variations can range from minutes to hours or months.

In this work, only wholesale energy arbitrage on the day-ahead market is considered. In this application, a battery operator has to put hourly bids into the market to buy and sell electricity (storing the energy in the storage unit between buying and selling). The market is cleared at a predefined hour, the day ahead of delivery, such that the operator knows which bids are accepted at which price well before the delivery needs to take place. A more detailed description is given in section 4.1.

Many other applications (e.g. trading on the intra-day or real-time market, behind-the-meter applications such as time-of-use tariffs or increased self-consumption of electricity generated by distributed assets, etc.) merely affect the price variation and time resolution without changing any of the constituent equations and would require only minimal adjustment in the methods used throughout this work.

1.1.2 Grid-connected batteries

The accelerating deployment of intermittent renewable energy sources, such as solar and wind generation, increases the variability on the electricity system. This increases the amount of frequency control and reserves required by the system, and causes larger price variations on many markets [15]. For instance, in the United Kingdom a new type of fast reserve was created, called ‘enhanced frequency response’. Although many technologies can take advantage of the opportunities this presents, battery energy storage systems are especially suited for such applications [16, 17].

Different types of battery storage systems exist, and various techno-economic analyses have compared them for various applications [18–20]. Many studies concluded that the business case is not yet profitable [19, 21–25]. However, lithium-ion batteries are becoming an important technology for the grid due to their decreasing costs [26, 27] and due to the increasing number of electric vehicles, whose batteries can deliver grid services when the cars are plugged in [28]. Various large-scale stationary batteries have already been installed [1, 29, 30].

The focus of this work is on stationary batteries, and vehicle-to-grid applications (and electric-vehicle batteries) are not discussed further, although they operate according to the same principles and could therefore be expected to lead to similar results. However, the optimisation problem will have more constraints relating to the availability of the battery for driving. Additionally, the degradation is more complicated due to the depreciation of the rest of the car and the option of a second-life application. Because both issues are worthy research topics on their own, they are considered to be out of scope of this work.

1.2 Lithium-ion batteries

Large battery systems consist of various components. Section 1.2.1 describes the different hardware and software elements in a grid-connected battery. Section 1.2.2 explains the cells making up the battery in more depth.

1.2.1 From energy storage system to cell

The energy is stored chemically in the cells, which tend to be very small (10 Wh to 100 Wh). Cells are grouped in modules which can consist of any number of series- or parallel-connected cells. In grid-connected batteries, modules are often combined into racks, which also have a power electronic converter, a cooling system, communication infrastructure, etc. A centralised battery management system (BMS) controls the battery, often assisted by a higher-level control system which allocates power to different parts of the battery [4].

The BMS keeps the battery in a safe operating condition and tries to keep all cells as uniform as possible. The BMS can use the balancing circuit to transfer energy between different parts of the battery (or selectively discharge certain parts) to equalise the voltage and state of charge of all cells. In large batteries with a forced cooling system, the BMS ensures the cells stay near the optimal operation temperature. Both centralised and decentralised BMSs exist, and if they succeed in keeping all cells uniform, the behaviour of a number of cells with minor cell-to-cell differences can be simulated by only considering one cell and multiplying by the number of cells [31, 32].

This work does not consider BMSs, cooling systems, power electronics etc. Therefore, a ‘perfect’ battery is simulated, where all components are assumed to behave ideally (and the power for the cooling system, BMS, etc. is taken from an external power source). Instead, only one cell is modelled and it is assumed this is representative of the entire battery. These assumptions are necessary to keep the optimisation problem tractable. It has been shown that the majority of the losses can be attributed to other components such as the inverter, transformer, and thermal management systems [33, 34]. The trade-off between efficiency and degradation was investigated in [35], which accounted for the power electronic converter and the cells but ignored other components. It showed that at low power levels, the efficiency of the converter dominates the operating cost. However, at the power levels which can be expected in the application studied here, the battery dominates the total cost of operation such that ignoring the power electronic converter is justified. Additionally, Schimpe et al. [36] did a thermal simulation of a 192 kWh grid-connected battery but only reported on the losses of the thermal system. Because the focus of this work is on the battery degradation, which takes place in the cells, all those other components are ignored in the analysis below.

1.2.2 Operating principles of a lithium-ion cell

A lithium-ion cell consists of two electrodes with a separator in between. The cell is soaked with a liquid electrolyte in which lithium ions can be transported. The electrodes have porous structures to enlarge the surface area and reduce the diffusion distances. During charge, lithium diffuses through the positive electrode and is de-intercalated at its surface, releasing an electron. The resulting lithium ion is transported in the electrolyte through the separator, intercalated at the negative electrode surface, where it absorbs an electron, and diffuses to the bulk material. The current collectors at both electrodes collect the electrons and conduct them to the external circuit. The state of charge (SoC) of a cell is an indication how much charge is stored in the cell relative to the maximum charge a cell can store within the safe operating region, which relates to the concentration of lithium in both electrodes [37].

Various different chemistries of lithium-ion cells exist. The most common anode[1] material is graphite, although lithium titanate and silicon have been used too. Various lithium metal oxides have been used as cathode, and sometimes different oxides are blended. The oxides can be classified in three groups based on their structure: ordered rock-salt (lithium cobalt oxide, nickel cobalt aluminium oxide, and nickel manganese cobalt oxide, NMC), spinel (lithium manganese oxide, LMO) or olivine (lithium iron phosphate, LFP) [37]. Detailed comparisons of the material properties of the different cathode materials are given in [38, 39]. Every chemistry has its own cell-level advantages and drawbacks; a detailed comparison is given by Zubi et al. [25]. Dubarry et al. [40] compared the calendar ageing of different cells, while Benato et al. [41] assessed the lifetimes of different batteries when they would be used for frequency regulation. In electric-vehicle applications, NMC is the dominant cathode chemistry, while for grid-connected storage both NMC and LFP are being used [25].

1.3 Lithium-ion battery degradation

This section gives a qualitative overview of the topic of battery degradation. It follows the same structure as section 2.2, which describes the models used to simulate the various mechanisms. The first four subsections describe the main mechanisms responsible for battery degradation, while section 1.3.5 lists other mechanisms not considered in the rest of this

---

[1] The terms anode and negative electrode are used interchangeably in this work, although strictly speaking the anode upon charge is the positive electrode and vice versa for the cathode.

work. Finally, section 1.3.6 describes how the different degradation mechanisms affect the performance of the cells.

1.3.1 Growth of the solid-electrolyte-interphase layer

At the graphite anode, lithium ions react with components of the electrolyte, forming solid reaction products which deposit on the graphite surface. This layer, called the solid-electrolyte-interphase (SEI) layer, passivates the surface and thus limits the side reaction. However, the isolation is not perfect and therefore the layer keeps growing, consuming lithium ions. Those ions can no longer participate in the main intercalation reaction, reducing the capacity of the cell. This is often considered to be the main degradation mechanism in lithium-ion cells [42, 43].

A comprehensive overview of the SEI formation and the reactions taking place is given in [44–47]. Zhuo et al. [48] noted that the composition of the SEI layer on formation depends on the cell voltage, and is not constant. The exact composition of the electrodes, electrolyte and additives also has a strong influence on the SEI layer [49, 50].

The side reaction is enhanced by pollution with other elements [51], especially by metal ions originating from the cathode. They provide electrically conductive paths through the SEI layer [42, 49, 50, 52].

The SEI layer can lead to other types of degradation. Gasses can be formed in related chemical reactions [42, 53] and the layer itself can clog pores in the anode. This isolates the active material ‘behind’ those pores, reducing the active surface area [42, 49, 53], which in turn can enhance other degradation mechanisms such as lithium plating [51].

Although not as important as on the anode, a passivation layer also grows on the cathode [45, 49–53]. This is not considered in this work.

1.3.2 Crack growth at the electrode surface

Lithium intercalation causes volume changes in the host material. When a cell is cycled, the alternating strain from the expansion and contraction causes alternating tension and compression. Volume changes, and subsequent stresses, can also be the result of phase changes in the electrode material.

Alternating stress cycles often result in crack growth (e.g. in metal fatigue). If cracks grow in the SEI layer, it can break apart and expose fresh graphite surface to the electrolyte. This causes the formation of a new SEI layer on those surfaces, accelerating the rate at which lithium ions are consumed by the SEI side reaction [49, 52, 54]. Cracks can also result from solvent co-intercalation, which will have the same effect [50].

1.3.3 Loss of active material

Loss of active material (LAM) is not a degradation mechanism as such, rather it is the result of a number of different mechanisms. To stay consistent with section 2.2[2], they are grouped into one category here.

Bernard et al. [55] described in detail how pores get blocked by the SEI layer and gas bubbles. This isolates the active material from the electrolyte, such that lithium ions can no longer intercalate and the active material becomes passivated.

Also, electrical contact between the active material and the current collector can be lost, often in a process similar to surface cracks from the previous section but with cracks growing inside the electrode, which causes the material to break off, or to lose contact with the binder. In this case, the electrons can no longer reach the current collector and vice versa, such that no lithium can (de)intercalate and the material is passivated [42, 51, 52, 56].

---

[2] Many physical degradation models simulate LAM directly, and therefore they are discussed in one section in chapter 2.

Cathode active material can also be lost by a dissolution side reaction. This is usually reported in LMO cells, where manganese is known to react with hydrogen fluoride, dissolve into the electrolyte and migrate to other parts of the cell (such as the SEI layer on the anode, where the Mn can be deposited and enhance the SEI growth) [42, 49]. Sahore et al. [57] investigated transition-metal dissolution in NMC cathodes and found that at low voltage, it was dominated by acid attack. However, at higher voltages, chemical and electro-chemical oxidation of the organic solvent in the electrolyte seem to contribute significantly to the metal dissolution.

Structural disorder reactions can also alter the composition of the cathode, occupying the lithium reaction sites [42].

1.3.4 Lithium plating

Instead of intercalating into the graphite anode, lithium ions can be deposited as metallic lithium on top of the graphite [49]. This can be due to kinetic effects (the deposition reaction is favoured due to low anode potential and large overpotentials on charge) or due to diffusion limitations (diffusion inside the graphite becomes slower than the transport to the surface, causing a surplus of lithium ions at the surface). Therefore, there is a ‘critical combination’ of operating conditions causing lithium plating [58]. Plating can be a local effect due to inhomogeneities in the current density or the electrode material [43, 59]. In theory, the plating is reversible as long as electrical contact with the graphite is present [52]. Liu et al. [60] and Waldmann et al. [61] given an extensive overview of lithium plating.

As was the case with the SEI layer, the plating side reaction removes lithium from the main intercalation reaction, thus reducing the capacity of the cell. While plated lithium is present, it can lead to excessive SEI layer growth. It also poses a safety risk because of dendrite formation, which can cause internal short circuits, and because it can engage in an exothermal reaction leading to thermal runaway [49, 52, 61].

1.3.5 Other degradation mechanisms

There are many other degradation mechanisms. All components of the cell can degrade due to alternating stress or side reactions. Binder degradation and current-collector corrosion increase the resistance [42, 62], electrolyte degradation reduces its transport capabilities [42, 49, 63], electrolyte dry-out can passivate entire electrode regions [64] and gas can be produced in a side reaction consuming electrolyte and/or active materials, which leads to a pressure build-up in the cell [42, 51]. Other design-related aspects can enhance existing degradation mechanisms, or introduce new mechanisms (uneven current distribution, pressure gradients, excess anode material, etc.) [49].

Inhomogeneities are often mentioned in relation to degradation. Inhomogeneities can originate from three sources: (1) differences in electrode compositions and material properties (e.g. particles of different size and shape [59], or porosity variations [65]); (2) differences in the operational state of the cell (local SoC differences [66], temperature gradients [67], or heterogeneous stress distributions [68]); (3) impurities (water enhances gas evolution, SEI growth, and $LiPF_6$ decomposition, which in turn produces hydrogen fluoride which can engage in acid attack on the cathode [42, 44, 49, 69], salt impurities form a resistive layer [44], fluoride ions react with lithium [70], etc.).

These inhomogeneities can greatly enhance the before-mentioned degradation mechanisms: pollution of the SEI layer increases its growth rate (section 1.3.1) and local effects such as larger overpotentials or concentrations increase the risk of lithium plating (section 1.3.4). Harris et al. [65] even claimed that "most Li-ion battery failure can be ascribed to the presence of nano- and microscale inhomogeneities".

Many researchers have studied the ‘knee’ or ‘roll-over’ point when the degradation rate of a cell suddenly increases. As mentioned in section 1.3.1, SEI layer growth can enhance lithium plating due to pore clogging. Because metallic lithium can react with the electrolyte and form its own SEI layer, this can result in a positive feedback loop accelerating the degradation rate of a battery [52, 71]. Others attribute the accelerated degradation to SEI only (clogging pores and enhancing itself) [51], to a positive interaction between anodic LAM and plating [71], or to heterogeneous effects [68].

1.3.6 Degradation effects

Some of the degradation mechanisms consume lithium ions, which can then no longer intercalate. This reduces the amount of charge which can be stored because per electron, one lithium ion is needed. Other mechanisms reduce the amount of (accessible) active material. This will also reduce the charge capacity because there are fewer sites in the electrode where lithium can react. LAM also increases the resistance of a cell because for the same total battery current, the current density on the remaining active material is larger. Some mechanisms directly increase the resistance but do not reduce the charge which can be stored in the cell (e.g. electrolyte decomposition or current collector corrosion).

The resistance increase reduces the power a cell can deliver, the charge which can be stored at a given current, and the efficiency of the cell (thus reducing the energy which can be stored). However, it does not affect the charge which can be stored in the cell at sufficiently low currents.

In this work, degradation always relates to a decrease in the total charge which can be accessed between the voltage limits of the cell. It therefore ignores the resistance increase. This is because the charge capacity is relatively well defined and constant (while the resistance depends on temperature, SoC, power, time step, etc.). The power degradation is not expected to be a large problem in the applications considered in this work given that grid-connected batteries rarely deliver high powers (above 1C[3]). The decreased efficiency is not directly considered as 'degradation' but it will be accounted for indirectly because a cell can deliver less usable energy (see section 4.3.2). Other secondary effects of degradation (increased

---

[3] The C-rate of a cell is the current divided by its nominal (charge) capacity. E.g. for a 2.7Ah cell, a 1C current is 2.7A.

cell-to-cell variation, more heat generation, higher failure rates, safety risks, etc.) are ignored throughout this work.

1.4 Battery data

This section shows the data which is used throughout this thesis. The data was collected by various partners in the Mat4Bat project from the European Union [72], which unfortunately introduced some challenges with the data[4]. The experiments used high-power, prismatic 16 Ah cells manufactured by Kokam (SLPB78205130H) [73]. The chemistry was reported to be NMC/C although analysis by Birkl et al. [74] of a very similar cell identified the cathode to be a mix of lithium cobalt oxide and lithium nickel cobalt oxide.

During the check-up tests, the resistance of the cells was measured with a 1C pulse test. Both charging and discharging resistances were measured at various SoCs and with different time delays. The resistance of fresh cells was below 5 mΩ for most test conditions; only at 0% SoC, the resistance measured at 1C measured over 30s increased to 20 mΩ but that is probably due to the change in open-circuit voltage (OCV). Over the cells' lifetime, the resistance slowly increased. At the end of life, it had doubled in cases where the cells had severely degraded, with smaller increases for less-degraded cells.

1.4.1 Characterisation data

The cells were disassembled and both electrodes combined with a lithium reference electrode in two separate coin cells. These were used to measure the half-cell potential[5] curves. When added up, they did not replicate the cell's measured OCV. The maximum recorded cathode voltage was 4.04 V, indicating that the cathode was not fully delitiated in the measurement.

---

[4] The raw data files were difficult to understand because every parter had their own format and data collection procedure. The only usable data was in the excel sheets which the partners used to communicate their findings.

[5] The terms 'potential' and 'OCV' are used interchangeably. Half-cell values are always measured with respect to Li/Li$^+$.

Therefore, additional data points were added at lower lithium concentrations and higher cathodic potential according to Awarke et al. [75]. Then the full cathode OCV curve was rescaled to produce the full-cell OCV curve. Fig. 1.1 shows the measurements with dots and the modified curves are shown with lines. Hysteresis of the OCV curve is ignored throughout this work.

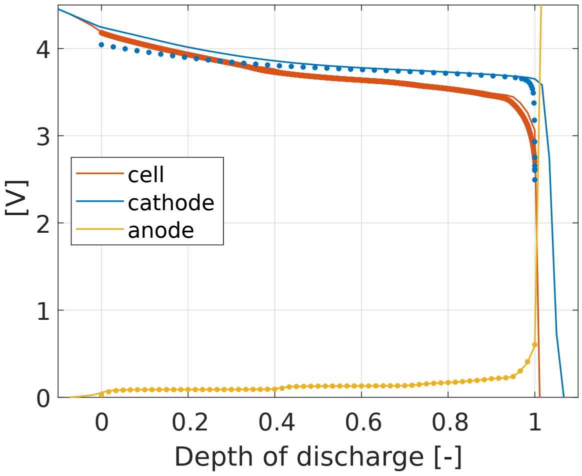

Fig. 1.1 Half-cell OCV data, the dots indicate the measured values, while the lines show the modified curves used in this work.

Fig. 1.2 shows the current and voltage measured during constant-current (CC) discharges at various C-rates. As can be seen, the capacity retention at high C-rates is still large because this is a high-power cell. No data from pulse tests or dynamic use profiles was available.

1.4.2 Calendar ageing

An extensive calendar ageing experiment was conducted within the Mat4Bat project. The cell degradation over time is shown on Fig. 1.3, note the different y-axis limits on the figures. The relative remaining capacity is obtained by dividing the capacity with the total initial capacity of each separate cell, such that they all start at 100% and the cell-to-cell variation is ignored. As can be seen, there is a large effect of SoC, especially at 45°C and 25°C. Calendar ageing at 60°C was also tested, but those cells degraded very rapidly due to decomposition

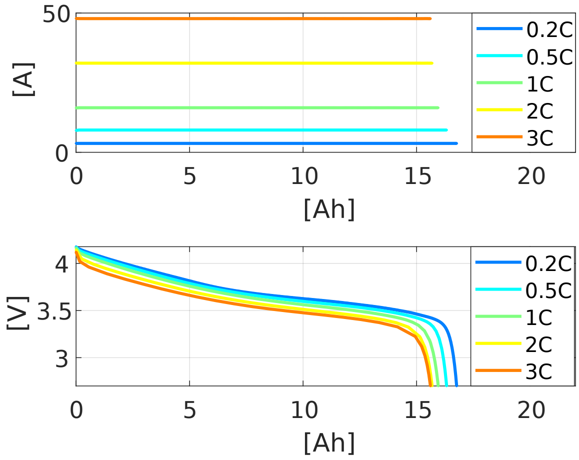

Fig. 1.2 Characterisation data for CC discharges at various C-rates. (A) current; (B) voltage.

of the electrolyte resulting in gas formation and electrode dry-out, which caused lithium plating during the check-up cycles [72, 76, 77]. Because those degradation mechanisms are not considered in this work, and the cell temperature in the application considered here will always remain well below 60°C, this data was not used in this work. Post-mortem studies identified SEI growth as the dominant degradation mechanism at 5°C, 25°C and 45°C [72, 78].

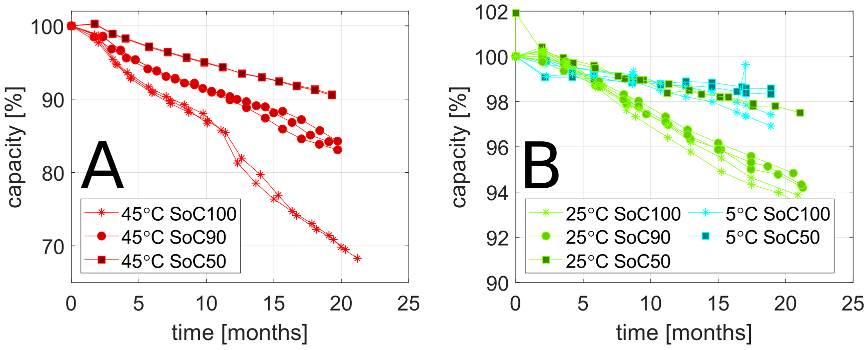

Fig. 1.3 Calendar ageing data at various temperatures and SoC levels. (A) at 45°C; (B) at 25°C and 5°C.

1.4.3 Cycle ageing

Fig. 1.4 shows the results of the cycle-ageing experiment. The relative remaining capacity is obtained by dividing the capacity with the total initial capacity of each separate cell, such that they all start at 100% and the cell-to-cell variation is ignored. Cells were cycled at various temperatures, charging currents and between different SoC windows, the discharge was always at 1C. The top two figures in Fig. 1.4 show degradation at a constant SoC window. Degradation at 25°C is less severe than at other temperatures, although no data for the SoC window 0%-100% at 5°C is available. The bottom figure shows degradation for all SoC windows at 45°C, and duplicates some data from the top two figures. Cycling at very high SoC-levels leads to excessive degradation. The 'middle' window between 10% and 90% results in the lowest degradation. There is no strong influence of the charging current except at 5°C and when cycling in high SoC windows at 45°C.

Post-mortem analyses identified certain causes of the observed degradation [72, 79, 80]: at 5°C, a homogeneous metallic lithium layer was deposited on the anode surface and at 45°C and high charging currents, lithium plating also occurred but in an inhomogeneous way, producing 'islands' of metallic lithium. No explanation is given for the rapid degradation for cells cycling at 1C and high SoC levels compared to the same tests at lower SoC windows. Both at 45°C and at 25°C, cycles with a maximum SoC of 100% increase the degradation compared with cycling to 80% or 90%. It is also not clear why the degradation of the cells cycled at 5°C levelled off after a few 100 cycles.

1.5 Thesis outline

Chapter 1 (Introduction) has outlined the two main fields which are combined in this work. One the one hand, lithium-ion batteries are being used increasingly for economic

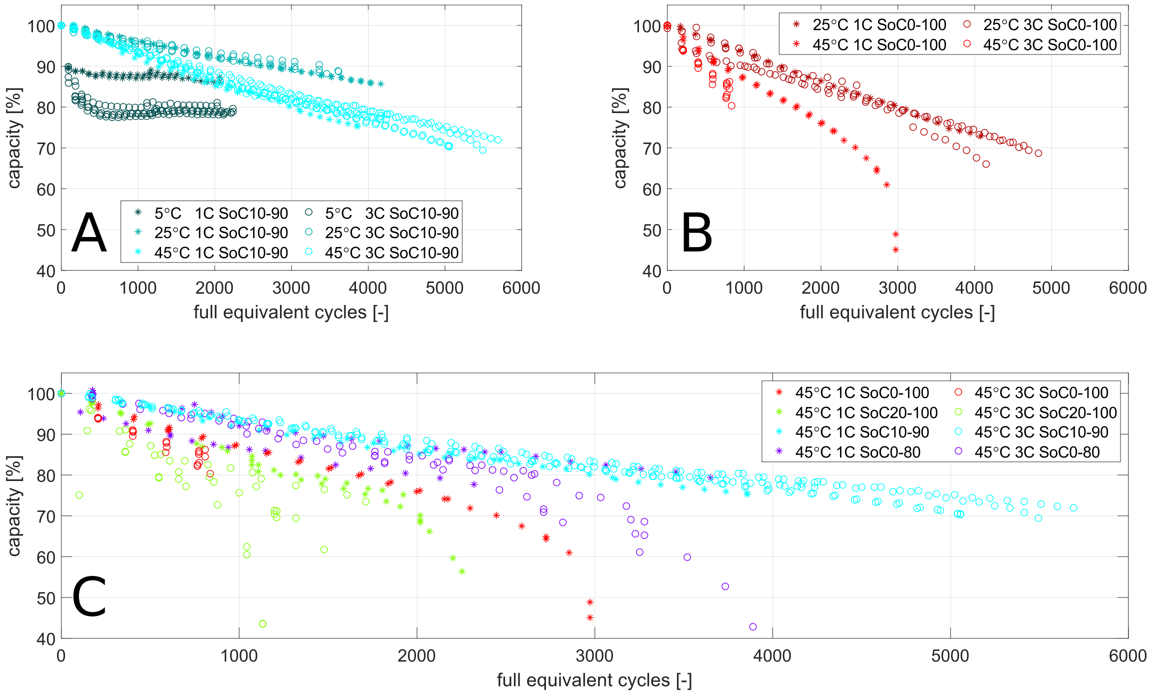

Fig. 1.4 Cycle ageing data at various temperatures, currents, and SoC windows. C denotes the C-rate on charge; all discharges were at 1C. (A) degradation for the SoC window between 10% and 90%; (B) degradation for the SoC window between 0% and 100%; (C) degradation for all SoC windows at 45°C.

applications on the power system. On the other hand, the lifetime of batteries is a hugely complicated process with many interacting degradation mechanisms. Combining both, the central research question is how the economic 'optimal' use of a lithium-ion battery is influenced by the degradation and vice versa.

Chapter 2 (Battery degradation modelling) drills deeper into the methods for simulating battery degradation. It presents a literature review of various physics-based models and identifies how different models are needed to capture different trends in a large data set.

Chapter 3 (Optimal control of nonlinear battery models) explains the model formulation and optimal control techniques used to optimise nonlinear battery and degradation models. It presents the spatial and temporal discretisation used to minimise the number of optimisation variables, how they can be decoupled, and which off-the-shelve software is used for the optimisation.

Chapter 4 (Optimal battery utilisation for electricity trading) finally combines the battery model and optimisation techniques with an economic framework. It presents the optimal outcomes according to battery models of different complexity and shows how the outcome from the physics-based battery and degradation model outperforms conventional models in a year-long experiment.

Chapter 5 (Conclusions) summarises the conclusions from the different chapters, points to the limitations of this work and suggests areas for future work.

Appendix A (Fits of the battery models) shows how well the different battery models used in the optimisation from chapter 4 fit a large data set. This gives an indication about how accurate the 'optimal' outcomes from the different models will be.

Appendix B (Simulation of the optimal usage profiles) discusses the different approaches for dealing with voltage limits when a cell tries to follow the 'optimal' profiles. It simulates three different approaches for each model, and discusses how the results differ for the various models.

Chapter 2

Battery degradation modelling

Section 1.3 gave a qualitative overview of the processes which cause battery degradation. This chapter discusses the different approaches taken in literature to simulate these processes. Firstly, the battery model is explained in section 2.1. This model comprises the equations to calculate the battery states related to the main lithium intercalation reaction. These states are time dependent but mostly independent of the lifetime of the battery, such as lithium concentration, temperature, etc. The next section, 2.2, introduces the models proposed in literature for the various degradation mechanisms. Sections 2.3 and 2.4 give details on how the equations were implemented and parametrised. The results of the simulations are given in section 2.5 and discussed in section 2.6. Finally, the conclusions are drawn in section 2.7 and future work is outlined in section 2.8.

The degradation processes decrease the battery's performance in different ways. As explained in section 1.3.6, the main focus of this work is the loss of capacity, defined as the total charge which can be stored between the safe operating limits of the cells. In the simulations, the capacity was 'measured' by simulating a full constant-current constant-voltage (CC-CV) charge-discharge cycle between the lower and upper voltage limits. The integral of the current gives the capacity of the cell. As is the case for experiments, the capacity depends on the exact cycle used, e.g. which current threshold is used for the CV phase. For the results in this chapter, the simulated capacity was obtained using a C/25 current in the CC phase and a 0.005 mA threshold for the CV phase. The resistance increase was accounted for in the simulations, but the analysis does not consider the resistance.

Most of this chapter has been published in [81].

2.1 The battery model

Many different models have been developed for lithium-ion batteries with a trade-off between more detailed insights and computational complexity. Atomistic models based on ab initio calculations can be used to simulate material properties [39], such as diffusion constants [82] or the effect of passivation layers on lithium intercalation [83]. On a molecular scale, phase changes can be studied with phase-field approaches [84], while microscale models using non-equilibrium thermodynamics can be used to simulate 3D microstructures of porous electrodes [85]. Continuum models assume more homogeneous behaviour, significantly reducing the computational complexity. The most popular continuum model is the so-called pseudo-two-dimensional (P2D) model, which was developed by Newman et al. [86]. It simulates lithium transport and diffusion in two dimensions: inside a solid particle and along the thickness of a cell, allowing a concentration gradient over the thickness of an electrode depending on the electrolyte transport and a gradient inside the particle depending on solid diffusion. Other, non-physics-based models such as equivalent-circuit models (ECMs), only describe the observed input and output measurements without considering the physical processes taking place inside the battery [87]. Although these models can be very accurate and useful in specific situations, their validity is limited to the specific operation conditions for which they have been developed and therefore they may lack generality [53, 87, 88]. Secondly, they don't explain why the observed behaviour is happening, making it more difficult to justify how the battery utilisation should change to avoid certain behaviours.

In order to have a model general enough for optimisation, a continuum model was used throughout this work. The P2D model has a complex mathematical structure, including algebraic constraints, making it computationally expensive to use. Therefore, it is not well suited for degradation simulations which need to model the entire battery lifetime, nor for optimisation purposes. By removing the ‘thickness’ dimension, i.e. assuming electrolyte transport and migration, and electrical conductivity in the electrodes and electrolyte is fast [89, 90], one of the simplest continuum models is obtained: the single-particle model (SPM). Based on early work by Atlung at al. in 1979 [91], it was fully developed in the late nineties by Haran et al. [92, 93], and later adapted for lithium-ion batteries by Ramadass et al. [94] and Ning et al. [95]. Ignoring the thickness-dimension is acceptable at low current, on the order of 1C [88, 96], even more so in high-power cells which have thin electrodes.

The SPM was selected for this work, because it can be solved fast enough for long-term simulations and is simple enough to be optimised. The SPM includes the most basic physical processes taking place, making it more general than ECM-style models. Because the current requirements of grid-connected batteries rarely exceed 1C, the SPM can considered to be valid. However, using the SPM introduces simplifications and limitations which are discussed in section 2.8.

Section 2.1.1 gives the equations for the SPM, comprising the diffusion partial differential equation (PDE), the insertion kinetics and the voltage equation. Section 2.1.2 explains the bulk thermal model used to calculate the cell temperature, and section 2.1.3 lists the equations to calculate the stress. The temperature model is coupled with the SPM, while the stress model only affects the degradation equations. Stress-induced diffusion is not considered as explained in section 2.1.3.

In this work, a negative current means the battery is charging, while a positive current discharges the battery. The terms anode and negative electrode are used interchangeably. Whilst this is correct for discharging, strictly speaking during charging the anode is the

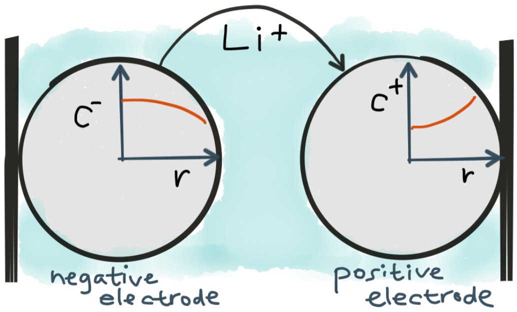

Fig. 2.1 The single-particle model.

positive electrode and the cathode is the negative electrode. Also the terms potential and open-circuit voltage (OCV) are used interchangeably, while the term voltage is used when a current is running in the cell. In the equations, time dependency is not written to simplify notation.

2.1.1 The single-particle model

In the single-particle model (SPM), shown on Fig. 2.1, every electrode is represented by one spherical particle [94, 95]. Lithium diffuses inside them as described by Fick's law of diffusion (2.1) where c is the lithium concentration in [mol m^{-3}], r is the radial coordinate in [m] and D is the diffusion constant in [m^2 s^{-1}] which is a function of the temperature T in [K]. The subscript $i \in \{p,n\}$ refers to the positive or negative electrode respectively.

$$\frac{\partial c_i(r)}{\partial t} = \frac{D_i(T)}{r^2}\frac{\partial}{\partial r}\left(r^2\frac{\partial c_i(r)}{\partial r}\right) \tag{2.1}$$

At the centre, the concentration gradient must be zero due to symmetry, see (2.2). At the surface, the concentration gradient is directly proportional to the molar lithium flux j in [mol m^{-2} s^{-1}], which is a function of the insertion current density i in [A m^{-2}], Faraday's constant F in [C mol^{-1}] and the number of electrons involved in the reaction n, which equals one for lithium. The electrode is assumed to be homogeneous such that the current density on the particle is the fraction of the total battery current I in [A] and the total active surface area, which is the product of the specific surface area a in [m^2 m^{-3}], the geometric surface area A in [m^2] and the electrode thickness τ in [m]. The sign is opposite for both electrodes, positive at the cathode and negative at the anode. Assuming perfectly spherical particles of radius R in [m], the specific surface area can be calculated by (2.4), where ε is the volume fraction of active material.

$$D_i(T)\left.\frac{\partial c_i(r)}{\partial r}\right|_{r=0} = 0 \tag{2.2}$$

$$D_i(T)\left.\frac{\partial c_i(r)}{\partial r}\right|_{r=R_i} = \pm j_i = \pm\frac{i_i}{nF} = \pm\frac{I}{nFa_iA_i\tau_i} \tag{2.3}$$

$$a_i = 3\frac{\varepsilon_i}{R_i} \tag{2.4}$$

At the surface, the lithium is intercalated into the active material, or deintercalated out of it. This process is assumed to follow Bulter-Volmer kinetics (2.5) with exchange current density i_0 in [A m^{-2}], transfer coefficient α, ideal gas constant R_g in [J mol^{-1} K^{-1}] and overpotential η in [V]. The exchange current density can be calculated by (2.6) with rate constant k in [m$^{4-3\alpha}$ s^{-1} mol$^{\alpha-1}$], constant lithium concentration in the electrolyte c_{el} in [mol m^{-3}] and maximum lithium concentration in the active material $c^{\max}$ in [mol m^{-3}].

$$i_i = i_{0,i}\left(\exp\left(-\frac{\alpha nF}{R_gT}\eta_i\right) - \exp\left(\frac{(1-\alpha)nF}{R_gT}\eta_i\right)\right) \tag{2.5}$$

$$i_{0,i} = nFk_i(T)c_i(R_i)^{\alpha}c_{\mathrm{el}}^{1-\alpha}\left(c_i^{\max} - c_i(R_i)\right)^{1-\alpha} \tag{2.6}$$

The total DC resistance of the cell, $R_{\text{dc,batt}}$ is the sum of the DC resistances of the anode, cathode and SEI layer (2.7), where r_{dc} is the specific DC resistance in [Ω m^2][1]. Since the electrolyte is not simulated, its contribution to the resistance is lumped into the resistances of the electrodes.

$$R_{\text{dc,batt}} = \frac{r_{\text{dc},n}}{a_n A_n \tau_n} + \frac{r_{\text{dc},p}}{a_p A_p \tau_p} + \frac{r_{\text{dc,sei}}}{a_n A_n \tau_n} \tau_{\text{sei}} \tag{2.7}$$

The open-circuit voltage (OCV), U in [V], can be calculated using (2.8), where $\frac{\partial U_{\text{batt}}}{\partial T}$ represents the entropic coefficient and the superscript ref indicates the property at reference conditions. The cell voltage is then the difference of the OCV and the kinetic and ohmic voltage drops, (2.9).

$$U_{\text{batt}} = \left(U_p^{\text{ref}} \left(c_p \left(R_p \right) \right) - U_n^{\text{ref}} \left(c_n \left(R_n \right) \right) \right) + \left(T - T^{\text{ref}} \right) \frac{\partial U_{\text{batt}}}{\partial T} \tag{2.8}$$

$$V_{\text{batt}} = U_{\text{batt}} - \left(\eta_n - \eta_p \right) - R_{\text{dc,batt}} I \tag{2.9}$$

2.1.2 Thermal model

The basic SPM was extended with a bulk thermal model developed by Guo et al. [97]. In this model, the cell has a uniform temperature which can differ from the environmental temperature due to three heat sources: ohmic, reaction and entropic heat originating from the DC resistance, lithium intercalation and entropic changes, respectively. There is convective heat transfer between the cell and the environment at temperature T_{env}. The heat balance of the cell determines the change in the battery temperature according to (2.10), where ρ_{batt} is the bulk density of the cell in [kg m^{-3}], the product of A_{batt} and τ_{batt} is the total cell volume,

---

[1] Except $r_{\text{dc,sei}}$ which has units of [Ω m] because the SEI resistance is relative to its thickness.

C_p is the heat capacity of the cell in [J kg^{-1} K^{-1}] and h is the convective heat transfer coefficient in [W m^{-2} K^{-1}].

$$\rho_{\text{batt}} A_{\text{batt}} \tau_{\text{batt}} C_{p,\text{batt}} \frac{\partial T}{\partial t} = I^2 R_{\text{dc,batt}} + I\left(\eta_n - \eta_p\right) + IT \frac{\partial U_{\text{batt}}}{\partial T} - hA_{\text{batt}}\left(T - T_{\text{env}}\right) \tag{2.10}$$

The diffusion and rate constants are temperature dependent according to Arrhenius' law with activation energies E_D and E_k in [J mol^{-1}] respectively (2.11) and (2.12).

$$D_i(T) = D_i^{\text{ref}} \exp\left[\frac{E_{D,i}}{R_g}\left(\frac{1}{T} - \frac{1}{T^{\text{ref}}}\right)\right] \tag{2.11}$$

$$k_i(T) = k_i^{\text{ref}} \exp\left[\frac{E_{k,i}}{R_g}\left(\frac{1}{T} - \frac{1}{T^{\text{ref}}}\right)\right] \tag{2.12}$$

2.1.3 Stress models

Some degradation models depend on the stress in the particles. The stress model developed by Dai et al. [98] was used although various other researchers arrived at similar equations [99–102]. They ignored phase changes and could therefore directly link the stress to the lithium concentration profile inside the spherical particles. The radial stress σ_r and the tangential stress σ_t, both in [Pa], as a function of radius are given respectively by (2.13) and (2.14) where Ω is the partial molar volume in [m^3 mol^{-1}], Y is the Young's modulus in [Pa], ν is the Poisson's ratio and ζ is a dummy integration variable. The radial and tangential stress can be combined to the hydrostatic stress σ_h (2.15). It should be noted that the stress does not affect the rest of the battery model, i.e. stress-driven diffusion is ignored, because it would make the model too complicated for the optimisation later on in this work. Additionally, stress-driven diffusion is not included in any of the papers simulating battery degradation. including those describing mechanical degradation. Fu et al. [102] showed that the effect of stress-driven diffusion during a 7C discharge accounts for about 0.01 V. Given that the currents in this work are much smaller, the impact of ignoring stress-driven diffusion seems rather limited.

$$\sigma_{r,i}(r) = \frac{2\Omega_i Y_i}{3\,(1-\nu_i)} \left(\frac{1}{R_i^3} \int_0^{R_i} c_i(r) r^2 \mathrm{d}r - \frac{1}{r^3} \int_0^{r} c_i(\zeta) \zeta^2 \mathrm{d}\zeta \right) \tag{2.13}$$

$$\sigma_{t,i}(r) = \frac{\Omega_i Y_i}{3\,(1-\nu_i)} \left(\frac{2}{R_i^3} \int_0^{R_i} c_i(r) r^2 \mathrm{d}r + \frac{1}{r^3} \int_0^{r} c_i(\zeta) \zeta^2 \mathrm{d}\zeta - c_i(r,t) \right) \tag{2.14}$$

$$\sigma_{h,i}(r) = \frac{\sigma_{r,i}(r) + 2\sigma_{t,i}(r)}{3} \tag{2.15}$$

Laresgoiti et al. [103] derived similar equations, but removed the assumption of a constant partial molar volume, i.e. Ω was a function of the lithium fraction in the particle. Using their model, they then calculated the maximum tangential stress in the SEI layer $\sigma_{t,\mathrm{sei}}$ as a function of the lithium fraction of the graphite and argued this stress was related to degradation (rather than the stress in the particles themselves as given by the previous equations).

2.2 Battery degradation models

There are three broad approaches to battery degradation modelling:

Empirical models are parametric functions interpolating data points from large-scale degradation experiments [104–108]. They are only accurate for the cell type used in the experiments and for the operating conditions which were tested. Extrapolation to different load profiles or different cells might lead to large inaccuracies (see section A.2.2). They are typically coupled with ECMs because the idea behind both approaches is similar, namely to simulate what can be observed without modelling the underlying physical phenomena.

Physical models are collections of differential equations describing the mechanical, electrical, chemical and thermal processes responsible for battery degradation [53, 88, 106, 109, 110]. They are more general and should be capable to extrapolate behaviour to different operating conditions as long as all relevant physical phenomena are modelled, but they are difficult to parametrise and often are computationally complex to solve. They are mostly used in conjunction with a physical battery model.

Machine learning models are typically black-box approaches using vast data sets [111–115]. They can be more flexible than empirical models, but require larger data sets and the outcomes might be difficult to interpret and explain.

In this work, physical degradation models are used because they are more reliable for extrapolation, such that the optimisation solver has more accurate simulation results available in a larger search space. This also facilitates a modular approach where different equations can be added as needed to fit the data. Therefore, it is possible to find a minimal viable set of model equations which can be used for optimal control in chapter 3.

For a single *mechanism*, i.e. a physical process that causes battery degradation, multiple *models*, i.e. sets of mathematical equations, have been proposed in the literature. Fig. 2.2 graphically illustrates the various mechanisms and Table 2.1 gives an overview of the different models that have been proposed in literature to simulate them. The following sections discuss a number of representative models in more detail, grouped per mechanism as explained in section 1.3: section 2.2.1 for the growth of the SEI layer, section 2.2.2 for cracking of the graphite surface and SEI layer, section 2.2.3 for loss of active material, section 2.2.4 for lithium plating, and 2.2.5 for other degradation mechanisms.

2.2.1 Growth of the solid-electrolyte-interphase layer

One of the most important degradation mechanisms in Li-ion batteries with graphite anodes is the growth of the solid-electrolyte-interphase (SEI) layer, as was described in section 1.3.1.

Table 2.1 Overview of various degradation models grouped by mechanism

Paper	SEI growth				Crack growth			LAM				
	kinetics	solvent diffusion	electron tunnelling	simplified model	stress	crack growth	simplified model	crack growth	simplified model	dissolution	li-plating	other
Appiah [116]	x									x		x
Barai [117]							x					
Cannarella [118]											x	
Christensen [119]	x	x								x		
Delacourt [120]	x								x			
Deshpande 2012 [121]				x	x	x						
Deshpande 2017 [122]				x			x					
Ekstrom [123]	x	x					x					
Ge [124]											x	
Jin [125]	x			x					x			
Kamyab [126]	x	x										
Kindermann [127]	x						x			x		
Kupper 2017 [128]	x			x								
Kupper 2018 [64]	x			x	x		x					x
Laresgoiti [103]					x	x	x					
Legrand [129]											x	
Li [130]			x									
Lin [131]	x			x						x		x
Narayanrao [56]				x				x	x			
Ning [95]	x											
Pinson [132]	x	x										
Ploehn [133]		x										
Prada [134]	x	x										
Purewal [135]				x	x	x						
Ramadass [94]	x											
Randall [136]	x											
Sarafi 2009 [137]	x	x										
Safari 2010 [138]	x						x					
Safari 2011 [139]	x	x										
Single [140]	x	x										
Sturm [141]											x	
Tahmasbi [142]	x	x										
Tang [143]	x		x	x								
Yang [144]	x	x									x	

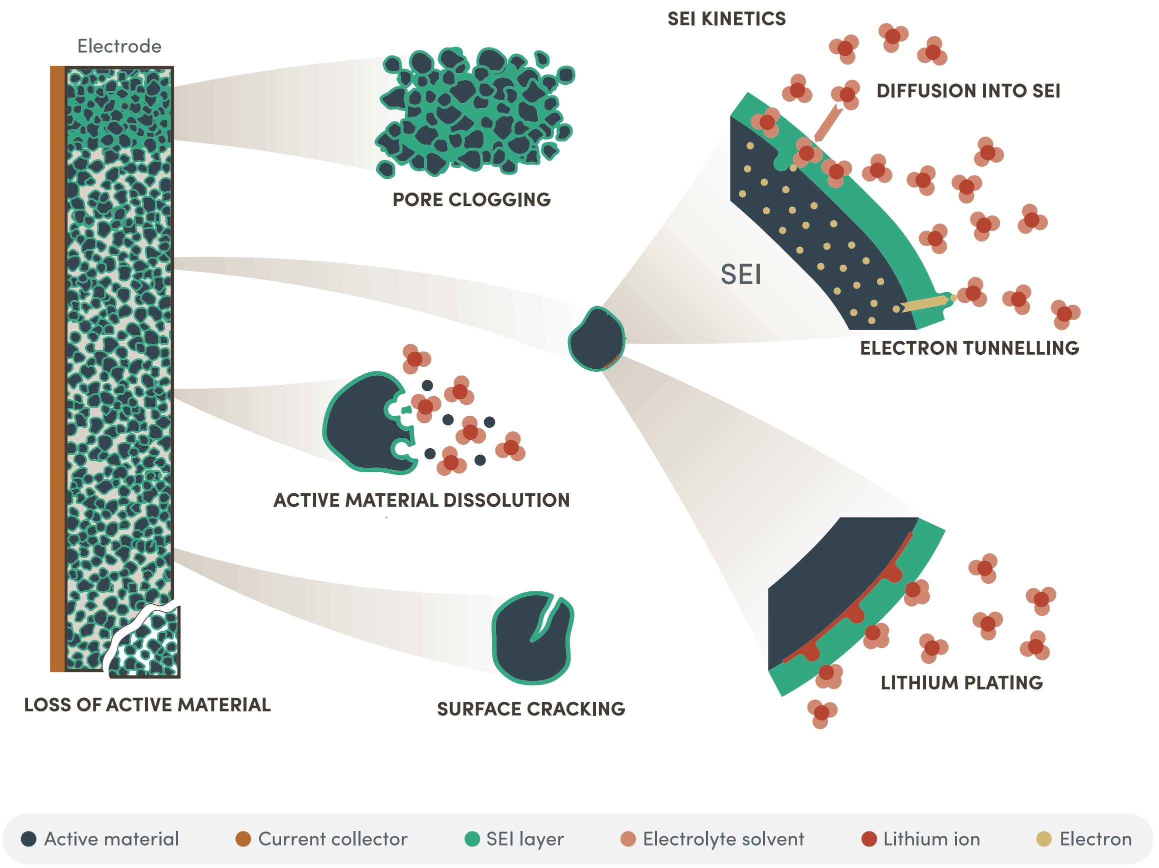

Fig. 2.2 Graphical illustration of the various degradation mechanisms.

The electrolyte solvent reacts with lithium ions and electrons at the surface of the graphite. The solid reaction products form a layer on the graphite which protects the surface from further reactions [44, 45, 47]. Various reactions have been suggested (depending on the local voltage) [46, 48], but the reaction modelled by most researchers is one between ethylene carbonate and lithium ions (2.16) [95, 128].

$$2\,C_3H_4O_3\,(l) + 2\,e^- + 2\,Li^+ \rightleftharpoons (CH_2OCO_2Li)_2\,(s) + C_2H_4\,(g) \tag{2.16}$$

Different models for this process have been suggested. Horstmann et al. [145] and Single et al. [146] give an overview of multi-scale models for SEI growth. For the continuum scale that is studied in this work, the models can be classified in four categories: kinetically limited, solvent diffusion limited, electron tunnelling and simplified models.

The most popular, and simplest, approach assumes that the layer grows at the interphase between the existing layer and the electrolyte such that no diffusion is required and the growth of the SEI layer is limited by the kinetics of the reaction [94, 95, 116, 120, 125, 127, 136, 138, 147]. Das et al. [148] propose a detailed kinetically limited SEI growth model with spatially resolved concentrations, but most authors use a Tafel equation[2] to determine the side reaction current density i_{sei} in [A m^{-2}] (2.17) where $i_{0,\mathrm{sei}}$ is the exchange current density in [A m^{-2}] as given by (2.18) and η_{sei} is the overpotential in [V] as given by (2.19). The reaction constant $k_{\mathrm{sei}}(T)$ is considered as a temperature-dependent fitting parameter, while the concentration of solvent in the electrolyte $c_{s,\mathrm{el}}$ is assumed to be constant. The OCV of the SEI growth side reaction U_{sei} is a constant with values between 0.4 V and 0.8 V with respect to Li/Li$^+$ [149]. Because the reaction takes place at the surface of the SEI layer, an extra term accounting for the resistive voltage drop across the SEI layer must be added to the equation for the SEI overpotential [126]. During calendar periods, the overpotential of the anode η_{n} is

---

[2] All papers use a conventional Tafel equation as indicated in (2.17). When the overpotential η_{sei} is zero, i_{sei} is not zero, causing an 'offset' error in the equation. However, the value of $i_{0,\mathrm{sei}}$ is extremely small, about 10^{-10} A m^{-2} in this work, compared to the current density from the main reaction which is in the order of 1 A m^{-2}. Therefore, this error is negligible; the 'offset' this causes is on the order of 1 Ah per billion years.

zero, but this is not the case for the SEI overpotential η_{sei} such that calendar ageing is still predicted. Therefore, this model can simulate both calendar and cycle ageing, where the latter is usually higher than the calendar ageing due to the nonzero anode overpotential and resistive voltage drop.

$$i_{\text{sei}} = i_{0,\text{sei}} \exp\left(-\frac{\alpha_{\text{sei}} nF}{R_g T} \eta_{\text{sei}}\right) \tag{2.17}$$

$$i_{0,\text{sei}} = nF k_{\text{sei}}(T) c_{s,\text{el}} \tag{2.18}$$

$$\eta_{\text{sei}} = U_{\text{n}} + \eta_{\text{n}} - U_{\text{sei}} + \frac{r_{\text{dc,sei}}}{a_n A_n \tau_n} \tau_{\text{sei}} I \tag{2.19}$$

Others assume that the SEI layer grows on the interphase between the graphite and the existing SEI layer, such that the solvent first has to diffuse through the existing layer before it can react. Some researchers explicitly simulate the diffusion of solvent through the SEI layer [133, 134, 137, 139, 140, 142, 144] but most assume linear diffusion of the solvent and an equilibrium concentration at the graphite surface. In the latter case, the solvent concentration at the surface can be eliminated by combining the kinetic and diffusion equations [119, 123, 126, 132, 144]. The resulting equation takes the form of (2.20), where $D_{\text{sei}}(T)$ is the temperature-dependent diffusion constant of solvent through the SEI layer of thickness τ_{sei} and the expression for the SEI overpotential η_{sei} now excludes the resistive voltage drop across the SEI layer compared to (2.19). Both $D_{\text{sei}}(T)$ and $k_{\text{sei}}(T)$ are treated as fitting parameters. If the diffusion constant is small, the reaction is diffusion limited which leads to a typical square root of time dependency of the layer thickness. If the rate constant is small, the reaction is kinetically limited and very similar to (2.17). If the diffusion and rate constant are of similar magnitude, the SEI growth can be both kinetically and diffusion limited, depending on the operating conditions and the lifetime of the battery. This model will predict both calendar and cycle ageing, but only if the kinetic term is dominant enough, the cycle ageing will be larger than the calendar ageing.

$$i_{\mathrm{sei}} = \frac{c_{s,\mathrm{el}}}{\frac{1}{nFk_{\mathrm{sei}}(T)exp\left(-\frac{\alpha_{\mathrm{sei}}nF}{R_gT}\eta_{\mathrm{sei}}\right)} + \frac{\tau_{\mathrm{sei}}}{nFD_{\mathrm{sei}}(T)}} \tag{2.20}$$

A third type of SEI growth model assumes electrons tunnel or migrate through (a part of) the existing SEI layer [130]. Tang et al. [143] give an overview of such models but so far they have not been widely used. These models are therefore not further considered in this work.

Finally, instead of complicating their models with extended equations, some researchers add an empirical correlation to their SEI growth model such that it produces the ‘desired’ outcome. Some enforce a square-root dependency of cycle number [121] or of time [125, 135], others add a factor $1/\tau_{\mathrm{sei}}$ [128] or $e^{-\beta\tau_{\mathrm{sei}}}$ [131] to guarantee a decreasing rate for the SEI growth.

The growth rate of the SEI layer thickness τ_{sei} is a direct function of the side reaction current density, accounting for the molecular weight M_{sei} in [kg mol^{-1}] and density of the reaction products ρ_{sei} in [kg m^{-3}] (2.21). A side effect is that the DC resistance of the cell as given by (2.7) increases.

$$\frac{\partial\tau_{\mathrm{sei}}}{\partial t} = \frac{i_{\mathrm{sei}}M_{\mathrm{sei}}}{\rho_{\mathrm{sei}}nF} \tag{2.21}$$

The main degradation effect of this side reaction is that cyclable lithium is lost (loss of lithium inventory, LLI). This is achieved by adding the side-reaction current density to the boundary condition of the diffusion in the negative particle only (2.22).

$$D_{\mathrm{n}}(T)\frac{\partial c_{\mathrm{n}}(r)}{\partial r}\bigg|_{r=R_n} = -\frac{i_{\mathrm{n}}}{nF} - \frac{i_{\mathrm{sei}}}{nF} \tag{2.22}$$

Finally, it has been suggested that the SEI layer might block the pores in a part of the anode, and that the active material behind that pore is no longer accessible, a type of loss of active material (LAM) [134, 144, 147]. As most models do not explicitly simulate the 3D porous structure, this can be achieved by reducing the volume fraction of active material in the anode (2.23) where β_1 is a fitting parameter. The effect this has on the cell is explained in section 2.2.3.

$$\frac{\partial \varepsilon_{\mathrm{n}}}{\partial t} = -\beta_1 i_{\mathrm{sei}} \tag{2.23}$$

2.2.2 Crack growth at the electrode surface

As explained in section 1.3.2, alternating stresses and volume changes can lead to cracks growing on the graphite surface or in the existing SEI layer. This exposes new graphite to the electrolyte, and an SEI layer will grow on this fresh surface, leading to more LLI. Since there is no model for a similar effect on the cathode, only cracks are the anode are considered.

Laresgoiti et al. [103], assumed the cracks grow in the SEI layer, and consequently used a correlation for the tangential stress in the SEI layer $\sigma_{t,\mathrm{sei}}$, see section 2.1.3. They then postulated that the Wöhler curves[3], originally developed for metal fatigue, can be used to simulate crack growth. This implies that the crack growth depends on the maximum and minimum stress experienced over one 'cycle', $\sigma_{t,\mathrm{sei}}^{\mathrm{max}}$ and $\sigma_{t,\mathrm{sei}}^{\mathrm{min}}$, relative to the yield stress of the SEI layer $\sigma_{\mathrm{yield,sei}}$, all in [Pa], and the slope of the Wöhler curve m. In their paper,

---

[3] Wöhler curves, also known as S-N curves, plot the 'stress per cycle' versus the 'number of cycles to failure', typically a straight line on a log-log scale. In case the stress changes, there are multiple approaches to accumulate the damage from each cycle, in the simplest approach they are simply added up.

they related this directly to the 'capacity loss per cycle' E_{ch}^{lost}/N (2.24). As before, β is a fitting parameter, and also m and $\sigma_{\text{yield,sei}}$ are considered as fitting parameters because they are difficult to measure.

$$\frac{E_{ch}^{\text{lost}}}{N} = \beta_2 \left(\frac{\sigma_{t,\text{sei}}^{\text{max}} - \sigma_{t,\text{sei}}^{\text{min}}}{\sigma_{\text{yield,sei}}} \right)^{\frac{1}{m_1}} \tag{2.24}$$

Deshpande et al. [122] started with the same approach of deriving the stress in the SEI layer, but then simplified the equations by realising that all the equations are linear functions of the change in the lithium fraction at the graphite surface $x(R_{\text{n}})$. They followed the same approach as Laresgoiti et al. and linked the degradation effect to the change over one 'cycle', $x^{\text{max}}(R_{\text{n}})$ - $x^{\text{min}}(R_{\text{n}})$, with a fitting parameter β and with $m = 0.5$. Deshpande et al. calculated the increase in the crack surface area per cycle $\partial A_{\text{cr}}/\partial N$ rather than directly calculating the lost capacity (2.25).

$$\frac{\partial A_{\text{cr}}}{\partial N} = \beta_3 \left(x^{\text{max}}(R_{\text{n}}) - x^{\text{min}}(R_{\text{n}}) \right)^2 \tag{2.25}$$

Barai et al. [117] cited experiments on material fatigue using acoustic waves to propose a new formulation where the crack surface area is a function of the charge throughput, which plateaus at some maximum value. Taking the derivative of this function results in (2.26), where β is again a fitting parameter and $A_{\text{cr}}^{\text{max}}$ is the maximum crack surface area, which could be experimentally determined but is treated as a fitting parameter for convenience.

$$\frac{\partial A_{\text{cr}}}{\partial t} = \beta_4 \left(A_{\text{cr}}^{\text{max}} - A_{\text{cr}} \right) |I| \tag{2.26}$$

Ekstrom et al. [123] took a different approach. Rather than relating crack growth to alternating stresses, they assumed the phase changes in the graphite were responsible for the growing cracks. Therefore, they could simulate the additional SEI layer growth on the crack surface by making the rate constant a function of the lithium fraction as well as of the temperature (2.27). In the ranges of the lithium fraction where a phase change occurs, the rate constant is non-zero, increasing the SEI layer growth if the cell is cycled in those ranges.

$$i_{\mathrm{cr}} = nFk_{\mathrm{cr}}\left(x_{\mathrm{n}}\left(R_{\mathrm{n}}\right), T\right)\exp\left(-\frac{\alpha_{\mathrm{sei}}nF}{R_gT}\eta_{\mathrm{sei}}\right) \tag{2.27}$$

As mentioned, the main degradation effect of the growing cracks is to enhance the growth of the SEI layer on the freshly exposed surface. The thickness of the layer on the crack surface will be different from the main layer because the layer is formed later and if certain assumptions are made about the growth rate, analytical solutions are possible [121, 135]. If no such assumptions are made, simulating the different areas of the SEI layer, each with their own thickness, becomes intractable. Therefore, most studies ignore the differences in thickness such that the original SEI side reaction current can simply be increased by some factor representing the crack surface [64, 123]. In this work, the factor used is the ratio of the crack surface area to the total anode surface because all models could be fit into this framework (2.28). Note that this factor only appears in the boundary condition of the anode diffusion equation (thus removing more cyclable lithium), not in the equation for the thickness of the SEI layer (2.21) or the pore clogging (2.23) because the increased reaction happens at a different surface[4].

$$D_n(T)\frac{\partial c_{\mathrm{n}}(r)}{\partial r}\bigg|_{r=R_n} = -\frac{i_{\mathrm{n}}}{nF} - \frac{i_{\mathrm{sei}}}{nF}\left(1+\frac{A_{\mathrm{cr}}}{a_nA_n\tau_n}\right) \tag{2.28}$$

Secondly, Barai et al. [117] argued that the cracks increase the tortuosity of the anode, decreasing the effective anode diffusion constant according to (2.29), which comes on top

---

[4] Given that cracks appear on the surface of one particle, the SEI layer covering the cracks cannot clog pores. The effect on resistance is less clear, since the crack surface increases the active surface (reducing the current density and therefore the total resistance) while the SEI layer on this surface will counter this effect. Neither of these factors are included, as is common in these types of models, because the net effect is considered to small.

of the temperature dependency of the diffusion constant as given by (2.11). Although this does not decrease the charge capacity of the anode directly, it reduces the charge which can be accessed at a given current and it increases the concentration gradient, which in turn can enhance other degradation mechanisms.

$$D_{\mathrm{n}} = D_{\mathrm{n}}^{ref} \left(1 - \frac{A_{\mathrm{cr}}}{A_{\mathrm{cr}}^{\max}}\right)^{\beta_5} \tag{2.29}$$

2.2.3 Loss of active material

As explained in section 1.3.3, there are many reasons why active material can get lost: cracks can grow and electrically isolate regions, pores can get blocked which isolates regions from the electrolyte, the cathodic active material can dissolve or dissociate, structural disordering can remove the free lithium locations, etc. This results in a wide variety of models.

The models which are based on the cracks and resulting isolated regions are similar to the models used for cracks growing at the surface because the underlying principles are the same. Narayanrao et al. [56] came up with a model to simulate the ‘isolated surface’, which will reduce the effective surface area a for the main intercalation reaction (2.30). They started with the same model for crack growth (originally developed for metal fatigue), but then simplified it to equation (2.30), where β is a fitting parameter. As can be seen in equation (2.31), this will increase the current density i_i on the particle for the same overall battery current, and therefore reduce the battery capacity through (2.3).

$$\frac{\partial a_i}{\partial t} = -\beta_6 a_i \tag{2.30}$$

$$i_i = \frac{I}{a_i A_i \tau_i} = \frac{I R_i}{3 \varepsilon_i A_i \tau_i} \tag{2.31}$$

Laresgoiti's model for surface crack growth (2.24) used the tangential stress in the SEI layer. Because the underlying physics are the same, the same equation was implemented to simulate LAM but using the hydrostatic stress inside the particle itself (2.15). The degradation effect modelled by (2.32) is to reduce the volume fraction of active material, which will have the same effect as reducing the effective surface area (2.31). Note that this was not suggested in the original papers, but this equation is included here because it is interesting to compare the results of this model versus Narayanrao's simplification, and versus Laresgoiti's surface crack growth model. β, σ_{yield} and m are again considered as fitting parameters. This model is referred to as Laresgoiti's LAM model with Dai's stress (compared to (2.24) which is Laresgoiti's crack growth model that used Laresgoiti's own stress model).

$$\frac{\partial \varepsilon_i}{\partial t} = \beta_7 \left(\frac{\sigma_{h,i}^{\max} - \sigma_{h,i}^{\min}}{\sigma_{\text{yield},i}} \right)^{\frac{1}{m_2}} \tag{2.32}$$

Delacourt et al. [120] proposed an empirical correlation between the decrease in volume fraction and the absolute value of the current (2.33) with two temperature-dependent fitting parameters. They did not explain which underlying physical phenomenon this equation was supposed to simulate.

$$\frac{\partial \varepsilon_i}{\partial t} = \beta_8(T)|i_i| + \beta_9(T)\sqrt{|i_i|} \tag{2.33}$$

Appiah et al. [116] and Lin et al. [131] proposed models for Mn dissolution and deposition. They include a few kinetic equations (such as the Bulter-Volmer equation), often coupled with the kinetics of other reactions. Christensen et al. [119] discussed a few different dissolution reactions, such as lithium dissolution and various paths for Mn dissolution, but did not give equations describing them. Kindermann et al. [127] proposed to use a single Bulter-Volmer equation to describe all cathode dissolution reactions (2.34) where the exchange current density $i_{0,\text{diss}}$ is a fitting parameter. As before, the volume fraction of active material reduces, thereby increasing the current density and reducing the capacity (2.3, 2.31). The overpotential for the dissolution reaction is given by (2.35), where U_{diss} is the constant OCV of the dissolution reaction, set to 4.0 V.

$$\frac{\partial \varepsilon_{\mathrm{p}}}{\partial t} = \frac{i_{0,\mathrm{diss}} \exp\left(\frac{nF}{R_g T} \eta_{\mathrm{diss}}\right)}{nF c_p^{\max} \tau_p} \tag{2.34}$$

$$\eta_{\mathrm{diss}} = U_{\mathrm{p}} + \eta_{\mathrm{p}} - U_{\mathrm{diss}} \tag{2.35}$$

2.2.4 Lithium plating

When the lithium flux on the graphite anode exceeds the intercalation or diffusion capacity of the graphite and the anode potential is driven below 0 V vs Li/Li$^+$, the lithium ions might be deposited as a metallic layer as explained in section 1.3.4. Most researchers use a Tafel equation to model this process (2.36) with an OCV for the plating reaction U_{pl} of 0 V. There are some differences regarding whether to include the resistance of the SEI layer in the equation for the overpotential (2.37) [124, 144] or not [118, 129]. Most researchers [141, 144, 150] use at least a P2D-style model in which case the model can account for the local concentration and potential, often resulting in more plating at the separator-anode interphase than in the region closer to the current collector as a result of low diffusion inside the anode. With the SPM, this is not possible and the diffusion is only indirectly accounted for by using the surface concentration when determining the anode potential.

$$i_{\mathrm{pl}} = i_{0,\mathrm{pl}} \exp\left(-\frac{\alpha_{\mathrm{pl}} nF}{R_g T} \eta_{\mathrm{pl}}\right) \tag{2.36}$$

$$\eta_{\mathrm{pl}} = U_{\mathrm{n}} + \eta_{\mathrm{n}} - U_{\mathrm{pl}} + \frac{r_{\mathrm{dc,sei}}}{a_n A_n \tau_n} \tau_{\mathrm{sei}} I \tag{2.37}$$

Some of the plated lithium can be stripped and re-intercalated into the graphite. Von Lüders et al. [150] simulated this by using the full Butler-Volmer equation instead of the Tafel equation. This is not included here, instead the side-reaction current density of the plating reaction (2.36) is simply added to the boundary condition at the negative particle (2.38).

$$D_n(T)\left.\frac{\partial c_{\mathrm{n}}(r)}{\partial r}\right|_{r=R_n} = -\frac{i_{\mathrm{n}}}{nF} - \frac{i_{\mathrm{sei}}}{nF}\left(1+\frac{A_{\mathrm{cr}}}{A_{\mathrm{n}}}\right) - \frac{i_{\mathrm{pl}}}{nF} \tag{2.38}$$

2.2.5 Other mechanisms

As explained in section 1.3.5, there are many other degradation mechanisms. For some of them, models have been proposed. Appiah et al. [116] added equations for the growth of a passivation layer on the cathode, similar to the SEI layer on the anode. Kupper et al. [64] modelled electrolyte dry-out and the subsequent loss of ionic contact (a type of LAM). Lin et al. [131] added equations for electrolyte oxidation and salt decomposition. Others coupled the degradation at the different electrodes, for instance the enhanced SEI growth due to the Mn originating from the cathode [42, 52, 116], increased ionic transport resistance at the anode-separator interphase [151] or shuttle reactions in the electrolyte as it reacts with both the anode and cathode [152].

These models have not been widely used in the literature, are typically much more complicated than needed for this work.

2.3 Model implementation

Many of the degradation models proposed in literature were used with a P2D battery model. In this work, the SPM model is used instead, and some simplifications have to be made, mainly in the definitions of the overpotentials which often included the (local) electrolyte potential and (local) lithium concentration.

Secondly, some models claimed to directly calculate the lost capacity such as Laresgoiti's crack growth model (2.24). To harmonise all equations and fit them in one framework, all equations are changed to calculate the conventional physical effect for that mechanism, such as increasing the crack surface.

The most important change however relates to equations which were not continuous in time, e.g. models which have an effect 'per cycle' such as Laresgoiti's and Despande's crack growth models (2.24, 2.25). In degradation experiments with well defined cycles, this might be possible. But when real-life battery usage is predicted, it is very difficult to define what a single cycle means. Some researchers have used rainflow counting to solve this problem [104, 153], but so far experimental proof that this is justified is lacking. Therefore, two main assumptions were made: one about the relation between cycle number and time, and one about monotonic variations.

The first problem is that such models calculate the degradation effect per cycle. To fit this to a battery model which takes as input the current for the next time step and calculates the outputs corresponding to that current, all derivatives have to be time derivatives. For the purpose of this work, it was assumed that there is a linear relationship between the cycle count and time, which assumes that the battery is continuously cycling, and that all cycles are identical and therefore take the same amount of time to complete. Although this is not the case for real-world battery usage profiles, it is a reasonable assumption for the simulations of the cycle ageing experiments from section 2.5.

Secondly, those models included a term giving the change in one parameter over one cycle, e.g. $\sigma_{t,\mathrm{sei}}^{\max} - \sigma_{t,\mathrm{sei}}^{\min}$. As cycles are not known in advance, these terms were approximated by taking the difference with the value at the previous time step , e.g. $\sigma_{t,\mathrm{sei}}(t) - \sigma_{t,\mathrm{sei}}(t-1)$. If the models are linear in the term, and the values evolve monotonically during one cycle, this will produce the same result. Unfortunately most of the models are not linear in those terms, introducing a discrepancy with the originally proposed model.

Because Deshpande's crack-growth model (2.25) is very similar to Laresgoiti's crack-growth model (2.24), a modification was made in the former one. This modification accounts for the spatial rather than the temporal variation by subtracting the lithium fraction at the centre and surface, rather than the minimum and maximum fractions over one cycle.

$$\frac{\partial A_{\mathrm{cr}}}{\partial N} = \beta_3 \left(x(0) - x(R_{\mathrm{n}})\right)^2 \tag{2.39}$$

All degradation models are coupled with the same battery model, automatically accounting for interactions. For instance, if negative active material is lost, the current density on the graphite will increase, enhancing the SEI growth. The only link between both electrodes is through the lithium, but this link allows the electrodes to 'shift' with respect to each other. For instance, as lithium is lost at the anode due to SEI growth, the concentration change at the graphite particle is different to the corresponding change at the cathodic particle. This causes the particles representing the electrodes to become 'misaligned', in other words, the half-cell OCV curves shift and the end-points on charge or discharge change over time [152], as shown on Fig. 2.3.

Details of the model formulation and numerical procedures used to solve them are given in section 3.3. The full code is available on GitHub [154].

2.4 Data and parameter estimation

The majority of data shown in the rest of this chapter has been introduced in section 1.4, which is referred to as data from the Kokam cell. However, one different degradation data set is used as well: data from the Everlasting project of the European Commission [155]. As was the case with the data from the Mat4Bat project, the experiments were done by

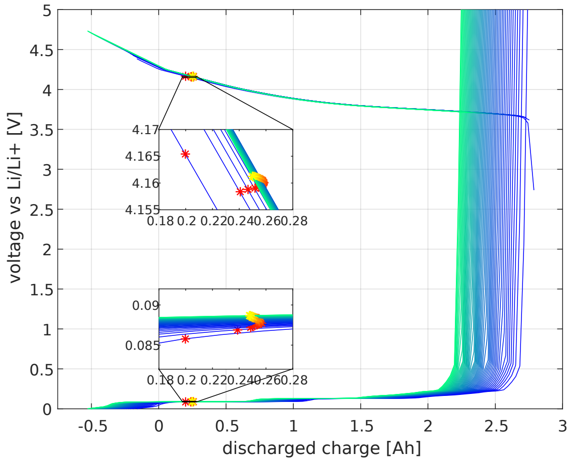

Fig. 2.3 Shifting half-cell OCV curves of a cell cycled at 1C and 25 degrees in an SoC window of 10 % and 90 %. The yellow-red stars shows the half-cell potential at the charged state (at 90 % SoC). Blue and red show the OCV at the beginning of life, while yellow and green show the OCV at the end of life.

various different partners in the project, reducing the quality of the data. Everlasting used a high-energy LG Chem NMC 18650 cell (INR18650 MJ1, [156]). The degradation data used here is for a cell which was cycled with a constant current, both on charge (1C) and on discharge (1.5C), at 25°C between 10 and 90% state of charge (SoC).

There are two sets of parameters which need to be fitted to the (Kokam or LG Chem) data. First, the battery model itself needs to be parametrised such that it predicts the correct voltages during cycling. Secondly, the fitting parameters from the degradation models can be set to simulate the measured degradation.

The SPM is heavily overdetermined. For instance to determine the current density (2.31), only the product of the radius, volume fraction, geometric surface area and thickness is relevant and changes in one of those parameters can be offset by changes in another parameter. Therefore, some parameters are set to values found in literature. This leaves the following parameters for fitting:

- the thickness of the electrodes τ_p and τ_n,
- the initial lithium concentrations at 50% state of charge,

- the diffusion constants at reference temperature D_p^{ref} and D_p^{ref} as well as their activation energies $E_{D,p}$ and $E_{D,n}$,
- the rate constants at reference temperature k_p^{ref} and k_p^{ref} as well as their activation energies $E_{k,p}$ and $E_{k,n}$,
- the total DC resistance of the cell $R_{\text{dc,batt}}$.

The fitting was a mix of manual tweaking and brute-force optimisation (i.e. trying all combinations). The cost function to minimise was the root-mean-squared difference between the simulated and measured voltage curves during the CC discharges from section 1.4.1. A search space was manually defined, and the error for a large number of combinations of parameters was calculated. The search space was then changed to reduce the overall error and a new set of combinations was tested. This continued until a satisfactory set of parameters was found.

Fig. 2.4 shows the local sensitivity to rate and diffusion constant in the optimal point, i.e. the figure shows how the error between simulations and data changes when two parameters are varied while all others are held constant at their best value. The sensitivity of the diffusion constants is largely a result of the collapse of the OCV at the end of discharge: if the anodic diffusion constant is too small, the anode potential increases too early (i.e. when too little charge has been discharged), giving large errors. Similarly, if the cathodic diffusion constant is too small, the cathode potential drops too early (i.e. before enough charge has been discharged). The sensitivity to larger diffusion constants is not as strong, since they will simply have a slightly more uniform concentration, and the voltage drop at the end of discharge is just a bit too late[5]. However, for values above $0.6e^{-12}$, the error quickly

---

[5] This asymmetry is down to the way the error is calculated. The RMSE only accounts for the difference between the measured and simulated curve up to the point where the measurements reached the minimum voltage. If the simulated voltage on discharge reaches the minimum voltage first, the error for the remaining part of the measurements is very large, namely $V_{\text{min}} - V_{\text{measured}}$. If however the simulated curve extends beyond the measurements, i.e. it reaches the minimum voltage after it has discharged more charge, the error is only calculated up to the point where the measurements reach the minimum voltage, such that there never is a large difference between measurements and simulations. This is a good example showing that a different cost function might give very different results, and that these sensitivities should be treated with care. If the

increases and eventually the diffusion equation becomes numerically unstable for the spatial and temporal discretisation used here. The sensitivity to the rate constants is very symmetric since kinetic voltage drops from both electrodes are subtracted from the cell's OCV, such that it cannot be determined which electrode is contributing to the total voltage drop.

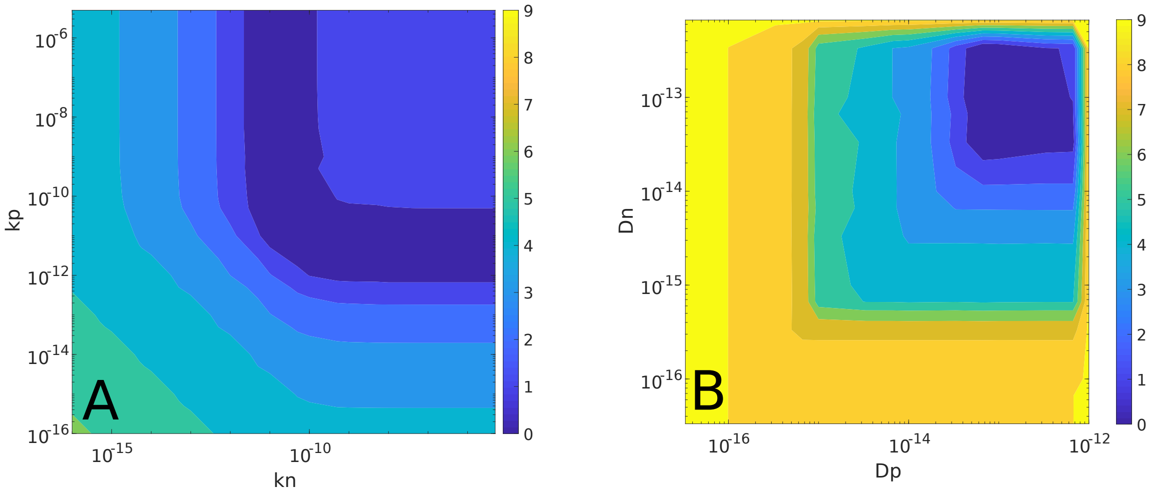

Fig. 2.4 Sensitivity of the SPM to diffusion and rate constants. The colour indicates the log of the mean root mean square error between the simulated and measured voltage during the different CC discharges shown in section 1.4.1. (A) errors for varying values of the rate constants when the other parameters have their optimal value; (B) errors for varying values of diffusion constants when other parameters have their optimal value.

The best-fitting parameters are given in table 4.3 in section 4.3.1 and the result is shown in section A.3.1. The SPM was fitted separately to the characterisation data from the LG Chem cell, resulting in a second set of parameters.

Once the battery model can predict the voltage, the degradation parameters can be fitted to the data from section 1.4.3 or to the data from the LG Chem cell, which was done in a similar way to the fitting of the battery model parameters. Fig. 2.5 shows the sensitivity to the diffusion and rate constants for an SPM with a kinetically and diffusion-limited SEI model to predict degradation. For each experiment, the root mean square error between the relative

---

error had been calculated symmetrically, i.e. always until the most discharged cell in either the simulation or measurements, the sensitivity for smaller and larger diffusion constants would have been much more symmetric too.

capacity in the data and in the simulation is calculated. Often, multiple experiments were done with the same test conditions. The error between each experiment and the simulation with the corresponding test conditions is calculated separately. The logarithm of the mean error for all cycle experiments is shown on the left of Fig. 2.5. Similarly, the right shows the logarithmic mean errors for the calendar ageing. As could be expected, the main result is that the product of the diffusion and rate constants has to be more or less constant. This is because at any time, the side reaction is either limited by the kinetics or by the diffusion. If both constants are too large, the cells degrade too much; similarly if both are too small, the cells degrade too slow. As long as one of them is in the correct range, the error does not change too much.

The figure is very dependent on how the error is calculated. For instance, all simulations of cycle experiments were for 4000 cycles so features in the data after 4000 cycles are not captured. Similarly, if an experiment finished early because the cell had died after 1000 cycles, the error is only calculated based on these 1000 cycles even if the simulation predicted the cell would still be fine for more cycles. Therefore, this sensitivity analysis does not give the full picture of how ‘accurate’ a fit is, and it is still down to the modellers themselves to pick the values which best predict the features they are interested in. For instance, from Fig. 2.5 the ‘cost function’ indicates that the problem is insensitive to a change in either variable as long as the ratio remains constant. However, this overall figure masks differences in which experimental conditions are predicted better than others and how evenly the error is distributed over the different experiments. Therefore, one combination might still be preferable over another.

In the results presented in the next section, different combinations of the models are compared with the experimental data. The parameters are fitted separately for every combination of degradation models. For example, when only SEI growth is considered, the values of the diffusion constant D_{sei} and the rate constant k_{sei} are set such that the predicted degradation

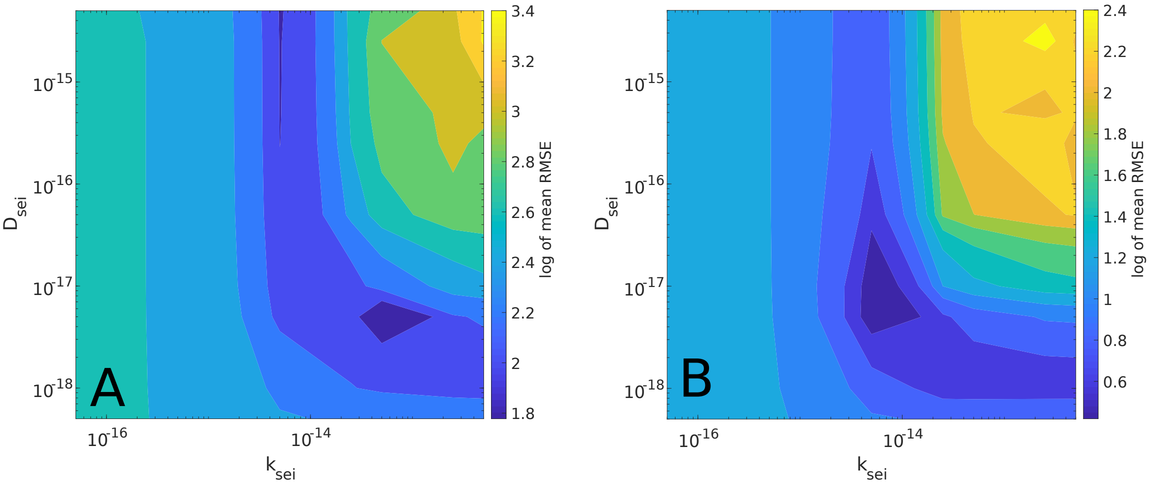

Fig. 2.5 Sensitivity of the degradation predictions of the SPM with an SEI model for variations in the diffusion and rate constant of the SEI reaction. The colour indicates the logarithm of the average root mean square error between the simulated and measured relative capacity for all cycle and calendar ageing data shown in section 1.4.(A) errors for cycle ageing; (B) errors for calendar ageing.

matches the data. When later SEI growth is combined with other degradation mechanisms, such as surface cracking, the diffusion and rate constants are changed such that the total predicted degradation fits the data. This is done because no assumptions are made a priori about which models are ‘correct’, the aim of the simulations is to see which (combinations of) models can predict different types of degradation trends. The following parameters are fitted:

- the rate- and diffusion constants of the SEI growth models k_{sei} and D_{sei}, as well as their activation energies,
- all parameters called β or m,
- the maximum crack surface area $A_{\mathrm{cr}}^{\mathrm{max}}$ in Barai’s crack-growth model (2.26) and (2.29),
- the rate constant $k_{\mathrm{cr}}\left(x_{\mathrm{n}}\left(R_{\mathrm{n}}\right), T\right)$ in Ekstrom’s crack-growth model (2.27),
- the exchange current density of the cathode dissolution side reaction $i_{0,\mathrm{diss}}$ in (2.34) and of the lithium plating side reaction $i_{0,\mathrm{pl}}$ in (2.36).

The parameters β and m (with various subscripts) have no direct physical interpretation and were therefore not constrained to any range. The parameters i_0, k and D (with various subscripts) are exchange current densities, and rate and diffusion constants which could be measured in theory, although this would be near impossible in practice [116, 132, 144]. Therefore, most papers treat them as fitting parameters. The values reported in the literature have a huge range, e.g. for the rate constant of the SEI growth reaction, k_{sei}, values between 10^{-8} and 10^{-16} have been reported, such that those parameters were not constrained to any range either.

2.5 Simulation results

The results presented here have been recently published in [81]. First the basic degradation trends predicted by each separate model are shown in section 2.5.1. Secondly, the interactions between different models are studied in section 2.5.2. Finally, the degradation effect of operating conditions according to different models is shown in section 2.5.3, which also shows the fit of a large degradation experiment with a combination of four models.

2.5.1 Classification of degradation models

Three basic trends can be observed within existing lithium-ion battery degradation data sets [61]. Some types of cells degrade faster at the start of life and their degradation rate decreases later in life [157, 158]. The degradation behaviour of other cells is more linear with time, with rate of capacity decrease being approximately constant for a fixed usage pattern [69, 159]. Other cells show an accelerating degradation, especially towards the end of their lifetime when the capacity suddenly decreases very strongly [52, 67, 144]. Sometimes, different operating conditions can lead to different degradation trends for the same cell type.

The degradation model equations from section 2.2 determine the trend of degradation over time and with usage.

The kinetically limited SEI growth model (2.17) will produce a constant capacity fade for fixed usage because the magnitude of the side reaction current is broadly independent of the past degradation. The same is true for all other models with Bulter-Volmer or Tafel equations: Ekstrom's crack growth model (2.27), Kindermann's model for electrode dissolution (2.34), and the models for lithium plating (2.36).

On the other hand, the diffusion-limited SEI growth model (2.20) will predict a decreasing rate of degradation for constant usage because the magnitude of the side reaction current is inversely proportional to past degradation, represented by the thickness of the existing SEI layer τ_{sei}, which will produce a square-root-of-time dependency.

Laresgoiti's and Despande's modified models for surface cracking (2.24, 2.39) will give a constant degradation trend because the stress is not affected by previous crack growth. Barai's crack-growth model (2.26) will give a decreasing trend because the bigger the crack surface, the smaller the remaining possible active area for crack growth $A_{\text{cr}}^{\text{max}} - A_{\text{cr}}$.

There is more variability in the effects of the models for loss of active material. Some models (2.32, 2.33) result in an accelerating degradation trend with time due to a strong positive feedback loop. On the other extreme, Narayanrao's model (2.30) gives an exponentially decreasing trend because the smaller the effective surface a_i, the less it will decrease.

As an example, Fig. 2.6 shows the different models classified by the trends they predict, along with a data set for each trend. None of the surface-crack-growth models are included because surface cracks do not decrease the capacity on their own, only when combined with an SEI growth model. It should be noted that the different trends can be difficult to see in the simulation results of Fig. 2.6 because in some cases the rate of change of the gradient is very gradual within the window shown. For instance, the capacity loss according to an exponential process is more or less linear at the start of the exponential (since $y = e^{-t/\theta} \approx 1 - t/\theta$ for large θ and small t). The fitting constant in Narayanrao's model had a small value to fit the absolute capacity lost after 1000 cycles, leading to a large time constant θ of about 40,000 h, such that even after 1000 cycles the exponential behaviour is not yet visible. Some exponential processes can decrease the capacity very suddenly, as is the case for Delacourt's LAM model. At the last successful capacity check in the simulation, the cell still has about 70% remaining capacity but then the cell degrades very quickly until it has no more remaining capacity. Kindermann's LAM model is for cathode dissolution while initially the cell capacity is limited by the anode. Therefore, the total capacity is constant until the cathode becomes the limiting electrode, after which the total cell capacity starts decreasing linearly.

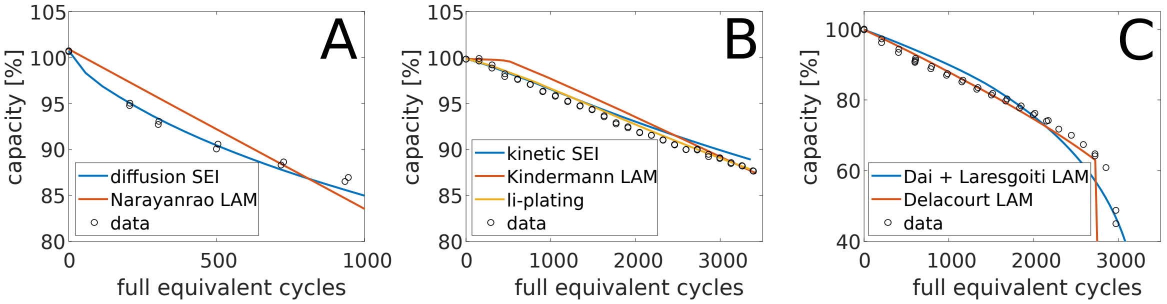

Fig. 2.6 Basic degradation trends of the individual degradation models. The black markers are experimental results as described section 2.4, while the lines are the simulations according to the various models. (A) decreasing degradation rate for the LG Chem cell; (B) constant degradation rate for the Kokam cell cycled at 25°C at a 1C charge and 1C discharge between 10 and 90% SoC; (C) increasing degradation rate the Kokam cell cycled at 45°C at a 3C charge and 1C discharge between 0 and 100% SoC.

2.5.2 Model combinations

This section discusses the results of combining two degradation models and how the interaction between both can alter the degradation trend. Fig. 2.7 shows an example set of results when an SEI growth model is combined with one other degradation model. As explained in section 2.4, the parameters for the degradation models were set differently for every combination of models in order to give a best fit against the available data. For reference, the solid lines show the degradation according to the SEI model alone; each different colour represents a different value of the diffusion and/or rate constant in the model. The dashed and dotted lines give combinations of SEI models with one other model, as indicated on the legend, such that the difference between the dashed/dotted and solid lines represents the additional degradation due to the second degradation model. The data and load cycles are the same as for Fig. 2.7.

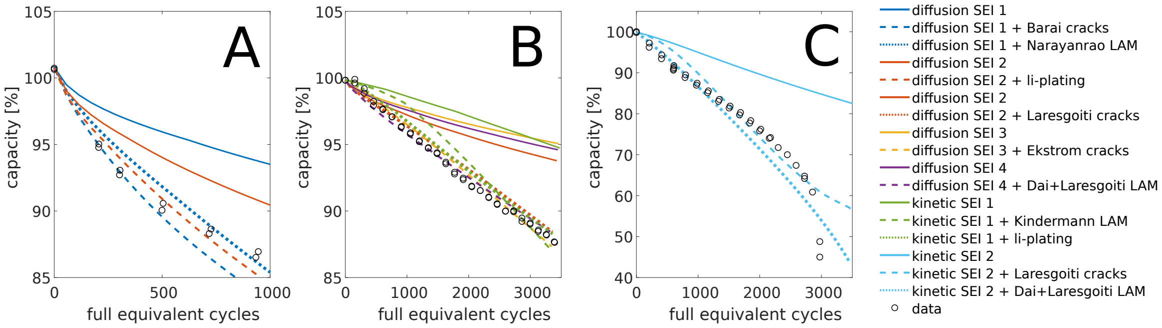

Fig. 2.7 Degradation trends according to a combination of two degradation models. The dashed and dotted lines show the results of combining an SEI model with one other degradation model. For reference, the solid line of the same colour indicates the degradation according to the SEI model only. The different colours represent SEI models with different diffusion and/or rate constants. The black data points are the same as in Fig. 2.6. (A) decreasing degradation rate; (B) constant degradation rate; (C) increasing degradation rate.

Mostly, the trend of the combined models is a clear result from the two individual models, e.g. a (decelerating) diffusion-limited model with another decelerating or constant degradation model produces a decelerating trend. The crack-growth models are an exception: the SEI layer grows on the total electrode surface area, implying that the degradation rate is proportional to the integral of the crack-growth rate. Therefore, a crack-growth model with a constant crack-growth rate will give an increasing degradation trend.

When Laresgoiti's crack-growth model is combined with a kinetically limited SEI-growth model, the degradation initially accelerates as expected. But towards the end of the cell's lifetime, at about 3000 cycles, the degradation levels off. This is because the cell has lost so much lithium, that the anode OCV curve has shifted by over 1 Ah. The shifting of the anode curve was shown conceptually on Fig. 2.3, but due to the much higher amount of LLI in the case of Laresgoiti's crack-growth model, the anode curve shifted much more 'to the left' such that the operating point at 100% SoC is on the next plateau of the anode OCV curve. This higher anode potential results in a large decrease of the overpotential for the SEI growth, such that the predicted degradation shows a decreasing trend after this point.

Two models can interact with each other. For instance, if the current density on the anode increases due to a LAM model (2.31), this results in higher kinetic and SEI overpotentials (2.5, 2.19), which in turn lead to higher SEI growth if a kinetically limited model is used (2.17). This effect is shown on Fig. 2.8, with Fig. 2.8(a) indicating the SEI layer thickness[6] and Fig. 2.8(b) indicating the specific electrode surface area on the anode a_n. The blue area shows the results when only the SEI growth is modelled; as can be seen the electrode surface area does not change in this scenario, and the layer thickness grows almost linearly with cycling. The yellow area shows the increase in the SEI layer growth and the decrease in surface area respectively when LAM is modelled alongside SEI growth. Although the LAM model alone produces a constant rate (a_n decreases linearly), when combined with the SEI growth model it results in an accelerating growth rate (τ_{sei} increases more than linearly). However, the total degradation will be more linear than the SEI thickness suggests, because although the thickness increases more, the surface area on which the SEI layer grows decreases (due to the LAM), reducing the increasing trend. Note that this feedback mechanism does not exist when a purely diffusion-limited SEI growth model is used because in that case, higher overpotentials do not lead to higher SEI growth rates. There are other similar cases, e.g. when the diffusion constant is reduced due to crack growth as given by (2.29) and active material is lost due to a physical stress model (2.32).

Negative feedback also exists, for example between kinetically limited SEI growth and lithium plating. Both models remove cyclable lithium, which increases the anode potential,

---

[6] The SEI thickness is determined by equation (2.21), where the values of M_{sei} and ρ_{sei} have been taken from Pinson et al. [132]. The absolute thickness is not of importance in the model given that all the fitted transport parameters appear relative to the thickness in the equations, e.g. D_{sei}/δ. In other words, only the ratio of the fitted transport parameter to the thickness is of importance in determining the degradation behaviour.

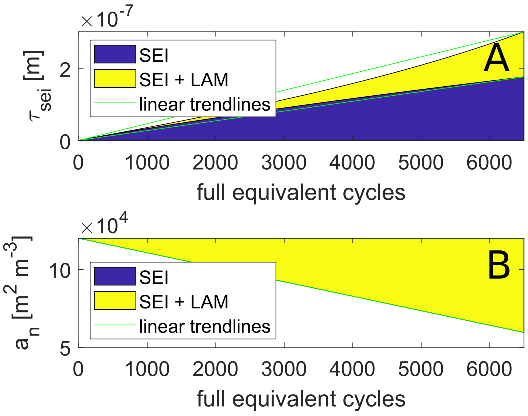

Fig. 2.8 Interaction between kinetically limited SEI growth and LAM. The blue area is the effect when only SEI growth is considered, while the yellow area gives the additional effect when both SEI growth and LAM are considered. (A) thickness of the SEI layer; (B) effective surface area.

while both are enhanced by lower voltages with respect to Li/Li$^+$. This means that if there is more/less SEI growth, the anode potential is higher/lower and there will be less/more lithium plating.

Finally, either electrode can be limiting. For example, Kindermann's model for cathode dissolution (2.34) reduces the cathode capacity, while the SEI growth models decrease the anode capacity by removing lithium ions irreversibly. If the SEI model is dominant, the capacity is limited by the anode, and adding Kindermann's degradation model will have no effect on the overall capacity and vice versa.

2.5.3 Influence of operating conditions

It is known that battery degradation is influenced by operational usage factors such as current, SoC and temperature [104, 107]. The different models of degradation respond very differently to varying operating conditions, as shown in Fig. 2.9.

The diffusion-limited SEI growth model (2.20) is independent of current and SoC but is enhanced by higher temperatures, on the condition that the temperature dependency of the diffusion constant is considered similar to (2.11). Therefore, the degradation of all cycles

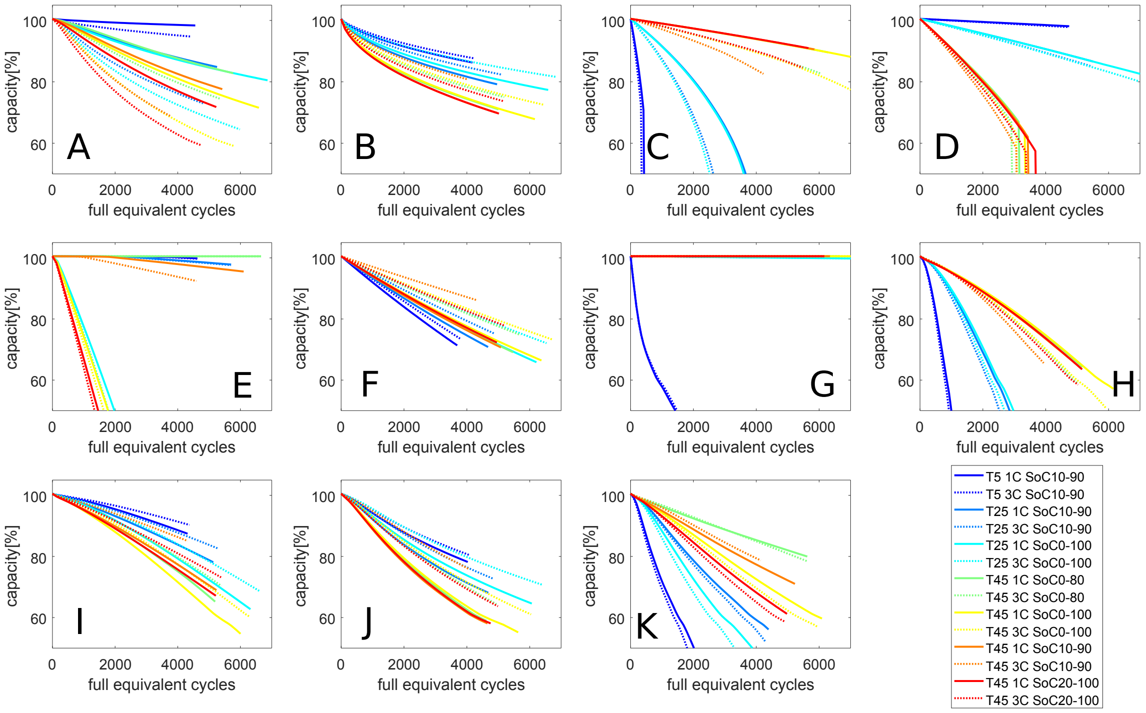

Fig. 2.9 Dependencies of the various degradation models on operating conditions. Each subplot gives the predictions according to one model, with the exception of the crack-growth models which are combined with a diffusion-limited SEI-growth model. Discharge is at 1C, and charging is CC-CV at various currents indicated by the legend. Ambient temperatures and SoC windows are indicated in the legend too. (A) kinetically limited SEI growth (2.17); (B) diffusion-limited SEI growth (2.20); (C) Laresgoiti's LAM with Dai's stress (2.32); (D) Delacourt's LAM (2.33); (E) Kindermann's dissolution LAM (2.34); (F) Narayanrao's LAM (2.30); (G) lithium plating (2.36); (H) diffusion-limited SEI growth + Deshpande's modified crack growth (2.39); (I) diffusion-limited SEI growth + Laresgoiti's crack growth (2.24); (J) diffusion-limited SEI growth + Barai's crack growth, (2.26); (K) diffusion-limited SEI growth + Ekstrom's crack growth (2.27).

with the same temperatures maps onto a single line if plotted against time on the x-axis. However, the x-axis of Fig. 2.9 is ‘full equivalent cycles’ (FEC), which is the total charge throughput divided by twice the nominal cell capacity. Because the different cycles take different amounts of time, the prediction does not map to a single line per temperature. This shows how changing the independent variable can reveal different trends in degradation data, which might be useful to identify which degradation models fit the data best. For reference, Fig. 2.10 shows the same simulations versus time.

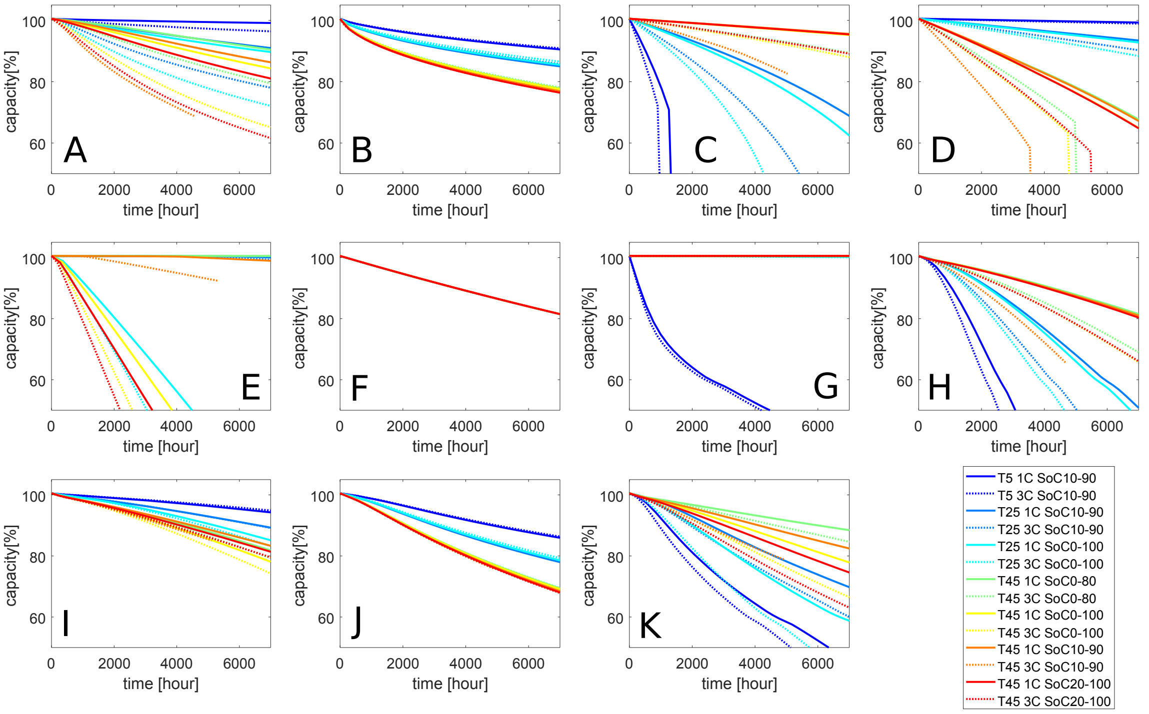

Fig. 2.10 Dependencies of the various degradation models on operating conditions with respect to time, identical to Fig. 2.9 but with time as x-axis. (A) kinetically limited SEI growth (2.17); (B) diffusion-limited SEI growth (2.20); (C) Laresgoiti’s LAM with Dai’s stress (2.32); (D) Delacourt’s LAM (2.33); (E) Kindermann’s dissolution LAM (2.34); (F) Narayanrao’s LAM (2.30); (G) lithium plating (2.36); (H) diffusion-limited SEI growth + Deshpande’s modified crack growth (2.39); (I) diffusion-limited SEI growth + Laresgoiti’s crack growth (2.24); (J) diffusion-limited SEI growth + Barai’s crack growth, (2.26); (K) diffusion-limited SEI growth + Ekstrom’s crack growth (2.27).

Lower temperatures and corresponding lower diffusion constants will always lead to larger spatial concentration gradients inside the active material, as well as to larger concentration swings on the surface of the electrode. If this effect is accounted for, and if the degradation model is heavily dependent on the stress, the simulated degradation will have a strong negative correlation with temperature, such as Deshpande's modified crack-growth model (2.39) and Laresgoiti's LAM model (2.32) which used Dai's stress model (2.13 - 2.15).

Other models are independent of any operating condition, such as Narayanrao's LAM model (2.30). If plotted versus time as in Fig. 2.10, all its predicted degradation falls onto one line, which is not the case if plotted versus FEC as in Fig. 2.9. The more empirical models such as Barai's crack-growth model (2.26) and Delacourt's LAM model (2.33) typically only depend on the current and temperature. Therefore, their predictions for constant temperatures will fall onto one line if plotted versus FEC as in Fig. 2.9, but not if plotted versus time as in Fig. 2.10.

This difference is most visible in the four crack-growth models. They are coupled with a diffusion-limited SEI growth model which predicts more degradation at higher temperature. Deshpande's modified model and Ekstrom's model predict much more crack growth at low temperature, which dominates the overall trend when they are combined with the SEI model. On the other hand, Laresgoiti's crack-growth model depends on the surface concentration, which does not depend on the temperature, and Barai's model has no temperature dependency either such that they predict more degradation at higher temperatures when they are combined with the SEI model.

To capture all trends in a large data set, a combination of various models is necessary. The generalised model illustrated here is a combination of diffusion-limited SEI (2.20), Delacourt's LAM model (2.33), Kindermann's model for cathode dissolution (2.34) and Yang's model for lithium plating (2.36)[7]. All the models interact with each other as explained previously. The parameters of each model are given in Table 2.2.

---

[7] After a visual comparison of Fig. 2.9 with the data from Fig. 1.4, various combinations of different models were simulated. The model parameters were tweaked manually to get a reasonable fit for each combination. Eventually, the combination of these four models produced the best result. This highly empirical approach

Table 2.2 Fitted parameters of the generalised degradation model

Parameter	Symbol	Value and unit
Rate constant of the SEI reaction	k_{sei}	2.75e-13 m s^{-1}
Arrhenius constant of k_{sei}	$E_{k,\text{sei}}$	130,000 J mol^{-1}
Diffusion constant of the SEI reaction	D_{sei}	1.125e-14 m^2 s^{-1}
Arrhenius constant of D_{sei}	$E_{D,\text{sei}}$	20,000 J mol^{-1}
Fitting constant in Delacourt's LAM model	β_8	-1.675e-5 m^2 C^{-1}
Arrhenius constant of β_8	E_{β_8}	54,611 J mol^{-1} 1
Fitting constant in Delacourt's LAM model	β_9	0 m $C^{-0.5}$ $s^{-0.5}$
Relative exchange current of Kindermann's LAM model	$\frac{i_{0,\text{diss}}}{c_p^{\max}\tau_p}$	1.25e-05 A mol^{-1}
Arrhenius constant of $i_{0,\text{diss}}$	$E_{i_{0,\text{diss}}}$	27,305 J mol^{-1}
Exchange current density of the plating reaction	$i_{0,\text{pl}}$	2.25e-10 A m^{-2}
Arrhenius constant of $i_{0,\text{pl}}$	$E_{i_{0,\text{pl}}}$	-201,400 J mol^{-1}

A best fit of this generalised model is shown across a selection of the experimental data set of the Kokam cell from section 1.4.3 on Fig. 2.11. The lithium plating model ensures the rapid degradation at low temperature is captured, but fails to capture the later decreasing degradation trend fast enough. It is unclear why the degradation flattened out in the experiment, but probably some negative feedback mechanism prevents further plating in the real cell, which is not included in the model. The cathode-dissolution model explains the degradation for cycles at high SoC windows, and the combination of the SEI-layer growth model and loss-of-active-material model explains the remaining degradation trends. The accelerating degradation trend for the cycles at high SoC window is not captured because the cathode-dissolution model has a constant degradation rate, which causes an overestimation of degradation in the middle of the cells' lifetime and an underestimation towards the end.

On the other hand, Fig. 2.12 shows the best fit achievable with only one degradation model[8]. The model used was the SEI growth model accounting for both diffusion and kinetic limitations (2.20) but with a small rate constant such that the model was influenced by the kinetics of the reaction, although the diffusion still limited the SEI growth in certain

---

was necessary due to the very large number of parameters to fit, and the time needed to simulate just one combination. A full parameter sweep such as in Fig. 2.5 was practically impossible.

[8] The values of the parameters producing this fit are given in Table 4.3 in section 4.3.1

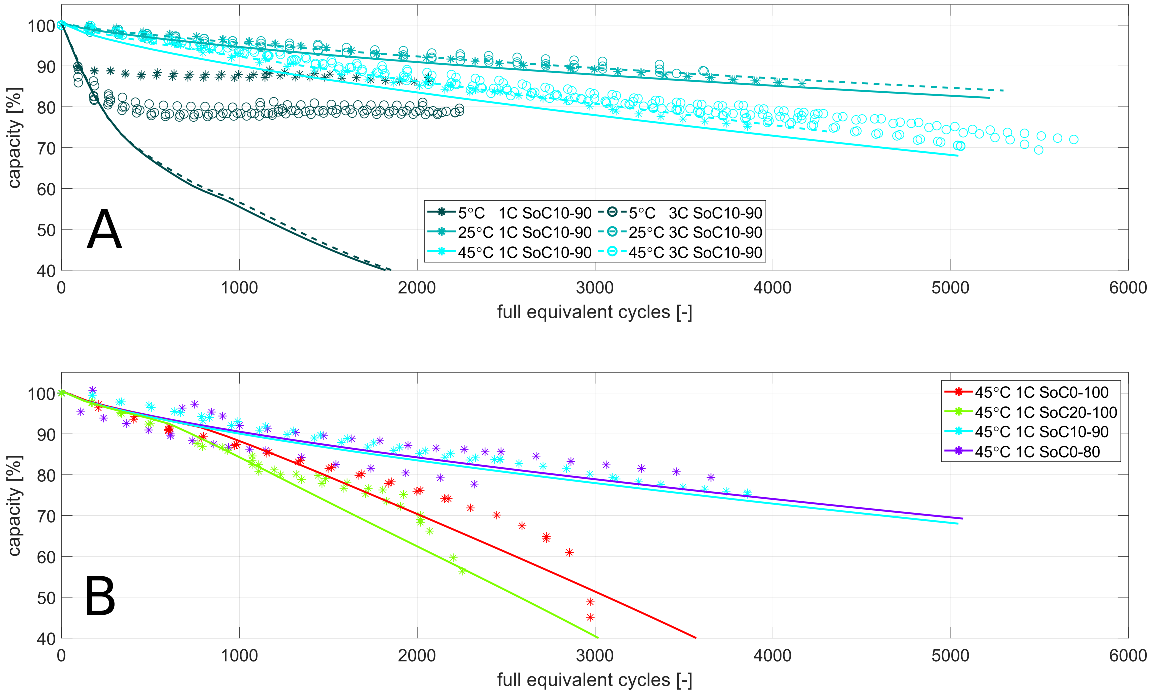

Fig. 2.11 Degradation predictions for various cycling regimes, comparing a generalised model (lines) vs. measured degradation data (markers) introduced in section 1.4.3. Not all data is shown for clarity. The generalised model combines a diffusion-limited SEI model, Delacourt's LAM model, Kindermann's model for cathode dissolution and Yang's model of lithium plating. (A) degradation at an SoC window between 10% and 90%; (B) degradation at 45°C and 1C.

conditions. As can be seen on Fig. 2.12, most of the initial degradation can be predicted by the SEI growth model, but there are some clear deficiencies: degradation at low temperature is severely underestimated. And although the kinetic limitation ensures more rapid degradation at high SoC (2.19), it fails to capture the knee point in those cycles.

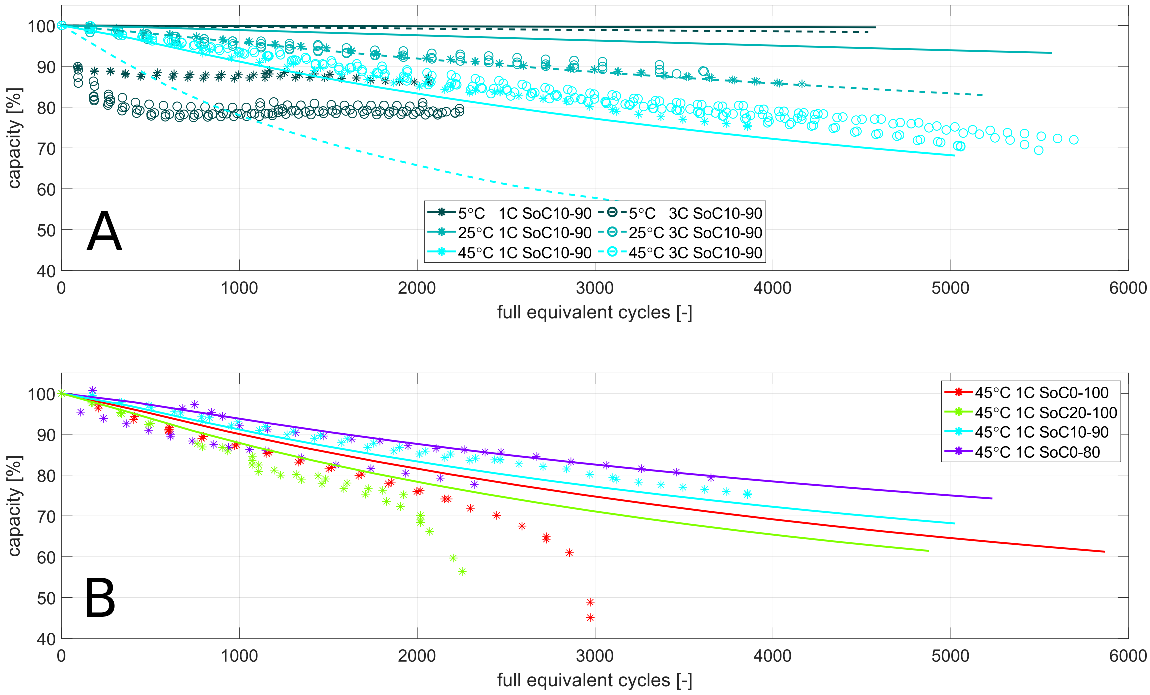

Fig. 2.12 Degradation predictions for various cycling regimes, comparing a diffusion and kinetically limited SEI model (lines) vs. measured degradation data (markers) introduced in section 1.4.3. Not all data is shown for clarity. (A) degradation at an SoC window between 10% and 90%; (B) degradation at 45°C and 1C.

2.6 Discussion

Often papers which propose degradation models 'validate' the predictions versus a small data set. Most of the equations have so many parameters which can be tuned, that they can all 'accurately' predict such a small data set. As has been shown in sections 2.5.1 and 2.5.2 and especially figures 2.6 and 2.7, many different models can indeed be fitted to the same (single line of) data. This illustrates that to fully validate a degradation model, a large degradation data set is needed, as shown in Figs. 2.11 and 2.12.

A related problem is the parametrisation of the various models. There are so many fitting variables that there is a clear risk of over-fitting, especially with small data sets. On the other hand, parametrisation becomes a very difficult task due to the high dimensionality of the fitting problem. Depending on the relative magnitude of the fitting parameters from the various degradation models, different trends might be predicted, e.g. the diffusion or kinetic limitation in (2.20). Equally important is the interaction between the various models, which also depends on the relative magnitude of the different models. This further complicates the parametrisation.

The advantage of going through the tedious process of combining multiple models to capture the different degradation trends is twofold. First of all, the resulting model is more general and will likely perform better when 'extrapolating' it to different operating conditions than the ones used to parametrise and validate it. Secondly, the models give insight in the various physical processes responsible for degradation. For instance in the case of the generalised model from Fig. 2.11, it became apparent that there was a problem with the cathode stability at high SoC, which was not obvious if only one model was used as in Fig. 2.12. However, as mentioned in section 1.4.3, the post-mortem analyses of the cells revealed localised lithium plating for cells cycled at high currents and high temperatures [79, 80]. This might have been related to electrolyte dry-out and gas formation, as was the case for the cells calendar aged at 60°C [72, 76, 77]. Such local effects cannot be simulated with the SPM, which is why they were not picked up by the simulation in this chapter. Furthermore, the post-mortem analyses did not explain the rapid degradation for the cells cycled at 1C at high SoC windows, so there might have been some cathode dissolution or another cathode-related degradation mechanism such as electrolyte oxidation taking place.

Finally, it can be noted that the fit with the SEI model (Fig. 2.12) performed relatively well for the degradation early in the cell's life time. When disregarding the low-temperature operation, the model error was below 7% [106]. Given that the application studied in this work (see chapter 4) is unlikely to result in low temperatures and that it will use new cells, it seems reasonable to use the SEI model only for the rest of this work. However, the methodology used will probably work equally well with more complicated (combinations of) degradation models as long as they do not alter the mathematical structure of the optimisation problem, see section 3.3.2.

2.7 Conclusions

This chapter presented a comprehensive overview of physical degradation models proposed in literature. The different equations for various physical mechanisms were listed, and the basic degradation trends predicted by each model were compared. In a second step, two models were combined to assess how the feedback mechanisms influenced the predicted degradation. The feedback mechanisms could both enhance and decelerate the effect of the individual degradation models. It was found that some models, such as the kinetically limited SEI growth, are more susceptible to feedbacks while others are more independent, such as the diffusion-limited SEI growth.

Then the effect of variable operating conditions was studied. It was shown how some models are highly dependent on how the battery is used, while others predict the same degradation for all conditions. Also the importance of independent variable (time or charge throughput) was explored. Finally, it was demonstrated how a combination of degradation models was needed to predict the distinctive degradation trends observed in large data sets. This indicated that it is unlikely a single model can accurately predict degradation in all cases.

However, if the expected operating conditions of the battery are known in advance, it might be sufficient to consider only one degradation model which captures the essential dependencies. This model will not be able to accurately predict degradation in all cases, but might give a strong indication about what types of operating conditions should be avoided. In a well-defined application using new cells, this might be sufficient to get a basic understanding of what (not) to avoid when controlling the battery. For the Kokam cell introduced in section 1.4, the SEI growth model combining both diffusion and kinetic limitations was shown to be such a ‘sufficient’ degradation model.

2.8 Limitations and future work

Although the previous analysis gave interesting insights in battery degradation modelling, there are some clear limitations. First and foremost, the battery model used, the SPM, is a significant simplification. It is only valid under certain conditions, which for instance exclude high currents or high-energy cells. Therefore, the presented analysis is not valid for applications such as fast charging, where the battery of an electric vehicle, usually made up of a high-energy cells, is charged at high power. A second consequence of using the SPM is that inhomogeneities, or other location-specific effects, could not be studied. For high-quality cells used in ‘average’ operating conditions, this might be a reasonable simplification but it introduces further limitations to the conclusions presented in this chapter.

A second limitation results from the complexity of the physical processes versus the relatively simple models. Partly this is due to a limited quantitative understanding of the physical processes, but equally important is the computational power and time available to solve the models. The cell-to-cell variations, especially between different cells (different shapes, manufacturers, chemistries, etc.) make it even more difficult to accurately predict the exact behaviour of one single cell used in a specific operating conditions. Therefore, no simulation should be considered as an accurate reflection of the reality, rather they should be used only to give an indication as to what might be expected to happen in certain conditions.

Models which incorporate more physical features seem more reliable and accurate than simplified models. For instance, the combination of Dai's stress model with Laresgoiti's model for LAM seems to give more realistic degradation predictions than the heavily simplified model from Delacourt for LAM. And if simplifications are made, it seems important to bear in mind which are the relevant physical processes causing the degradation. For instance, Ekstrom's crack-growth model is 'only' a simple Tafel equation, but since it accounts for phase changes in the graphite, its results are well interpretable and more reliable than other simple models such as Barai's crack-growth model. However, more work is needed to asses what are exactly the 'important' physical processes under which operating conditions such that reliable simplified physics-based degradation models can be developed.

Although it is desirable to get more accurate models, the limitations mentioned above might make it difficult to ever arrive at a generally applicable degradation model. Therefore, future work should aim to maximise the use of available models. A special focus should be on model selection and parametrisation: there exists a whole range of models predicting very different degradation behaviours. But given a data set, it is not straightforward to determine which models are best suited to simulate the observed trends and therefore are most likely to predict degradation in different operating conditions.

Chapter 3

Optimal control of nonlinear battery models

This chapter explains the numerical methods used to solve and optimise the equations characterising the battery's electrochemical behaviour mentioned in chapter 2. Instead of focussing on methods for integrating the coupled PDEs and ODEs in time, as considered by the papers referenced in the previous chapter, the novelty of this work is related to the optimal use of the battery. Specifically, numerical methods are developed to find the current sequence which gives the largest benefits of using the battery while limiting the degradation. Because the battery model is nonlinear, specialised methods have to be used to enable such optimal control. The first section gives a literature review on optimal control of nonlinear battery models, while the rest of the chapter explains the techniques used in this work.

First and foremost, the number of variables was reduced to keep the resulting optimisation problem tractable. Most of the methods were developed by Adrien Bizeray [160], who implemented the SPM with a bulk thermal model. The only addition here is an equation to capture degradation. The number of state variables was limited by using an efficient spatial discretisation method for the diffusion partial differential equation (PDE) using Chebyshev spectral methods, which are introduced in section 3.2. Section 3.3 applies this technique to the lithium diffusion PDE (2.1) and shows how the boundary conditions (2.2, 2.3) are accounted for. Together with the other ordinary differential equations (ODEs), they are arranged to formulate a state-space model. Lastly, this section outlines the generic procedure for using a state-space model in an optimisation problem.

Secondly, an efficient method for time integration is needed to reduce the number of discretised time nodes, which also reduces the number of optimisation variables. Section 3.4 firstly introduces the basic time integration method, and then explains how multiple shooting can be used to reduce the number of time steps at which optimisation variables are needed.

Section 3.5 digs deeper into the model formulation for optimisation purposes, showing how the different optimisation variables can be decoupled such that the Jacobian becomes sparse. Section 3.6 then lists the resulting formulation after applying the techniques from sections 3.2 to 3.5.

Section 3.7 explains the method used to obtain the derivatives required by the optimisation algorithm, and section 3.8 shows how problems with long time horizons can be broken up. Finally, section 3.9 brings it all together and lists the procedure used to solve the optimisation problem.

3.1 Literature review of optimisation constrained by physical battery models

This section gives an overview of the literature which used physical battery models within some optimisation problem. Section 4.2.3 gives an overview of optimisation approaches using other battery models, such as equivalent-circuit models and empirical degradation models. Section 4.2.4 gives an overview of physical models used in case studies for power system applications although the papers discussed do not include an optimisation of the battery models.

Moura et al. [161, 162] studied the power management in a plug-in hybrid car. They used a 'low-order equivalent-circuit model' for the optimisation while a 'high-fidelity electrochemical-based model' was used to verify the constraints of the cell. The optimisation with the ECM used a modified policy-evaluation-improvement algorithm. They then used a single-particle model to verify the voltage constraints of the battery and to estimate the degradation of the cell. Their SPM was extended with electrolyte dynamics, a bulk thermal model and a kinetically limited SEI growth model (2.17). It was solved using a Padé approximation and finite differences. Although this produced good results, the optimisation itself used a linear ECM and the main contribution of this paper was to use a physical model to check the outcome.

Campbell et al. [163] also used a physical model, the P2D model extended with lithium plating, to validate the outcome of an optimisation. They optimised the number of layers a cell should have in order to maximise the stored energy while avoiding lithium plating during fast charging. As before, the main contribution was to use a physics-based model to evaluate the optimisation outcome and check it satisfies the operational limits of a lithium-ion cell, rather than optimising the physical model itself. Qi et al. [164] also used the P2D model for optimal cell design, rather than for optimal control as is done in this work.

The research group lead by Plett at the University of Colorado Colorado Springs pioneered the practice of using physical models for optimal control of a battery, in particular through the application of reduced-order models [165]. These models were used in a model-predictive control (MPC) framework for fast charging. Unfortunately, this work was patented and not published, making it difficult to assess their exact methods and results [166, 167]. For instance, it is not clear whether or not battery degradation was included in the MPC or how the optimisation was done.

Similar work with reduced-order models was presented by Suthar et al. [168] although they did not include degradation in the model nor in the optimisation. They used 'simultaneous nonlinear programming', the same technique used in this work (see section 3.3.4).

Instead of reducing the physical models, Torchio et al. [169] linearised the equations to perform MPC. Lucia et al. [170] also started from physical models but approximated the concentration profiles with polynomial expressions.

Perez et al. [171] on the other hand directly used the SPM with electrolyte dynamics (SPMe) and a two-state thermal model to optimise the fast charging of a cell, although no degradation was considered. They used finite differences for the spatial discretisation and existing software (GPOPS-II) for the optimal control. This involved using pseudo-spectral methods for time integration and IPOPT for the optimisation. Note that this approach is similar to the one followed in this work: here spectral methods are used for spatial discretisation (see section 3.2) and finite differences for time integration (see section 3.4). The results from Perez et al. clearly indicate that using electro-chemical models for optimisation produces better results compared to conventional charging profiles, although the authors only optimised over short time horizons and did not consider degradation. Klein et al. [172] did similar work in 2011, using `fmincon` in Matlab to solve the optimisation. They did not specify how they discretised and formulated the model.

Finally, Pathak et al. [173] used a P2D model which was extended with a kinetically limited SEI growth model (2.17) to find optimal profiles for fast charging. They tried three different optimisation techniques: (1) simultaneous discretisation using finite differences for spatial discretisation, backward Euler time integration, and IPOPT, an existing optimisation solver, to optimise the resulting problem; (2) control vector parametrisation where the problem is simplified by limiting the number of free optimisation variables to six and the `NLPSolve` optimiser from Maple was used to optimise those six variables; (3) modified control vector parametrization where there are still only six free optimisation variables, but the current varied linearly between those six values. The first technique (simultaneous discretisation) is the same as ‘simultaneous nonlinear programming’ from Suthar et al. [168], which is also used in this work, although here different discretisation schemes were used and the model was formulated differently to allow optimisation over a much longer time horizon. All three approaches tried by Pathak et al. produced quite different ‘optimal’ profiles for fast charging, indicating that the optimisation was not very successful. Nevertheless, the profiles were an improvement over conventional fast charging protocols and the lifetime of the cell could be more than doubled, which was validated experimentally.

Subramanian’s research group has continued to work on the optimisation, e.g. [174] used an AI-inspired optimiser with neural network to solve the parametrisation problem. Pathak et al. [175] have also developed a ‘generic model control’, where physical models are used to determine the set-points of a control method, rather than controlling the battery directly. Aduru et al. [176] are still working on nonlinear optimal control using physical models but so far have not published about it.

3.2 Spatial discretisation using Chebyshev spectral methods

Most commonly, finite differences or finite elements are used to solve PDEs. However, such methods often need many nodes to guarantee accuracy and stability. The problem explored in this work however is to optimise a nonlinear battery model, in which case it is essential to keep the number of optimisation variables as low as possible. This motivated the use of Chebyshev spectral methods for spatial discretisation, as used by Bizeray at al. for the SPM and P2D model. A comprehensive discussion of this discretisation approach and its application to batteries is given in [160], of which a summary is presented below. Section

3.2.1 explains Chebyshev interpolation, and section 3.2.2 explains how this can be used for spatial differentiation.

3.2.1 Chebyshev interpolation

The fist step of spectral methods is to interpolate the real solution c at location x and time t, $c(x,t)$, of the PDE with an interpolant $\bar{c}(x,t)$, which is a sum of N_c functions of known form $T_k(x)$, called basis functions. The interpolant must be equal to the real solution in the N_c discretisation nodes x_j (3.1), which allows computation of the coefficients $\hat{y}_k$. The higher N_c, the better the interpolating function $\bar{c}(x)$ will approximate the real function $c(x)$.

$$c(x_j) = \bar{c}(x_j) = \sum_{k=1}^{N_c} \hat{y}_k T_k(x_j) \qquad \forall j = 1,2,..,N_c \tag{3.1}$$

In theory, different types of basis functions could be used. Polynomial functions lead to the Runge phenomenon[1] and are therefore not feasible. Chebyshev functions are a more common choice due to their good numerical properties such as orthogonality [177]. In Chebyshev interpolation, the locations of the nodes x_j are usually distributed along a horizontally projected semicircle from -1 to 1 (3.2). This necessitates a coordinate transformation from the physical ($-R \leq r \leq R$) to the computational domain ($-1 \leq \bar{x} \leq 1$) as explained in section 3.3.

$$x_j = \cos\left(\frac{(j-1)\pi}{N_c - 1}\right) \qquad j = 1,2,..,N_c \tag{3.2}$$

---

[1] The Runge phenomenon occurs when the interpolating function starts oscillating around the solution, especially at the edges of the interpolation interval. This happens when high-order polynomials are used on an equidistant grid and implies that the interpolant does not converge to the solution with increasing order. It is similar to Gibb's phenomenon in Fourier interpolation [177].

Due to the orthogonal basis functions given by (3.3) and fast convergence, called spectral accuracy, only a few nodes are needed to produce an accurate fit [177], reducing the number of variables needed in the model.

$$\begin{aligned} T_0(\bar{x}) &= 1 \\ T_1(\bar{x}) &= \bar{x} \\ T_{k+1}(\bar{x}) &= 2\bar{x}T_k(\bar{x}) - T_{k-1}(\bar{x}) \end{aligned} \tag{3.3}$$

3.2.2 Differentiation

The second step when applying spectral methods is approximating the p$^{\text{th}}$ spatial derivative of the real solution $c(x,t)$ with the derivative of the interpolant $\bar{c}(x,t)$ (3.4).

$$\left.\frac{\partial^p c(\bar{x})}{\partial \bar{x}^p}\right|_{\bar{x}=x_j} \approx \left.\frac{\partial^p \bar{c}(\bar{x})}{\partial \bar{x}^p}\right|_{\bar{x}=x_j} \qquad \forall j = 1,2,..,N_c \tag{3.4}$$

Because the form of the basis functions and the location of the nodes is known a priori, the derivatives of the terms $T_k(x_j)$ are known and constant. The coefficients $\hat{y}_k$ are fully determined by (3.1), which is a linear system of equations. Combining this, the right hand side of (3.4) can be expressed as a linear equation with constant coefficients. Grouping all nodes $\bar{c}(x_j)$ into a vector $\bar{\mathbf{c}}$, (3.4) can thus be written as (3.5) where $D_c^{(p)}$ is the Chebyshev differentiation matrix of order p. Furthermore, the interpolant is exact in the discretisation nodes, such that $\bar{\mathbf{c}} = \mathbf{c}$.

$$\frac{\partial^p \mathbf{c}}{\partial \bar{x}^p} \approx \frac{\partial^p \bar{\mathbf{c}}}{\partial \bar{x}^p} = D_c^{(p)}\bar{\mathbf{c}} = D_c^{(p)}\mathbf{c} \tag{3.5}$$

The Matlab package `DMSUITE` developed by Weideman et al. [178] was used to calculate the Chebyshev discretisation nodes and differentiation matrices.

3.3 Battery model formulation

This section explains the formulation of the battery's state-space model. It extends the work by Bizeray et al. [160] who developed a state-space model comprising the diffusion PDEs and the thermal ODE. Section 3.3.1 describes the formulation of the diffusion PDE while section 3.3.2 explains the formulation for the other ODEs in the model. Section 3.3.3 shows how the previous equations can be grouped in a state-space model, and section 3.3.4 explains the general procedure to optimise state-space models followed in this work.

3.3.1 Diffusion model

This section is a summary of the work described in section 3.2.3 from [160]. Due to the radial symmetry, the constant radius and spatial independence of the diffusion constant, a change of variable from the concentration $c_i(r)$ to $u_i(r) = rc_i(r)$ simplifies the spatial derivative in the diffusion PDE (2.1) to (3.6), where $D_i(T)$ is the temperature-dependent diffusion coefficient of electrode i.

$$\frac{\partial u_i(r)}{\partial t} = D_i(T)\frac{\partial^2 u_i(r)}{\partial r^2} \tag{3.6}$$

The centre boundary condition (2.2) has to be replaced with a Dirichlet boundary condition to ensure a finite concentration (3.7). Since $u_i(0) = 0 \cdot c_i(0)$, it could only be nonzero if $c_i(0)$ were infinite. The surface boundary condition (2.3) becomes (3.8). Note that the side reaction current densities due to degradation mechanisms, e.g. (2.38), can be simply added on the right-hand side.

$$u_i(0) = 0 \tag{3.7}$$

$$\frac{D_i(T)}{R_i}\left(\frac{\partial u_i(r)}{\partial r}\bigg|_{r=R_i} - \frac{u_i(R_i)}{R_i}\right) = \pm j_i = \pm\frac{i_i}{nF} = \pm\frac{I}{nFa_iA_i\tau_i} \tag{3.8}$$

As mentioned in section 3.2, a coordinate transformation from the physical domain to the computational domain is needed because Chebyshev nodes must be on [-1, 1]. The procedure from [177] is followed, which is a slight deviation from section 3.2.3 of Bizeray [160], but which is explained in Appendix B of the same thesis. The nodes are distributed in both the positive and negative half of the particle, i.e. $-R_i \leq r_i \leq R_i$, such that $\bar{x} = r/R_i$. Due to the symmetry $c_i(-r_i) = c_i(r_i)$ so $u_i(-r_i) = -u_i(r_i)$, only the positive half of the domains, i.e. $0 \leq r_i \leq R_i$ and $0 \leq \bar{x} \leq 1$, have to be used in the computation[2]. The advantage of this approach over the one followed by Bizeray at al., who mapped the positive physical domain to the full computational domain, i.e. $0 \leq r_i \leq R_i$ and $-1 \leq \bar{x} \leq 1$, is that there are fewer points near the centre, where little variation in the concentration profile can be expected. Applying this, (3.6) and (3.8) become (3.9) and (3.10) respectively.

$$\frac{\partial u_i(\bar{x})}{\partial t} = \frac{D_i(T)}{R_i^2}\frac{\partial^2 u_i(\bar{x})}{\partial \bar{x}^2} \tag{3.9}$$

$$\frac{D_i(T)}{R_i^2}\left(\frac{\partial u_i(\bar{x})}{\partial \bar{x}}\bigg|_{\bar{x}=1} - u_i(1)\right) = \pm j_i = \pm\frac{i_i}{nF} = \pm\frac{I}{nFa_iA_i\tau_i} \tag{3.10}$$

Using the differentiation matrices, (3.9) can be written as (3.11) where it should be remembered that $D_i(T)$ is the temperature-dependent diffusion coefficient of electrode i, while $D_c^{(p)}$ is the differentiation matrix of order p.

---

[2] When interpolating using the Chebyshev basisfunctions as in (3.1), the advantage of the symmetry in u means that the coefficients y_k for even basis functions will be zero such that only half the number of basis functions needs to be used (and the negative half of the problem can be ignored). On the other hand, the differentiation matrix is still full since the value at any node still depends on the value at all other nodes through the odd basis functions. However, the negative half of the differentiation matrix can still be ignored, and due to the symmetry the ‘right half’ can be incorporated in the ‘left half’ such that for a problem with N_c nodes, the resulting matrix is $N_c/2$ x $N_c/2$.

$$\frac{\partial \mathbf{u}_i}{\partial t} = \frac{D_i(T)}{R_i^2} D_c^{(2)} \mathbf{u}_i \tag{3.11}$$

Finally, the boundary conditions can be implicitly written in the system by eliminating the centre and surface nodes, whose value is determined by the boundary conditions. The full derivation can be found in Appendix B of [160], the resulting equation is (3.12), where the subscripts indicate which nodes are considered[3]. The concentration at all nodes can be calculated using (3.13). The matrices $\bar{A}_i$ and $\bar{C}_i$, and the arrays $\mathbf{b}_i$ and $\mathbf{d}_i$ are known and constant for each electrode i.

$$\frac{\partial \mathbf{u}_{2:N_c-1,i}}{\partial t} = D_i(T) \bar{A}_i \mathbf{u}_{2:N_c-1,i} + \mathbf{b}_i j_i \tag{3.12}$$

$$\mathbf{c}_{1:N_c,i} = \bar{C}_i \mathbf{u}_{2:N_c-1,i} + \mathbf{d}_i \frac{j_i}{D_i(T)} \tag{3.13}$$

In section 3.4.4 of [160], Adrien Bizeray analysed the number of nodes needed in the solid particles of the P2D model to simulate a dynamic current profile. He concluded that about 15 nodes was sufficient. However, due to the symmetric location of the nodes in this work, the number of nodes can be decreased. Furthermore, no dynamic profiles will be used, reducing the concentration gradients at the surface, which in turn allows a reduction in the number of nodes needed. Simulations with various values of N_c showed little difference during CC discharges. Therefore, a total of 11 nodes were used, resulting in 5 nodes in the 'inner' positive domain, which excludes the centre and surface nodes, or in other words, N_c from (3.12) is 7.

---

[3] e.g. $\mathbf{u}_{2:N_c-1,i}$ is the (transformed) concentration in nodes 2 to $N_c - 1$, i.e. the inner nodes without the centre (1) and surface (N_c) nodes, in electrode i.

3.3.2 Other model equations

The remaining equations that describe the behaviour of the battery are nonlinear ODEs. They are coupled because they depend on the same physical properties such as the surface concentration. First of all, the bulk thermal model given by (2.10) depends on the overpotential, which in turn depends on the surface concentration. And through the Arrhenius relations of the diffusion constant (2.11), the diffusion PDE is linked back to the thermal ODE.

The degradation models are also nonlinear ODEs which can be implemented alongside the diffusion and thermal equations; some of the models are linked through the stress models, others depend directly on the concentration and temperature. For the remainder of this work, only one degradation model was considered: the diffusion and kinetically limited SEI growth model (2.20). The growth of this layer is linked with the concentration (through the anode potential and overpotential), the temperature (through the Arrhenius relations for the rate and diffusion constants) and the input current, with its thickness is given by (2.21), and the boundary condition of the anode diffusion PDE is given by (2.22), which removes lithium from the main reaction.

The same procedure as outlined below would also work with other degradation models, but it would increase the complexity of the model and thus increase the computational time. To verify this, a second version of the model was developed which included Narayanrao's LAM model (2.30). This degradation model consisting of both an SEI model and Narayanrao's LAM model was fitted to the degradation behaviour of a different cell. This cell was used for a different experiment which is described in section 4.7. However, the optimisation did not produce good outcomes with these models because the optimisation solver failed to converge to acceptable points. This is probably due to the much more complicated structure of the model as the amount of active material becomes a state variable which links all other variables together (resulting in a full Jacobian). This point was not investigated in more detail since the experiment never took place as described in section 4.7.

Using the full ‘generalised degradation model’ from section 2.5.3 would have been very difficult. It adds three state variables but more importantly, it adds coupling to the existing state variables because the amount of active material appears in all equations. As explained in section 3.5, a higher degree of coupling between variables makes the optimisation problem much more difficult to solve. None of the stress models from section 2.1.3 are needed.

3.3.3 State-space formulation

The equations can be grouped in a state-space model with input current I, voltage V being the model output and therefore representing the measurement variable, state $\mathbf{s}$, the evolution of which is described by a nonlinear mapping f and a nonlinear output mapping, or measurement equation, g (3.14). As before, the time dependency of the variables is not written to simplify notation.

$$\begin{aligned}\frac{\partial \mathbf{s}}{\partial t} &= f(\mathbf{s}, I) \\ V &= g(\mathbf{s}, I)\end{aligned} \tag{3.14}$$

The states in the model are: the transformed concentration in the inner Chebyshev nodes in both electrodes $\mathbf{u}_{2:N_c-1,i}$, the cell temperature T, and the thickness of the SEI layer τ_{sei} (3.15).

$$\mathbf{s} = \begin{pmatrix} \mathbf{u}_{2:N_c-1,p} \\ \mathbf{u}_{2:N_c-1,n} \\ T \\ \tau_{\text{sei}} \end{pmatrix} \tag{3.15}$$

The nonlinear state function f is given by (3.16). This is the combination of (3.12) for both the positive and negative electrode, where the current density on the anode is increased with the side reaction current density as given by (2.22), the thermal ODE (2.10), and the increase in the thickness of the SEI layer (2.21). All the PDEs and ODEs are linked by the various equations described in section 3.3.2.

$$\frac{\partial \mathbf{s}}{\partial t} = \begin{pmatrix} D_p(T)\bar{A}_p\mathbf{u}_{2:N_c-1,p} + \mathbf{b}_p\frac{i_p}{nF} \\ D_n(T)\bar{A}_n\mathbf{u}_{2:N_c-1,n} + \mathbf{b}_n\left(-\frac{i_\mathrm{n}}{nF} - \frac{i_\mathrm{sei}}{nF}\right) \\ \frac{1}{\rho_{batt}A_\mathrm{batt}\tau_\mathrm{batt}C_{p,\mathrm{batt}}}\left(I^2R_\mathrm{dc,batt} + I\left(\eta_n - \eta_p\right) + IT\frac{\partial U_\mathrm{batt}}{\partial T} - hA_\mathrm{batt}\left(T - T_\mathrm{env}\right)\right) \\ \frac{i_\mathrm{sei}M_\mathrm{sei}}{\rho_\mathrm{sei}nF} \end{pmatrix} \tag{3.16}$$

Here, i_p is the current density on the positive electrode obtained by dividing the total battery current I by the total active surface area $a_pA_p\tau_p$ as defined in (2.3) and similarly for the current density on the negative electrode i_n. The SEI current density i_sei is given by (2.20) and is a nonlinear function of both the battery state and the total current.

The measurement equation g is the voltage equation (3.17), which is the same as (2.9). The cell's OCV U_batt depends on the surface concentration of both the anode and cathode $\mathbf{c}_{N_c,i}$, which can be calculated using (3.13). The overpotentials also depend on the surface concentrations, as well as the current and temperature. The ohmic resistance of the cell $R_\mathrm{dc,\ batt}$ depends on the thickness of the SEI layer as given by (2.7).

$$V_\mathrm{batt} = U_\mathrm{batt} - (\eta_n - \eta_p) - R_\mathrm{dc,batt}I \tag{3.17}$$

3.3.4 Optimal control of state-space models

The terminology for optimal control is different from the terminology used before: the *input* variable is called the *control* variable (the current, I), and the *measurement* variable is called an *algebraic* variable (the voltage, V) [179, 180]. A generic optimal control problem is given by (3.18 - 3.20). The objective function Π is a function of the state, control and algebraic variables. The state-space model f (3.16), and measurement equation g (3.17) appear as constraints in (3.19). There can be upper and lower limits (3.20) with subscripts u and l respectively, on the state, control and algebraic variables.

$$\max \Pi \left(\mathbf{s}\left(t\right), I\left(t\right), V\left(t\right)\right) \tag{3.18}$$

subject to

$$\begin{aligned} \frac{\partial \mathbf{s}\left(t\right)}{\partial t} &= f\left(\mathbf{s}\left(t\right), I\left(t\right)\right) \\ V\left(t\right) &= g\left(\mathbf{s}\left(t\right), I\left(t\right)\right) \end{aligned} \tag{3.19}$$

$$\begin{aligned} \mathbf{s}_l &\le \mathbf{s}\left(t\right) \le \mathbf{s}_u \\ I_l &\le I(t) \le I_u \\ V_l &\le V(t) \le V_u \end{aligned} \tag{3.20}$$

Several approaches have been developed to optimally control state-space models, including variational calculus, Pontryagin's maximum principle, control vector iteration (also called sequential optimisation), simultaneous nonlinear programming, etc. [168]. Here simultaneous programming is used, where both the state variable $\mathbf{s}$ and the control variable, I, are discretised in time. This results in a large set of nonlinear equations which can be optimised with conventional nonlinear optimisation algorithms. This approach has two main advantages: it performs well with unstable control problems[4], and path constraints (such as the state equations and temperature and voltage limits) are easy to include [179, 180].

---

[4] The battery model is very stiff, but this results in numerical instability and not necessarily in control instability.

For the optimisation, all variables are treated equally as ‘optimisation variables’ with constraints linking them. The vector of all optimisation variables **W** consists of the transposed state vector $\mathbf{s}^T(t)$, the control variable $I(t)$, and the algebraic variable $V(t)$ at every time step (3.21), where N_1 is the number of time steps.

$$\mathbf{W} = \left[\mathbf{s}^T(1)\ I(1)\ V(1)\ \mathbf{s}^T(2)\ I(2)\ V(2)\ ...\ \mathbf{s}^T(N_1)\ I(N_1)\ V(N_1)\right] \tag{3.21}$$

Using this vector, the optimisation problem can be re-written as (3.22 - 3.24). The constraint function Γ enforces the state-space equation f and measurement equation g at every time step (3.23).

$$\max \Pi(\mathbf{W}) \tag{3.22}$$

subject to

$$\Gamma(\mathbf{W}) = 0 \tag{3.23}$$

$$\mathbf{W}_l \leq \mathbf{W} \leq \mathbf{W}_u \tag{3.24}$$

3.4 Time discretisation

Various software packages can be used to integrate state-space models, for instance, `ODE45` or `ODE15s` in Matlab. However, these functions cannot be used for the optimisation problem because they are not compatible with the software packages for automatic differentiation and optimisation. Instead, other time integration approaches have to be used, as described in section 3.4.1, while section 3.4.2 explains multiple shooting, a technique used here to reduce the number of optimisation variables. Finally, section 3.4.3 compares the approach followed here with the conventional time integration from simultaneous discretisation.

3.4.1 Time integration

There are various standard schemes for time integration, which will give different formats for the constraints in the optimisation problem. The simplest scheme is forward Euler time integration (3.25) with a discrete time step Δt and f the function calculating the time derivatives[5] (3.16). Drawbacks of this scheme are its small stability region and low numerical accuracy, with the stability of time integration related to the eigenvalues of the linearised state-space representation [177]. The battery model described above was implemented both in Matlab and in C++. Time integration in Matlab was done with the standard schemes `ODE45` and `ODE15s` while forward Euler was used in C++. A comparison of the results showed no difference in the voltage during CC (dis)charges for Euler time steps of 5 seconds or below. Above 5 seconds, the forward Euler scheme became numerically unstable, mostly due to the thermal ODE. For low temperatures and small currents, the time step could be increased without loss of stability or accuracy but this was not exploited in the C++ code because variable time stepping would make the rest of the optimisation problem too difficult, in particular calculating the derivatives would be almost impossible.

$$\mathbf{s}(t) = \mathbf{s}(t-1) + f\left(\mathbf{s}(t-1), I(t)\right)\Delta t \qquad \forall t = 1, 2, .., N_2 \tag{3.25}$$

More complicated time integration schemes with larger stability windows exist, such as fourth-order Runge-Kutta schemes, which would allow to increase the time step. However, when they were applied to the battery state-space model, they increased the computational

---

[5] This is used as shorthand notation for the nonlinear mapping $\mathbb{R}^n \mapsto \mathbb{R}^n$, which is applied to the state $\mathbf{s}$ and produces the time derivative $\frac{\partial \mathbf{s}}{\partial t}$.

time, indicating that the higher computational cost per step outweighed the benefit of needing fewer steps. Additionally, to keep the optimisation problem as simple as possible, it is important to keep the time integration formula as simple as possible. If the time derivate at t depends on function values at multiple time steps, e.g. t, $t-1$ and $t-2$ then the optimisation variables at those time steps are linked too due to the time-integration constraints. This will cause the Jacobian to be less sparse, complicating the time integration as explained in section 3.5. Backward Euler time integration, which only depends on two function evaluation as was the case for forward Euler, introduces a nonlinear system of equations which has to be solved at every time step, which would be computationally expensive and might not work with the software packages for differentiation and optimisation.

3.4.2 Multiple shooting

Having small time steps necessitates a large number of steps N to cover the entire time horizon, resulting in a large number of optimisation variables and a large number of constraints. Multiple shooting is an established technique to solve this problem [180, 181]. In multiple shooting, there are two different time steps: Δt_1 for the optimisation (3.26) and Δt_2 for time integration (3.27). Note that for this work, the current had values at the larger Δt_1 limiting the rate at which it could change.

$$\mathbf{W} = \left[\mathbf{s}^T(\Delta t_1)\; I(\Delta t_1)\; V(\Delta t_1)\; \mathbf{s}^T(2\Delta t_1)\; I(2\Delta t_1)\; V(2\Delta t_1)\; ...\; \mathbf{s}^T(N\Delta t_1)\; I(N\Delta t_1)\; V(N\Delta t_1)\right] \tag{3.26}$$

$$\mathbf{s}(t_2) = \mathbf{s}(t_2 - 1) + f\left(\mathbf{s}(t_2 - 1), I(t_1)\right)\Delta t_2 \qquad \forall t_2 = 1,..,N_2 \tag{3.27}$$

Therefore, the constraint in the optimisation problem determining the relation between optimisation variables and which appears in the constraint function Γ (3.23), is given by (3.28).

$$\mathbf{s}(t_1) = \mathbf{s}(t_1 - 1) + \sum_{t_2=1}^{N_2} \left(f\left(\mathbf{s}(t_2 - 1), I(t_1)\right) \Delta t_2 \right) \tag{3.28}$$

Fig. 3.1 illustrates the concept for one state variable, but is just a conceptual visualisation which does not reflect the values used in this work. In the traditional approach, the same time step is used for both optimisation (red) and time integration (blue). With multiple shooting, time integration is performed repeatedly, each with a small time step. Only once the larger time period is covered is there a new optimisation variable.

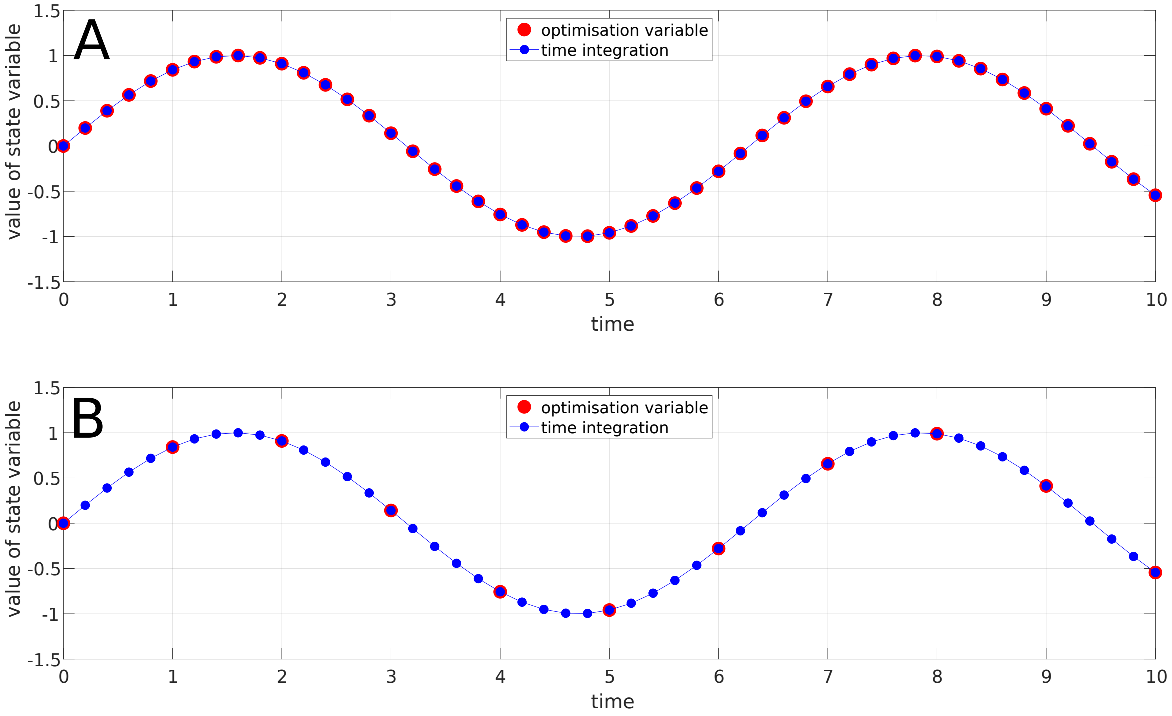

Fig. 3.1 Conceptual graphical illustration of multiple shooting for time integration. (A) traditional approach; (B) multiple shooting.

Different values and a different ratio between Δt_1 and Δt_2 are possible and will affect the computational time. For this work, Δt_1 was chosen to be 15 minutes because the application considered in the optimisation works with time steps of 15 minutes (see section 4.1). Since only the average behaviour over those 15 minutes matters, limiting the rate of change of the current has only a limited impact. Δt_2 was kept at 5 seconds to ensure accuracy and stability as explained in the previous section.

3.4.3 Comparison to time integration for simultaneous optimisation

In conventional simultaneous optimisation, the goal is to find continuous functions for the optimisation variables. The total time horizon is divided in ‘finite elements’, and within one such ‘element’ a functional form is assumed for each variable, for instance a polynomial function of time with constant coefficients. Using a Runge-Kutta scheme with a monomial basis on nodes q, this results in (3.29), where the value of the state variable s at continuous time t, which is in element i, depends on the time derivatives at all K nodes inside this element, where Ω_q is a polynomial of degree K, s_i is the value at the beginning of the element, at time t_i, and h is the length of the element [179, 180]. Once the optimisation has determined the values of s_i at the element boundaries and nodes q, the coefficients of Ω_q can be determined (or vice versa) and the value of s can be calculated at every point in time. This is sometimes referred to as ‘pseudo-spectral methods’ [171].

$$s_i(t) = s_i + h \sum_{q=1}^{K} \Omega_q \left(\frac{(t - t_i)}{h} \right) \left. \frac{\partial s}{\partial t} \right|_{t=t_{i,q}} \tag{3.29}$$

This could be compared to the dual-time-step approach followed here, where the optimisation time step, Δt_1, is similar to an ‘element’ and the integration time step, Δt_2, is similar to the nodes inside elements. However, the discretisation of variables inside the ‘elements’ is different. The control variable (current) is not discretised at a smaller time step, or in other words, the polynomial function for the control variable is simply a constant. The state and algebraic variables are discretised on a equidistant grid using finite differences as in (3.30), where $\Delta t_1 / N_2 = \Delta t_2$. The resulting equation is discrete in time, only values at the nodes j

are calculated by the optimisation. The key difference with (3.29) is that the values for the discrete time step t_j involve the time derivatives of the preceding nodes (instead of involving all nodes), and that the polynomial Ω_q is omitted.

$$s_i(t_j) = s_i + \frac{\Delta t_1}{N_2} \sum_{q=1}^{j} \left. \frac{\partial s}{\partial t} \right|_{t=t_{i,q}} \tag{3.30}$$

In this case, the optimisation determines $s_i(t_j)$ and states at intermediate time steps have to be calculated by interpolating between those points, or by re-calculating the state-space model.

3.5 Decoupling of variables

Applied to the battery control problem, spectral methods for spatial discretisation reduced the number of state variables, and multiple shooting for time discretisation reduced the number of time steps at which optimisation variables were needed. The combination of both dramatically reduced the size of the optimisation problem. The remaining variables are the state-space variables, current and voltage at the integration time step as given by (3.26). They are tightly coupled, leading to a dense Jacobian which complicates the optimisation. The discretised diffusion PDE at the integration time step t_2 is given by (3.31), where the total lithium flux on the particles is the sum of the main battery current I and the SEI current density i_{sei}, which is 0 for the positive particle, and given by (2.20) for the negative particle.

$$\left. \frac{\partial \mathbf{u}_{2:N_c-1,i}}{\partial t} \right|_{t=t_2} = D_i\left(T\left(t_2\right)\right) \bar{A}_i \mathbf{u}_{2:N_c-1,i}\left(t_2\right) + \mathbf{b}_i \left(\frac{I\left(t_2\right)}{nFa_iA_i\tau_i} + \frac{i_{\mathrm{sei},i}\left(t_2\right)}{nF} \right) \tag{3.31}$$

Different dimensions in $\mathbf{u}$ are coupled in two ways: direct spatial coupling due to the dense matrix $\bar{A}_i$ and indirect coupling through the temperature-dependent diffusion constant $D_i(T)$, and the SEI current density on the anode i_{sei}, both of which depend on the concentration at all nodes. Section 3.5.1 explains how the direct coupling through $\bar{A}_i$ is eliminated, and section 3.5.2 does the same for the indirect coupling.

3.5.1 Direct spatial decoupling

The traditional methods of spatial discretisation, finite differences or finite elements, would have resulted in a large but sparse matrix in the state-space model. Spectral methods on the other hand result in a small but dense matrix $\bar{A}_i$ (3.31). In control theory, a conventional approach in such cases is to do a similarity transformation to a different basis in which the problem has a more suitable representation. In many cases, an eigenvalue decomposition of $\bar{A}_i$ is possible[6]and results in a diagonal state matrix [182]. Using $\bar{A}_i = \bar{Q}_i^{-1} \bar{\Lambda}_i \bar{Q}_i$ and $\mathbf{z}_i = \bar{Q}_i \mathbf{u}_i$, (3.31) becomes (3.32).

$$\left.\frac{\partial \mathbf{z}_{2:N_c-1,i}}{\partial t}\right|_{t=t_2} = D_i\left(T\left(t_2\right)\right)\bar{\Lambda}_i \mathbf{z}_{2:N_c-1,i}\left(t_2\right) + \bar{Q}_i \mathbf{b}_i \left(\frac{I\left(t_2\right)}{nFa_iA_i\tau_i} + \frac{i_{\text{sei},i}\left(t_2\right)}{nF}\right) \tag{3.32}$$

Before this transformation, the model was working in the regular domain where the unit vectors are the concentrations (multiplied by their radius) at the various nodes. The eigenvalue transformation can be seen as a similarity transformation to a different basis where the unit vectors are the eigendimensions. Therefore, z_j does not represent some function of the concentration in node j, but a value in eigendimension j of the diffusion PDE. Fig. 3.2 shows the concentration profiles corresponding with the various dimensions in the eigenspace for the case of 7 Chebyshev nodes in the positive domain, resulting in a matrix $\bar{A}_i$ of size 5 after the boundary conditions have been accounted for. Whenever

---

[6] $\bar{A}_i$ is a square n-by-n matrix with n distinct eigenvalues, n-1 of which are negative and the remaining one is 0. Given that $\bar{A}_i$ results from a discretisation of a (linear) diffusion PDE, there can be no oscillatory behaviour for constant boundary conditions, ruling out complex eigenvalues.

the concentration at individual nodes is needed, the reverse transformation $\mathbf{c}_i = \frac{\mathbf{u}_i}{\mathbf{r}_i} = \frac{\bar{Q}_i^{-1}\mathbf{z}_i}{\mathbf{r}_i}$ can be used, where $\mathbf{r}_i$ is an array with the radius of all nodes and the division should be interpreted as an element-wise division, i.e. $c_{j,i} = \frac{u_{j,i}}{r_j}$ for node j and eletrode i.

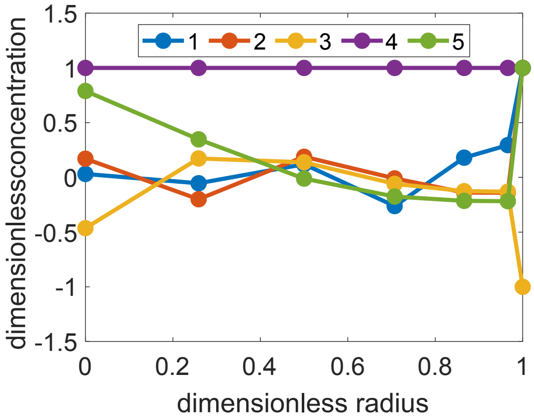

Fig. 3.2 The concentration profiles according to the various dimensions in the eigenspace for 7 Chebyshev nodes.

The transformation to the eigenspace has an additional advantage for the SPM. Finite difference schemes sometimes suffer from so-called ‘lithium leakage’ because the spatial discretisation of the diffusion PDE does not satisfy conservation laws exactly [183]. This means that due to the non-ideal mathematical properties of the scheme, the total amount of lithium is not constant. The longer the simulation, the worse this problem is because the error keeps adding up. Bizeray encountered this problem when using Chebyshev discretisation if few nodes were used [160]. The transformation to the eigenspace solves this problem: one of the eigenvalues of the differentiation matrix is always zero. Therefore, the discretised diffusion PDE (3.32) has a perfect integrator and lithium leakage is impossible (unless it is explicitly removed due to degradation), removing one of the main concerns for long-term simulations. The dimension with the zero eigenvalue represents a uniform concentration[7]. In

---

[7] This could facilitate an easy SoC estimation or a source to account for LLI although neither is necessary in this work. The SoC is calculated by integrating the current and lithium is subtracted through the boundary condition on the anodic particle.

the example from Fig. 3.2, the fourth dimension represents this uniform concentration. The other dimensions will give different deviations from this uniform concentration.

The new matrix $\bar{\Lambda}_i$ in the state-space model is diagonal, implying that the time derivative of one dimension does not depend directly on a different dimension. Additionally, the computation speeds up because time integration no longer involves a matrix-vector product. Only when the voltage has to be calculated, the inverse transformation is needed, which does involve a full matrix-vector computation.

3.5.2 Indirect temporal decoupling

The previous section decoupled the concentrations according to the different dimensions. However, they are still linked indirectly at every integration time step t_2 through the temperature and SEI current density as shown in Fig. 3.3. The eigenspace concentration at node k and time t_2 influences the transformed concentration at all nodes $\mathbf{u}$ through the reverse eigenvalue decomposition. The surface concentration c_{N_c} is determined by the transformed concentration at all inner nodes. The anode overpotential and OCV are a function of this surface concentration and they themselves influence the thermal ODE and SEI side reaction. The former changes the cell's temperature, and therefore diffusion constant at the next time step. The latter changes the boundary condition on the anode. Both terms appear in the PDE for all nodes, such that ultimately, the eigenspace concentration at node l is affected by node k, where $k \neq l$. Therefore, the concentrations at different dimensions are still coupled and the entries in the Jacobian, which contains the cross derivatives at the optimisation time step t_1, would be non-zero[8].

This is solved by relaxing these dependencies. The coupling is not considered at the smaller t_2 time steps used for time integration, only at the larger t_1 time steps used for the

---

[8] The temperature at time $t_2 + 1$ depends on the concentration at all nodes, and is not an optimisation variable. Therefore, if the concentration depends on the temperature at time $t_2 + 1$, it will depend on all the optimisation variables on which this temperature depends, which is both the temperature at t_1 and the concentration at all nodes at t_1.

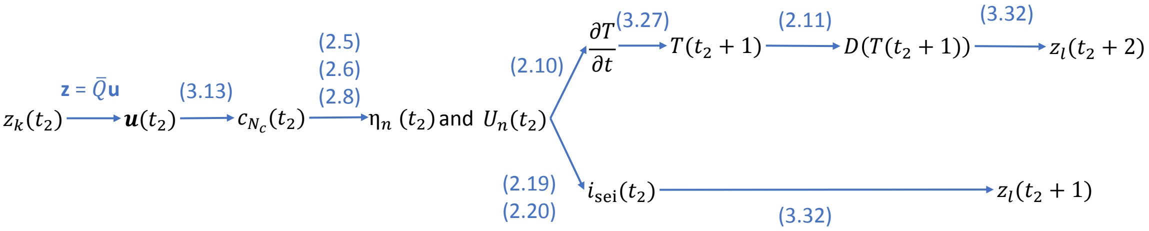

Fig. 3.3 The sequence indirectly coupling the concentrations at two different nodes k and l at the integration time step t_2. The blue numbers refer to the equations causing the link.

optimisation variables as shown in orange on Fig. 3.4. The temperature dependency is relaxed by only accounting for the changed diffusion and rate constant (2.11, 2.12) at the larger t_1 periods. In other words, the temperature used in the Arrhenius relation is the temperature at the optimisation time step $T(t_1)$, not at the integration time step $T(t_2)$. Therefore, changes in the thermal ODE will still affect the temperature at the integration time step t_2, but only at the end of the optimisation time step, this changed temperature is reflected in the diffusion (and rate) constants. This delays the effect of the temperature on everything else by one Δt_1 period but does not eliminate it. This will introduce some inaccuracies but given that the use profiles are piecewise constant (constant current in Δt_1), and the high-power cells considered do not heat up very much for the current levels in the application considered, the error is not expected to be large.

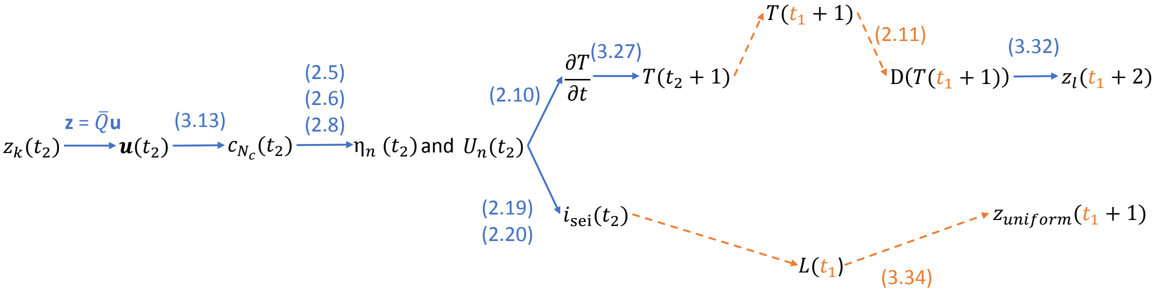

Fig. 3.4 Relaxed temporal coupling. The blue numbers refer to the equations causing the link. The orange dotted lines show how effects are accumulated in one variable, and only at the end of the optimisation time step t_1, they are accounted for.

For the lithium loss due to SEI growth, this is done by adding a separate variable L in [Ah] which accumulates all the lithium lost over one Δt_1 period. At the end of the t_1 period, this lithium is subtracted as a uniform concentration, and because one eigenspace dimension represented a uniform concentration, this will only affect one dimension of $\mathbf{z}$ at the next optimisation time step t_1+1. Therefore, the LLI is not directly included in the time integration and coupling due to degradation at the integration time step t_2 is eliminated. Given that degradation acts on a much longer time scale compared to cycling the cell, this will not have a major impact on the outcome.

Applying these two relaxations changes the discretised diffusion PDE at the integration time step to (3.33). Compared to (3.32), the time of the temperature has changed to t_1 and the SEI current density is removed. Instead, the effect of the SEI is added after N_2 integration time steps (i.e. at the next integration time step since $N_2 = \Delta t_1/\Delta t_2$) where $\bar{C}$ is the matrix from (3.13) which calculates the transformed concentration u from a concentration c, $\bar{Q}$ does the transformation to the eigenspace, the product of A_n, τ_n and ε_n gives the active volume and the factor nF converts between charge and mol.

$$\left.\frac{\partial \mathbf{z}_{2:N_c-1,i}}{\partial t}\right|_{t=t_2} = D_i\left(T\left(t_1\right)\right)\bar{\Lambda}_i \mathbf{z}_{2:N_c-1,i}\left(t_2\right) + \bar{Q}_i \mathbf{b}_i \left(\frac{I\left(t_2\right)}{nFa_iA_i\tau_i}\right) \tag{3.33}$$

$$\mathbf{z}_{\text{uniform},n}\left(t_1+1\right) = \mathbf{z}_{\text{uniform},n}\left(N_2 t_2\right) - \bar{Q}_n \bar{C}_n^{-1} \frac{L}{3600nFA_n\tau_n\varepsilon_n} \tag{3.34}$$

After applying the decoupling techniques, the different dimensions of $\mathbf{z}$ are independent (except the dimension of the uniform concentration). This means the cross derivatives of the Jacobian are zero (3.35) where k and l refer to different dimensions in $\mathbf{z}$ and k is not the dimension of the uniform concentration while i refers to the positive or negative electrode.

$$\frac{\partial z_{k,i}(t)}{\partial z_{l,i}(t-1)} = 0 \qquad \forall k \neq l \tag{3.35}$$

3.6 Optimisation formulation

This section details the exact formulation used for the optimisation, including all the previously explained techniques. The objective function is specific to the application and will be discussed in the next chapter. Here, only the aspects related to the battery model are included. Section 3.6.1 gives the optimisation variables, and section 3.6.2 gives the constraints.

3.6.1 Optimisation variables

The first choice is which variables to include as explicit optimisation variables and which to replace by a function. For instance, is the voltage an optimisation variable with a constraint given by (3.17), or is (3.17) evaluated every time the voltage is needed? The same applies to the state variables. The former approach leads to more variables, but with simpler constraints linking them, while the latter results in a smaller problem but with complex nonlinear constraints. Both approaches were tested, and it was found that the former approach worked better with the optimisation software used[9].

The only exception was the surface concentration, which is calculated every time when needed. The original SPM from Bizeray et al. [160] was formulated in that way and because the equation to calculate the surface concentration is a simple linear matrix-vector multiplication, it was left this way. Due to the simple equation, the derivatives would not be complicated - unlike the voltage, which includes nonlinear terms for the OCV and overpotentials (2.5-2.9), for which derivatives are much more difficult to compute.

The double time steps used for multiple shooting explained in section 3.4.2 necessitate some additional variables. Firstly, as explained in section 3.5.2, an extra variable is needed to accumulate the lost lithium within one larger t_1 period. Secondly, although the current is constant within one period, the voltage is not. The applications considered here relate to

---

[9] This could have been expected given that the software used, IPOPT (see section 3.9), has been designed for large problems arising due to simultaneous discretisation [179, 184], while using a function to calculate the variables corresponds to a sequential approach.

the average power within one period, and therefore a variable with the average voltage of one period is needed, $V^{\mathrm{mean}}(\mathbf{t_1})$, where $\mathbf{t_1}$ represents an array with one element for every optimisation time step. Finally, the voltage limits of the cell must be satisfied. Because the current is constant, the voltage will evolve monotonically within one period[10] such that the voltage limits will be respected if the voltage at the end of the period respects the limits. Therefore, a second voltage variable is needed, with the voltage at the end of the t_1 period, $V^{\mathrm{end}}(\mathbf{t_1})$.

Therefore, the optimisation variables are given by (3.36). It consists of the eigenspace representation of the transformed concentration in the positive inner Chebyshev nodes in the cathode and anode, the cell temperature, the thickness of the SEI layer, the lost lithium in each optimisation time step, the mean voltage in each optimisation time step, the voltage at the end of each optimisation time step, and the current in each time step. Variables are grouped per type, i.e. the first N_1 variables of $\mathbf{W}$ are the eigenspace representation of the transformed concentration in the first node in the positive electrode at all optimisation time steps $z_{2,p}(\mathbf{t_1})$, and the last N_1 variables are the current at each optimisation time step $I(\mathbf{t_1})$. Note that this is a different order compared to (3.21) and (3.26), which grouped variables per time step. The order does not matter for the optimisation, but the structure of the Jacobian in Fig. 3.5 is easier to understand visually if variables are grouped per type.

---

[10] The diffusion PDE is linear with real eigenvalues, and all degradation processes are monotonic, such that for constant boundary conditions, no oscillations are possible.

$$\mathbf{W} = \begin{pmatrix} \mathbf{z}_{2:N_c-1,p}(\mathbf{t_1}) \\ \mathbf{z}_{2:N_c-1,n}(\mathbf{t_1}) \\ T(\mathbf{t_1}) \\ \tau_{\text{sei}}(\mathbf{t_1}) \\ L(\mathbf{t_1}) \\ V^{\text{mean}}(\mathbf{t_1}) \\ V^{\text{end}}(\mathbf{t_1}) \\ I(\mathbf{t_1}) \end{pmatrix} \tag{3.36}$$

3.6.2 Constraints of the battery model

The state-space model and the voltage equation (3.19) have to be included in the constraint function Γ of the optimisation problem (3.23). Firstly, function $S(\mathbf{s}(t_2), I(t_1))$ will integrate the state-space model equation $f(\mathbf{s}(t_2), I(t_1))$ given by (3.14) and (3.16) over one Δt_1 time step by repeatedly applying forward Euler over small time steps Δt_2 as indicated on the right hand side of (3.28). At every integration time step, the voltage is calculated according to (3.17) and the SEI current density according to (2.20). This represents the multiple shooting approach from section 3.4.2. There are three small modifications to f as it was defined in section 3.3.3 because the optimisation uses the decoupled diffusion PDE (3.33): (1) the optimisation uses the transformed concentration in the eigenspace $\mathbf{z}_i$ rather than transformed concentration $\mathbf{u}_i$ as explained in section 3.5.1; (2) the diffusion and rate constants are not updated to reflect the actual cell temperature but are calculated once based on the temperature at the beginning of that optimisation time step $T(t_1)$ as explained in section 3.5.2; (3) the LLI is not accounted for in the surface boundary condition (2.22) but instead the side reaction current is added to the new variable $L(t_1)$ as explained in section 3.5.2.

At the end of the integration, the lost lithium is subtracted from the anode as a uniform decrease in the concentration in the entire particle (3.34). This subtraction only affects the dimension representing a uniform concentration. The function S' does both the time integration and the lithium subtraction. The equations for the voltage are straightforward and the lost lithium is simply the integral of the SEI current density multiplied by the electrode surface area. All equations of the state-space model can then be included in the constraint function Γ (3.37). As before, similar constraints at different time steps are grouped first, i.e. the first N_1 elements of the array are constraints on the eigenspace representation of the transformed concentration in the first node in the positive electrode at every time step $z_{2,p}(\mathbf{t_1})$, and the last N_1 elements are the constraints determining the end voltage at every time step $V^{\text{end}}(\mathbf{t_1}+1)$. Note that the voltage limits of the cell can be imposed by restricting the upper and lower limits of the optimisation variable V^{end} in (3.24) which eliminates the need to include them in the constraint function.

$$\Gamma(\mathbf{W}) = \begin{pmatrix} \mathbf{s}(\mathbf{t_1}+1) - S'(\mathbf{s}(\mathbf{t_1}),\, I(\mathbf{t_1})) \\ L(\mathbf{t_1}+1) - A_n \tau_n a_n \sum_{\mathbf{t_1}}^{\mathbf{t_1}+1} i_{\text{sei}}(t_2)\Delta t_2 \\ V^{\text{mean}}(\mathbf{t_1}+1) - \frac{\Delta t_2}{\Delta t_1} \sum_{\mathbf{t_1}}^{\mathbf{t_1}+1} V(t_2) \\ V^{\text{end}}(\mathbf{t_1}+1) - V(t_2)|_{t_2=\mathbf{t_1}+1} \end{pmatrix} = 0 \tag{3.37}$$

Fig. 3.5 shows the sparsity structure of the Jacobian of the constraints with the example of 7 Chebyshev nodes (resulting in 5 inner nodes in $\mathbf{s}$). One block matrix represents the derivative of one constraint (at all optimisation time steps) to one optimisation variable (at all optimisation time steps), such that one block matrix has N_1 rows and columns. Blue or green dots indicate non-zero elements, respectively on the sub-diagonal or diagonal of the block matrix. The effect of the spatial decoupling is clear by considering how few non-zero elements there are in the upper left part. Only the constraint for the fourth node in the negative electrode depends on the concentration in all other nodes, which is due to the uniform subtraction of lithium due to the growth of the SEI layer[11]. All other constraints (temperature, SEI thickness, LLI, mean and end voltage) depend on the surface concentration, which depends on the concentration in all other nodes, resulting in the many sub-diagonals in the bottom left part[12]. Finally, all constraints depend on the temperature of the previous time step and the current of the present time step.

3.7 Automatic differentiation

The nonlinear optimisation algorithm used here requires derivatives of the objective and constraint functions to the optimisation variables. The derivatives of the state-space model could be calculated symbolically, but these would be the partial derivatives to the time integration variables at t_2, not the derivatives to the optimisation variables at t_1. Due to the multiple shooting approach from (3.28), all partial derivatives to the integration variables need to be added up within one optimisation time step to get the derivative to the optimisation variable. This would be feasible for the concentration states, because they behave linearly and are fully decoupled. However, the other state variables are nonlinearly coupled to the concentration at every dimension at every integration time step. Calculating these derivatives symbolically is nearly impossible. Finite differences could be used, but given the large

---

[11] According to equation (3.34), the LLI is subtracted from the fourth node through L, which should result in a nonzero derivative of $z_{4,n}$ to L and the derivatives of $z_{4,n}$ to the concentration in the other dimensions should be zero. However, due to practical coding limitations, the LLI was accumulated in another variable and directly subtracted from $z_{4,n}$ in the function S'. The LLI was added separately to L to keep track of the total lost lithium. Therefore, the derivative of $z_{4,n}$ to all other dimensions is nonzero while its derivative to L is zero.

[12] This could not be solved by adding an optimisation variable for the surface concentration. The surface concentration is directly coupled to the eigenspace concentration at all nodes at every integration time step t_2, not to the surface concentration at the previous time step. Therefore, variables depending on the surface concentration such as the voltage still depend on the concentration at all nodes at the optimisation time step t_1: $V(t_2) = f(c_{surf}(t_2)) = f(g(\mathbf{z}(t_2))) = f(g(h(\mathbf{z}(t_1))))$ where f, g, and h are all generic functions. The mean voltage at the optimisation time step $V^{\mathrm{mean}}(t_1)$ depends on the voltage at every integration time step t_2 such that the derivative of $V^{\mathrm{mean}}(t_1)$ to the concentration at all nodes $\mathbf{z}(t_1)$ is nonzero even if the surface concentration is an optimisation variable. The same argument applies for the other variables such as temperature, LLI, etc.

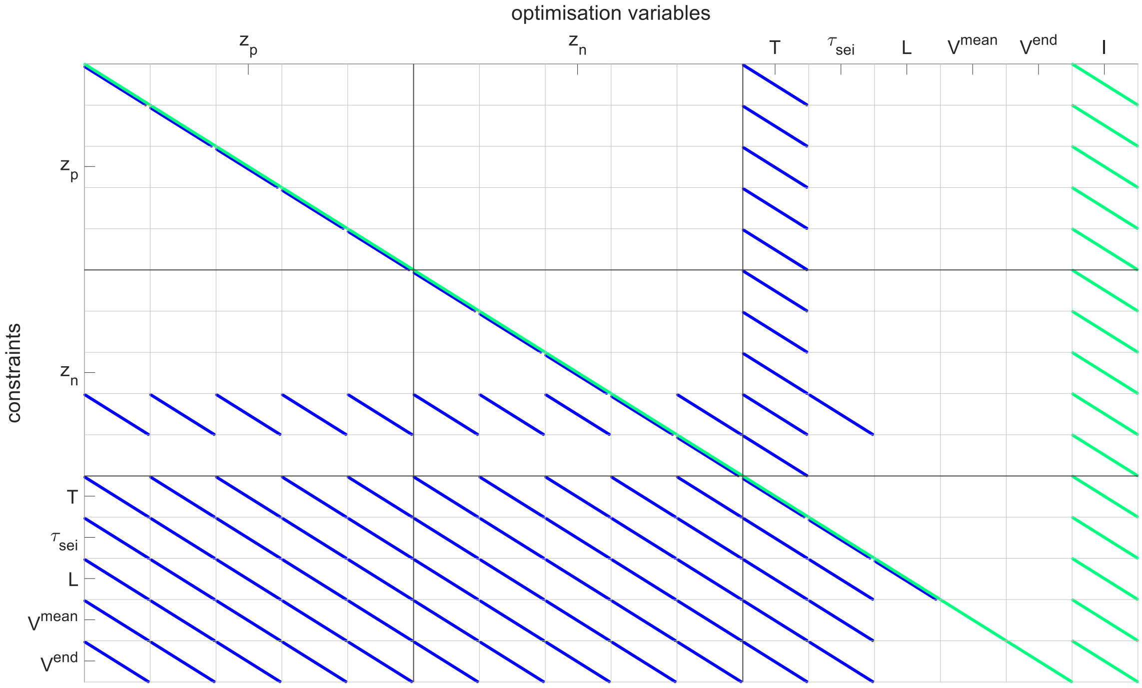

Fig. 3.5 The sparsity structure of the Jacobian of the constraint function. Rows represent the derivatives of the constraints and column the derivatives to the optimisation variables. Light grey lines separate the different constraints and variables, while darker lines separate the 5 constraints and variables related to the concentration. Blue indicates sub-diagonal entries and green indicates entries on the main diagonals of the block matrices.

number of variables this would be very expensive. Therefore, automatic differentiation has been used [185].

Automatic differentiation works by differentiating every line of a computer program and applying the chain rule to find the overall derivatives. It imposes some constraints on the code, for instance no if-statements are allowed, but otherwise is a very powerful technique. ADOL-C is a software package designed to do automatic differentiation in C++ [186]. It was made to work in tandem with IPOPT, the optimisation solver used here, see section 3.9. ColPack is an add-on feature for ADOL-C to make it more efficient when dealing with sparse problems like the one considered here [187].

Before the optimisation starts, ADOL-C and ColPack process the code and write so-called 'tapes' which contain the derivatives of every line of code, and the chain rules linking them. These 'tapes' are stored in memory and whenever the derivatives are needed at a specific point, they are evaluated at that point. For small- and medium-sized problems, this works well but for very large problems (e.g. optimising over a time horizon of weeks), the 'tapes' become too large to fit in memory and have to be stored on the hard drive. In this case, the computational time increases significantly.

3.8 Sliding-window optimisation

With the previously explained techniques, problems with a time horizon of a few days can be simulated. There are two factors preventing longer time horizons. Firstly, the computational time and memory required for the automatic differentiation (see section 3.7) become too large for long horizons. Secondly, the optimisation solver does not converge well enough for large problems, in some cases the 'optimal' point was even worse than the starting point. A common approach is to use a rolling time horizon, also called sliding-window optimisation [11, 188].

Instead of one optimisation over all time steps in the full horizon, multiple optimisations are done over a smaller number of time steps N_1. After each optimisation over N_1 steps, the time horizon is moved forward by N^{m} steps. The initial battery state of the next optimisation is the state after those N^{m} time steps. Note that this is a kind of open-loop control given that there is no feedback loop to measure the actual battery state as would be the case in conventional model-predictive control [189].

In a real-life implementation, this would be the natural approach because the economic data, such as the price information, is not known for the far future. Therefore, the optimal load schedules are often calculated one day at a time and the asset is subsequently controlled according to that load schedule for the given period. In section 4.7, such a setup is described.

Maheshwari followed a totally different approach [190]. He first optimised for the entire period with a very large time step before then optimising the periods within one time step, where the initial and end state of the battery were the outcomes of the first optimisation. However, this was deemed not appropriate to use with a physics-based battery model because fixing the exact battery state at the end of the optimisation period would significantly reduce the freedom to use the cell. Because Maheshwari used a simple linear battery model which only accounted for the SoC, he did not encounter this problem.

3.9 Optimisation procedure

The techniques and formulation explained above are a flexible framework for the optimal control of battery models. The objective function can be chosen depending on the application considered, and more constraints and/or optimisation variables can also be added if needed. See section 4.1 for the details of the application considered in this work.

Section 3.6 described the optimisation variables and constraints related to the battery model, where the constraints impose the time integration of the state-space model over time using multiple shooting. For an optimisation time horizon of N_1 periods and 7 Chebyshev nodes (of which 2 are eliminated due to the boundary conditions), there are $16N_1$ variables, $15N_1$ constraints and $30N_1 + 90(N_1 - 1)$ non-zero elements in the Jacobian. For a time horizon of 2 days with optimisation periods Δt_1 of 15 minutes, i.e. $N_1 = 192$, this result in 3072 variables, 2880 constraints and 22,950 nonzeros in the Jacobian. ADOL-C and ColPack have been used to evaluate the Jacobian and gradient as explained in section 3.7. They offer library functions that can be called whenever the derivatives are needed.

IPOPT was used as the optimisation solver [191, 184]. It is a barrier method which solves a sequence of optimisation problems with decreasing values of the barrier parameter which reduces the error tolerance on the variables. The initial point of the next iteration is the approximate optimal outcome of the previous iteration. One iteration is solved by applying a damped Newton's method on the dual formulation, which itself involves iteratively converging to the optimal point. During one step, the search direction is calculated by solving a linearised formulation of Newton's method and a line-search algorithm calculates the step size in these directions, while applying a filter to ensure new points satisfy the constraints to an acceptable level. Full details are given in [191].

IPOPT offers an interface to C++ where the programmer has to implement the standard functions (objective, constraints, gradient, Jacobian, bounds, intitial values, etc.). These functions are inherited from a super class, such that an object of this class represents one optimisation problem. Library functions can then be called which will run the optimisation algorithm. IPOPT offers various options for the users, the most important one is the 'limited memory' option in which case the Hessian matrix is approximated by an algorithm implemented in IPOPT. If this option is not used, the Hessian must be calculated by ADOL-C and ColPack in every iteration, which requires a huge amount of memory and computational time.

Given that the problem considered here is nonlinear and may be non-convex, the optimal solution found by IPOPT might not be the global optimum. However, it was verified that for a range of different starting points, IPOPT converges to the same solution. It needs a few hundred iterations per optimisation, which takes around 15 minutes. Only for large problems, e.g. when optimising for weeks, did IPOPT converge to a non-optimal point. Another case in which IPOPT struggles is when there are multiple points, all (more or less) equally good. For instance if the SEI growth is purely diffusion limited, the battery utilisation has no effect on the degradation. In this case, the convergence time of IPOPT was found to be very long and the outcomes are often worse than the initial points.

Chapter 4

Optimal battery utilisation for electricity trading

This chapter studies battery degradation in a realistic electricity system application. It shows how including degradation alters the usage profiles, and what effect this has on the revenue and degradation.

Section 4.1 introduces the grid application considered, wholesale energy arbitrage, in which electricity can be traded on a liberalised market where the price changes over time. Section 4.2 describes how this problem is traditionally solved by state-of-the-art battery models and optimisation techniques. Section 4.3 gives the values of the parameters of the different battery models and economic equations used for the optimisation.

The results of the optimisation are given in section 4.4. Section 4.5 shows what happens if the different 'optimal' usage profiles are simulated with a generalised degradation model. Then six batteries are cycled with the 'optimal' usage profiles to validate the optimisation and simulations. The results are shown in section 4.6.

These results indicate the improvements which can be made by using physical models in the optimisation, but there are significant barriers before such methods can be used in the real world. Therefore, section 4.7 discusses how the results obtained here can be implemented in a real-world grid-connected battery.

A discussion of the results is given in section 4.8, and conclusions are drawn in section 4.9. Finally, section 4.10 outlines the limitations and highlights potential areas of future work.

Parts of this chapter, mainly sections 4.1 to 4.4, have been published in [106].

4.1 Wholesale arbitrage

Since the liberalisation of the energy market, companies can trade electricity on various time scales in different markets, see section 1.1.1. In this work, a battery operator is assumed to trade electricity on the day-ahead market. A detailed description of the market rules can be found in [192]. Because the focus here is not on the economic detail, most market rules are ignored. For instance, the battery operator does not have to bid into the market, but can simply trade electricity at the market clearing price. This price is only known after bids have been placed but is well predictable with errors below 10% [193–195]. Therefore, the price was assumed to be known a priori. The price of the Belgian day-ahead market, λ, in 2014 [196] was used; it is shown on Fig. 4.1. There is a diurnal pattern with price peaks in the morning and evening. In the summer, prices are lower due to solar electricity generation. Most day-ahead markets operate hourly, but because market actors have to be ‘balanced’ over a 15-minute period, i.e. they have to provide the energy they promised every quarter hour, the market considered here operates every 15 minutes but the price is constant for four consecutive periods.

The energy management system (EMS), which does the scheduling of the battery, has to decide when to buy electricity, charging the battery, and when to sell it, discharging the battery. Taking advantage of the price differential, revenue can be made. However, using the battery will lead to efficiency losses as well as battery degradation. The former is typically

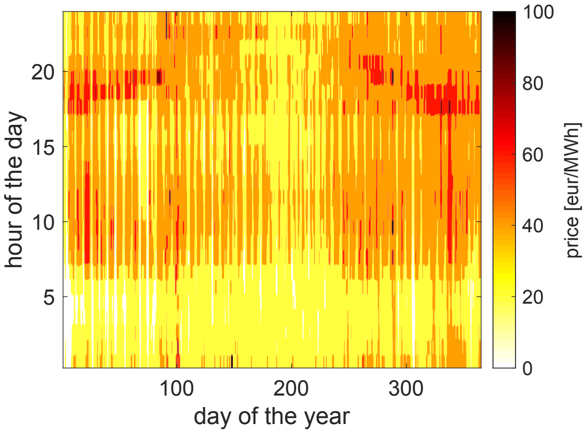

Fig. 4.1 The price of electricity on the day-ahead market in Belgium in 2014.

included in the decision because it is easily quantifiable. The latter is much more difficult to predict, as explained in chapter 2. The next section shows how state-of-the-art EMSs try to include degradation in the optimisation.

4.2 State-of-the-art battery energy management systems

This section describes the state of the art in EMSs and optimisation of batteries in grid applications. Sections 4.2.1 and 4.2.2 introduce the battery and degradation models typically used in EMSs, and section 4.2.3 gives a literature review of how these models are used for economic optimisations. In section 4.2.4 some studies from other authors which used physical models for EMSs are described, although none of them included an optimisation.

4.2.1 Bucket model

The simplest model for a battery is to consider it as a ‘bucket’ of energy as on Fig. 4.2. This battery model has one state variable, the dimensionless SoC Q, and one input (or control) variable, the battery power P in [MW] (4.1). The (energy) capacity of the battery is E_{en} in [MWh]. Sometimes an efficiency-factor is added to such models, but this is not included here. The bucket model, BM, does not distinguish between current and voltage but is completely linear, making optimisation very easy. However, it is clear that this model can not capture important effects in a battery, such as the diffusion limitation. This means that a battery controlled by the bucket model will not be able to use the full battery capacity, for instance because it will do a full-power charge until the maximum voltage is reached (even though more capacity could be accessed at a lower power).

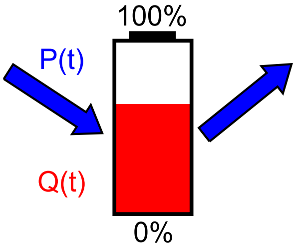

Fig. 4.2 Bucket model for a battery, where red indicates state variables, blue are control variables and black are parameters.

$$\frac{\partial Q}{\partial t} = \frac{P}{3600 E_{en}} \tag{4.1}$$

If degradation is included in this model, it typically comes in the form of a ‘penalisation’ per energy throughput [18], which implies the battery can do a given number of cycles over its lifetime (4.2) where E_{en}^{lost} indicates the lost (energy) capacity in [MWh] and β_{10} is a fitting constant. This degradation model is linear, facilitating an easy optimisation, but ignores the effect of operating conditions such that all predictions will fall onto one line as was the case for Delacourt’s model for LAM (2.33), shown in Fig. 2.9D.

Sometimes, some form of calendar ageing is included too, but this is not considered here because the calendar ageing for the cell is small for the expected operating conditions (mainly due to the environmental temperature of 25°C and the inability to access high SoC regions), see section 1.4.2.

$$\frac{\partial E_{en}^{\text{lost}}}{\partial t} = \beta_{10} |P| \tag{4.2}$$

4.2.2 Equivalent-circuit model

The second popular battery model is an equivalent-circuit model where a battery is simulated by a network of classical electrical components. Various circuits have been proposed, the simplest given by Fig. 4.3. In this circuit, there are two state variables: the SoC, Q, and the current through the parallel resistor, I_r^{ecm}. The state-space model (4.3) is linear where R_p^{ecm} and C_p^{ecm} are the parallel resistor and capacitor in the network, and R_s^{ecm} is the series resistance. The open-circuit voltage U is a nonlinear function of the SoC, causing the measurement function (or algebraic constraint) of the state-space model, the voltage, to be nonlinear. Although not all physical properties are included, ECMs can often predict the measured voltage very accurately, and the circuits can be extended with more elements if needed. They are therefore often used for battery management systems, SoC estimation and control of batteries [31].

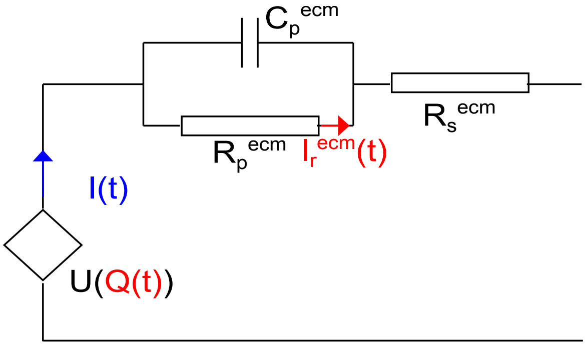

Fig. 4.3 Equivalent-circuit model for a battery, where red indicates state variables, blue are control variables and black are parameters.

$$\begin{aligned}\frac{\partial Q}{\partial t} &= \frac{P}{3600E_{en}}\\ \frac{\partial I_r^{ecm}}{\partial t} &= \frac{1}{R_p^{ecm}C_p^{ecm}}I - \frac{1}{R_p^{ecm}c_p^{ecm}}I_r^{ecm}\end{aligned} \tag{4.3}$$

These models are often coupled with empirical degradation models. After doing a large-scale degradation experiment (similar to the one presented in section 1.4), parametric functions are fitted through the data points. These functions are often nonlinear and can be very accurate [70]. However, because they are interpolations in a data set, using such models for operating conditions different to the ones which have been tested often results in large errors due to extrapolation [53]. Indeed, the models proposed in literature have very different equations, e.g. [107] and [197] for LFP or [158] and [105] for NMC. Secondly empirical degradation models often have terms like the 'depth of discharge' or the 'average voltage', which might be well defined in degradation experiments where the same cycles are repeated throughout the experiment, but are much less clearly interpretable in real-life applications. The model used here (4.4) is from [158] because it was for the same chemistry (NMC) and a because it was based on a very large degradation experiment. The energy capacity lost after a period of time t is a function of that time and the square root of the charge throughput during that period. There are two nonlinear parametric functions, f_1 and f_2, of the mean voltage V^{mean}, the temperature T, the root-mean-square voltage V^{RMS} and the 'depth of discharge' ΔD, which is the difference between the maximum and minimum SoC.

$$E_{en}^{\text{lost}} = f_1\left(V^{\text{mean}}, T\right) t^{0.75} + f_2\left(V^{\text{RMS}}, \Delta D\right) \sqrt{\int_0^t |I| dt} \tag{4.4}$$

4.2.3 Optimisation for grid applications

Goebel et al. [198] compared an optimisation-based strategy with a 'naive' rule-based usage of batteries in the secondary reserve market. Using an ECM with an empirical degradation model they found the savings of an optimisation strategy were about triple compared to the rule-based approach.

Various researchers have used the BM or ECM with empirical degradation models to optimise the battery utilisation for different grid applications. Ortega-Vazquez et al. [199] studied how the batteries of electric vehicles could be used to trade electricity when the cars were plugged in. Corengia et al. [200] and Kruger et al. [201] used a battery to reduce the electricity bill of a residential consumer facing a time-varying price. Xu [202] included some more market rules in his models, e.g. by explicitly accounting for the bidding process in the wholesale markets. He used rainflow counting to calculate the parameters needed for the empirical degradation model when using a real load profile [203]. Hashmi et al. [204] considered a larger-scale battery used to trade electricity while providing ancillary services. Sarker et al. [205] also used a battery for trading electricity, discussing the trade-off between revenue and degradation: to decrease degradation, they had to reduce the utilisation of the battery, which would decrease the revenue. Maheshwari [190] considered this as a multi-objective optimisation to find the Pareto-front. Sun et al. [206] aggregated multiple small batteries to provide grid services and came up with an optimisation to allocate the overall energy to individual batteries in order to even out the degradation amongst them all.

Muller [10] encountered a similar problem but in a different setting. He studied how one large battery could be used to deliver different applications at the same time. His solution was to dedicate certain racks of the battery to certain applications, where a rack is a combination of various battery modules with one power converter. He then did an ‘ageing-optimised distribution’ to allocate racks to individual applications which involved a rule-based allocation rather than an actual optimisation.

Perez et al. [11] also studied the degradation of a battery used for multiple applications. They optimised the utilisation of the battery for a combination of various services while respecting market rules, such as putting aside capacity to provide reserves. However, degradation was not accounted for in this optimisation. After the ‘optimal’ use profiles had been calculated, they used an empirical degradation model to assess how much the battery would degrade. In order to reduce the degradation, they limited the usable SoC region of the battery between various limits, e.g. $25\% <\text{SoC}< 75\%$. They found that lower SoC regions reduced the degradation, although their degradation model was very simple and they did not publish the data on which it was based.

Finally, Fortenbacher et al. [189] optimised an ECM with an empirical degradation model over multiple time horizons. First, the battery was scheduled to optimise the solar electricity production without violating the voltage limits of the transmission lines (including optimal power flow) while minimising the battery degradation. This optimisation provided setpoints for the battery. The real-time controller also solved an optimisation to minimise the network losses, battery losses, and the deviations from the setpoints. Interestingly, they used a P2D battery model to simulate the 'real' battery behaviour, which was being controlled by the real-time controller which used an ECM. Their simulations predicted a 30% decrease in losses and a doubling of the lifetime of the battery.

4.2.4 Case studies with physical battery models

Both Lawder et al. [207] and Lee et al. [208] used the P2D model to simulate a battery which balanced a microgrid with a given solar power production profile and given demand. The battery simply absorbs or produces the difference between the production or demand such that no optimisation is involved. They also only looked at one day rather than considering a whole year which would be more representative. Lee et al. included a kinetically limited SEI growth model similar to (2.17) but because there was no optimisation and the time horizon was only one day, they did not comment on the effect of degradation on the application or vice versa.

Weißhar et al. [209] studied the same application with a multi-scale multi-physics battery model which also included a detailed model for the growth of the SEI layer similar to the one from Kupper et al. [64, 128], see Table 2.1. Weißhar considered a full year for both a family and an office, and found that most SEI growth happened due to charging the battery in the high SoC region, rather than due to resting at a high SoC. To reduce degradation, they suggested to decrease the maximum SoC of the battery. By decreasing the usable capacity by two thirds, they reduced the degradation by a factor of 2.5.

Patsios et al. [33] combined models for a distribution network, a transformer, and a power electronic converter with an SPM which was extended with a kinetically limited model for SEI growth (2.17). While enforcing the voltage limits of the network, they studied the losses in all components and the battery degradation over one day. They compared four different days to account for seasonal variations. The battery's utilisation was determined by pre-defined rules rather than an optimisation. Different sets of rules could significantly affect the degradation, e.g. degradation could be halved by floating the battery around 30% SoC instead of 100%. They also found that the SoC of the cell had a large impact on the losses in the system, driven by the lower cell voltage at low SoC which required a larger current to deliver the same power. Operational rules which aimed to minimise the losses could reduce them by up to 43% but this increased battery degradation.

Section 3.1 discussed work about optimising physical battery models. The few papers attempting this mostly focussed on fast charging. To the author's knowledge, no paper has used a physical battery model to optimise battery utilisation over a time horizon beyond a few hours, nor has work been found which used a physical model in an optimisation to study electricity system applications, apart from the author's own work [106].

4.3 Model parameters

This section gives the parameters of the optimisation problem solved in this work. Section 4.3.1 gives the parameters of the three different battery models: the bucket model (see section 4.2.1), the equivalent-circuit model (see section 4.2.2) and the single-particle model (see sections 2.1 and 2.2). Section 4.3.2 gives the economic parameters, such as the cost of battery degradation. Finally, section 4.3.3 gives the parameters relating to the optimisation algorithm.

4.3.1 Battery models

In order to assess the effect of using more accurate battery models, the same economic application was optimised with three different battery models. The objective function was the same for all three cases, only the constraints describing the battery behaviour were different. The bucket model (BM) and equivalent-circuit model (ECM) represent the state of the art in optimisation as discussed in section 4.2. The single-particle model (SPM) explained in the previous chapters represents the novelty in this work, which is using physical models for optimal control in EMSs.

In this section, values of the model parameters are listed. The cycling and degradation data from section 1.4 has been simulated with each model (with the parameters mentioned below). The simulations and data are compared in the various sections of Appendix A.

Bucket model The BM was introduced in section 4.2.1. It is a linear battery and degradation model which only considers the SoC of the battery, the battery power and the total (energy) capacity (4.1, 4.2). A regularisation term for the maximum power $\beta_{11}|P|^{\max}$ has to be added to (4.2) to guarantee a sensible outcome (e.g. use a constant power for the whole hour rather than fully charging the cell in the first 15 minutes and resting for the remaining 45 minutes; without the regularisation term both solutions would be equally valid). Integrating (4.2) over time and adding the regularisation term results in (4.5), where the maximum power is calculated over the optimisation time horizon. Table 4.1 gives the values of the model parameters. The fit from the BM (without the regularisation term) with the data from section 1.4 is shown in Appendix section A.1.

Table 4.1 Model parameters of the bucket model.

parameter	symbol	value
energy capacity	E_{en}	$9.97 \cdot 10^{-6}$ MWh
fitting constant	β_{10}	$1.2626 \cdot 10^{-5}$ h s^{-1}
fitting constant	β_{11}	$2.1212 \cdot 10^{-4}$ h

$$E_{en}^{\text{lost}} = \beta_{11}|P|^{\max} + \sum_{t_1=1}^{N_1} (\beta_{10}|P(t_1)|\Delta t_1) \tag{4.5}$$

Equivalent-circuit model ECMs were introduced in section 4.2.2. They have a linear state-space structure (4.3), but a nonlinear measurement equation (or algebraic constraint) for the voltage and their associated degradation models are usually nonlinear too. Different types of circuits exist, the one used here is shown on Fig. 4.3. The degradation model considered here (4.4) was developed by Schmalstieg et al. [158]. The mean and root-mean-square voltage were calculated over the optimisation time horizon. The depth of discharge was calculated as the average deviation from the mean SoC over the optimisation time horizon. The parameters of the circuit are given in Table 4.2 and were obtained from [210]. The OCV curve was obtained for the cell used in this work, see section 1.4. The degradation functions f_1 and f_2 were taken from [158]. The ‘average’ parameters (mean voltage, root-mean-square voltage and depth of discharge) were calculated over the two-day optimisation horizon. The fits from the ECM to the data from section 1.4 are shown in section A.2, with the only difference that the ‘average’ parameters were calculated as the moving average. As explained in section A.2.3, the empirical degradation model predicted too fast initial degradation which would mean that the battery would not be used at all. Therefore, f_1 and f_2 were divided by a factor of 5 compared to the functions reported by Schmalstieg et al. [158].

Note that the parameters of the ECM and the degradation model were taken directly from literature and not fitted to the cell used in this work, unlike the other two battery models. This was done to demonstrate that taking a model from literature and applying it in a different

Table 4.2 Model parameters of the equivalent-circuit model.

parameter	symbol	value
energy capacity	E_{en}	$9.97 \cdot 10^{-6}$ MWh
parallel resistance	R_p^{ecm}	$15.8 \cdot 10^{-3}\ \Omega$
parallel capacitance	C_p^{ecm}	38,000 F
series resistance	R_s^{ecm}	$8.2 \cdot 10^{-3}\ \Omega$

context might lead to wrong results due to the limitations of each model. Therefore, a comparison between the results of the ECM and the two other battery models is not a ‘fair’ comparison, which will be taken into account in the results later in this chapter.

Single-particle model The SPM used for the optimisation consists of the regular SPM equations (2.1 - 2.9), the bulk thermal model (2.10 - 2.12), and a SEI growth model accounting for both kinetics and diffusion (4.6) which increases the thickness of the SEI layer (2.21) and removes cyclable lithium (2.22). Note that the equation for the SEI side-reaction current density is taken from [119] and differs slightly compared to (2.20).The difference stems from the assumption from Christensen et al. in [119] that electrons diffuse from the graphite surface through the existing SEI layer and react with the electrolyte components at the ‘outside’ of the SEI layer, which grows at the interface between the layer and the electrolyte. This is unlike (2.20), where it was assumed electrolyte molecules diffuse from the electrolyte through the SEI layer to the graphite surface, where they react with the electrons such that the layer grows ‘inwards’. As was the case with the other SEI models, both calendar and cycle ageing is predicted by (4.6); the anode overpotential η_n is zero during calendar periods but because it appears in the exponential term, this still causes SEI growth. The calendar ageing is dependent on the SoC through the anode potential U_n which appears in the kinetic term in the denominator.

The fitting parameter β_{12} can be incorporated in the rate and diffusion constants to reduce the number of parameters. The sensitivity analysis of this model between k_sei and D_sei was shown on Fig. 2.5. There is no pore clogging due to the SEI layer, i.e. β_1 from (2.23) is zero.

$$i_{\mathrm{sei}} = \frac{\beta_{12}\exp\left(-\frac{\alpha_{\mathrm{sei}} nF}{R_g T}\eta_{\mathrm{n}}\right)}{\frac{1}{nFk_{\mathrm{sei}}(T)\exp\left(-\frac{\alpha_{\mathrm{sei}} nF}{R_g T}(U_{\mathrm{n}}-U_{\mathrm{sei}})\right)} + \frac{\tau_{\mathrm{sei}}}{nFD_{\mathrm{sei}}(T)}} \tag{4.6}$$

The model is formulated as discussed in depth in chapter 3. The OCV for the cell was measured, while the entropic coefficient was obtained from [211]. The parameters given in Table 4.3[1] were fitted to the data from section 1.4. The resulting fits are shown in sections A.3.1 and A.3.2.

4.3.2 Economic details

As explained in section 4.1, the batteries are used to trade in the wholesale market. The price of electricity λ changes in hourly intervals and is assumed to be known. It is shown on Fig 4.1. The EMS makes a revenue Φ in [€] by buying electricity at times of low prices, and selling electricity later when the price is higher. Therefore, the revenue can be calculated by (4.7). The current I in [A] and price λ in [€MWh^{-1}] are constant within one optimisation time step t_1, which has a duration of Δt_1 in [s]. The voltage changes within one step, such that the mean voltage V^{mean} in [V] is used. Note that when the BM is used to simulate the battery, the battery power $P(t_1)$ can be used directly instead of the product of the current and the mean voltage. The optimisation time step Δt_1 was taken to be 15 minutes as explained in section 4.1, such that the price is constant for four consecutive steps.

$$\Phi = \sum_{t_1=1}^{N_1} I(t_1)V^{\mathrm{mean}}(t_1)10^{-6}\lambda(t_1)\frac{\Delta t_1}{3600} \tag{4.7}$$

While maximising revenue, the optimisation should also minimise the battery degradation. This can be considered a multi-objective optimisation as in [190] or the degradation can be expressed in monetary terms Ψ such that it can be directly compared with the revenue. The

---

[1] ‘reference T’ stands for reference temperature, taken as 25°C

Table 4.3 Model parameters of the single-particle model.

parameter	symbol	value
geometric surface area of the cell	A_{batt}	$0.0079\ \mathrm{m}^2$
geometric surface area of the anode	A_{n}	$0.0982\ \mathrm{m}^2$
geometric surface area of the cathode	A_{p}	$0.0982\ \mathrm{m}^2$
Li-concentration in the electrolyte	c_{el}	$1000\ \mathrm{mol\ m}^{-3}$
maximum Li-concentration in the anode	$c_{\mathrm{n}}^{\mathrm{max}}$	$30{,}555\ \mathrm{mol\ m}^{-3}$
maximum Li-concentration in the cathode	$c_{\mathrm{p}}^{\mathrm{max}}$	$51{,}385\ \mathrm{mol\ m}^{-3}$
heat capacity of the cell	$C_{p,\mathrm{batt}}$	$750\ \mathrm{J\ kg}^{-1}\ \mathrm{K}^{-1}$
diffusion constant of the anode at reference T	$D_{\mathrm{n}}^{\mathrm{ref}}$	$7 \cdot 10^{-14}\ \mathrm{m}^2\ \mathrm{s}^{-1}$
diffusion constant of the cathode at reference T	$D_{\mathrm{p}}^{\mathrm{ref}}$	$8 \cdot 10^{-14}\ \mathrm{m}^2\ \mathrm{s}^{-1}$
diffusion constant of the SEI layer at reference T	$D_{\mathrm{sei}}^{\mathrm{ref}}$	$0.5 \cdot 10^{-16}\ \mathrm{m}^2\ \mathrm{s}^{-1}$
activation energy for the Arrhenius relation on D_{n}	$E_{D,\mathrm{n}}$	$35{,}000\ \mathrm{J\ mol}^{-1}$
activation energy for the Arrhenius relation on D_{p}	$E_{D,\mathrm{p}}$	$29{,}000\ \mathrm{J\ mol}^{-1}$
activation energy for the Arrhenius relation on D_{sei}	$E_{D,\mathrm{sei}}$	$200{,}000\ \mathrm{J\ mol}^{-1}$
activation energy for the Arrhenius relation on k_{n}	$E_{k,\mathrm{n}}$	$20{,}000\ \mathrm{J\ mol}^{-1}$
activation energy for the Arrhenius relation on k_{p}	$E_{k,\mathrm{p}}$	$58{,}000\ \mathrm{J\ mol}^{-1}$
activation energy for the Arrhenius relation on k_{sei}	$E_{k,\mathrm{sei}}$	$130{,}000\ \mathrm{J\ mol}^{-1}$
convective heat-transfer coefficient	h	$90\ \mathrm{W\ m}^{-2}\ \mathrm{K}^{-1}$
rate constant of the anodic reaction at reference T	$k_{\mathrm{n}}^{\mathrm{ref}}$	$1.764 \cdot 10^{-11}$
rate constant of the cathodic reaction at reference T	$k_{\mathrm{p}}^{\mathrm{ref}}$	$5 \cdot 10^{-11}$
rate constant of the SEI reaction at reference T	$k_{\mathrm{sei}}^{\mathrm{ref}}$	$0.25 \cdot 10^{-14}$
molecular weight of the SEI reaction product	M_{sei}	$26 \cdot 10^{-3}\ \mathrm{kg\ mol}^{-1}$
number of Chebyshev nodes	N_c	7
specific DC resistance of the anode	$r_{\mathrm{dc},n}$	$0.0212\ \Omega\ \mathrm{m}^2$
specific DC resistance of the cathode	$r_{\mathrm{dc},p}$	$0.0212\ \Omega\ \mathrm{m}^2$
specific DC resistance of the sei layer	$r_{\mathrm{dc,sei}}$	$1764\ \Omega\ \mathrm{m}$
radius of the anodic particle	R_{n}	$12.5 \cdot 10^{-6}\ \mathrm{m}$
radius of the cathodic particle	R_{p}	$8.5 \cdot 10^{-6}\ \mathrm{m}$
OCV of the SEI reaction	U_{sei}	$0.4\ \mathrm{V}$
transfer coefficient	α	0.5
transfer coefficient of the SEI reaction	α_{sei}	1
fitting parameter	β_{12}	0.134461
volume fraction of active material in the anode	ε_{n}	0.5
volume fraction of active material in the cathode	ε_{p}	0.5
density of the total cell	ρ_{batt}	$1626\ \mathrm{kg\ m}^{-3}$
density of the SEI layer	ρ_{sei}	$2.6 \cdot 10^{3}\ \mathrm{kg\ m}^{-3}$
thickness of the total cell	τ_{batt}	$1.685 \cdot 10^{-4}\ \mathrm{m}$
thickness of the anode	τ_{n}	$73.5 \cdot 10^{-6}\ \mathrm{m}$
thickness of the cathode	τ_{p}	$70 \cdot 10^{-6}\ \mathrm{m}$

latter approach is followed here, representative of the decision EMSs have to make on how to use the battery. The BM and ECM directly calculate the lost energy capacity, respectively by (4.5) and (4.4). This can be multiplied by the 'cost of battery degradation' $\lambda_{\text{deg, en}}$ in [€MWh^{-1}]. In 2014, the cost of a battery pack was around 450 \$/kWh [26], which was converted to 330,000 €/MWh. The SPM does not directly decrease the capacity, instead the SEI growth removes cyclable lithium and to measure the capacity, one would have to simulate a full charge and discharge between the voltage limits of the cell. However, this is too complicated for the optimisation, such that the penalisation is directly on the LLI rather than the lost capacity. Simulations have shown that at the beginning of the cell life, they are more or less equivalent when only SEI growth is considered as degradation mechanism. Therefore, the degradation cost of the SPM is given by (4.8) where $L(t_1)$ is the lost lithium in the optimisation time step in [Ah] and $\lambda_{\text{deg,lli}}$[2] which is 1.20 €Ah^{-1}.

As explained in section 1.3.6, this work does not focus on the resistance increase as a degradation metric, although this could be included by adding a second term to (4.8). The decreased efficiency is indirectly accounted for because more electricity will have to be bought than can be sold later. If other degradation mechanisms are added, extra terms will have to be added to (4.8), e.g. to account for the lost active material. As mentioned in section 3.3.2, adding additional degradation models might make the optimisation problem much more difficult to solve due to the additional state variables and the higher degree of coupling. Additionally, the shape of the objective function might alter, which again might make the optimisation much more difficult.

$$\Psi = \sum_{t_1=1}^{N_1} L(t_1)\lambda_{\text{deg,lli}} \tag{4.8}$$

---

[2] Calculated using the nominal cell voltage of 3.7 V.

Two objective functions are considered: one where the EMS does not care about degradation and therefore only maximises the revenue Φ; in a second case, the EMS tries to maximise the revenue while minimising the degradation, or in other words maximise the profit $\Pi = \Phi - \Psi$. The results from the former are indicated by a subscript R (e.g. BM_R for the bucket model maximising revenue) and the latter by a subscript P (e.g. BM_P for the bucket model maximising profit).

The application does not enforce further constraints on the optimisation, such that only the constraints from the battery models as given in section 4.3.1 are in the constraint function, see also section 3.6 for the details of the SPM formulation. In theory, a maximum power and efficiency curve would have to be added due to the power electronic converter but this was not included here and neither was the efficiency curve of the converter or the thermal management system as was discussed in section 1.2.1. The standard boundaries apply for all optimisation variables, enforcing the voltage or SoC limits.

4.3.3 Optimisation settings

Most of the settings of the optimisation have already been mentioned in section 3.9, but they are repeated here. The optimisation time step Δt_1 is set to 15 minutes reflecting the balancing period (see section 4.1), and the integration time step Δt_2 to 5 seconds (see section 3.4.2). As explained in section 3.8, a sliding-window optimisation is used. The window advances one day a time, corresponding to the nature of the day-ahead market. The time horizon of a single optimisation is two days, i.e. N_1 is 192. Longer time horizons do not improve the optimisation outcome, while they do increase the computational time .

Mostly, the standard settings of IPOPT have been used, see section 3.9. The 'limited memory' option is used such that IPOPT approximates the Hessian matrix with its internal algorithms because calculating the Hessian matrix requires too much memory and computational time. All the standard options of Adol-C and ColPack have been used, see section 3.7.

IPOPT failed to converge to an acceptable solution on a few days. The algorithm tries to improve the solution every iteration by increasing the objective while reducing the error on the constraints. However, it allows some points which significantly improve the objective or the constraints if the other is not impacted too much. This behaviour can be changed with settings, such as algorithms for linear solvers to find the search directions, allowable step sizes, etc. The standard settings worked well for almost all days. However, a few days had very small or very large price variations, in which case the algorithm occasionally failed because it converged to a point which has a high value of the objective function, but which was too far out of the allowable range for the tolerances on the constraints or vice versa. In such cases, the optimisation simply needed to be done again with slightly different settings. Changing the linear solver was sufficient in all cases.

Different choices of the linear solver (to calculate the search direction) only led to marginal differences, and the maximum number of iterations (3000) was only reached for a few exceptional days.

4.4 Optimisation results

This section discusses the outcomes of the optimisation. Fig. 4.4 shows the power from the battery to the grid[3]. It can be seen that the utilisation increases when degradation is not accounted for, and only the revenue is maximised. Overall, all profiles follow the price which was shown on Fig. 4.1 with the clear diurnal pattern of price peaks in the morning when people wake up and after sunset when solar panels stop producing while demand surges. Therefore, all batteries charge in the early morning and afternoon. The SPM charges at lower

---

[3] 'BM_P' refers to the optimisation outcome from the EMS which used the bucket model and maximised profit (revenue minus degradation cost).

powers so it has to start earlier to charge the battery compared to the BM. In summer, the price variation is much lower due to the high degree of renewable energy, therefore most batteries are used less. There were a few days with exceptional price variations which causes the battery to be used much more. This is best visible on subplot A of Fig. 4.4 (where the maximum power on other days is explicitly limited due to the degradation from (4.5)), or on the price profile of Fig. 4.1. The profit-maximising ECM barely uses the battery because the estimated degradation according to (4.4) is much larger than the revenue the battery could make. This is especially the case at the beginning of the year, due to the square-root dependency on the charge throughput and the time dependency at a power of 0.75 (4.4). Later in the year, the predicted degradation decreases such that using the battery becomes profitable.

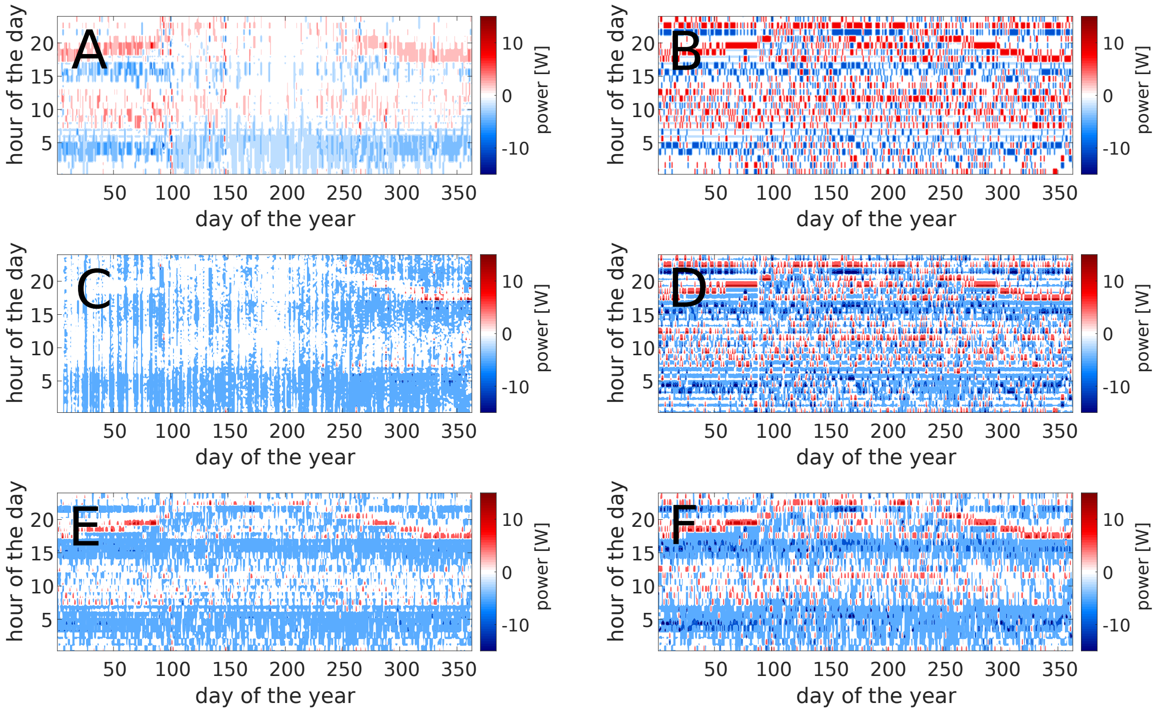

Fig. 4.4 Optimal battery power for the six optimisations, where negative values indicate charging. (A) BM maximising profit, BM_P; (B) BM maximising revenue, BM_R; (C) ECM maximising profit, ECM_P; (D) ECM maximising revenue, ECM_R; (E) SPM maximising profit, SPM_P; (F) SPM maximising revenue, SPM_R.

Fig. 4.5 shows the SoC, which is calculated by integrating the current to the battery (the power in the case of the BM). The BM produces relatively simple profiles where the battery is always charged from 0% to 100% SoC, and more frequently when revenue is maximised. When the ECM maximises profit, the battery is barely used in the beginning of the year due to the high degradation. The SPM maximising profit clearly produces more complicated usage profiles where the cell is often only partially (dis)charged because the additional degradation of (dis)charging fully is not compensated by the additional revenue which would be made.

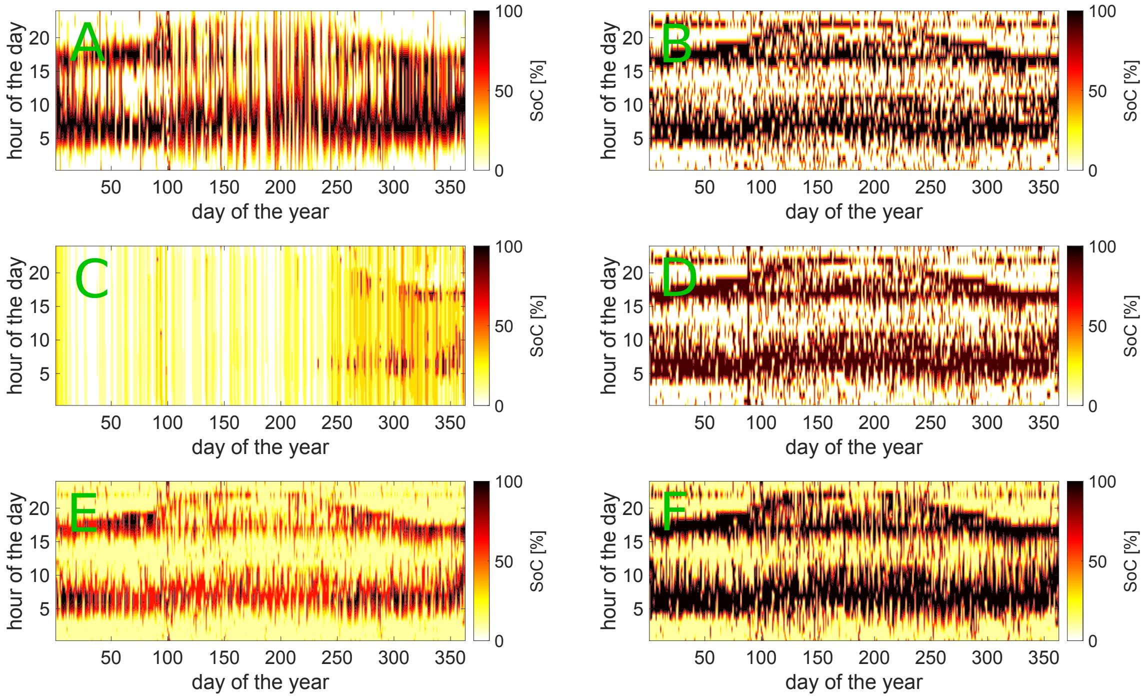

Fig. 4.5 Optimal battery state of charge for the six optimisations. (A) BM maximising profit, BM$_P$; (B) BM maximising revenue, BM$_R$; (C) ECM maximising profit, ECM$_P$; (D) ECM maximising revenue, ECM$_R$; (E) SPM maximising profit, SPM$_P$; (F) SPM maximising revenue, SPM$_R$.

Fig. 4.6 shows the histogram of the optimal profiles. It can be seen all cells spend most of their time resting. The profiles from the bucket models are relatively simple with only a few different power and SoC levels being used. The BM cell often rests at a fully charged or discharged state and charges at constant power levels between these states. When maximising revenue, the battery always charges at 1C between 0% and 100%, giving rise to the distinct cycling states at 25%, 50% and 75% SoC between those states. When maximising profit, the BM often uses a maximum power of C/2 or C/3, where the exact value depends on the price profile and is determined for every two-day optimisation window by the degradation model. Because the model is linear, the power will always be either 0 or this maximum value, giving the distinct bands of constant power and increasing or decreasing SoC.

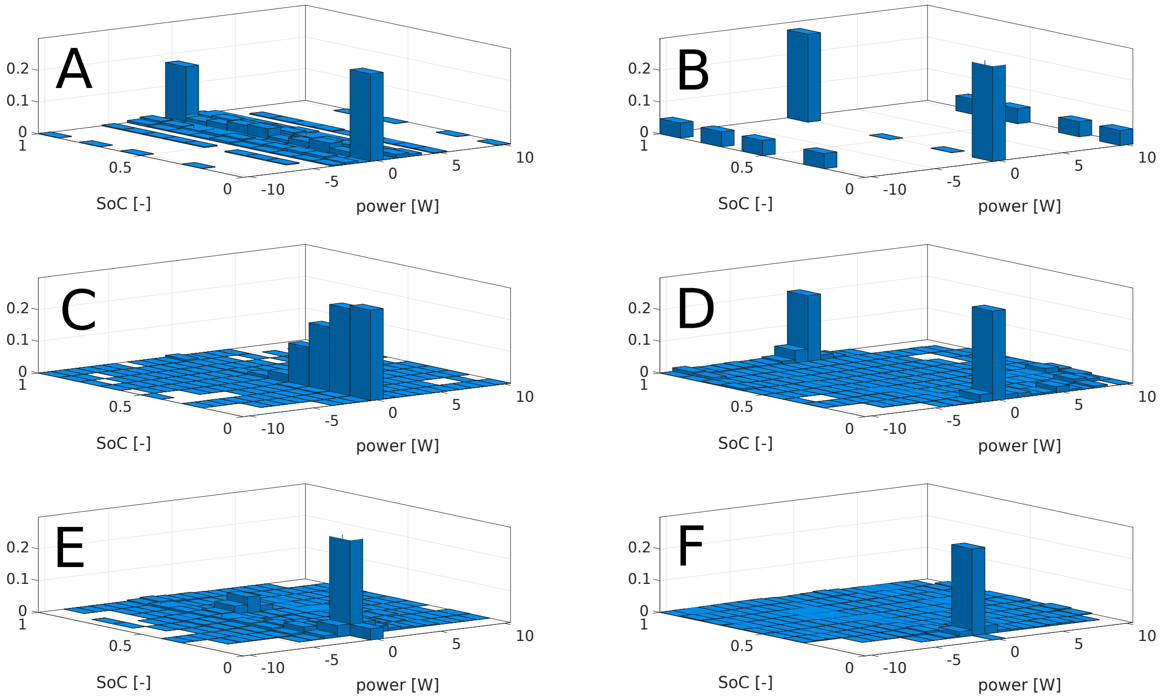

Fig. 4.6 Histogram of power and state of charge of the optimal profiles of the six optimisations, where negative power values indicate charging. (A) BM maximising profit, BM$_P$; (B) BM maximising revenue, BM$_R$; (C) ECM maximising profit, ECM$_P$; (D) ECM maximising revenue, ECM$_R$; (E) SPM maximising profit, SPM$_P$; (F) SPM maximising revenue, SPM$_R$.

The ECM has a similar behaviour, but because the model is not linear, most states are ‘spread out’. When maximising profit, the battery is barely used and spend most of its time at a low SoC and 0 W. The calendar ageing model from [158] minimised degradation when the voltage was close to 3.15 V, which is why the cell rests at a low but non-zero SoC. When maximising revenue, the battery continuously cycles between fully charged and discharged but at all power levels due to the nonlinearity in the model.

The SPM maximising profit also spends most time resting at low SoC, but cycles more often than the ECM maximising profit. The degradation model of the SPM (4.6) instructs the battery to rest at the lowest possible SoC, although reaching abololute 0% is very difficult due to the diffusion delays and voltage drops. When cycling, the SPM maximising profit uses all power levels due to the nonlinear model. Unlike the BM, the SPM rarely instructs the battery to rest at high SoC because this would lead to too much degradation. Instead, the cell often only charges to medium SoC levels where it can rest without too much calendar ageing. When the cell is fully charged, it is often discharged very soon afterwards. When maximising revenue, the SPM is either resting fully discharged, or cycling the cell. Whereas the BM can easily reach 100% SoC, the diffusion delay as well as kinetic and resistive voltage drops mean the SPM is often charging at low power levels to try and charge just a little bit more, similar to a CV phase in a conventional charge. This does not happen on discharge due to the steep drop in OCV, just like a CV discharge usually does not take long in a conventional discharge.

Fig. 4.7 shows the histogram of the optimal profiles when the cells are cycling, i.e. the ‘top view’ of Fig. 4.6. The points where the cell was resting have been removed for visibility because they massively outweigh the other conditions. Note that the total probability of each cell still adds up to 100%, but this only represents the fraction of time the cell is cycling, given on top of the graphs. The colour scale has been limited to 8% for visibility, this is a problem only for the BM_R, where each cycling condition happens exactly 12.5% of time.

Similar conclusions can be drawn as from the previous figure but they are better visible now. The BM uses always the same power because it is a linear model, when maximising revenue this is always 1C while the profit-maximising model has bands of constant power depending on the value of the maximum power determined by the degradation model for each two-day optimisation. It might seem counter-intuitive that the cycling probability of the profit- and revenue-maximising bucket models is the same, while this is not the case

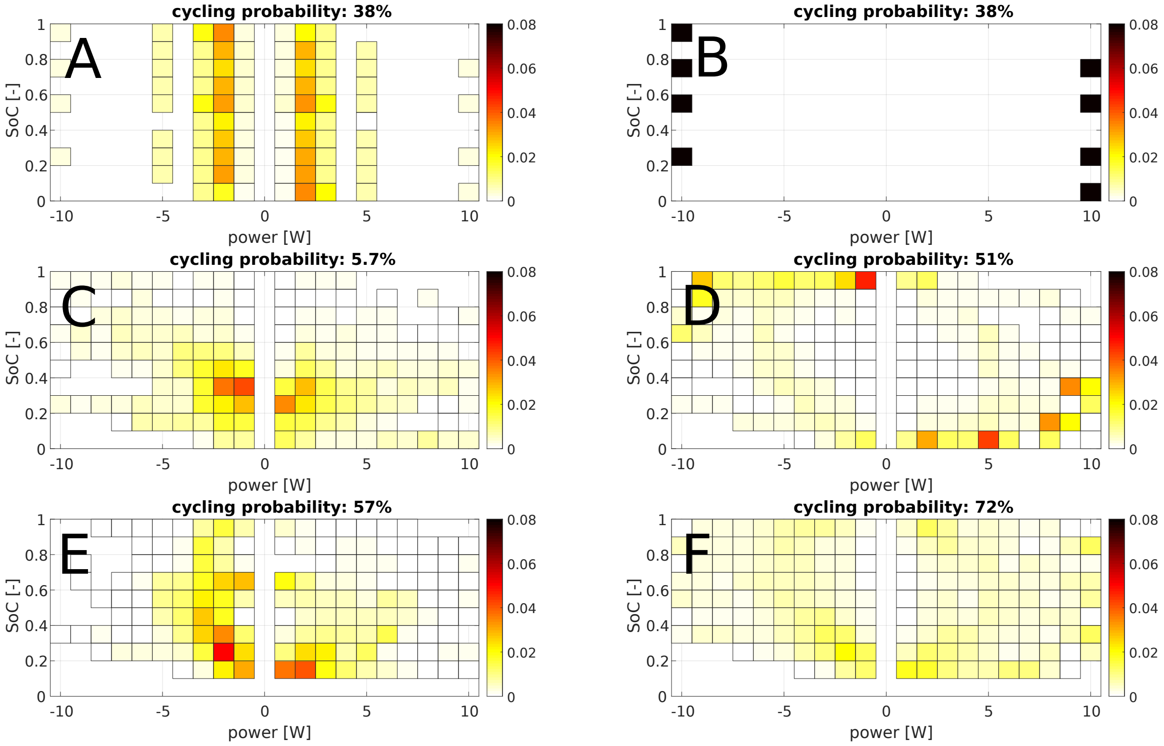

Fig. 4.7 Histogram of power and state of charge of the optimal profiles excluding resting periods of the six optimisations, where negative power values indicate charging. The title of each subplot indicates the percentage of time the cell is cycling. (A) BM maximising profit, BM_P; (B) BM maximising revenue, BM_R; (C) ECM maximising profit, ECM_P; (D) ECM maximising revenue, ECM_R; (E) SPM maximising profit, SPM_P; (F) SPM maximising revenue, SPM_R.

for the other battery models. This is due to the clear difference in power levels for the BM: when maximising revenue all its cycles are at 1C so a full charge and discharge takes 2 hours; when maximising profit, most cycles are at lower power levels and take longer. Therefore, the total time spent cycling is very similar for both models. This effect is not as pronounced for the other models because they are not linear and include the voltage curve, which makes it more difficult to (dis)charge at a high power. Therefore, the ECM and SPM maximising revenue charge at lower power and spend more time cycling.

The ECM minimised degradation by staying close to 3.15 V which is about 35% SoC. The battery was often charging or discharging at very lower power levels to get exactly to this voltage. Overall, the cell spent less than 6% of the time cycling because the degradation associated with (dis)charging was larger than the potential revenue. When maximising revenue, the ECM tries to fully charge and discharge the cell. Due to the diffusion delay and voltage drops, this often involves decreasing power levels at high SoC, similar to a CV charge, while higher powers can be used during discharge due to the steep change in the OCV curve.

The SPM maximising profit has a similar behaviour to the ECM maximising profit, namely spending lots of time at low power trying to get exactly to the voltage which minimises calendar ageing. However, for the SPM this means it has to discharge as low as possible, hence it spends most time at a very low SoC. Reaching absolute 0 requires such low powers that they are classified as resting (below 0.5 W or C/20). The ‘CV charging effect’ is visible by the yellow boxes at high SoC and low negative powers. When maximising revenue, it is clearly visible that all possible powers are used to make as much revenue as it can.

Fig. 4.8 shows the predicted revenue and degradation cost for all six optimisations, as well as the relative remaining capacity in each case. Note that the degradation is calculated according to each different model (BM, ECM and SPM) and therefore cross-comparisons between models are not justified. As could be expected, the revenue maximising optimisations, in blue hues, lead to a high revenue, but they also degrade the battery a lot, and the degradation cost is larger than the revenue for the BM and ECM. The profit maximising optimisations, in red hues, are more conservative. Although they maximised revenue minus degradation, they might still end up with a negative profit. Even when the batteries are not used, the ECM and SPM will incur a degradation cost due to the calendar ageing. Therefore, their 'baseline' is a certain negative number and they try to get a less negative, or more positive, outcome by cycling the cell, which incurs additional degradation but also some revenue. The ECM did increase on its baseline but did not succeed to make enough revenue to compensate all degradation. Therefore, its net profit was still negative (but this was the least negative outcome it could achieve). The SPM could easily make enough revenue to earn a positive profit.

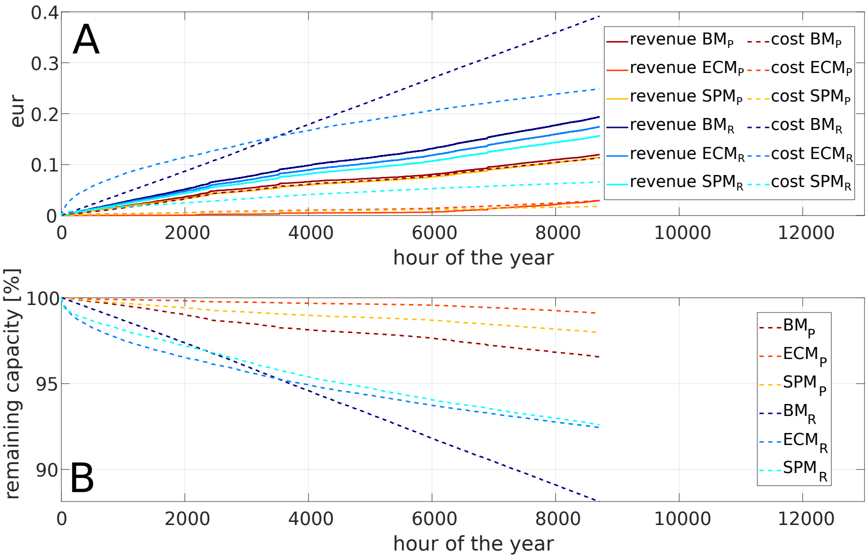

Fig. 4.8 Overview of the battery performance. (A) revenue and degradation cost of each of the six optimisations; (B) relative remaining capacity for each of the six optimisations.

4.5 Simulations of the optimal profiles

The results from the previous section were obtained with three different battery and degradation models so they cannot be compared with each other. In this section, the optimal profiles are given as input to one battery and degradation model, which will simulate how the battery responds to each profile.

The battery model used for the simulation is very similar to the generalised degradation model developed in chapter 2. The battery model is the SPM used throughout this work (i.e. with the equations from sections 2.1.1 and 2.1.2 and parameter values from Table 4.3 with the only exception being the values of the parameters of the SEI growth model). The fit of the SPM to the cycling data from section 1.4.1 is shown in section A.3.1.

While the SPM for the optimisation only included an SEI growth model (see section 4.3.1), the degradation model used here is more extended. It contains the equations from the 'generalised degradation model' from section 2.5.3[4], but with different fitting parameters and an additional model for kinetically-limited SEI growth (2.17). These changes were necessary to improve the fit for calendar ageing, because the generalised model from chapter 2 was only fit to the cycle ageing. The fit from this updated model to the degradation data from sections 1.4.2 and 1.4.3 with the parameter values used here is shown in section A.3.3. The SPM in the optimisation had to be simple enough so including all degradation models was not possible. As shown in section 2.5.3, there is a significant difference compared to the full degradation model, so in this section we verify that the degradation as predicted by the simplified degradation model is broadly accurate according to the full degradation model.

The optimal profiles are current profiles which the (simulated) battery should follow. The optimisations with the ECM and SPM directly produced these current profiles. The outcome

---

[4] The generalised model is a combination of diffusion limited SEI (2.20), Delacourt's LAM model (2.33), Kindermann's model for cathode dissolution (2.34) and Yang's model for Li-plating (2.36). During calendar periods, only the SEI growth is responsible for degradation, while all four models remove capacity during cycling.

of the BM optimisations was the power profile, which is divided by the nominal voltage of the cell (3.7 V as reported by the manufacturer) to get the current profile.

The BM did not account for the voltage during the optimisation, so when the same current profile is simulated with the model in this section, it might exceed the minimum and maximum voltage of the cell. The ECM did account for the voltage in the optimisation, but the battery model used in this section is different and might give a different voltage for the same current. Therefore, it is still possible that the voltage limits are exceeded although this should happen much less often than for the BM. The SPM optimisation also accounted for the voltage and only the degradation model is different compared to this section. Due to the different degradation, it is possible that the voltage limits are exceeded in the simulation of this section, but this should be very exceptional. When the (simulated) battery reaches its minimum or maximum voltage, it can no longer follow the optimal profile. In this case, there are two options: either the battery stops delivering power altogether for the remaining time of this step in the profile, or the battery can do a CV (dis)charge at its voltage limit. In the former case, the outcome is similar to what would happen if the optimisation was done with a 'smaller' capacity, often called the 'usable capacity'[5]. In the latter case, the battery does a 'best effort' to follow the profile at all times as it delivers the maximum power it can deliver without violating its voltage limits.

The results of the simulations are shown in full in Appendix B. Section B.1 shows what happens if the battery stops giving power when the voltage limit is reached, while section B.2 shows the results when a CV phase is done at the voltage limits. A third scenario is presented in section B.3, where only the middle 80% of the SoC window can be used. This is achieved by imposing tighter voltage limits and doing a CV (dis)charge at those voltage limits. This is a middle approach between the two previous ones and is similar to real battery systems where

---

[5] The capacity a battery can access depends on the power level and temperature due to diffusive and resistive effects [11, 31, 212]. There is no clear definition of the 'usable capacity' but in this work it is defined as the middle 80% of the SoC window. In reality, it would be the capacity which can be accessed at the expected power level and temperature for the given application and cell type.

the BMS restricts the SoC windows by adding safety margins to avoid overcharging and underdischarging (although the BMS would probably enforce this constraint on the estimated SoC rather than doing a CV phase at the reduced voltage limits).

Out of the 18 options (6 profiles and 3 approaches for voltage limits), three were selected to be experimentally validated. The ECM optimisation heavily overestimated the degradation because its empirical degradation formula was not accurate for the operating conditions and cell type considered here, as shown in section A.2. As explained before, this was because the ECM was taken directly from literature and not fitted to the cell used in this work. Therefore, the ECM profiles perform very badly in the simulation and are discarded henceforth. A more detailed discussion is given in section B.4, but the three profiles retained are:

- BM maximising revenue, BM_R, which can access the full battery SoC window and does a CV phase when a voltage limit is reached. This represents a battery which is very heavily used, and makes as much revenue as possible without considering degradation.
- BM maximising profit, BM_P, which can access the middle 80% of capacity of the cell and does a CV phase when a voltage limit is reached. The BM maximising profit is closest to the EMS used by most grid-connected batteries. It was limited to the middle 80% SoC because most grid-connected batteries employ the concept of the ‘usable capacity’ which is typically lower than the full capacity of the cell. Therefore, this approach is considered the baseline battery control as it is done today.
- SPM maximising profit, SPM_P, which can access the full battery SoC window and does a CV phase when a voltage limit is reached. The SPM maximising profit represents the most complicated control and would be the most interesting profile. Because the SPM already accounted for the diffusion, resistive and temperature effects in the optimisation, it does not often violate the voltage limits such that there is very little difference between the three approaches for dealing with voltage limits.

Fig. 4.9 shows the power delivered by the (simulated) battery[6]. The profiles look very similar to the corresponding subplots of Fig. 4.4 indicating that on average, the batteries could deliver the required power.

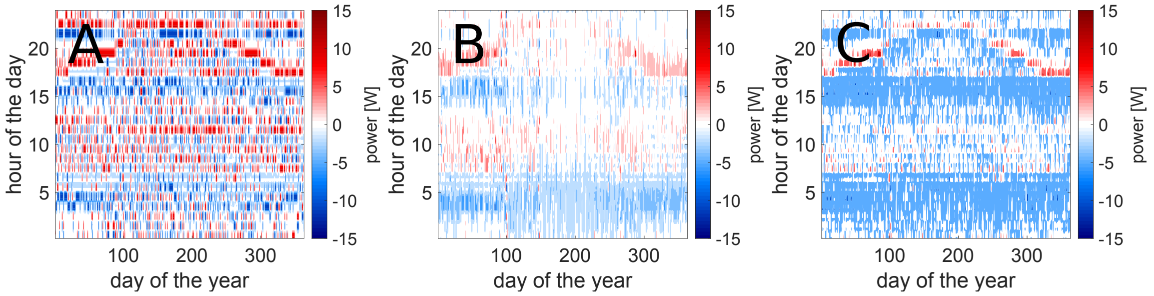

Fig. 4.9 Simulated optimal battery power for the three profiles used for the experimental validation, where negative values indicate charging. (A) BM_R; (B) BM_P; (C) SPM_P.

Fig. 4.10 shows the corresponding SoC profiles, which are calculated by integrating the battery current divided by the nominal capacity. As a result of the way in which SoC was calculated, it drifts due to the battery degradation: the real SoC is determined by the lithium concentration in the particles, which is determined by the main lithium intercalation current density. This current density differs from the total battery current due to LLI (part of the total current goes to growing the SEI layer) and due to LAM (affecting the effective surface over which the current is spread).

The BM-controlled cells spend most of their time at the minimum or maximum SoC while the SPM_P cell is often (dis)charged to intermediate SoC levels, as was the case in the original profiles from Fig. 4.5. The effect of limiting the SoC region for the BM_P simulation (subplot B in Fig. 4.10) is indicated by the absence of white and black, which represent the top and bottom regions of the SoC respectively. The difference for the SPM is smaller. There is a drift in SoC because the cell in the simulation degrades more than the cell in the optimisation. After one year, the former has lost 2.77% and the latter only 2.02%[7].

---

[6] 'BM_P' refers to the simulation of the cell which followed the optimisation outcome from the EMS which used the bucket model and maximised profit (revenue minus degradation cost).

[7] Additionally, errors in Matlab's plotting functions and the conversion of graphs from Matlab to pdf cause some colours to look different even though the actual values are very similar. Especially at the beginning of the

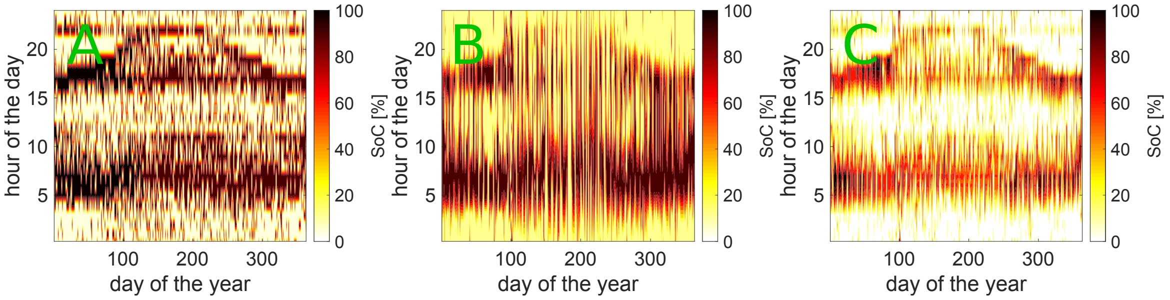

Fig. 4.10 Simulated optimal battery SoC for the three profiles used for the experimental validation. (A) BM_R; (B) BM_P; (C) SPM_P.

Table 4.4 Comparison of the simulated optimal profiles.

model	revenue [€]	degradation cost [€]	FEC [-]	lost capacity [%]
BM_R	0.1246	0.3393	1522	10.4799
BM_P	0.0992	0.0974	408	3.0094
SPM_P	0.1142	0.0897	672	2.7711

Fig. 4.11 compares the revenue, degradation and degradation cost of each profile. For all cases, the degradation cost is calculated by multiplying the lost capacity[8] in [Ah] by the aforementioned cost of degradation, 1.2 €Ah^{-1}. The BM_R simulation gets the highest revenue but the degradation cost is even larger than this revenue after the cell has lost over 10% of its capacity in just one year. The BM_P simulation achieves a smaller revenue, but loses only 3% of its capacity. The SPM_P simulation has a revenue between the two BM models, but it has the lowest degradation of all. This means that compared to the BM_P simulation, it has simultaneously increased the revenue by 15% and decreased the degradation by 8%, although the model errors for degradation are larger than the 0.3 percentage points difference (see section A.3.3). Table 4.4 summarises the performance at the end of the year for each simulated cell, where FEC gives the full equivalent cycles (calculated by dividing the charge throughput by twice the nominal cell capacity of 2.7Ah).

---

cell's life, the SoC values are identical and yet they are shown as pale yellow on subplot E of Fig. 4.5 and as white on subplot C of Fig. 4.10

[8] calculated as mentioned at the beginning of chapter 2 by simulating a full charge and discharge with a CC-CV current between the voltage limits of the cell. The integral of the current gives the charge capacity, similarly to how it is measured in experiments.

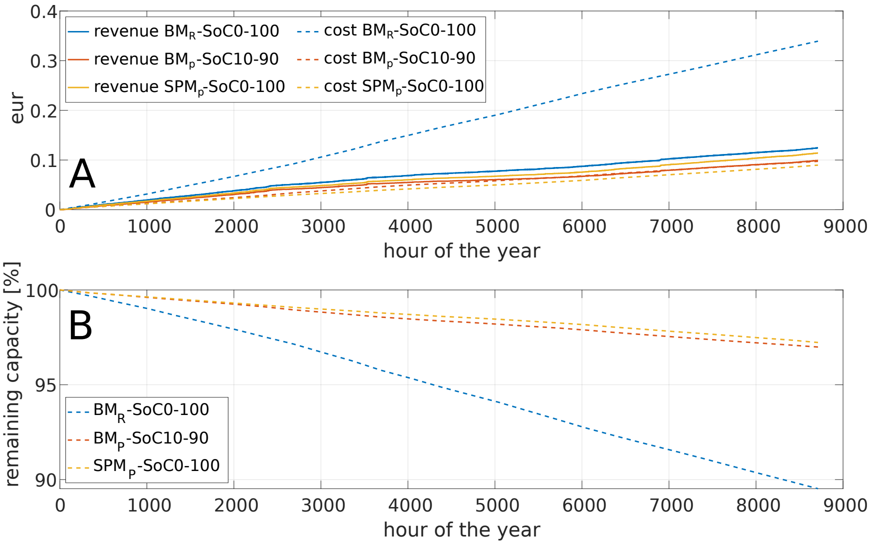

Fig. 4.11 Overview of the simulated battery performance. (A) revenue and degradation cost of each of the three profiles; (B) relative remaining capacity for each of the three profiles.

4.6 Experimental validation

This section presents the results of the experiments conducted to validate the optimisation and simulations from the previous sections.

4.6.1 Experimental setup

The experiments were conducted using a PEC battery tester (SBT8050). The cell used for the experiments was a high-power Kokam cell, the same as used in section 1.4. It has a nominal capacity of 16 Ah (the real initial capacities are closer to 17 Ah) such that all profiles were rescaled (the optimisation and simulation was done for a 2.7 Ah cell)[9]. The cells were not in a thermal chamber, but the temperature in the lab was controlled to be 25 ± 0.5 °C.

---

[9] The simulation with the SPM was done for an 18650 with 2.7 Ah capacity since a good parameter set for this cell was already gathered, and initially 18650s would be used for this work due to limitations of the equipment. However, due to the availability of the degradation data of section 1.4, the large pouch cells were used for the experiment. The SPM has a scaling factor relating the total current to the current density, and only the current density is used in the model, see (2.3). Therefore, the results of the SPM do not change for a larger cell, the current density values are simply multiplied by a larger value. Instead of changing the simulation, the current values of the experimentally measured cell were reduced by the same factor, which produces exactly the same outcome. This was done because the 2.7 Ah cell has an energy capacity of 10 Wh which makes it easy to calculate the revenue or degradation cost per Wh of installed capacity.

The battery tester was programmed to follow the rescaled current profiles which came out of the optimisation (and were used as input for the simulations from section 4.5): BM maximising revenue (BM$_R$), BM maximising profit (BM$_P$), and SPM maximising profit (SPM$_P$). The voltage limits were imposed in the same way as described in section 4.5: the cells following the BM$_R$ profile did a CV for the remaining time when they reached 2.7 V or 4.2 V; the cells following the BM$_P$ profile did a CV for the remaining time when they reached 3.42 V or 4.08 V (corresponding to 10 % and 90 % SoC respectively); and the cells following the SPM$_P$ profile did a CV for the remaining time when they reached 2.7 V or 4.2 V. Every 30 days, the experiment was interrupted and capacity was measured by doing 4 cycles with a full discharge and charge, both with a CC phase at 1C and with a CV phase until a limit current of 0.01C with a 1h rest in between. Two cells were used for each profile. The experiment was set up and conducted by project partners from VITO, and they shared the raw test data for analysis in this work.

The experiment failed a few times. For three periods of a few days each (around days 30, 60, and 90), there was a mistake in the test procedure (the current had the opposite sign). The cell followed these wrong profiles, but the cycling data was removed when calculating the revenue (although the effects on the degradation could not be cancelled out). The experiment was down for several weeks after a fault was discovered in the firmware of the tester (related to data storage) and there have been a few other interruptions of short duration, due to power cuts, recalibration, etc. However, 347 days of correct data have been collected in a total period of about 461 days. Almost all of the failures and down time were at the start of the experiment. In the last 9 months, there were only 2 days of down time.

4.6.2 Experimental results

The cell used for the experiments has 16 Ah capacity. The results presented here have been rescaled down to a cell of 2.7 Ah so they can be compared with the results from the previous sections.

The results presented in this section account only for when the cells were trading electricity. The ‘full equivalent cycles’ are calculated by dividing the traded energy by twice the energy capacity of the cell, i.e. ignoring the throughput from capacity check-up tests and periods when the experiment was conducted with the wrong sign for the current (see the previous section). Together, this accounted for 60 FECs for the SPM_P and BM_R cells and 40 FECs for the BM_P cells. Similarly, the ‘cumulative time’ ignores the time required for capacity check-up tests, which together took about 200 h or 2% of the total runtime, and down time.

Fig. 4.12 shows the power delivered by each cell[10]. The three periods when there was a mistake in the test procedure have been omitted from the power measurements because the measured power was completely different from what it should have been. Both cells following the same profile delivered the same power. As could be expected, the measured power matches the simulated power very well.

The SoC could not be calculated by integrating the measured current due to the quality of the collected data (the time interval was too large) and the interruptions for capacity measurements. Instead, Fig. 4.13 shows the mean voltage during each 15-minute period. Although the terminal voltage is not exactly the same as the SoC, it allows a relative comparison between cells. The three periods when there was a mistake in the test procedure have again been omitted from the voltage measurements.

The same trends as before can be observed. The BM_R cells are heavily used, introducing frequent voltage changes. The cells are usually fully discharged or fully charged. The BM_P

---

[10] ‘BM_P’ refers to the measurements of the cell which followed the optimisation outcome from the EMS which used the bucket model and maximised profit (revenue minus degradation cost).

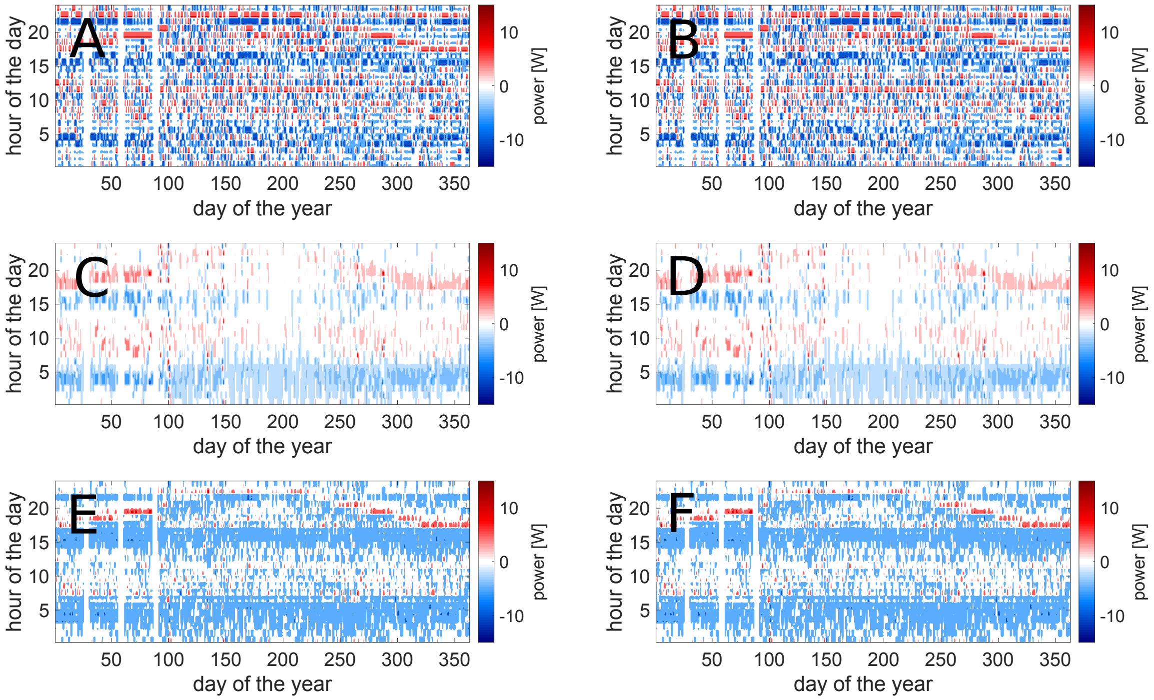

Fig. 4.12 Battery power for the six cells in the experiment, where negative values indicate charging. (A) BM_R cell 1; (B) BM_R cell 2; (C) BM_P cell 1; (D) BM_P cell 2; (E) SPM_P cell 1; (F) SPM_P cell 2.

cells can only access the middle voltage region. The SPM_P cells spend more time at lower voltage regions to minimise the degradation when little money could be made by charging the cell. Only occasionally, the cells are fully charged.

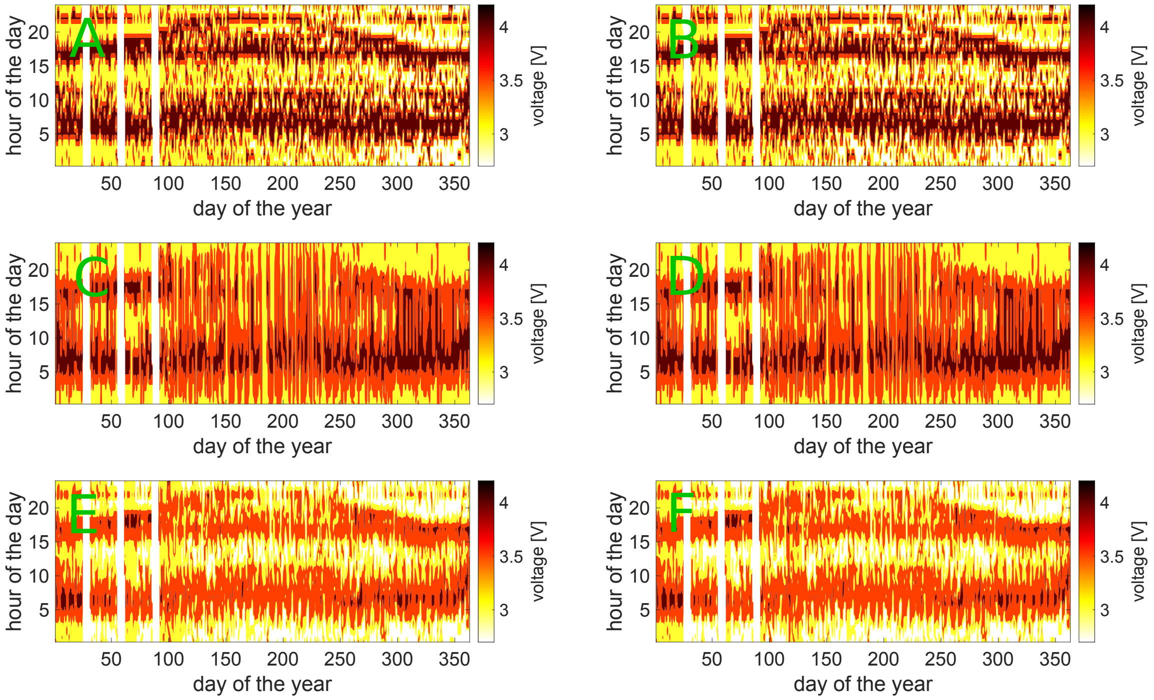

Fig. 4.13 Battery voltage for the six cells in the experiment. (A) BM_R cell 1; (B) BM_R cell 2; (C) BM_P cell 1; (D) BM_P cell 2; (E) SPM_P cell 1; (F) SPM_P cell 2.

Fig. 4.14 shows the histogram of the power and voltage of the measured profiles. Note that they cannot be directly compared with the optimal profiles of Fig. 4.6 because the mapping from voltage to SoC is not linear. Additionally, the BM_P cells could not access the top and bottom voltage regions in the experiment, unlike in the optimisation where the SoC could go to 0% and 100%. Another difference between the optimal and measured power is due to the settings of the experiment: the testers were made to follow a current profile (not a power profile), and for both BM profiles, the current was obtained by dividing the power by the nominal voltage of 3.7 V. The measured power will therefore deviate from the optimal value if the cell voltage is not 3.7 V, and the power is no longer constant as it was in the optimal profiles. This is not the case for the SPM$_P$ cells, because they accounted for the voltage in the optimisation.

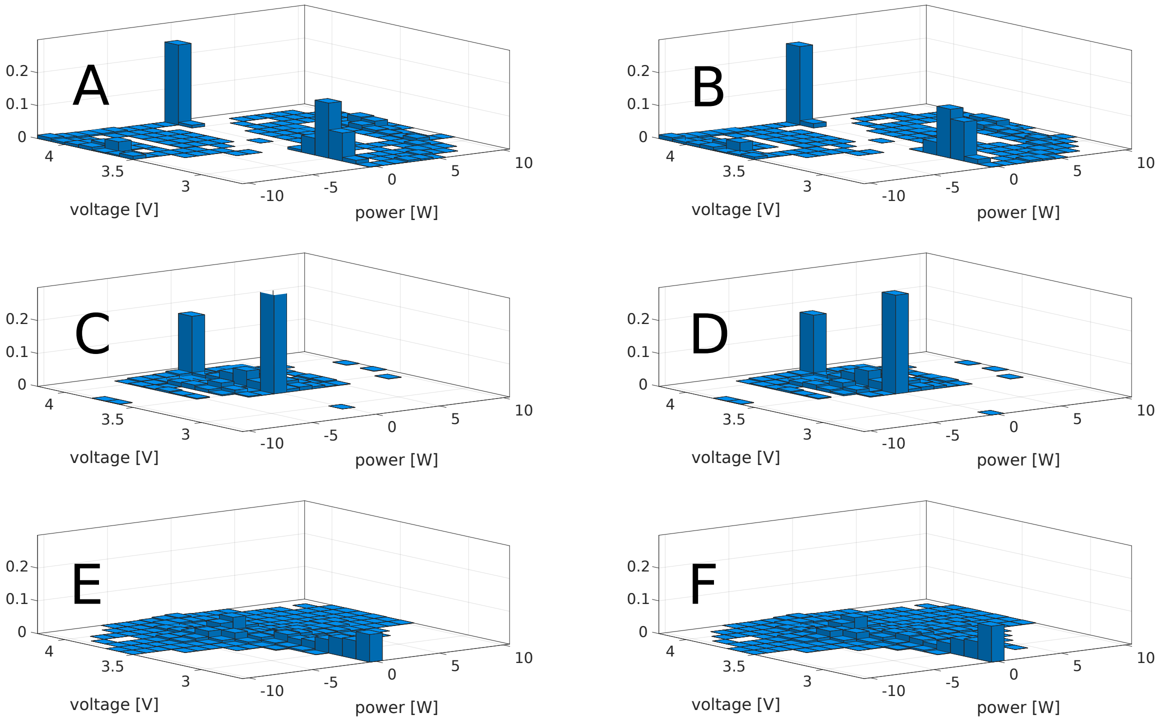

Fig. 4.14 Histogram of power and state of charge of the measured optimal profiles of the six cells in the experiment, where negative power values indicate charging. (A) BM$_R$ cell 1; (B) BM$_R$ cell 2; (C) BM$_P$ cell 1; (D) BM$_P$ cell 2; (E) SPM$_P$ cell 1; (F) SPM$_P$ cell 2.

There is a larger difference for the BM$_R$ cells. In the optimisation, the cell was always fully charging or discharging at 10 W. In the experiment, the cells still spent most of their time at high powers, but not at the fixed value of 10 W and occasionally very low power levels occur. A first explanation is that the voltage is not always 3.7 V, as mentioned in the previous paragraph. Secondly, the voltage limits will also cause reduced power levels: if a cell reaches the maximum voltage during the experiment, it does a CV phase, reducing the current and therefore the power. Finally, the profile used for the experimental validation was obtained with the same equations and parameter values mentioned before, but using a different solver[11]. Occasionally, this solver did instruct the battery to charge or discharge at lower power levels, for instance when the price was constant for two or more consecutive hours.

On Fig. 4.14, it can still be seen that the cycles done by the SPM$_P$ cells are more complicated, but more importantly, they spend much more time at lower voltages, especially when resting. There is no clear cut-off voltage above which they are not used, because the optimisation will determine for every cycle whether the revenue the cell can make justifies the extra degradation which the cell would incur if it were charged a bit more. This will also account for the time the cell will subsequently rest at this higher voltage, and thus the increased calendar ageing.

Fig. 4.15 shows the histogram of the measured power and voltage when the cell was cycling, i.e. excluding periods when the power was below 0.5 W. In all cases, it is important to remember that the voltage curve is relatively flat around 3.6 V. Therefore, a constant current or constant power (dis)charge will spend more time in that voltage region than at other voltages. This implies that such a constant (dis)charge will not give boxes of the same colour scale on Fig. 4.15. Indeed, all cells have their darkest colour at these voltage levels.

Comparing this figure to the optimisation outcome from Fig. 4.7 reveals the same differences as explained in the previous paragraphs. For the BM$_R$ cells, it is clearly visible the cells charge at a high power until they reach the voltage limit of 4.2 V, after which the power decreases due to the CV charging phase. No low-power charge (below 5 W) is done because the BM$_R$ profile will only instruct the cell to charge for a given time period (1C for 1 hour), such that the CV phase is stopped usually stopped before the power drops below 5 W. Overall, the cells spend a large fraction of their time charging at high power and at high voltage, which will lead to excessive degradation for these cells. On discharge, the effect of the voltage decrease at low SoC regions is also well visible: the current stays constant and

---

[11] For practical reasons, the profile used in the validation was calculated with the same software as was used for the other battery models, i.e. IPOPT in a C++ environment. The optimal profiles presented in section 4.4 were obtained with Matlab's linear optimiser.

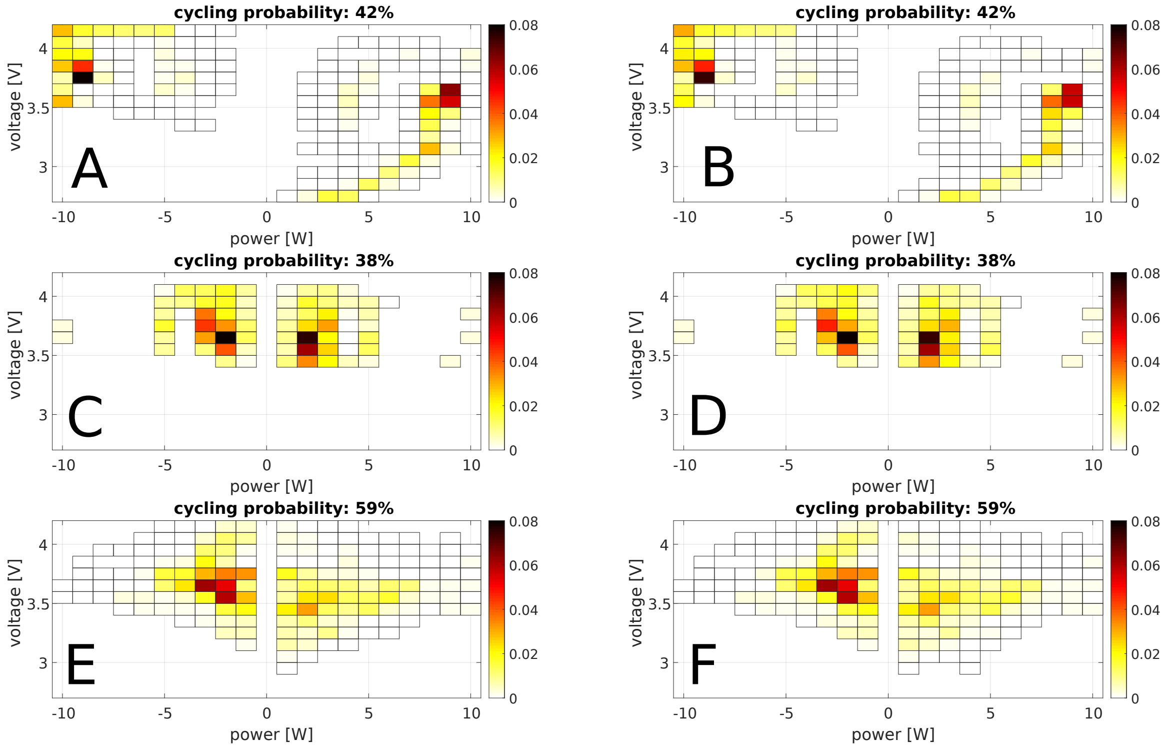

Fig. 4.15 Histogram of power and state of charge of the measured optimal profiles excluding resting periods for the six cells in the experiment, where negative power values indicate charging. The title of each subplot indicates the percentage of time the cell is cycling. (A) BM_R cell 1; (B) BM_R cell 2; (C) BM_P cell 1; (D) BM_P cell 2; (E) SPM_P cell 1; (F) SPM_P cell 2.

due to the decreasing voltage, the power decreases proportionally. There is much less CV discharging at the minimum voltage because the overpotentials are much smaller than the change in the OCV curve.

The safety margins which have to be respected by the BM_P cells are clearly visible: they can only be used the middle 80% of the SoC region, so their voltage cannot go above 4.08 V or below 3.42 V. These cells use lower power levels to minimise the degradation except on a few days with very large price fluctuations, as was explained at the beginning of section 4.4, when it is worth cycling at 10 W (which is 1C). Due to the changing voltage, the power was less constant than on Fig. 4.7.

The SPM_P cells behave very similar to the optimisation outcome from Fig. 4.7. They clearly avoid the region on the top left, charging at high power and high SoC, in which the BM_R cells spend a significant amount of time. This is one of the reasons why the SPM_P cells will degrade less. It is also visible that on some occasions, these cells are fully charged to the maximum voltage, which is on days where the price fluctuations are very large. However, on most other days, the cells are cycled in a lower SoC window. From this graph it might seem as if the SPM_P cells are never fully discharged to the lowest voltage, but that is not the case. The discharge to this lowest voltage limit happened at such low power levels (below 0.5 W) that they were classified as ‘resting’. This becomes clear when looking at Fig. 4.14, where the SPM_P cells have a ‘tail’ of resting at increasingly low voltages even though there is no discharge at these low voltages.

The behaviour during discharge is also informative of the SPM and BM models. The BM_R cells did high power discharges to the minimum voltage, often the cell wanted to discharge at 10 W because the optimisation did not account for the voltage limit. As explained in the previous section, the experiment was set up such that it would do a CV discharge when this happens. Therefore, the BM_R cells start from about 10 W and do a CV discharge, which still involves relatively high power levels at the low voltage region. The SPM on the other hand accounts for the voltage limitations in the optimisation such that it is much more ‘careful’ when discharging at low voltage to not exceed the limit. Therefore, the profile instructed the cells to discharge at low power levels, ultimately so low power levels that they were classified as resting as was explained in the previous paragraph.

Fig. 4.16 shows the revenue and degradation cost of each cell, as well as the relative remaining capacity. Again this confirms the trends observed before. The BM_R cells get a higher revenue, but this leads to very large degradation losses. The cost associated with this degradation is much larger than their revenue. The BM_P cells degrade less, but their revenue is lower too. The SPM_P cells have the lowest degradation of all, on average 31% below the BM_P cells, and 88% below the BM_R cells. At the same time, the revenue from the SPM_P cells is about 17% higher than the revenue from the BM_P cells, but 6% lower than the revenue from the BM_R cells. As mentioned in the previous section, the experimental setup failed a few times while collecting the data of the first three months of data. There were about 80 days of down time, or in other words, collecting 2200 hours of data took over 4000 hours. At that point, which is the fourth data point on Fig. 4.16, the SPM_P and BM_P cells had lost about the same capacity (about 0.4%). In the nine months after that point, the capacities of the cells started diverging as the experiment ran smoothly for all but two days. This indicates that the SPM optimisation was successful in reducing degradation, and if there had been less down time, the difference would probably have been larger.

Table 4.5 gives an overview of the performance of all six cells over the entire experimental period. It should be noted that the number of full equivalent cycles is calculated based on the energy, not the charge, and accounts only for the throughput while trading electricity.

Fig. 4.17 is similar to Fig. 4.16 except that the x-axis has been changed to FECs. As before, those FECs are calculated based on the traded energy, ignoring capacity check-up tests. The cells maximising revenue are used much more than the others. The SPM_P cells are used about 60% more than the BM_P ones. It should be no surprise that the revenue

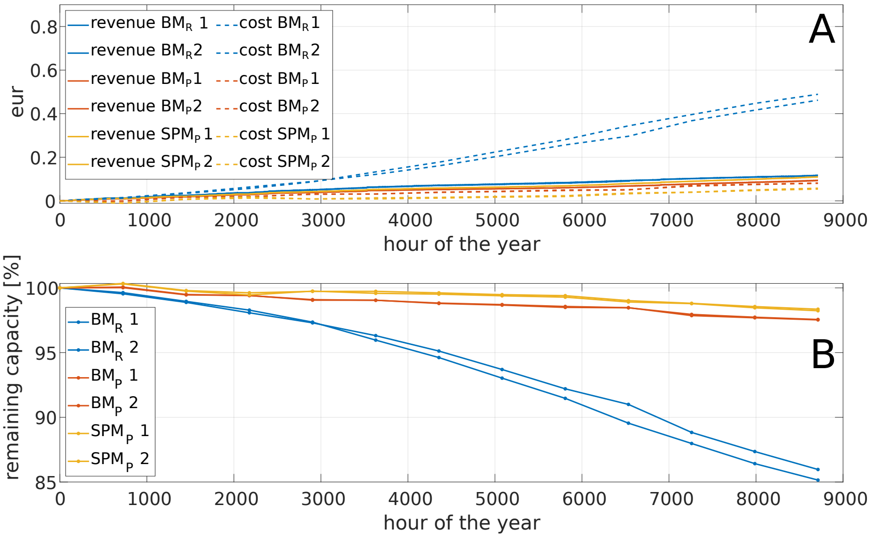

Fig. 4.16 Overview of the experimental battery performance over time. (A) revenue and degradation cost of each of the six cells; (B) relative remaining capacity for each of the six cells.

Table 4.5 Comparison of the different cells of the experiment.

model	revenue [€]	degradation cost [€]	FEC [-]	lost capacity [%]
BM$_R$ 1	0.1174	0.4890	1429.9	14.8514
BM$_R$ 2	0.1161	0.4619	1432.2	14.0338
BM$_P$ 1	0.0930	0.0805	387.2	2.4415
BM$_P$ 2	0.0944	0.0814	386	2.4742
SPM$_P$ 1	0.1103	0.0579	623.4	1.7667
SPM$_P$ 2	0.1098	0.0541	622.7	1.6478

achieved per cycle for the profit-maximising cells is significantly larger than for the revenue-maximising cells because the former ones only do a cycle if the revenue is large enough to justify the degradation. The revenue per cycle of the SPM$_P$ cells is lower than for the BM$_P$ cells because the former ones are used more often and thus also capture periods with smaller price differentials. The SPM$_P$ optimisation can reduce the degradation associated with those cycles such that it is still profitable to use the cell even with the lower revenue.

In terms of degradation per FEC, it seems like all the cells controlled by the BM are following a very similar trajectory. This indicates that the total degradation is heavily dominated by cycle ageing: because BM$_P$ cells have rested much longer than the cells maximising revenue, their calendar ageing should be much larger; however, their cycle ageing is more similar. This also indicates that the BM$_P$ cells would outperform the BM$_R$ cells over their lifetime, given that the former one achieves a higher revenue and similar degradation per cycle. This is however complicated by the different SoC regions they can access (BM$_P$ cells are limited to the middle 80%, the BM$_R$ cells can use the full cell). See section 4.8 for a full analysis.

The SPM$_P$ cells degrade less per cycle than the BM cells. After 386 FECs, the SPM$_P$ cells have degraded on average 73% less compared to both the BM$_P$ and the BM$_R$ cells. This indicates that the optimisation with the SPM is capable of reducing the cycle ageing of the cell. It also means that the SPM therefore outperforms both the BM$_P$ (similar revenue but less degradation per cycle) and the BM$_R$ (more revenue and less degradation per cycle).

4.7 Realistic implementation of the control algorithm

The results from the previous section identified significant gains in performance using advanced battery control. However, the experiments were done with just one cell connected to a battery tester. Real batteries do not allow such a detailed control, and rely on BMSs and inverters. Therefore, this section describes a realistic implementation with the small

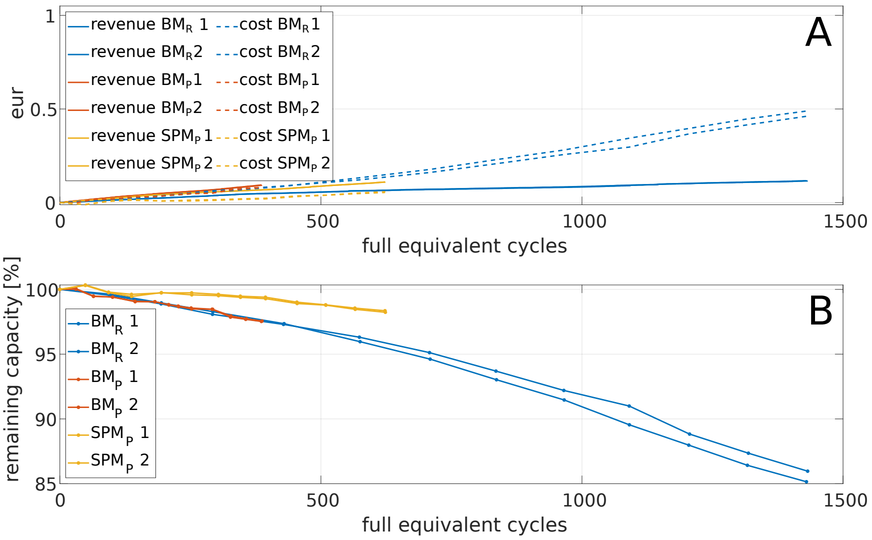

Fig. 4.17 Overview of the experimental battery performance versus FEC. (A) revenue and degradation cost versus full equivalent cycles for all six cells; (B) relative remaining capacity versus full equivalent cycles for all six cells.

battery shown on Fig. 4.18. The hardware and associated software interfaces were built by collaborators from VITO. The battery consisted of 14 LG Chem cells (INR18650 MJ1 3500 mAh) connected in series. The pack was enclosed in a plastic housing which had a fan for cooling the cells. The pack was connected to a BMS designed by VITO, which measured the voltage and current of individual cells and read out the three temperature sensors in the pack. The BMS also delivered standard BMS services such as cell balancing, SoC estimation, and enforcing the standard safety features by disconnecting the battery when the voltage or thermal limits were reached. The power to the BMS was delivered by an external voltage source. A controllable bi-directional inverter was used to supply/consume the electricity to/from the battery.

The schematic operation of the setup is shown on Fig. 4.19. The setup was called the ‘market-trading test bench’ (MTTB). The optimisation described before was not changed, and is included in the EMS. It assumes the price of the wholesale market is known, and once a day it computes the optimal usage profiles for the battery for the next day. These profiles are then sent to a real-time control unit, which was implemented on the same computer as the

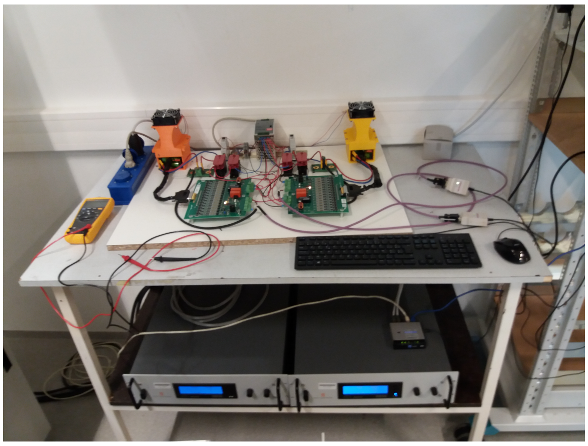

Fig. 4.18 Experimental setup of the market-trading test bench. Two identical setups are shown, each with a battery in the yellow or orange housing for the cooling, a BMS running on the green circuit boards, and bi-directional loads on the bottom shelf.

EMS. The objective of the control unit is to ensure the battery follows these profiles without violating voltage or thermal limits, as well as to take care of data logging. The control unit gets real-time measurements from the BMS via TCP/IP[12] messages and is therefore aware of the actual battery state. The control unit then decides the current or power the battery should deliver in the next few seconds, and sends this command to the inverter, again via TCP/IP. Note that the EMS does not get input from the control unit, and therefore the optimisation is still an open-loop control system. The EMS and control unit were coded in the framework of this DPhil, while the inverter, battery pack, BMS and software interfaces were implemented by collaborators.

This setup worked, and was capable of tracking the optimal profiles. Fig. 4.20 compares the measured battery behaviour with the optimal profile (obtained with the SPM optimisation maximising revenue but with parameters for the MJ1 cell, so this is a different profile from the SPM$_R$ profile shown before which had parameters for the Kokam cell). Initially the battery pack was at a completely wrong SoC and voltage, so the first three 15-minute periods were used to align the pack's state with the optimal profile, hence the large difference between

---

[12] TCP stands for 'transport control protocol' and IP for 'internet protocol'. They are the standard protocols to relay data over the internet. The physical connection can be anything ranging from Ethernet cables to wifi.

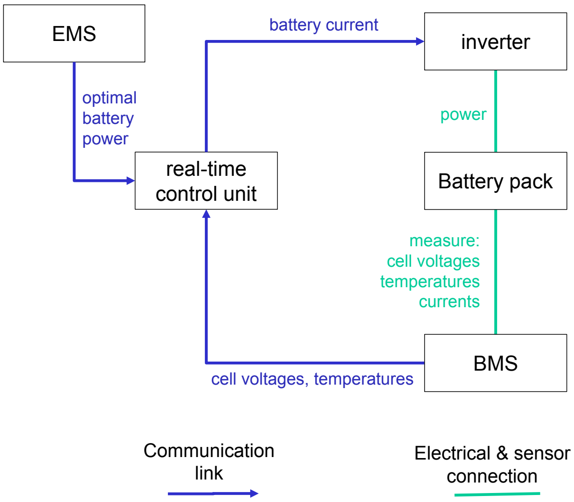

Fig. 4.19 Overview of the market-trading test bench.

the planned and measured behaviour. The rest of the two days, the battery was controlled to follow the current profile. Only occasionally, a voltage limit forced the control unit to reduce the current (for instance between hours 8 and 9). This had barely any effect on the resulting power, such that the battery could mostly honour its market commitment (where power is traded, not current). After 51 hours, a communication error with the inverter meant the cell stopped following the profile.

Note that during prolonged periods without current, such as between hours 10 and 15, the measured voltage relaxes while this is not captured by the battery model used in the EMS. This is a limitation of the SPM, which is not capable of simulating long-time relaxation in the high-energy cells. This effect is more pronounced at low SoC when the OCV of the cell changes more than at high SoC.

It is not clear why the measured temperature increased between hours 12 and 27 even though initially there was no current running in the battery. The anomaly persisted until hour 27, when the temperature on rest came back to 25°C, which was the temperature of the lab.

The intention was to have 6 identical setups. They could then use different battery algorithms for the optimisation in the EMS to compare it with the experiments using a single

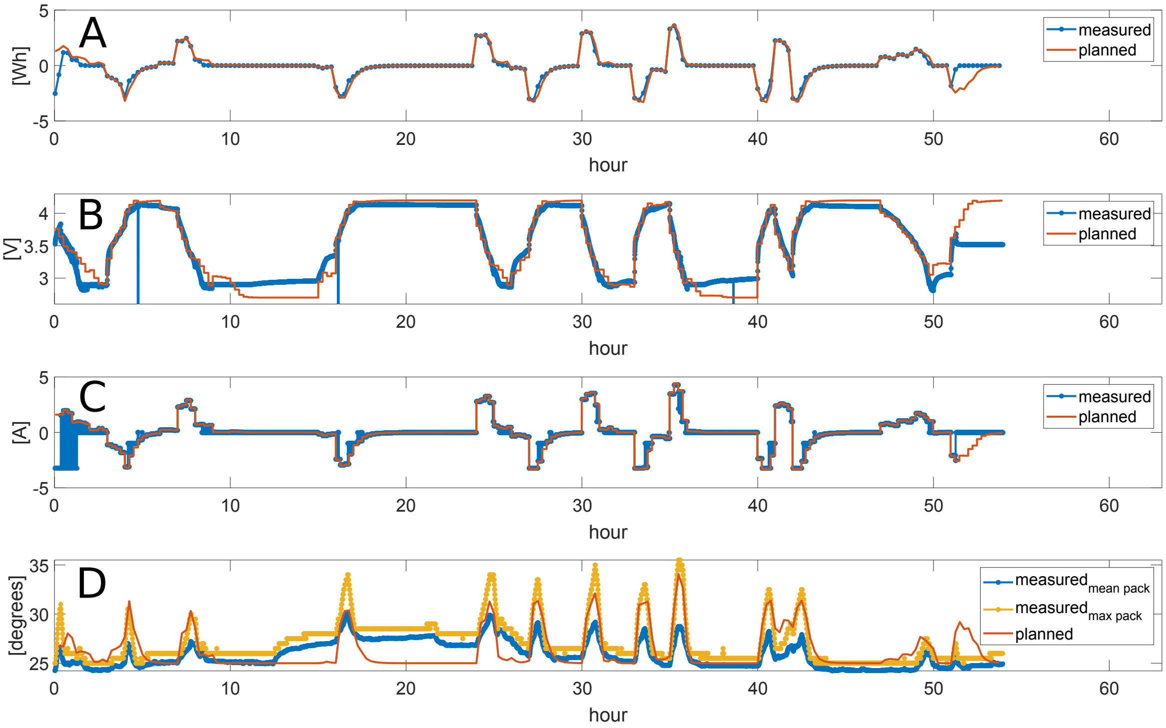

Fig. 4.20 Comparison of the expected and measured behaviour of the battery used in the MTTB. In blue are the measurements from the battery; in red is the planned behaviour as scheduled by the EMS. (A) energy delivered in every 15 minute period; (B) average cell voltage; (C) cell current; (D) average, maximum and expected temperature.

cell from section 4.6.2. Especially the effect of limiting the ‘usable capacity’ was going to be investigated, because this setup could limit the battery’s operation to an SoC range (as would probably happen in real battery systems) and did not have to rely on reduced voltage limits and CV phases to achieve the same effect. Due to limitations in the available hardware (specifically the bi-directional inverters) this was not possible. Because there was little benefit in running one system for longer time periods, the MTTB never operated for longer than a few days but it is a good starting point for future work as mentioned in section 4.10.

4.8 Discussion

The cost of battery degradation was determined by dividing the initial investment cost by the installed capacity, resulting in a fixed value of 330 € kWh^{-1} (or 1.20 € Ah^{-1}) of lost capacity, as explained in section 4.3.2. This implies that the initial investment cost has been accounted for when the cell has fully degraded. However, batteries are typically considered to have reached their end of life when they have lost 20% of capacity, at which point only 20% of the investment cost has been accounted for. Therefore, the 330 € kWh^{-1} could be interpreted as a degradation cost only one fifth of the investment cost and the numerical results obtained here represent a future when the cost of batteries has fallen significantly.

Secondly, there are many different ways in which the degradation cost can be calculated, e.g. by using the cost for replacing degraded cells (instead of the original cost of the cells), by accounting for inflation, etc. The effect of degradation is that the battery can store less energy, and the EMS can trade less energy. Therefore, a second type of ‘degradation cost’ is the revenue which is lost in the future. The two-day optimisation horizon was too short to account for this effect. Increasing the time horizon led to worse outcomes because the optimisation solver did not converge properly, indicating that this effect is probably rather small on the time scales simulated, although over the full battery’s lifetime this might be a significant factor. Alternatively, this effect could be accounted for by assuming an average value for future revenue per capacity of the cell, and adding this value to the 'pure' cost of degradation.

As stated in section 4.5, the optimal profiles from the ECM-optimisations were not considered further in this work due to inaccurate degradation predictions. The empirical degradation formula (4.4) was not suitable to predict the degradation of the cell used in this work (see section A.2), mainly because it enforces a square-root dependency on charge throughput, which is not observed in the data used in this work but which was clearly present in the data from [158][13]. It also attributes a large importance to the average SoC but for the cycles tested in the experimental data from section 1.4.3, there was very little change in the average SoC. The same is expected to happen in arbitrage: the battery will usually charge and discharge equal amounts around the average SoC, such that the detailed effect of one charging or discharging action (e.g. at which SoC to stop charging) is too small to be considered by the optimisation solver. Finally, the empirical degradation model overestimates the initial degradation. Even when the predicted degradation was divided by a factor of five (see section 4.3.1), it still overestimated the initial degradation. This meant that in the optimal profile, the battery was barely used for most of the year. Therefore, this profile was not experimentally validated. However, it is likely that if a better empirical degradation model would be used, the ECM would produce a better usage profile. Also enlarging the optimisation time horizon could improve the outcome because it would decrease the relative importance of the initial degradation.

Table 4.6 compares the results at the end of the year for the optimisation, simulation and experimental validation, for which the average of both cells in each conditions is given. The SPM$_P$ optimisation was relatively accurate for both the revenue and degradation. The

---

[13] As explained in section A.2, the ECM is included to demonstrate that taking existing models from literature and adding them to a different application gives unrealistic results due to the limitations of ECMS, namely their limited applicability to the cell and usage conditions for which they have been designed. If a fair comparison between an ECM and SPM would be the purpose, then the ECM would have to be parametrised for the cell used here, in which case it would have performed much better.

Table 4.6 Comparison of the optimisation, simulation and experimental validation after one year.

	revenue [€]			degradation [%]		
	optimisation	simulation	measured	optimisation	simulation	measured
BM_R	0.19401	0.1246	0.1168	11.8658	10.4799	14.4426
BM_P	0.1199	0.0992	0.0937	3.4412	3.0094	2.4579
SPM_P	0.1145	0.1142	0.1101	2.0259	2.7711	1.7073

BM_P and BM_R optimisations overestimated the revenue by 22% to 40% respectively, while the former overestimated degradation by 29 % and the latter underestimated degradation by 22%. The simulation could predict the revenue accurately with errors from 3% to 6%, but overestimated degradation for the SPM_P and BM_P cells by respectively 38% and 18% while underestimating it for the BM_R cells by 38%, although those large relative differences represent smaller absolute differences, of 1, 0.55, and -4 percentage points respectively. Given the accuracy of the generalised degradation model as discussed in section A.3.3, these errors could be expected.

When comparing the degradation vs. FEC shown on Fig. 4.17 with the original data from the degradation experiment with the same cell (Fig. 1.4), it can be seen that the trajectory of the SPM_P cells is lower than any of the degradation from the cycles tested. This is probably because the cycles from the SPM_P are minimising degradation (e.g. limiting the current at higher voltages) rather than being standard full charge-discharge cycles. The BM_R cell is being used similar to the cells cycled at 1C between 0% and 100% SoC at 25°C, but while the latter has only lost about 10% after 1400 FECs, the BM_R cells have lost 14%. This can be due to the higher calendar ageing experienced by the BM_R cells, which needed a full year to cover 1400 FECs while the standard-cycle cells only needed 6000 h. The degradation trends of the BM_P cells is much higher than the trend of the cells following a standard cycle of 1C between 10% and 90% SoC at 25°C. Those latter cells have lost only about 1% after 380 FECs, while the BM_P cells have lost almost 2.5% even though they also cycled at about 1C, 25°C and were limited to the middle 80% of their SoC window. Again, a possible explanation is the higher calendar ageing, given that for the same number of FECs, the cells with the standard cycle only took 2000 h to 2500 h to cover 380 FEC instead of the full year from the BM_P cells. Combining this with the observation from Fig. 4.17 that the degradation per cycle for the BM_P and BM_R cells is very similar, this would suggest that the higher calendar ageing of a cell doing fewer cycles in a reduced SoC window (such as the BM_P cells) will increase the degradation per cycle to the same level as a cell doing more cycles in the full SoC window (such as the BM_R cells), which might have more cycle but less calendar ageing.

If that conclusion is valid, and the results can be extrapolated to the future, this suggests that the BM_R cells will die quickly, mainly due to cycle ageing, while the BM_P cells will die due to a mix of cycle and calendar ageing. However, both cells will have done the same number of full equivalent cycles, again on the condition that the trends persist to the future. The BM_P cells will then be able to achieve a higher profit given that they capture a higher revenue per cycle.

The SPM_P cells outperform the BM cells due to the decreased cycle ageing, and thus the cells can do more cycles and extend their useful lifetime. While doing this, they can also increase their revenue. This is an important conclusion, falsifying the 'conventional' idea that there is a clear trade-off between making more revenue or decreasing degradation, resulting in a Pareto-front of optimal outcomes. By using more complicated models to control the battery, it seems both objectives can be achieved at the same time when compared with more simplistic models. In other words, the Pareto-front is pushed 'outward' where a better result on all individual objectives can be achieved. However, when compared with itself, there is still a trade-off: the SPM_P cells could have achieved an even larger revenue at the cost of a higher degradation (as shown by the simulations from the SPM_R profile in Appendix B) and vice versa. Therefore, the SPM cells will have a Pareto-front of their own, but every point on it will outperform the corresponding point on the Pareto-front of the BM cells.

To unlock the benefits from the SPM_P cells, a closer integration between the control system and the BMS is needed. As was done in the MTTB from section 4.7, the control unit needs to have access to the low-level data such as voltages and temperatures, rather than relying on processed information like the SoC. The reason is that calculating the SoC introduces an error, and most BMS systems will add a further safety margin to avoid overcharging or underdischarging the cells. Therefore, increasing the usable capacity as done by the SPM_P cells would not be possible if the EMS relies on this higher-level info. The same is true for limiting the temperature in the pack, and for getting the battery to the low SoC region whenever possible to reduce the calendar ageing. However, in large battery systems it might not be feasible for the controller to use this low-level data due to the sheer volume of the data. Therefore, it should be established what information the control system needs to have such that it can safely control the battery.

4.9 Conclusion

Three different battery models were used to optimise the utilisation of a battery which could trade electricity on the day-ahead market, with the goal to maximise revenue while minimising degradation. The bucket model (BM) and equivalent-circuit model (ECM) have been used in the past, but through careful formulation, the nonlinear single-particle model (SPM) could be included in the optimisation as well.

The empirical degradation model used with the ECM significantly overestimated degradation, especially in the beginning of the cell's lifetime (see sections 4.3 and A.2). This illustrates one of the main shortcomings of such models: they are not general enough to be used in different operating conditions other than the ones for which they have been designed. Therefore, the optimal profiles according to the ECM seemed suboptimal (see section 4.5), and their results were not considered in the subsequent analysis.

Cells were cycled according to the optimal profiles produced by the BM and SPM. Two BM profiles were used, one where the optimisation did not consider degradation and only maximised the revenue, and a second one where both revenue and degradation were optimised, which is called profit-maximising. Comparing the results from the four BM cells showed that with respect to time, the revenue-maximising cells degraded much faster. However, with respect to utilisation, both cells degraded at the same rate. It is suggested this was because the higher calendar ageing from the BM-cell maximising profit made up for the slightly lower cycle ageing it experienced because it could not access the highest SoC regions, unlike the revenue-maximising cells (as discussed in section 4.8). If this trend can be extrapolated to the future, it would imply that batteries controlled by a bucket model could always do the same total number of cycles, irrespective of whether they were maximising revenue or profit.

The SPM-controlled cells on the other hand experienced less degradation than the BM_P-controlled cells, both with respect to time (31%) and to utilisation (73%). It is thought this happened because the SPM successfully decreased the cycle ageing by following more complicated cycles, i.e. not simply fully charging and discharging at a constant power. The SPM also minimised calendar ageing by reducing the SoC at which the cell rested. If those trends persist, SPM-controlled cells could extend their lifetime, both in terms of time and in terms of cycles.

At the same time as reducing degradation, the SPM-controlled cells could also increase their revenue by 17% compared to the BM_P-controlled cells (over the same time period). This is due to an increase in the usable capacity of the cells: the BM will instruct to fully charge the cells at a constant power; while the SPM will reduce the power level when the cell is almost fully (dis)charged and therefore can access more of the stored energy.

To translate those gains in usable capacity to a real-world setup, a closer interaction between the BMS and the EMS is needed. In traditional battery systems, the BMS will estimate the SoC of the cell, and inform the EMS how much more energy can be stored or extracted. However, when estimating the SoC, the BMS introduces an error, which is often exacerbated by including a conservative safety margin. If this is the case, even an SPM cell cannot access the additional capacity because the BMS will block the battery from coming closer to its real limits. However, this can be overcome by a closer exchange of information between the BMS and the EMS.

4.10 Limitation and future work

Although this work aimed to quantify the economic impact of accounting for battery degradation, the amount of economic details included in the optimisation was relatively limited. Future work can expand on this by adding more realistic conditions (such as price predictions), more market rules (such as bidding into a market), and more applications (such as trading in the intra-day and real-time balancing market or delivering reserves).

A second topic for future work could be to improve the control in the realistic implementation, which was an open-loop optimisation. By adding state-estimation and parameter-estimation in a feedback loop, the optimisation could account for the real battery behaviour rather than relying on historic simulations. This leads to a closed-loop optimisation system which can account better for model errors by updating the state variables if needed, for instance to account for the real SoC at the start of the optimisation for the next day rather than assuming the batter is exactly at the SoC which the model predicted. Over time, this system could then update its parameters to reduce the model errors if they are persistent, for instance updating the nominal capacity and resistance of the cell such that the optimisation is always done for a cell of the correct size.

Controlling larger battery packs will introduce further challenges. Enforcing the safety limits, such as the minimum and maximum voltage, without limiting the usable capacity will pose challenges for the SPM control. The EMS using the SPM pushes the cells to their limits but it only models a single cell. Due to the cell-to-cell variation and imperfect balancing, the SPM might overestimate how much energy it can store in the battery. To solve this, the BMS needs to enforce less stringent limits, e.g. instead of limiting the SoC to a certain window it should only enforce the voltage limits. If the BMS then gives more information of the EMS about the battery state, the EMS can take advantage of this 'additional' capacity. This will be complicated in practice due to the inaccuracies in both the BMS and EMS combined with the hard voltage limit of the cell. A first step in this direction would be to perform the planned experiments with the MTTB to analyse the effect of the BMS's SoC estimation and safety limits (see section 4.7).

The efficiency losses of other components, such as the thermal management system and the power electronic converters, in a large-scale battery might also alter the optimal profiles. As mentioned in section 1.2.1, especially operation at low power levels will lead to significant losses. The bucket models never instruct the battery to use such power levels, but the SPM does often use low currents to get to exactly the 'best' voltage. This will probably not be done when the efficiency losses in other components are added. The effect on the revenue will be minimal due to the low energy involved. Also the effect on degradation will probably be minimal because the total battery states changes only moderately during these low-power events. For instance, resting at 2.9 V instead of 2.8 V is unlikely to accelerate degradation by a large amount.

Finally, the future work from chapter 2 will also have an impact on the optimisation and validation simulations. Inaccuracies when predicting degradation undermine the business case, and the challenge is how to decrease the errors without increasing the model complexity. Especially model selection (which degradation model to use) and automatic parameter estimation (fitting the parameters of the selected models to the data) might prove valuable.

Chapter 5

Conclusions

This work has investigated the effect of battery degradation on optimal control of batteries. This chapter summarises the contributions and conclusions of each preceding chapter in section 5.1, as well as discussing its limitations and outlining future work in section 5.2.

5.1 Contributions and conclusions

5.1.1 Battery and degradation modelling

Many different physical degradation models were implemented in one flexible framework which uses the single-particle model to simulate the cell behaviour. The degradation models can interact with each other, and it is shown that feedback loops can alter the trends predicted by the constituent models. This is in line with the findings from experimental studies reported in section 1.3, for instance the positive interaction between SEI growth and loss of active material was reported previously and is confirmed in the simulations. Some models, such as kinetically limited SEI growth, are more susceptible to such interactions than others, such as diffusion-limited SEI growth.

A second expectation from experiments is that different degradation mechanisms are enhanced by different operating conditions. The flexible simulation framework allows comparison of how different models respond to changing operating conditions, and the outcomes can aid researchers in selecting the models needed to explain the degradation trends observed in their experiments. It is also shown that a combination of various models is needed to explain trends observed in a large degradation experiment because those trends are likely to be the result of different (interacting) degradation mechanisms. However, if the operating conditions of a cell are known approximately, certain degradation mechanisms can be excluded from the model. For instance, if no low temperature or high power levels will occur, lithium plating is unlikely to have much effect.

A final conclusion was that changing the independent variable when plotting data can reveal different trends in the data. This is because certain mechanisms (and models) are mainly a function of time, while charge throughput might be more important for others.

5.1.2 Optimisation procedure

Because many physical degradation models are nonlinear, solving optimisation problems including these models is challenging. Particular attention should be paid to the formulation, both in terms of the number of variables and the complexity of the relationships between them. Chebyshev spectral methods are well suited for the spatial discretisation of the diffusion PDE because they require fewer nodes. The eigenvalue decomposition eliminates the dependencies between the concentrations at different nodes, reducing the model complexity, and introduces a perfect integrator into the model, avoiding lithium leakage. The choice of a time integration scheme is a trade-off between complexity and the number of variables, since more complicated schemes allow larger time steps. With the optimisation software used in this work, simpler schemes resulted in an easier optimisation. Multiple shooting was used to reduce the number of optimisation variables, and states were decoupled within one optimisation time step, which otherwise would increase the complexity of the model.

Existing software was used to calculate the derivatives and Jacobians of the model. ADOL-C and ColPack use automatic differentiation, which requires a large upfront calculation to generate the derivative functions before the optimisation starts. During the optimisation these functions only need to be evaluated, limiting the computational cost. IPOPT is used to optimise the resulting model, and succeeds to find optimal outcomes from a variety of different starting points.

5.1.3 Economic effects

The economic impact of degradation predictions of three different models was studied by using the different battery models to decide how to control a battery which trades electricity on the wholesale market for one year. It was shown that the empirical degradation model used with the equivalent-circuit model is not general enough to produce a sensible outcome. It predicted a very fast initial degradation, which caused problems due to the limited time horizon in the optimisation.

The optimal use profiles according to three optimisation approaches were experimentally validated: the linear bucket model maximising revenue (i.e. ignoring degradation), BM_R, the same linear bucket model maximising revenue while minimising degradation (i.e. maximising net profit), BM_P, and the single-particle model also maximising revenue while minimising degradation (i.e. maximising net profit), SPM_P. Two cells have been cycled for one year according to each profile. When comparing the results over the same time period, the revenue-maximising cells degraded significantly faster, and the SPM_P cells degraded 31% less than the BM_P cells, while increasing the revenue by 17%.

This changed when the results were compared over the same number of full equivalent cycles. Then all BM-cells degraded at the same rate, indicating that the BM_P cells may have the same useful lifetime (i.e. number of cycles over their lifetime) as the BM_R cells. This is suggested to be because the higher cycle ageing experienced by BM_R cells is compensated by a higher calendar ageing for the BM_P cells, which take more time to cover the same number of cycles. The SPM_P cells outperformed all the BM cells, and their degradation was 73% lower than the BM cells. This is because the cycles undertaken by the SPM_P cells were not simply full charge-discharge cycles, but instead they were more complicated cycles which minimised the cycle ageing such that the cells experienced less degradation per full equivalent cycle than a simple full charge-discharge cycle.

Most importantly, the experimental results confirmed what was found in the simulations: the SPM-control was able to simultaneously increase revenue and decrease degradation compared to the traditional BM-control. Often, the trade-off between revenue and degradation is seen as a multi-objective optimisation problem with a resulting optimal pareto-front. Using a physics-based battery degradation model can therefore push the pareto-front ‘outwards’, achieving a better result on both objectives. Over the same time period, the SPM_P cells increased revenue by 31% and decreased degradation by 17% with respect to the BM_P cells.

To achieve these benefits in a real battery, a closer interaction between the battery management system and the battery controller is needed. It was demonstrated such a setup is possible, and a real-time controller can track the optimal profiles for an entire module as long as it has access to low-level operational data.

5.2 Limitations and future work

5.2.1 Battery and degradation modelling

The single-particle model (SPM) was used throughout this work. Although it models the basic physical processes of a Li-ion battery, it makes a number of simplifications. The SPM is only valid at low currents, so this model cannot be used for certain applications such as fast charging. Secondly, the SPM assumes the entire cell behaves uniformly and localised effects (e.g. inhomogeneities and diffusion-induced lithium plating) cannot be simulated. Using the P2D model might alleviate some of those limitations although the computational complexity of the P2D model would pose problems for degradation simulations and optimal control. Similar comments can be made about the bulk thermal model used with the SPM. It ignores temperature gradients, which can cause volume expansions and thermally-induced crack growth as well as enhancing other inhomogeneous behaviour such as the current density. More spatially-resolved thermal models might give insights into those phenomena, which to date are often ignored.

The degradation models are all simplifications compared to the complex processes taking place inside a battery. Therefore, many effects cannot be included and the models might instill a false confidence in their ‘physical’ nature. Even if they can correctly predict the observed data, it does not mean the underlying equations are correct and they might predict wrong degradation in other cases.

A final area for future research is the parameterisation and model selection of the various degradation models. The models have a large number of parameters and fitting simulations to experimental data is non trivial, especially when multiple degradation models are combined. A first attempt could be made with conventional optimisation methods which find the ‘optimal’ values of the parameters by minimising some error function. This optimisation is very different from the one in this work since it involves a small number of variables, but evaluating the objective function is very expensive, and calculating derivatives is almost impossible.

5.2.2 Optimisation procedure

Even though the optimisation procedure succeeded in optimising the nonlinear model, it had four limitations. First of all, only SEI growth was included. Adding more degradation models might prove more complicated because this might couple different battery states together.

The procedure limited the applications that can be considered due to two more simplifications. The software requires a continuous model, which limits the possible applications, especially those where batteries can either commit or not (e.g. delivering primary or secondary frequency reserves). Secondly, the temporal decoupling will introduce larger errors for very dynamic use cases. This again might prove to be a problem when considering applications such as frequency control.

Finally, the optimisation was only successful over a maximum time horizon of a few days. This is problematic for certain degradation models (such as the empirical degradation models used with the equivalent-circuit model), certain use cases (such as investment decisions), and it ignores long-term effects of degradation (such as lost future revenue).

5.2.3 Economic effects

All the previously mentioned limitations have a knock on effect on the economic results. The limitations with the battery and degradation model will lead to suboptimal outcomes and over- or underestimation of the revenue and degradation, and the limitations with the optimisation procedure constrain the economic detail which can be included.

Adding more detail about the operation of large-scale batteries will ensure more realistic outcomes. Especially scaling the model up from one cell to a whole battery system will add value. As mentioned in section 1.2.1, losses in other parts of the battery such as the power electronic converter and thermal management system often outweigh losses in the cells. Especially at low power levels, this reduces the efficiency of the total system dramatically. The optimal profile according to the physics-based model did spend most time at low power levels to reduce degradation and to ensure the cell is exactly at the ‘best’ voltage during resting periods. When the efficiency of other components is added, this optimal profile will probably change. Secondly, thermal gradients in a large batteries will lead to different characteristics and ageing in different parts of the battery. This can also affect the optimal profile, for instance by avoiding high SoC resting even more to not damage the cells in the hot part of the battery. Thirdly, cell-to-cell variations will have a similar effect as the thermal gradients. Given that the capacity of a series string is limited by the smallest cells, the interplay between the cell-to-cell variation, the pack design and the balancing circuit might alter the optimal profiles to remove stressful operations from the smallest cell.

A second avenue for future work focusses more on the economic aspects. They were mostly ignored in this work, but market rules will alter the optimal profiles. Some applications, such as frequency control, require the commitment of power or capacity in advance, while the exact delivery is unknown. Such multi-stage processes might seriously affect how a battery should be used due to the uncertainty when deciding in the first stage. On the other hand, a battery might give a trader more flexibility in dealing with the uncertainty. Especially for applications like the real-time balancing market this might prove interesting.

Finally, the real-time control of the battery needs further development. To ensure the benefits from the advanced optimisation models can be realised, a closer interaction between the battery management system and the control system is needed. The first steps were made in this work, but more work is needed, for instance in state estimation and data management.

References

[1] C. Doetsch, B. Droste-Franke, G. Mulder, Y. Scholz, and M. Perrin, “Electric energy storage - future energy storage demand,” International Energy Agency, Tech. Rep. January, 2015.

[2] B. Zakeri and S. Syri, “Electrical energy storage systems: A comparative life cycle cost analysis,” *Renewable and Sustainable Energy Reviews*, vol. 42, pp. 569–596, Feb. 2015.

[3] B. Battke and T. S. Schmidt, “Cost-efficient demand-pull policies for multi-purpose technologies – the case of stationary electricity storage,” *Applied Energy*, vol. 155, pp. 334–348, Oct. 2015.

[4] H. Hesse, M. Schimpe, D. Kucevic, and A. Jossen, “Lithium-ion battery storage for the grid—a review of stationary battery storage system design tailored for applications in modern power grids,” *Energies*, vol. 10, no. 12, p. 2107, Dec. 2017.

[5] E. Lemaire, N. Martin, P. Nørgård, E. De Jong, R. De Graaf, J. Groenewegen, E. Kolentini, and S. Tselepis, “European white book on grid-connected storage,” European Distributed Energy Resources Laboratories, Tech. Rep., 2011.

[6] A. Zucker, T. Hinchliffe, and A. Spisto, “Assessing storage value in electricity markets, a literature review,” European Commission, Joint Research Centre, Tech. Rep., 2013.

[7] EPRI, “Electricity energy storage technology options, a white paper primer on applications, costs, and benefits,” Electric power research institute, Palo Alto, CA, US, Tech. Rep., 2010.

[8] I. Gyuk and S. Eckroad, “Epri-doe handbook of energy storage for transmission & distribution applications,” Electric power research institute, US Department of Energy, Tech. Rep. December, 2003.

[9] M. Kintner-Meyer, M. Elizondo, P. Balducci, C. Jin, T. Nguyen, F. Tuffner, and X. Guo, “Energy storage for power systems applications: a regional assessment for the northwest power pool (nwpp),” US Department of Energy, Pacific Northwest National Laboratory, Tech. Rep. April, 2010.

[10] M. Müller, “Stationary lithium-ion battery energy storage systems a multi-purpose technology,” Ph.D. dissertation, TU Munich, 2018.

[11] A. Perez, R. Moreno, R. Moreira, M. Orchard, and G. Strbac, “Effect of battery degradation on multi-service portfolios of energy storage,” *IEEE Transactions on Sustainable Energy*, vol. 7, no. 4, pp. 1718 – 1729, 2016.

[12] T. Brijs, “Electricity storage participation and modeling in short-term electricity markets,” Ph.D. dissertation, KU Leuven, 2017.

[13] R. Moreira, R. Moreno, and G. Strbac, “Synergies and conflicts among energy storage services,” in *2016 IEEE International Energy Conference (ENERGYCON).* IEEE, Apr. 2016, pp. 1–6.

[14] R. Lee, S. Homan, N. Mac Dowell, and S. Brown, “A closed-loop analysis of grid scale battery systems providing frequency response and reserve services in a variable inertia grid,” *Applied Energy*, vol. 236, pp. 961–972, Feb. 2019.

[15] A. Solomon, D. M. Kammen, and D. Callaway, “The role of large-scale energy storage design and dispatch in the power grid: A study of very high grid penetration of variable renewable resources,” *Applied Energy*, vol. 134, pp. 75–89, Dec. 2014.

[16] D. Greenwood, K. Lim, C. Patsios, P. Lyons, Y. Lim, and P. Taylor, “Frequency response services designed for energy storage,” *Applied Energy*, vol. 203, pp. 115–127, Oct. 2017.

[17] B. Mantar Gundogdu, S. Nejad, D. T. Gladwin, M. P. Foster, and D. A. Stone, “A battery energy management strategy for u.k. enhanced frequency response and triad avoidance,” *IEEE Transactions on Industrial Electronics*, vol. 65, no. 12, pp. 9509–9517, Dec. 2018.

[18] B. Battke, T. S. Schmidt, D. Grosspietsch, and V. H. Hoffmann, “A review and probabilistic model of lifecycle costs of stationary batteries in multiple applications,” *Renewable and Sustainable Energy Reviews*, vol. 25, pp. 240–250, Sep. 2013.

[19] R. Dufo-López and J. L. Bernal-Agustín, “Techno-economic analysis of grid-connected battery storage,” *Energy Conversion and Management*, vol. 91, pp. 394–404, Feb. 2015.

[20] M. Hiremath, K. Derendorf, and T. Vogt, “Comparative life cycle assessment of battery storage systems for stationary applications,” *Environmental Science & Technology*, vol. 49, no. 8, pp. 4825–4833, Apr. 2015.

[21] J. D. Bishop, C. J. Axon, D. Bonilla, and D. Banister, “Estimating the grid payments necessary to compensate additional costs to prospective electric vehicle owners who provide vehicle-to-grid ancillary services,” *Energy*, vol. 94, pp. 715–727, Jan. 2016.

[22] R. L. Fares and M. E. Webber, “A flexible model for economic operational management of grid battery energy storage,” *Energy*, vol. 78, pp. 768–776, Dec. 2014.

[23] M. Ippolito, S. Favuzza, E. Sanseverino, E. Telaretti, and G. Zizzo, “Economic feasibility of a customer-side energy storage in the italian electricity market,” in *2015 IEEE 15th International Conference on Environment and Electrical Engineering (EEEIC).* IEEE, Jun. 2015, pp. 938–943.

[24] K. Uddin, R. Gough, J. Radcliffe, J. Marco, and P. Jennings, “Techno-economic analysis of the viability of residential photovoltaic systems using lithium-ion batteries for energy storage in the united kingdom,” *Applied Energy*, vol. 206, pp. 12–21, 2017.

[25] G. Zubi, R. Dufo-López, M. Carvalho, and G. Pasaoglu, “The lithium-ion battery: State of the art and future perspectives,” *Renewable and Sustainable Energy Reviews*, vol. 89, pp. 292–308, Jun. 2018.

[26] B. Nykvist and M. Nilsson, “Rapidly falling costs of battery packs for electric vehicles,” *Nature Climate Change*, vol. 5, no. 4, pp. 329–332, Mar. 2015.

[27] B. Nykvist, F. Sprei, and M. Nilsson, “Assessing the progress toward lower priced long range battery electric vehicles,” *Energy Policy*, vol. 124, pp. 144–155, Jan. 2019.

[28] K. Uddin, M. Dubarry, and M. B. Glick, “The viability of vehicle-to-grid operations from a battery technology and policy perspective,” *Energy Policy*, vol. 113, pp. 342–347, Feb. 2018.

[29] EA Technology, “A good practice guide on electrical energy storage,” Energy storage operators forum, Tech. Rep., 2014.

[30] P. Papadopoulos, A. Laguna-Estopier, and I. Cooper, “Smarter network storage,” UK Power Networks, London, Tech. Rep., 2016.

[31] J. V. Barreras, “Practical methods in li-ion batteries for simplified modeling, battery electric vehicle design, battery management system testing and balancing system control,” Ph.D. dissertation, Aalborg university, 2017.

[32] D. F. Frost and D. A. Howey, “Completely decentralized active balancing battery management system,” *IEEE Transactions on Power Electronics*, vol. 33, no. 1, pp. 729–738, Jan. 2018.

[33] C. Patsios, B. Wu, E. Chatzinikolaou, D. J. Rogers, N. Wade, N. P. Brandon, and P. Taylor, “An integrated approach for the analysis and control of grid connected energy storage systems,” *Journal of Energy Storage*, vol. 5, pp. 48–61, 2016.

[34] M. Schimpe, “System simulation of utility-scale lithium-ion battery energy storage systems,” Ph.D. dissertation, TU Munich, 2019.

[35] M. Schimpe, C. N. Truong, M. Naumann, A. Jossen, H. C. Hesse, J. M. Reniers, and D. A. Howey, “Marginal costs of battery system operation in energy arbitrage based on energy losses and cell degradation,” in *2018 IEEE International Conference on Environment and Electrical Engineering and 2018 IEEE Industrial and Commercial Power Systems Europe (EEEIC / I&CPS Europe)*. IEEE, Jun. 2018, pp. 1–5.

[36] M. Schimpe, M. Naumann, N. Truong, H. C. Hesse, S. Santhanagopalan, A. Saxon, and A. Jossen, “Energy efficiency evaluation of a stationary lithium-ion battery container storage system via electro-thermal modeling and detailed component analysis,” *Applied Energy*, vol. 210, no. November 2017, pp. 211–229, 2018. [Online]. Available: https://doi.org/10.1016/j.apenergy.2017.10.129

[37] T. B. Reddy and D. Linden, Eds., *Linden’s handbook of batteries*, 4th ed. McGraw-Hill, 2011.

[38] C. Julien, A. Mauger, K. Zaghib, and H. Groult, “Comparative issues of cathode materials for li-ion batteries,” *Inorganics*, vol. 2, no. 1, pp. 132–154, Mar. 2014.

[39] M. D. Radin, S. Hy, M. Sina, C. Fang, H. Liu, J. Vinckeviciute, M. Zhang, M. S. Whittingham, Y. S. Meng, and A. Van der Ven, "Narrowing the gap between theoretical and practical capacities in li-ion layered oxide cathode materials," *Advanced Energy Materials*, vol. 7, no. 20, p. 1602888, Oct. 2017.

[40] M. Dubarry, N. Qin, and P. Brooker, "Calendar aging of commercial li-ion cells of different chemistries – a review," *Current Opinion in Electrochemistry*, vol. 9, pp. 106–113, Jun. 2018.

[41] R. Benato, S. Dambone Sessa, M. Musio, F. Palone, and R. Polito, "Italian experience on electrical storage ageing for primary frequency regulation," *Energies*, vol. 11, no. 8, p. 2087, Aug. 2018.

[42] J. Vetter, P. Novák, M. Wagner, C. Veit, K.-C. Möller, J. Besenhard, M. Winter, M. Wohlfahrt-Mehrens, C. Vogler, and A. Hammouche, "Ageing mechanisms in lithium-ion batteries," *Journal of Power Sources*, vol. 147, no. 1-2, pp. 269–281, Sep. 2005.

[43] E. Sarasketa-Zabala, F. Aguesse, I. Villarreal, L. M. Rodriguez-Martinez, C. M. López, and P. Kubiak, "Understanding lithium inventory loss and sudden performance fade in cylindrical cells during cycling with deep-discharge steps," *The Journal of Physical Chemistry C*, vol. 119, no. 2, pp. 896–906, Jan. 2015.

[44] V. A. Agubra and J. W. Fergus, "The formation and stability of the solid electrolyte interface on the graphite anode," *Journal of Power Sources*, vol. 268, pp. 153–162, Dec. 2014.

[45] M. Gauthier, T. J. Carney, A. Grimaud, L. Giordano, N. Pour, H.-H. Chang, D. P. Fenning, S. F. Lux, O. Paschos, C. Bauer, F. Maglia, S. Lupart, P. Lamp, and Y. Shao-Horn, "Electrode–electrolyte interface in li-ion batteries: Current understanding and new insights," *The Journal of Physical Chemistry Letters*, vol. 6, no. 22, pp. 4653–4672, Nov. 2015.

[46] P. Lu, C. Li, E. W. Schneider, and S. J. Harris, "Chemistry, impedance, and morphology evolution in solid electrolyte interphase films during formation in lithium ion batteries," *Journal of Physical Chemistry C*, vol. 118, no. 2, pp. 896–903, 2014.

[47] P. Verma, P. Maire, and P. Novák, "A review of the features and analyses of the solid electrolyte interphase in li-ion batteries," *Electrochimica Acta*, vol. 55, no. 22, pp. 6332–6341, Sep. 2010.

[48] Z. Zhuo, P. Lu, C. Delacourt, R. Qiao, K. Xu, F. Pan, S. J. Harris, and W. Yang, "Breathing and oscillating growth of solid-electrolyte-interphase upon electrochemical cycling," *Chemical Communications*, vol. 54, no. 7, pp. 814–817, 2018.

[49] M. R. Palacín, "Understanding ageing in li-ion batteries: a chemical issue," *Chemical Society Reviews*, vol. 47, no. 13, pp. 4924–4933, 2018.

[50] G. Sarre, P. Blanchard, and M. Broussely, "Aging of lithium-ion batteries," *Journal of Power Sources*, vol. 127, no. 1-2, pp. 65–71, Mar. 2004.

[51] M. Broussely, P. Biensan, F. Bonhomme, P. Blanchard, S. Herreyre, K. Nechev, and R. Staniewicz, “Main aging mechanisms in li ion batteries,” *Journal of Power Sources*, vol. 146, no. 1-2, pp. 90–96, Aug. 2005.

[52] S. F. Schuster, T. Bach, E. Fleder, J. Müller, M. Brand, G. Sextl, and A. Jossen, “Nonlinear aging characteristics of lithium-ion cells under different operational conditions,” *Journal of Energy Storage*, vol. 1, no. 1, pp. 44–53, Jun. 2015.

[53] A. Barré, B. Deguilhem, S. Grolleau, M. Gérard, F. Suard, and D. Riu, “A review on lithium-ion battery ageing mechanisms and estimations for automotive applications,” *Journal of Power Sources*, vol. 241, pp. 680–689, 2013.

[54] M. Broussely, S. Herreyre, P. Biensan, P. Kasztejna, K. Nechev, and R. Staniewicz, “Aging mechanism in li ion cells and calendar life predictions,” *Journal of Power Sources*, vol. 97-98, pp. 13–21, Jul. 2001.

[55] P. Bernard, H. Martinez, C. Tessier, E. Garitte, S. Franger, and R. Dedryvere, “Role of negative electrode porosity in long-term aging of nmc//graphite li-ion batteries,” *Journal of The Electrochemical Society*, vol. 162, no. 13, pp. A7096–A7103, Sep. 2015.

[56] R. Narayanrao, M. M. Joglekar, and S. Inguva, “A phenomenological degradation model for cyclic aging of lithium ion cell materials,” *Journal of the Electrochemical Society*, vol. 160, no. 1, pp. A125–A137, Nov. 2013.

[57] R. Sahore, D. C. O’Hanlon, A. Tornheim, C.-W. Lee, J. C. Garcia, H. Iddir, M. Balasubramanian, and I. Bloom, “Revisiting the Mechanism Behind Transition-Metal Dissolution from Delithiated LiNi x Mn y Co z O 2 (NMC) Cathodes,” *Journal of The Electrochemical Society*, vol. 167, no. 2, p. 020513, January 2020. [Online]. Available: https://iopscience.iop.org/article/10.1149/1945-7111/ab6826

[58] T. Waldmann, B.-I. Hogg, M. Kasper, S. Grolleau, C. G. Couceiro, K. Trad, B. P. Matadi, and M. Wohlfahrt-Mehrens, “Interplay of operational parameters on lithium deposition in lithium-ion cells: Systematic measurements with reconstructed 3-electrode pouch full cells,” *Journal of The Electrochemical Society*, vol. 163, no. 7, pp. A1232–A1238, Apr. 2016.

[59] S. Müller, J. Eller, M. Ebner, C. Burns, J. Dahn, and V. Wood, “Quantifying inhomogeneity of lithium ion battery electrodes and its influence on electrochemical performance,” *Journal of The Electrochemical Society*, vol. 165, no. 2, pp. A339–A344, Jan. 2018.

[60] Q. Liu, C. Du, B. Shen, P. Zuo, X. Cheng, Y. Ma, G. Yin, and Y. Gao, “Understanding undesirable anode lithium plating issues in lithium-ion batteries,” *RSC Advances*, vol. 6, no. 91, pp. 88 683–88 700, 2016.

[61] T. Waldmann, B.-I. Hogg, and M. Wohlfahrt-Mehrens, “Li plating as unwanted side reaction in commercial li-ion cells – a review,” *Journal of Power Sources*, vol. 384, pp. 107–124, Apr. 2018.

[62] A. M. Grillet, T. Humplik, E. K. Stirrup, S. A. Roberts, D. A. Barringer, C. M. Snyder, M. R. Janvrin, and C. A. Apblett, "Conductivity degradation of polyvinylidene fluoride composite binder during cycling: Measurements and simulations for lithium-ion batteries," *Journal of The Electrochemical Society*, vol. 163, no. 9, pp. A1859–A1871, Jul. 2016.

[63] B. Stiaszny, J. C. Ziegler, E. E. Krauß, M. Zhang, J. P. Schmidt, and E. Ivers-Tiffée, "Electrochemical characterization and post-mortem analysis of aged limn 2o4-nmc/graphite lithium ion batteries part ii: Calendar aging," *Journal of Power Sources*, vol. 258, pp. 61–75, 2014.

[64] C. Kupper, B. Weißhar, S. Rißmann, and W. G. Bessler, "End-of-life prediction of a lithium-ion battery cell based on mechanistic aging models of the graphite electrode," *Journal of The Electrochemical Society*, vol. 165, no. 14, pp. A3468–A3480, Nov. 2018.

[65] S. J. Harris and P. Lu, "Effects of inhomogeneities -nanoscale to mesoscale -on the durability of li-ion batteries," *Journal of Physical Chemistry C*, vol. 117, no. 13, pp. 6481–6492, 2013.

[66] D. Burow, K. Sergeeva, S. Calles, K. Schorb, A. Börger, C. Roth, and P. Heitjans, "Inhomogeneous degradation of graphite anodes in automotive lithium ion batteries under low-temperature pulse cycling conditions," *Journal of Power Sources*, vol. 307, pp. 806–814, Mar. 2016.

[67] M. Klett, R. Eriksson, J. Groot, P. Svens, K. Ciosek Högström, R. W. Lindström, H. Berg, T. Gustafson, G. Lindbergh, and K. Edström, "Non-uniform aging of cycled commercial lifepo4//graphite cylindrical cells revealed by post-mortem analysis," *Journal of Power Sources*, vol. 257, pp. 126–137, Jul. 2014.

[68] T. C. Bach, S. F. Schuster, E. Fleder, J. Müller, M. J. Brand, H. Lorrmann, A. Jossen, and G. Sextl, "Nonlinear aging of cylindrical lithium-ion cells linked to heterogeneous compression," *Journal of Energy Storage*, vol. 5, pp. 212–223, 2016.

[69] K. Jalkanen, J. Karppinen, L. Skogström, T. Laurila, M. Nisula, and K. Vuorilehto, "Cycle aging of commercial nmc/graphite pouch cells at different temperatures," *Applied Energy*, vol. 154, pp. 160–172, Sep. 2015.

[70] A. Ahmadian, M. Sedghi, A. Elkamel, M. Fowler, and M. Aliakbar Golkar, "Plug-in electric vehicle batteries degradation modeling for smart grid studies: Review, assessment and conceptual framework," *Renewable and Sustainable Energy Reviews*, vol. 81, pp. 2609–2624, Jan. 2018.

[71] S. Schindler, M. Bauer, H. Cheetamun, and M. A. Danzer, "Fast charging of lithium-ion cells: Identification of aging-minimal current profiles using a design of experiment approach and a mechanistic degradation analysis," *Journal of Energy Storage*, vol. 19, pp. 364–378, Oct. 2018.

[72] European Commission, "Mat4bat," 2016. [Online]. Available: http://cordis.europa.eu/project/rcn/109052{_}en.html

[73] Kokam, “Kokam li-ion / polymer cell,” 2016. [Online]. Available: http://kokam.com/wp-content/uploads/2016/03/SLPB-Cell-Brochure.pdf

[74] C. R. Birkl, M. R. Roberts, E. McTurk, P. G. Bruce, and D. A. Howey, “Degradation diagnostics for lithium ion cells,” *Journal of Power Sources*, vol. 341, pp. 373–386, Feb. 2017.

[75] A. Awarke, M. Jaeger, O. Oezdemir, and S. Pischinger, “Thermal analysis of a li-ion battery module under realistic ev operating conditions,” *International Journal of Energy Research*, vol. 37, no. 6, pp. 617–630, May 2013.

[76] B. P. Matadi, S. Geniès, A. Delaille, T. Waldmann, M. Kasper, M. Wohlfahrt-Mehrens, F. Aguesse, E. Bekaert, I. Jiménez-Gordon, L. Daniel, X. Fleury, M. Bardet, J.-F. Martin, and Y. Bultel, “Effects of biphenyl polymerization on lithium deposition in commercial graphite/nmc lithium-ion pouch-cells during calendar aging at high temperature,” *Journal of The Electrochemical Society*, vol. 164, no. 6, pp. A1089–A1097, Mar. 2017.

[77] A. Iturrondobeitia, “Post-mortem analysis of commercial nmc/graphite li-ion pouch cells within mat4bat european project,” in *18th International Meeting on Lithium Batteries (June 19-24, 2016).* Chicago: ECS, 2016.

[78] A. Iturrondobeitia, F. Aguesse, S. Genies, T. Waldmann, M. Kasper, N. Ghanbari, M. Wohlfahrt-Mehrens, and E. Bekaert, “Post-mortem analysis of calendar-aged 16 ah nmc/graphite pouch cells for ev application,” *The Journal of Physical Chemistry C*, vol. 121, no. 40, pp. 21 865–21 876, Oct. 2017.

[79] N. Ghanbari, T. Waldmann, M. Kasper, P. Axmann, and M. Wohlfahrt-Mehrens, “Detection of li deposition by glow discharge optical emission spectroscopy in post-mortem analysis,” *ECS Electrochemistry Letters*, vol. 4, no. 9, pp. A100–A102, Jul. 2015.

[80] N. Ghanbari, T. Waldmann, M. Kasper, P. Axmann, and M. Wohlfahrt-Mehrens, “Inhomogeneous degradation of graphite anodes in li-ion cells: A postmortem study using glow discharge optical emission spectroscopy (gd-oes),” *The Journal of Physical Chemistry C*, vol. 120, no. 39, pp. 22 225–22 234, Oct. 2016.

[81] J. M. Reniers, G. Mulder, and D. A. Howey, “Review and performance comparison of mechanical-chemical degradation models for lithium-ion batteries,” *Journal of The Electrochemical Society*, vol. 166, no. 14, pp. A3189–A3200, Sep. 2019.

[82] K. Persson, V. A. Sethuraman, L. J. Hardwick, Y. Hinuma, Y. S. Meng, A. van der Ven, V. Srinivasan, R. Kostecki, and G. Ceder, “Lithium diffusion in graphitic carbon,” *The Journal of Physical Chemistry Letters*, vol. 1, no. 8, pp. 1176–1180, Apr. 2010.

[83] A. Von Wald Cresce, O. Borodin, and K. Xu, “Correlating li+ solvation sheath structure with interphasial chemistry on graphite,” *Journal of Physical Chemistry C*, vol. 116, no. 50, pp. 26 111–26 117, 2012.

[84] P. Bai, D. A. Cogswell, and M. Z. Bazant, “Suppression of phase separation in lifepo4 nanoparticles during battery discharge,” *Nano Letters*, vol. 11, no. 11, pp. 4890–4896, 2011.

[85] A. Latz, T. Danner, B. Horstmann, and T. Jahnke, “Microstructure- and theory-based modeling and simulation of batteries and fuel cells,” *Chemie-Ingenieur-Technik*, vol. 91, no. 6, pp. 758–768, 2019.

[86] M. Doyle, T. F. Fuller, and J. Newman, “Modeling of galvanostatic charge and discharge of the lithium/polymer/insertion cell,” *Journal of The Electrochemical Society*, vol. 140, no. 6, p. 1526, 1993.

[87] M. T. Lawder, B. Suthar, P. W. C. Northrop, S. De, C. M. Hoff, O. Leitermann, M. L. Crow, S. Santhanagopalan, and V. R. Subramanian, “Battery energy storage system (bess) and battery management system (bms) for grid-scale applications,” *Proceedings of the IEEE*, vol. 102, no. 6, pp. 1014–1030, Jun. 2014.

[88] A. Jokar, B. Rajabloo, M. Désilets, and M. Lacroix, “Review of simplified pseudo-two-dimensional models of lithium-ion batteries,” *Journal of Power Sources*, vol. 327, pp. 44–55, Sep. 2016.

[89] S. G. Marquis, V. Sulzer, R. Timms, C. P. Please, and S. J. Chapman, “An Asymptotic Derivation of a Single Particle Model with Electrolyte,” *Journal of The Electrochemical Society*, vol. 166, no. 15, pp. A3693–A3706, nov 2019.

[90] S. J. Moura, F. B. Argomedo, R. Klein, A. Mirtabatabaei, and M. Krstic, “Battery state estimation for a single particle model with electrolyte dynamics,” *IEEE Transactions on Control Systems Technology*, vol. 25, no. 2, pp. 453–468, Mar. 2017.

[91] S. Atlung, K. West, and T. Jacobsen, “Dynamic aspects of solid solution cathodes for electrochemical power sources,” *Journal of The Electrochemical Society*, vol. 126, no. 8, p. 1311, 1979.

[92] B. S. Haran, B. N. Popov, and R. E. White, “Theoretical analysis of metal hydride electrodes,” *Journal of The Electrochemical Society*, vol. 145, no. 12, p. 4082, 1998.

[93] B. S. Haran, B. N. Popov, and R. E. White, “Determination of the hydrogen diffusion coefficient in metal hydrides by impedance spectroscopy,” *Journal of Power Sources*, vol. 75, no. 1, pp. 56–63, Sep. 1998.

[94] P. Ramadass, B. Haran, P. M. Gomadam, R. White, and B. N. Popov, “Development of first principles capacity fade model for li-ion cells,” *Journal of The Electrochemical Society*, vol. 151, no. 2, p. A196, 2004.

[95] G. Ning and B. N. Popov, “Cycle life modeling of lithium-ion batteries,” *Journal of The Electrochemical Society*, vol. 151, no. 10, p. A1584, 2004.

[96] S. Santhanagopalan, Q. Guo, P. Ramadass, and R. E. White, “Review of models for predicting the cycling performance of lithium ion batteries,” *Journal of Power Sources*, vol. 156, no. 2, pp. 620–628, Jun. 2006.

[97] M. Guo, G. Sikha, and R. E. White, “Single-particle model for a lithium-ion cell: Thermal behavior,” *Journal of The Electrochemical Society*, vol. 158, no. 2, p. A122, 2011.

[98] Y. Dai, L. Cai, and R. E. White, “Simulation and analysis of stress in a li-ion battery with a blended limn 2 o 4 and lini 0.8 co 0.15 al 0.05 o 2 cathode,” *Journal of Power Sources*, vol. 247, pp. 365–376, Feb. 2014.

[99] B. Wu and W. Lu, “Mechanical-electrochemical modeling of agglomerate particles in lithium-ion battery electrodes,” *Journal of The Electrochemical Society*, vol. 163, no. 14, pp. A3131–A3139, 2016.

[100] B. Wu and W. Lu, “A battery model that fully couples mechanics and electrochemistry at both particle and electrode levels by incorporation of particle interaction,” *Journal of Power Sources*, vol. 360, pp. 360–372, Aug. 2017.

[101] J. Li, N. Lotfi, R. G. Landers, and J. Park, “A single particle model for lithium-ion batteries with electrolyte and stress-enhanced diffusion physics,” *Journal of The Electrochemical Society*, vol. 164, no. 4, pp. A874–A883, Feb. 2017.

[102] R. Fu, M. Xiao, and S.-Y. Choe, “Modeling, validation and analysis of mechanical stress generation and dimension changes of a pouch type high power li-ion battery,” *Journal of Power Sources*, vol. 224, pp. 211–224, Feb. 2013.

[103] I. Laresgoiti, S. Käbitz, M. Ecker, and D. U. Sauer, “Modeling mechanical degradation in lithium ion batteries during cycling: Solid electrolyte interphase fracture,” *Journal of Power Sources*, vol. 300, pp. 112–122, Dec. 2015.

[104] J. de Hoog, J.-M. Timmermans, D. Ioan-Stroe, M. Swierczynski, J. Jaguemont, S. Goutam, N. Omar, J. Van Mierlo, and P. Van Den Bossche, “Combined cycling and calendar capacity fade modeling of a nickel-manganese-cobalt oxide cell with real-life profile validation,” *Applied Energy*, vol. 200, pp. 47–61, Aug. 2017.

[105] M. Petit, E. Prada, and V. Sauvant-Moynot, “Development of an empirical aging model for li-ion batteries and application to assess the impact of vehicle-to-grid strategies on battery lifetime,” *Applied Energy*, vol. 172, pp. 398–407, 2016.

[106] J. Reniers, G. Mulder, S. Ober-Blöbaum, and D. Howey, “Improving optimal control of grid-connected lithium-ion batteries through more accurate battery and degradation modelling,” *Journal of Power Sources*, vol. 379, 2018.

[107] M. Schimpe, M. E. von Kuepach, M. Naumann, H. C. Hesse, K. Smith, and A. Jossen, “Comprehensive modeling of temperature-dependent degradation mechanisms in lithium iron phosphate batteries,” *Journal of The Electrochemical Society*, vol. 165, no. 2, pp. A181–A193, Jan. 2018.

[108] K. Smith, A. Saxon, M. Keyser, B. Lundstrom, Ziwei Cao, and A. Roc, “Life prediction model for grid-connected li-ion battery energy storage system,” in *2017 American Control Conference (ACC)*. IEEE, May 2017, pp. 4062–4068.

[109] D. U. Sauer and H. Wenzl, “Comparison of different approaches for lifetime prediction of electrochemical systems-using lead-acid batteries as example,” *Journal of Power Sources*, vol. 176, no. 2, pp. 534–546, 2008.

[110] C. Su and H. J. Chen, “A review on prognostics approaches for remaining useful life of lithium-ion battery,” *IOP Conference Series: Earth and Environmental Science*, vol. 93, no. 1, 2017.

[111] K. Goebel, B. Saha, A. Saxena, J. Celaya, and J. Christophersen, “Prognostics in battery health management,” *IEEE Instrumentation & Measurement Magazine*, vol. 11, no. 4, pp. 33–40, Aug. 2008.

[112] A. A. Hussein, “Capacity fade estimation in electric vehicle li-ion batteries using artificial neural networks,” *IEEE Transactions on Industry Applications*, vol. 51, no. 3, pp. 2321–2330, May 2015.

[113] J. Snoek, H. Larochelle, and R. P. Adams, “Practical bayesian optimization of machine learning algorithms,” in *Advances in Neural Information Processing Systems 25*, F. Pereira, C. J. C. Burges, L. Bottou, and K. Q. Weinberger, Eds. Curran Associates, Inc., 2012, pp. 2951–2959.

[114] A. Nuhic, T. Terzimehic, T. Soczka-Guth, M. Buchholz, and K. Dietmayer, “Health diagnosis and remaining useful life prognostics of lithium-ion batteries using data-driven methods,” *Journal of Power Sources*, vol. 239, pp. 680–688, Oct. 2013.

[115] J. Zhang and J. Lee, “A review on prognostics and health monitoring of li-ion battery,” *Journal of Power Sources*, vol. 196, no. 15, pp. 6007–6014, Aug. 2011.

[116] W. A. Appiah, J. Park, S. Byun, M.-H. Ryou, and Y. M. Lee, “A mathematical model for cyclic aging of spinel limn 2 o 4 /graphite lithium-ion cells,” *Journal of The Electrochemical Society*, vol. 163, no. 13, pp. A2757–A2767, Oct. 2016.

[117] P. Barai, K. Smith, C.-F. Chen, G.-H. Kim, and P. P. Mukherjee, “Reduced order modeling of mechanical degradation induced performance decay in lithium-ion battery porous electrodes,” *Journal of the Electrochemical Society*, vol. 162, no. 9, pp. A1751–A1771, 2015.

[118] J. Cannarella and C. B. Arnold, “The effects of defects on localized plating in lithium-ion batteries,” *Journal of The Electrochemical Society*, vol. 162, no. 7, pp. A1365–A1373, Apr. 2015.

[119] J. Christensen and J. Newman, “Cyclable lithium and capacity loss in li-ion cells,” *Journal of The Electrochemical Society*, vol. 152, no. 4, p. A818, 2005.

[120] C. Delacourt and M. Safari, “Life simulation of a graphite/lifepo 4 cell under cycling and storage,” *Journal of The Electrochemical Society*, vol. 159, no. 8, pp. A1283–A1291, Jan. 2012.

[121] R. Deshpande, M. Verbrugge, Y.-T. Cheng, J. Wang, and P. Liu, “Battery cycle life prediction with coupled chemical degradation and fatigue mechanics,” *Journal of The Electrochemical Society*, vol. 159, no. 10, pp. A1730–A1738, Jan. 2012.

[122] R. D. Deshpande and D. M. Bernardi, “Modeling solid-electrolyte interphase (sei) fracture: Coupled mechanical/chemical degradation of the lithium ion battery,” *Journal of The Electrochemical Society*, vol. 164, no. 2, pp. A461–A474, Jan. 2017.

[123] H. Ekström and G. Lindbergh, "A model for predicting capacity fade due to sei formation in a commercial graphite/lifepo 4 cell," *Journal of The Electrochemical Society*, vol. 162, no. 6, pp. A1003–A1007, Mar. 2015.

[124] H. Ge, T. Aoki, N. Ikeda, S. Suga, T. Isobe, Z. Li, Y. Tabuchi, and J. Zhang, "Investigating lithium plating in lithium-ion batteries at low temperatures using electrochemical model with nmr assisted parameterization," *Journal of The Electrochemical Society*, vol. 164, no. 6, pp. A1050–A1060, 2017.

[125] X. Jin, A. Vora, V. Hoshing, T. Saha, G. Shaver, R. E. García, O. Wasynczuk, and S. Varigonda, "Physically-based reduced-order capacity loss model for graphite anodes in li-ion battery cells," *Journal of Power Sources*, vol. 342, pp. 750–761, Feb. 2017.

[126] N. Kamyab, J. W. Weidner, and R. E. White, "Mixed mode growth model for the solid electrolyte interface (sei)," *Journal of The Electrochemical Society*, vol. 166, no. 2, pp. A334–A341, Jan. 2019.

[127] F. M. Kindermann, J. Keil, A. Frank, and A. Jossen, "A sei modeling approach distinguishing between capacity and power fade," *Journal of The Electrochemical Society*, vol. 164, no. 12, pp. E287–E294, Aug. 2017.

[128] C. Kupper and W. G. Bessler, "Multi-scale thermo-electrochemical modeling of performance and aging of a lifepo 4 /graphite lithium-ion cell," *Journal of The Electrochemical Society*, vol. 164, no. 2, pp. A304–A320, Dec. 2017.

[129] N. Legrand, B. Knosp, P. Desprez, F. Lapicque, and S. Raël, "Physical characterization of the charging process of a li-ion battery and prediction of li plating by electrochemical modelling," *Journal of Power Sources*, vol. 245, pp. 208–216, 2014.

[130] D. Li, D. Danilov, Z. Zhang, H. Chen, Y. Yang, and P. H. L. Notten, "Modeling the sei-formation on graphite electrodes in lifepo4 batteries," *Journal of the Electrochemical Society*, vol. 162, no. 6, pp. A858–A869, 2015.

[131] X. Lin, J. Park, L. Liu, Y. Lee, A. M. Sastry, and W. Lu, "A comprehensive capacity fade model and analysis for li-ion batteries," *Journal of the Electrochemical Society*, vol. 160, no. 10, pp. A1701–A1710, 2013.

[132] M. B. Pinson and M. Z. Bazant, "Theory of sei formation in rechargeable batteries: Capacity fade, accelerated aging and lifetime prediction," *Journal of The Electrochemical Society*, vol. 160, no. 2, pp. A243–A250, Dec. 2013.

[133] H. J. Ploehn, P. Ramadass, and R. E. White, "Solvent diffusion model for aging of lithium-ion battery cells," *Journal of The Electrochemical Society*, vol. 151, no. 3, p. A456, 2004.

[134] E. Prada, D. Di Domenico, Y. Creff, J. Bernard, V. Sauvant-Moynot, and F. Huet, "A simplified electrochemical and thermal aging model of lifepo 4 -graphite li-ion batteries: Power and capacity fade simulations," *Journal of The Electrochemical Society*, vol. 160, no. 4, pp. A616–A628, Feb. 2013.

[135] J. Purewal, J. Wang, J. Graetz, S. Soukiazian, H. Tataria, and M. W. Verbrugge, "Degradation of lithium ion batteries employing graphite negatives and nickel-cobalt-manganese oxide + spinel manganese oxide positives: Part 2, chemical-mechanical degradation model," *Journal of Power Sources*, vol. 272, pp. 1154–1161, 2014.

[136] A. V. Randall, R. D. Perkins, X. Zhang, and G. L. Plett, "Controls oriented reduced order modeling of solid-electrolyte interphase layer growth," *Journal of Power Sources*, vol. 209, pp. 282–288, Jul. 2012.

[137] M. Safari, M. Morcrette, A. Teyssot, and C. Delacourt, "Multimodal physics-based aging model for life prediction of li-ion batteries," *Journal of The Electrochemical Society*, vol. 156, no. 3, p. A145, 2009.

[138] M. Safari, M. Morcrette, A. Teyssot, and C. Delacourt, "Life-prediction methods for lithium-ion batteries derived from a fatigue approach: I introduction: Capacity-loss prediction based on damage accumulation," *Journal of The Electrochemical Society*, vol. 157, no. 6, p. A713, 2010.

[139] M. Safari and C. Delacourt, "Simulation-based analysis of aging phenomena in a commercial graphite/lifepo4 cell," *Journal of The Electrochemical Society*, vol. 158, no. 12, p. A1436, 2011.

[140] F. Single, B. Horstmann, and A. Latz, "Revealing sei morphology: In-depth analysis of a modeling approach," *Journal of The Electrochemical Society*, vol. 164, no. 11, pp. E3132–E3145, 2017.

[141] J. Sturm, A. Rheinfeld, I. Zilberman, F. B. Spingler, S. Kosch, F. Frie, and A. Jossen, "Modeling and simulation of inhomogeneities in a 18650 nickel-rich, silicon-graphite lithium-ion cell during fast charging," *Journal of Power Sources*, vol. 412, pp. 204–223, 2019.

[142] A. A. Tahmasbi, T. Kadyk, and M. H. Eikerling, "Statistical physics-based model of solid electrolyte interphase growth in lithium ion batteries," *Journal of The Electrochemical Society*, vol. 164, no. 6, pp. A1307–A1313, 2017.

[143] M. Tang, S. Lu, and J. Newman, "Experimental and theoretical investigation of solid-electrolyte-interphase formation mechanisms on glassy carbon," *Journal of the Electrochemical Society*, vol. 159, no. 11, pp. A1775–A1785, 2012.

[144] X.-G. Yang, Y. Leng, G. Zhang, S. Ge, and C.-Y. Wang, "Modeling of lithium plating induced aging of lithium-ion batteries: Transition from linear to nonlinear aging," *Journal of Power Sources*, vol. 360, pp. 28–40, Aug. 2017.

[145] B. Horstmann, F. Single, and A. Latz, "Review on multi-scale models of solid-electrolyte interphase formation," *Current Opinion in Electrochemistry*, vol. 13, pp. 61–69, 2019.

[146] F. Single, A. Latz, and B. Horstmann, "Identifying the mechanism of continued growth of the solid–electrolyte interphase," *ChemSusChem*, vol. 11, no. 12, pp. 1950–1955, 2018.

[147] T. Ashwin, Y. M. Chung, and J. Wang, "Capacity fade modelling of lithium-ion battery under cyclic loading conditions," *Journal of Power Sources*, vol. 328, pp. 586–598, Oct. 2016.

[148] S. Das, P. M. Attia, W. C. Chueh, and M. Z. Bazant, "Electrochemical kinetics of sei growth on carbon black: Part ii. modeling," *Journal of The Electrochemical Society*, vol. 166, no. 4, pp. E107–E118, 2019.

[149] M. T. Lawder, P. W. C. Northrop, and V. R. Subramanian, "Model-based sei layer growth and capacity fade analysis for ev and phev batteries and drive cycles," *Journal of the Electrochemical Society*, vol. 161, no. 14, pp. A2099–A2108, 2014.

[150] C. von Lüders, J. Keil, M. Webersberger, and A. Jossen, "Modeling of lithium plating and lithium stripping in lithium-ion batteries," *Journal of Power Sources*, vol. 414, pp. 41–47, Feb. 2019.

[151] D. Pritzl, J. Landesfeind, S. Solchenbach, and H. A. Gasteiger, "An analysis protocol for three-electrode li-ion battery impedance spectra: Part ii. analysis of a graphite anode cycled vs. lnmo," *Journal of The Electrochemical Society*, vol. 165, no. 10, pp. A2145–A2153, Jul. 2018.

[152] J. Xu, R. D. Deshpande, J. Pan, Y.-T. Cheng, and V. S. Battaglia, "Electrode side reactions, capacity loss and mechanical degradation in lithium-ion batteries," *Journal of The Electrochemical Society*, vol. 162, no. 10, pp. A2026–A2035, 2015.

[153] S. Pelletier, O. Jabali, G. Laporte, and M. Veneroni, "Battery degradation and behaviour for electric vehicles: Review and numerical analyses of several models," *Transportation Research Part B: Methodological*, vol. 103, pp. 158–187, Sep. 2017.

[154] D. A. Howey and J. M. Reniers, "Slide," Oxford, 2019. [Online]. Available: https://github.com/davidhowey/SLIDE

[155] European Commission, "Everlasting," 2018. [Online]. Available: https://ec.europa.eu/inea/en/horizon-2020/projects/h2020-transport/green-vehicles/everlasting

[156] LG Chem, "Rechargeable lithium ion battery model : Inr18650 mj1 3500mah," Jan. 2016. [Online]. Available: https://www.nkon.nl/sk/k/SpecificationINR18650MJ122.08.2014.pdf

[157] M. Dubarry, A. Devie, and K. McKenzie, "Durability and reliability of electric vehicle batteries under electric utility grid operations: Bidirectional charging impact analysis," *Journal of Power Sources*, vol. 358, pp. 39–49, Aug. 2017.

[158] J. Schmalstieg, S. Käbitz, M. Ecker, and D. U. Sauer, "A holistic aging model for li(nimnco)o2 based 18650 lithium-ion batteries," *Journal of Power Sources*, vol. 257, pp. 325–334, Jul. 2014.

[159] Y. Wu, P. Keil, S. F. Schuster, and A. Jossen, "Impact of temperature and discharge rate on the aging of a licoo 2 /lini 0.8 co 0.15 al 0.05 o 2 lithium-ion pouch cell," *Journal of The Electrochemical Society*, vol. 164, no. 7, pp. A1438–A1445, May 2017.

[160] A. Bizeray, “State and parameter estimation of physics-based lithium-ion battery models,” Ph.D. dissertation, University of Oxford, 2016.

[161] S. J. Moura, “Techniques for battery health conscious power management via electrochemical modeling and optimal control,” Ph.D. dissertation, University of Michigan, 2011.

[162] S. J. Moura, J. L. Stein, and H. K. Fathy, “Battery-health conscious power management in plug-in hybrid electric vehicles via electrochemical modeling and stochastic control,” *IEEE Transactions on Control Systems Technology*, vol. 21, no. 3, pp. 679–694, May 2013.

[163] I. D. Campbell, K. Gopalakrishnan, M. Marinescu, M. Torchio, G. J. Offer, and D. Raimondo, “Optimising lithium-ion cell design for plug-in hybrid and battery electric vehicles,” *Journal of Energy Storage*, vol. 22, pp. 228–238, Apr. 2019.

[164] Y. Qi, S. Kolluri, M. Pathak, D. T. Schwartz, and V. R. Subramanian, “Simultaneous optimization approach for optimal electrode design of lithium-ion batteries,” in *235th ECS Meeting*, Dallas, 2017, pp. MA2017–02 2033.

[165] A. R. Marco, “Improvements to fidelity , generation and implementation of physics-based lithium-ion reduced-order models,” Ph.D. dissertation, University of Colorado Colorado Springs, 2017.

[166] M. S. Trimboli, G. L. Plett, R. Zane, K. A. Smith, D. Maksimovic, M. Evzelman, D. Costinett, and R. D. Anderson, “Model predictive control and optimization for battery charging and discharging,” 2019. [Online]. Available: https://patentimages.storage.googleapis.com/2b/10/7a/78868d421a8b39/US10298026.pdf

[167] R. A. Zane, M. Evzelman, D. Costinett, D. Maksimović, R. D. Anderson, K. A. Smith, M. S. Trimboli, and G. L. Plett, “Autonomous battery control and optimization,” 2019. [Online]. Available: https://patentimages.storage.googleapis.com/c2/99/a5/83ee231bc28363/US10277041.pdf

[168] B. Suthar, V. Ramadesigan, P. W. C. Northrop, B. Gopaluni, S. Santhanagopalan, R. D. Braatz, and V. R. Subramanian, “Optimal control and state estimation of lithium-ion batteries using reformulated models,” *2013 American Control Conference*, pp. 5350–5355, 2014.

[169] M. Torchio, L. Magni, R. D. Braatz, and D. M. Raimondo, “Optimal health-aware charging protocol for lithium-ion batteries: A fast model predictive control approach,” *IFAC-PapersOnLine*, vol. 49, no. 7, pp. 827–832, 2016.

[170] S. Lucia, M. Torchio, D. M. Raimondo, R. Klein, R. D. Braatz, and R. Findeisen, “Towards adaptive health-aware charging of li-ion batteries: A real-time predictive control approach using first-principles models,” in *2017 American Control Conference (ACC)*. IEEE, May 2017, pp. 4717–4722.

[171] H. E. Perez, S. Dey, X. Hu, and S. J. Moura, “Optimal charging of li-ion batteries via a single particle model with electrolyte and thermal dynamics,” *Journal of The Electrochemical Society*, vol. 164, no. 7, pp. A1679–A1687, Jun. 2017.

[172] R. Klein, N. A. Chaturvedi, J. Christensen, J. Ahmed, R. Findeisen, and A. Kojic, "Optimal charging strategies in lithium-ion battery," in *Proceedings of the 2011 American Control Conference*. IEEE, Jun. 2011, pp. 382–387.

[173] M. Pathak, D. Sonawane, S. Santhanagopalan, R. D. Braatz, and V. R. Subramanian, "Analyzing and minimizing capacity fade through optimal model-based control - theory and experimental validation," *ECS Transactions*, vol. 75, no. 23, pp. 51–75, Jan. 2017.

[174] N. Dawson-Elli, S. Kolluri, K. Mitra, and V. R. Subramanian, "On the creation of a chess-ai-inspired problem-specific optimizer for the pseudo two-dimensional battery model using neural networks," *Journal of The Electrochemical Society*, vol. 166, no. 6, pp. A886–A896, Mar. 2019.

[175] M. Pathak, S. Kolluri, and V. R. Subramanian, "Generic model control for lithium-ion batteries," *Journal of The Electrochemical Society*, vol. 164, no. 6, pp. A973–A986, Mar. 2017.

[176] S. V. Aduru, M. Pathak, S. Kolluri, R. D. Braatz, and V. R. Subramanian, "Nonlinear model predictive control strategies for optimal charging of a lithium-ion battery," in *235th ECS Meeting*, Dallas, 2019, pp. MA2019–01 106.

[177] L. N. Trefethen, *Spectral methods in Matlab*. SIAM, 2000.

[178] J. A. C. Weideman and S. C. Reddy, "A matlab differentiation matrix suite," *ACM Transactions on Mathematical Software*, vol. 26, no. 4, pp. 465–519, Dec. 2000.

[179] L. T. Biegler, "An overview of simultaneous strategies for dynamic optimization," *Chemical Engineering and Processing: Process Intensification*, vol. 46, no. 11, pp. 1043–1053, Nov. 2007.

[180] S. Kameswaran and L. T. Biegler, "Simultaneous dynamic optimization strategies: Recent advances and challenges," *Computers & Chemical Engineering*, vol. 30, no. 10-12, pp. 1560–1575, Sep. 2006.

[181] J. Stoer and R. Bulirsch, *Introduction to Numerical Analysis*, 3rd ed. New-York: Springer-Verlag New York, 2002.

[182] T. Kailath, *Linear Systems*. Prentice-Hall, 1980.

[183] T. J. Grant, "Characteristics of Conservation Laws for Finite Difference Equations," PhD, University of Surrey, 2011.

[184] L. Biegler and V. Zavala, "Large-scale nonlinear programming using ipopt: An integrating framework for enterprise-wide dynamic optimization," *Computers & Chemical Engineering*, vol. 33, no. 3, pp. 575–582, Mar. 2009.

[185] L. B. Rall, Ed., *Automatic Differentiation: Techniques and Applications*, ser. Lecture Notes in Computer Science. Berlin, Heidelberg: Springer Berlin Heidelberg, 1981, vol. 120.

[186] A. Walther and A. Griewank, "Getting started with adol-c," in *Combinatorial Scientific Computing*, U. Naumann and O. Schenk, Eds. Chapman-Hall CRC Computational Science, 2012, pp. 181–202.

[187] A. H. Gebremedhin, D. Nguyen, M. M. A. Patwary, and A. Pothen, “Colpack: Software for graph coloring and related problems in scientific computing,” *ACM Transactions on Mathematical Software*, vol. 40, no. 1, pp. 1–31, Sep. 2013.

[188] M. A. Xavier and M. S. Trimboli, “Lithium-ion battery cell-level control using constrained model predictive control and equivalent circuit models,” *Journal of Power Sources*, vol. 285, pp. 374–384, Jul. 2015.

[189] P. Fortenbacher, J. L. Mathieu, and G. Andersson, “Modeling and optimal operation of distributed battery storage in low voltage grids,” *IEEE Transactions on Power Systems*, vol. 32, no. 6, pp. 4340–4350, Mar. 2017.

[190] Maheshwari, “Modelling , aging and optimal operation of lithium-ion batteries,” Ph.D. dissertation, TU Eindhoven, 2018.

[191] A. Wächter and L. T. Biegler, “On the implementation of an interior-point filter line-search algorithm for large-scale nonlinear programming,” *Mathematical Programming*, vol. 106, no. 1, pp. 25–57, Mar. 2006.

[192] T. Brijs, C. De Jonghe, B. F. Hobbs, and R. Belmans, “Interactions between the design of short-term electricity markets in the cwe region and power system flexibility,” *Applied Energy*, vol. 195, pp. 36–51, Jun. 2017.

[193] X. Chen, Z. Y. Dong, K. Meng, Y. Xu, K. P. Wong, and H. W. Ngan, “Electricity price forecasting with extreme learning machine and bootstrapping,” *IEEE Transactions on Power Systems*, vol. 27, no. 4, pp. 2055–2062, Nov. 2012.

[194] A. Conejo, M. Plazas, R. Espinola, and A. Molina, “Day-ahead electricity price forecasting using the wavelet transform and arima models,” *IEEE Transactions on Power Systems*, vol. 20, no. 2, pp. 1035–1042, May 2005.

[195] S. Voronin and J. Partanen, “Price forecasting in the day-ahead energy market by an iterative method with separate normal price and price spike frameworks,” *Energies*, vol. 6, no. 11, pp. 5897–5920, Nov. 2013.

[196] Belpex, “Market data services,” 2016. [Online]. Available: https://www.belpex.be/services/market-data-services/

[197] E. Sarasketa-Zabala, I. Gandiaga, E. Martinez-Laserna, L. Rodriguez-Martinez, and I. Villarreal, “Cycle ageing analysis of a lifepo4/graphite cell with dynamic model validations: Towards realistic lifetime predictions,” *Journal of Power Sources*, vol. 275, pp. 573–587, Feb. 2015.

[198] C. Goebel, H. Hesse, M. Schimpe, A. Jossen, and H.-A. Jacobsen, “Model-based dispatch strategies for lithium-ion battery energy storage applied to pay-as-bid markets for secondary reserve,” *IEEE Transactions on Power Systems*, vol. 32, no. 4, pp. 2724–2734, Jul. 2017.

[199] M. A. Ortega-Vazquez, “Optimal scheduling of electric vehicle charging and vehicle-to-grid services at household level including battery degradation and price uncertainty,” *IET Generation, Transmission & Distribution*, vol. 8, no. 6, pp. 1007–1016, Jun. 2014.

[200] M. Corengia and A. Torres, "Effect of tariff policy and battery degradation on optimal energy storage," *Processes*, vol. 6, no. 10, p. 204, Oct. 2018.

[201] E. Kruger and Q. T. Tran, "Minimal aging operating strategies for battery energy storage systems in photovoltaic applications," in *2016 IEEE PES Innovative Smart Grid Technologies Conference Europe (ISGT-Europe)*. IEEE, Oct. 2016, pp. 1–6.

[202] B. Xu, "Batteries in electricity markets: Economic planning and operations," Ph.D. dissertation, University of Washington, 2018.

[203] B. Xu, J. Zhao, T. Zheng, E. Litvinov, and D. S. Kirschen, "Factoring the cycle aging cost of batteries participating in electricity markets," *IEEE Transactions on Power Systems*, vol. 33, no. 2, pp. 2248–2259, Mar. 2018.

[204] M. U. Hashmi, W. Labidi, A. Busic, S.-E. Elayoubi, and T. Chahed, "Long-term revenue estimation for battery performing arbitrage and ancillary services," in *2018 IEEE International Conference on Communications, Control, and Computing Technologies for Smart Grids (SmartGridComm)*. IEEE, Oct. 2018, pp. 1–7.

[205] M. R. Sarker, M. D. Murbach, D. T. Schwartz, and M. A. Ortega-Vazquez, "Optimal operation of a battery energy storage system: Trade-off between grid economics and storage health," *Electric Power Systems Research*, vol. 152, pp. 342–349, Nov. 2017.

[206] S. Sun, M. Dong, and B. Liang, "Real-time power balancing in electric grids with distributed storage," *IEEE journal of selected topics in signal processing*, vol. 8, no. 6, pp. 1167–1181, 2014.

[207] M. T. Lawder, V. Viswanathan, and V. R. Subramanian, "Balancing autonomy and utilization of solar power and battery storage for demand based microgrids," *Journal of Power Sources*, vol. 279, pp. 645–655, Apr. 2015.

[208] S. B. Lee, C. Pathak, V. Ramadesigan, W. Gao, and V. R. Subramanian, "Direct, efficient, and real-time simulation of physics-based battery models for stand-alone pv-battery microgrids," *Journal of The Electrochemical Society*, vol. 164, no. 11, pp. E3026–E3034, Feb. 2017.

[209] B. Weißhar and W. G. Bessler, "Model-based lifetime prediction of an lfp/graphite lithium-ion battery in a stationary photovoltaic battery system," *Journal of Energy Storage*, vol. 14, pp. 179–191, Dec. 2017.

[210] G. L. Plett, *Battery modeling*. Norwood: Artech House Publishers, 2015.

[211] A. Eddahech, O. Briat, and J.-M. Vinassa, "Thermal characterization of a high-power lithium-ion battery: Potentiometric and calorimetric measurement of entropy changes," *Energy*, vol. 61, pp. 432–439, Nov. 2013.

[212] T. Beck, H. Kondziella, G. Huard, and T. Bruckner, "Assessing the influence of the temporal resolution of electrical load and pv generation profiles on self-consumption and sizing of pv-battery systems," *Applied Energy*, vol. 173, pp. 331–342, Jul. 2016.

Appendix A

Fits of the battery models

This appendix shows how well the various battery models from chapter 4 fit the data used in this work, shown in section 1.4. There is one section for each battery model (bucket, equivalent circuit, and single particle). For each model, there is a figure showing how well the model can predict the voltage during CC discharges at various currents. Note that the data, collected for a cell with 16 Ah capacity, is scaled down to a 2.7 Ah cell as was used in the simulations. Then the degradation predictions for calendar and cycle ageing are compared with the data. All degradation data and simulation are shown on one graph to give an overall view of the accuracy of each model.

A.1 Bucket model

The bucket model (BM) was introduced in section 4.2.1. It is a simple linear battery model where the state of charge (SoC) is the integral of the power to and from the battery, and degradation is a linear function of the energy throughput. The parameters of the model are given in Table 4.1 in section 4.3.1, although in this appendix, the regularisation term is omitted, i.e. $\beta_{11} = 0$.

A.1.1 Cycling data

The BM only simulates power and SoC. The voltage is assumed to be constant and equal to the nominal voltage of the cell, 3.7 V, as shown on Fig. A.1. There is no diffusion or rate limitation, such that the capacity which can be accessed at various C-rates is constant. Temperature is not included in this model.

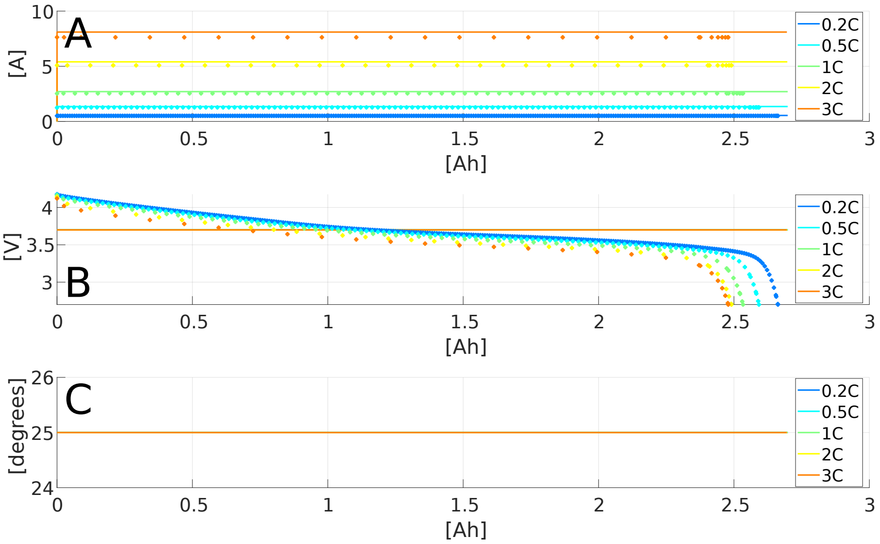

Fig. A.1 Characterisation fit of the BM (lines) with the data (markers) for CC discharges at various C-rates. The data has been scaled down to a 2.7 Ah cell. (A) current; (B) voltage; (C) temperature.

A.1.2 Degradation data

There is no calendar ageing in the BM, such that all simulations map to one line at 100% on Fig. A.2. The degradation model (4.2) is a linear function of the energy throughput. Given that the voltage is constant, the lost capacity is directly dependent on the charge throughput. The x-axis from Fig. A.3 shows full equivalent cycles, which is the division of the charge throughput and (twice) the nominal capacity. Therefore, all simulations map onto one line. There are no temperature, power, or SoC dependencies.

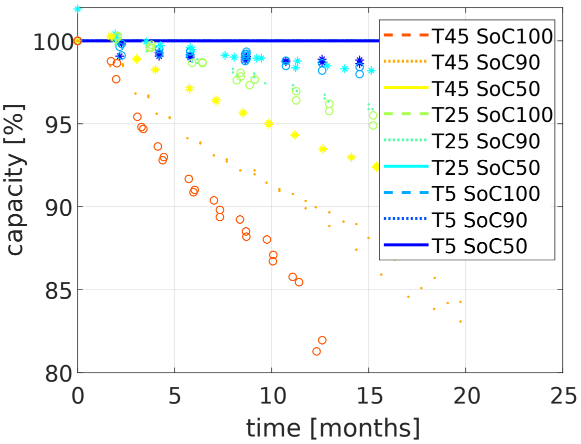

Fig. A.2 Comparison of the degradation simulations of the BM with the linear degradation model (lines) with the data (markers) for calendar ageing at various temperatures and SoC levels. For clarity, line styles and marker symbols indicate the SoC level on top of the colour scale: solid lines and stars are for 50%, dotted lines and dots are for 90%, and dashed lines and circles are for 100%.

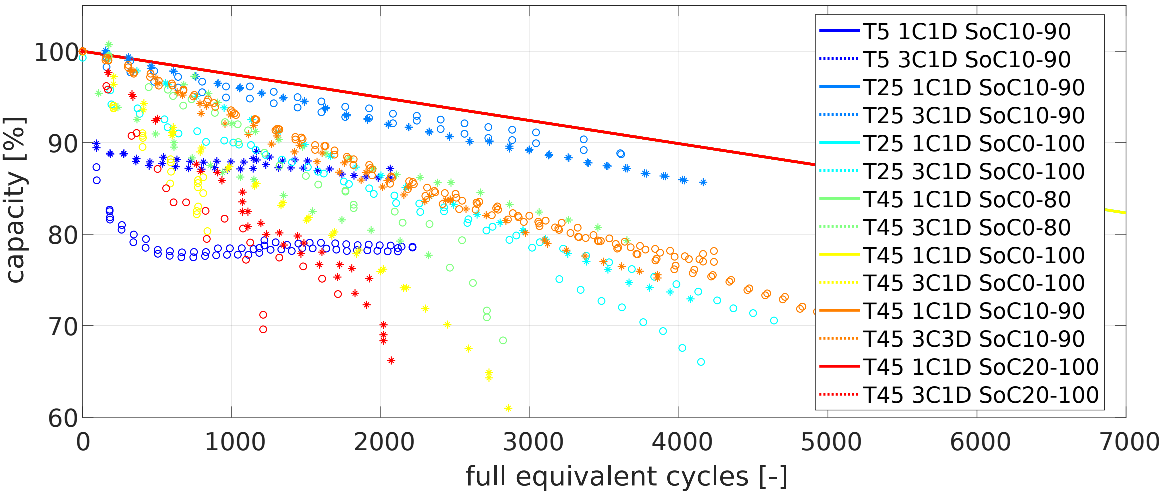

Fig. A.3 Comparison of the degradation simulations of the BM with the linear degradation model (lines) with the data (markers) for cycle ageing at various temperatures, currents, and SoC windows. C denotes the C-rate on charge, D the C-rate on discharge. For clarity, line styles and marker symbols indicate the charging current: solid lines and stars for 1C, and dotted lines and circles for 3C.

A.2 Equivalent-circuit model

The equivalent-circuit model (ECM) was introduced in section 4.2.2. A battery is simulated by a network of electrical components, in this case a nonlinear and SoC-dependent voltage source, a series resistance, and a resistor and capacitor in parallel. An empirical degradation model (4.4) from literature was combined with this network to reduce the capacity. The parameters of the model are given in Table 4.2 in section 4.3.1. Subsection A.2.2 shows the degradation predictions from that model. Subsection A.2.3 shows the predictions if the degradation model parameters are divided by a factor of 5 as was done for the optimisation as mentioned in section 4.3.1.

All values of the ECM and its degradation model are taken directly from literature. Therefore, large errors between the ECM simulations and the data for this specific cell can be expected. This is done to show that one cannot simply take a model and its parameter values from literature and add this to some other model or optimisation. The goal of this work is not to compare ECMs with physics-based models, in which case the parameters of the ECM should be fitted to the data for this cell as was done for the physics-based cell.

A.2.1 Cycling data

As can be seen on Fig. A.4, there is a significant improvement compared to the BM by adding the OCV. The parameters of the network were taken from literature, and it seems they did not work very well for the cell considered here. The resistance values should have been larger (to decrease the voltage at higher current), and also the capacitance should have been larger (to decrease the accessible capacity at the current). Temperature is not included in the model. Note that both the data and simulation had the same value for the C-rate, but a slightly different value in Amperes because the experiment used the nominal capacity while the simulation used the total capacity.

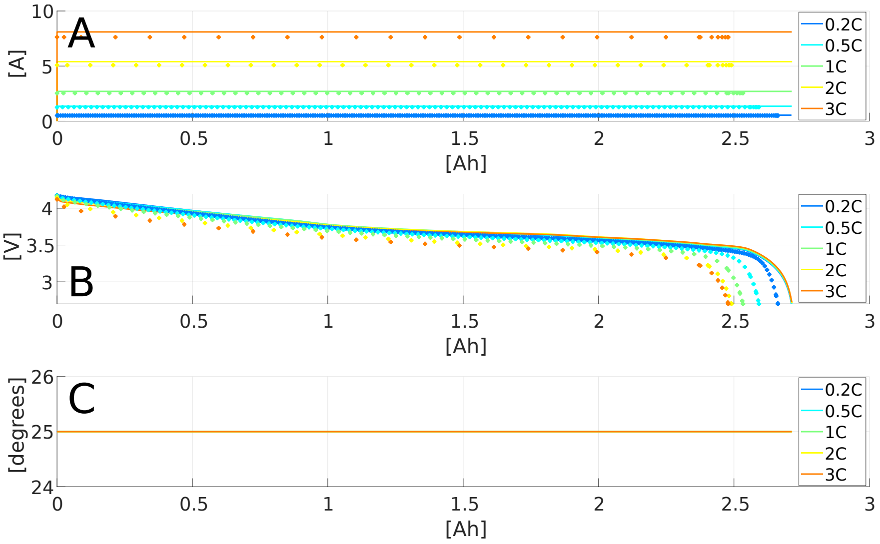

Fig. A.4 Characterisation fit of the ECM (lines) with the data (markers) for CC discharges at various C-rates. The data has been scaled down to a 2.7 Ah cell. (A) current; (B) voltage; (C) temperature.

A.2.2 Degradation data

This section shows the predictions from the degradation model as proposed in literature. The calendar ageing is very well predicted, with the exception of the degradation at 90% and 50% SoC and 45°C as can be seen on Fig. A.5. Also the acceleration in the degradation at 100% SoC and 45°C in the later states of the cell's life is not present in the simulation, which overestimates the degradation early in the lifetime.

The fit for cycle ageing, shown on Fig. A.6 is worse. First of all, the degradation model had a square-root dependency on charge throughput (of which FEC is a linear function), while the data has very different trends: there might be a square-root in some conditions, but others are more linear or accelerating.

Secondly, there is very little difference in the simulations for the different cycles. This is because the degradation model depended mostly on 'average' parameters (the mean voltage, the depth of discharge, etc.), and from that perspective, the cycles tested here are very similar to each other (e.g. the depth of discharge is 80% for all but one condition). The degradation model was made for a data set which consisted mostly of cycles with widely varying mean

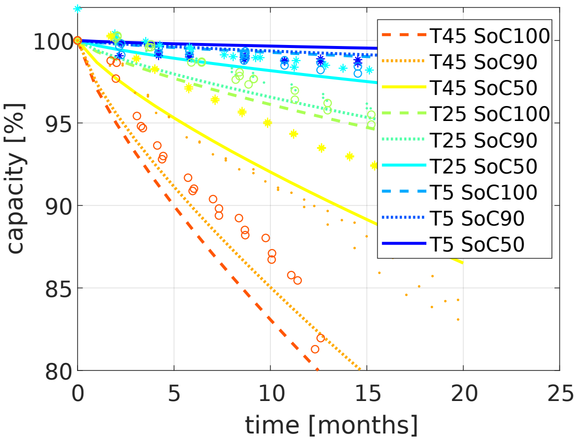

Fig. A.5 Comparison of the degradation simulations of the ECM with the empirical degradation model (lines) with the data (markers) for calendar ageing at various temperatures and SoC levels. For clarity, line styles and marker symbols indicate the SoC level on top of the colour scale: solid lines and stars are for 50%, dotted lines and dots are for 90%, and dashed lines and circles are for 100%.

SoC values and depth of discharge (e.g. cycles between 5% and 15% or between 10% and 90%) [158].

This illustrates the point made in section 2.2 that empirical degradation models are only valid for the operating conditions considered in their data sets. Extrapolation to different conditions can result in large errors, as is the case here.

A.2.3 Degradation data with empirical degradation divided by 5

A problem with the empirical degradation model is that it predicts very fast degradation for the first few cycles (due to the square-root dependency). Because the optimisation from chapter 4 has only a 2-day time horizon, it will only ‘see’ this initial large degradation without ‘seeing’ that once the cell gets through this stage the degradation will flatten out. Therefore, the cost of using the cell for these first few cycles is larger than the revenue which could be made, and consequently the optimal choice is to not use the cell.

This problem could be solved by increasing the time horizon (then the optimisation could ‘see’ the benefit of getting over this initial degradation because it can use the cell in the

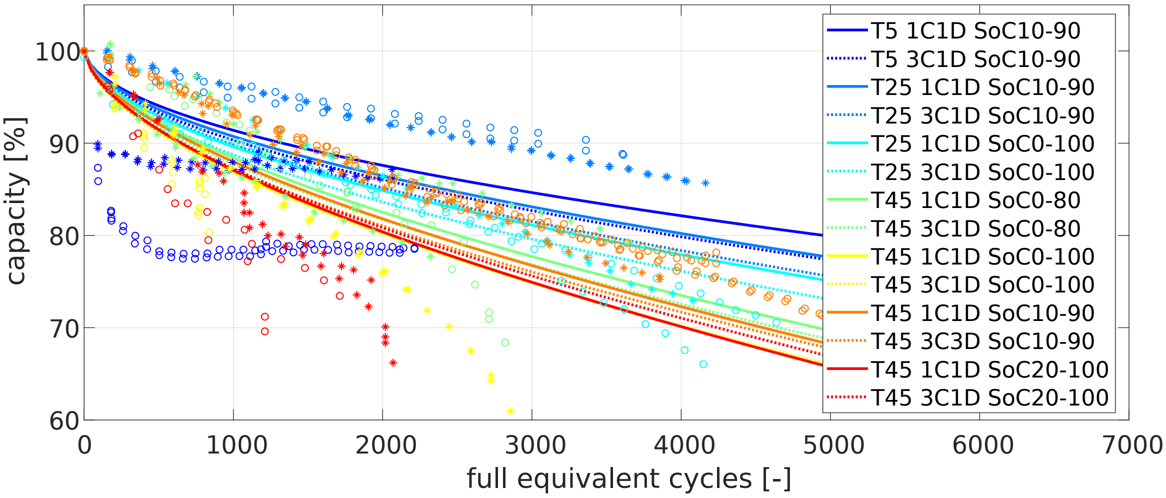

Fig. A.6 Comparison of the degradation simulations of ECM with the empirical degradation model (lines) with the data (markers) for cycle ageing at various temperatures, currents, and SoC windows. C denotes the C-rate on charge, D the C-rate on discharge. For clarity, line styles and marker symbols indicate the charging current: solid lines and stars for 1C, and dotted lines and circles for 3C.

more flat degradation region). Unfortunately, the optimisation solver could not converge for sufficiently large time horizons. Therefore, the predicted degradation was decreased by a factor of 5, i.e. the constants in the empirical function were divided by 5. This decreases the initial degradation, and allowed the cell to be used. Figs. A.7 and A.8 show the corresponding calendar and cycle ageing respectively. The same comments can be made as in section A.2.2 about the accuracy, except that now all degradation later in life is underestimated. However, the initial cycle degradation has a correct slope.

A.3 Single-Particle Model

The single-particle model (SPM) is described extensively in section 2.1. It simulates diffusion in spherical particles, a kinetically limited intercalation reaction at the surface and includes a bulk thermal model and a stress model (note that the stress has no effect on the diffusion, intercalation or temperature, it is only considered for degradation). Various degradation models can be added on, as described in chapter 2. Two combinations are discussed here:

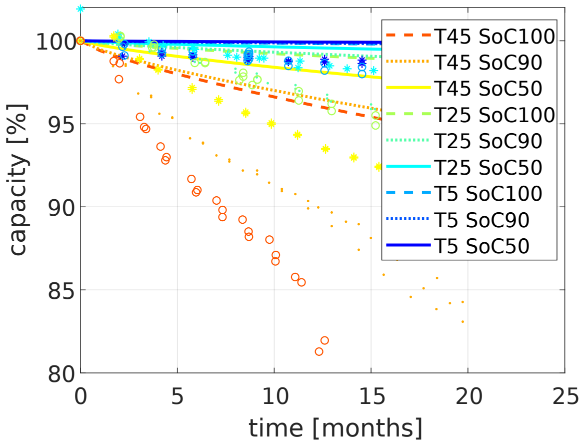

Fig. A.7 Comparison of the degradation simulations of the ECM with the empirical degradation model decreased by a factor of 5 (lines) with the data (markers) for calendar ageing at various temperatures and SoC levels. For clarity, line styles and marker symbols indicate the SoC level on top of the colour scale: solid lines and stars are for 50%, dotted lines and dots are for 90%, and dashed lines and circles are for 100%.

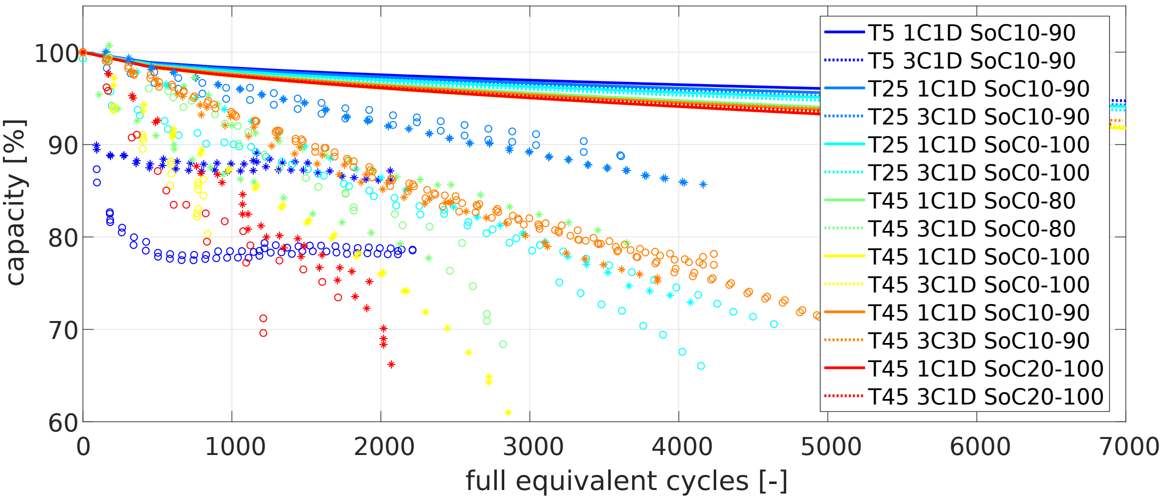

Fig. A.8 Comparison of the degradation simulations of the ECM with the empirical degradation model decreased by a factor of 5 (lines) with the data (markers) for cycle ageing at various temperatures, currents, and SoC windows. C denotes the C-rate on charge, D the C-rate on discharge. For clarity, line styles and marker symbols indicate the charging current: solid lines and stars for 1C, and dotted lines and circles for 3C.

the optimisation from chapter 4.4 is done with only an SEI growth model in order to limit the computational complexity, but the validation simulation from section 4.5 is done with a generalised degradation model including various degradation mechanisms. The parameters of the SPM and the SEI-only degradation model are given in Table 4.3 and its fit is shown in section A.3.2. The simulations with the generalised degradation model are shown in section A.3.3.

A.3.1 Cycling data

The characterisation fit of the SPM is shown on Fig. A.9. The half-cell OCV curves were measured, while the rate and diffusion constants were fitted to the data. Consequently, the fit is much better than for the ECM (where the parameters were taken from literature). The SPM is only considered to be valid at low C-rates because it does not include electrolyte transport or diffusion along the thickness of the electrodes. Therefore, the errors at 2C and 3C are larger compared to lower C-rates, especially the voltage drops are overestimated. The bulk thermal model also shows how the cell temperature increases at higher C-rates, unfortunately there was no temperature data available with which the simulations could be compared. As was the case with the ECM, both the data and simulation had the same value for the C-rate, but a slightly different value in Amperes because the experiment used the nominal capacity while the simulation used the total capacity.

A.3.2 Degradation data with SEI only

The simulations in this section are done with the degradation model considered in the optimisation (4.6). The results from this model were shown in a different format on Fig. 2.12. The calendar fit from Fig. A.10 is less good than the one achieved by the empirical degradation model from Fig. A.5, almost all degradation is underestimated. However,

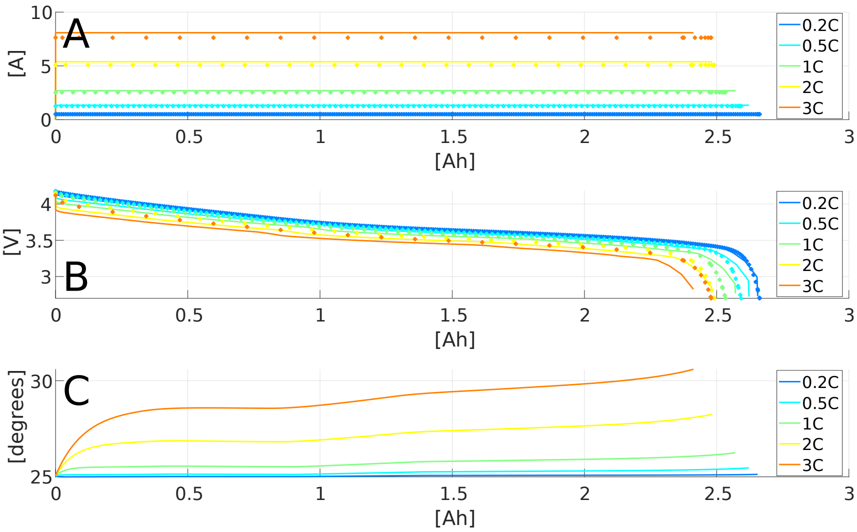

Fig. A.9 Characterisation fit of the SPM (lines) with the data (markers) for CC discharges at various C-rates. The data has been scaled down to a 2.7 Ah cell. (A) current; (B) voltage; (C) temperature.

crucially the relative difference between the different SoC levels at 25° is correct, which means that the optimisation will get the correct ‘incentives’ to control the SoC during rest.

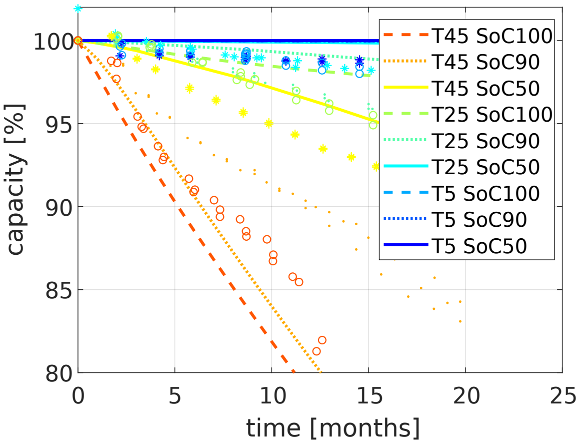

Fig. A.10 Comparison of the degradation simulations of the SPM with only SEI growth (lines) with the data (markers) for calendar ageing at various temperatures and SoC levels. For clarity, line styles and marker symbols indicate the SoC level on top of the colour scale: solid lines and stars are for 50%, dotted lines and dots are for 90%, and dashed lines and circles are for 100%.

The simulated cycle ageing is shown on Fig. A.11. The predictions at 5°C are completely inaccurate because lithium plating is not included in the model. Degradation at 25°C and

45°C is predicted more accurately, although the accelerating trends from the cycles at high SoC is missed. However, the initial degradation is correct, and the basic underlying effects are present such that the optimisation will aim to minimise the SoC and current.

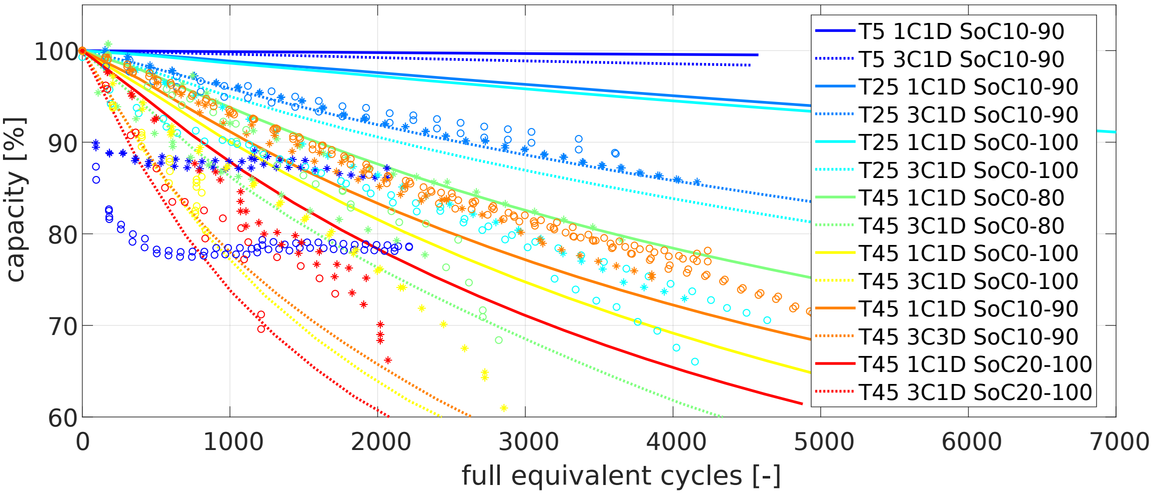

Fig. A.11 Comparison of the degradation simulations of the SPM with only SEI growth (lines) with the data (markers) for cycle ageing at various temperatures, currents, and SoC windows. C denotes the C-rate on charge, D the C-rate on discharge. For clarity, line styles and marker symbols indicate the charging current: solid lines and stars for 1C, and dotted lines and circles for 3C.

A.3.3 Degradation data with a generalised degradation model

The results from this section show the fit of a generalised degradation model. The model is very similar to the generalised degradation model developed in section 2.5.3 and shown on Fig. 2.11. Two modifications were made: an equation for kinetically-limited SEI growth (2.17) was added and the fitting parameters of the other mechanisms were changed marginally to accommodate this new model. The fit from Fig. 2.11 worked well for the cycle ageing, but hugely overestimated the calendar ageing. The model presented here is a compromise between fitting calendar and cycle ageing and is used for the validation simulations in section 4.5.

The calendar predictions are shown on Fig. A.12. If a purely diffusion-limited SEI growth model would have been used, there would have been no difference between the different resting SoCs (see subplot B from Fig. 2.10). The kinetically-limited model ensures there is more calendar ageing at high SoC levels, although it does not make enough difference between 100% and 90%. Note that the fit is different from the one in the previous section (which also used a kinetically-limited SEI growth model) because here other models will contribute to cyle ageing, which was not the case in the previous section. Therefore, the parameters of the SEI growth model are different which will also affect the calendar ageing from Fig. A.12.

The simulation from section 4.5 is for a year-long current profile with frequent rests (when no electricity is being traded) at an environmental temperature of 25°C. As can be seen on Fig. A.12, at this temperature the calendar ageing at 100% SoC is overestimated by a few percentage points, which will have more effect for cells which are used less (i.e. profit-maximising cells).

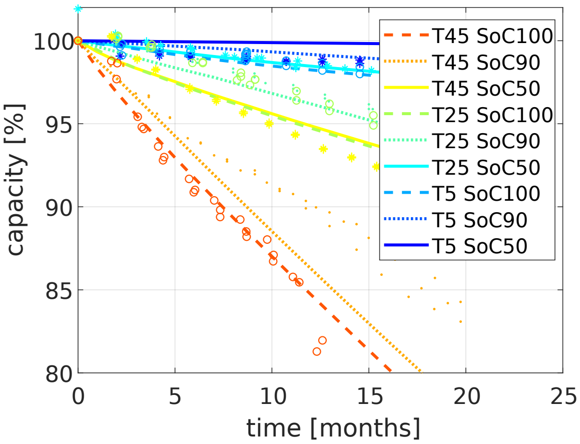

Fig. A.12 Comparison of the degradation simulations of the SPM with the generalised degradation model (lines) with the data (markers) for calendar ageing at various temperatures and SoC levels. For clarity, line styles and marker symbols indicate the SoC level on top of the colour scale: solid lines and stars are for 50%, dotted lines and dots are for 90%, and dashed lines and circles are for 100%.

The predicted cycle ageing is shown on Fig. A.13. Although the fit is less good than the one from Fig. 2.11, it is still relatively good. Most degradation from the cycles at 3C charging (dashed lines and circles) is overestimated due to the kinetically-limited SEI growth model. Additionally, the degradation of the cycle at 25°C in the full SoC window at 1C is overestimated (blue line with the least degradation of all simulations and data), especially after the first 1000 cycles.

As mentioned in the previous section, this model will be used for a simulation of cells which are cycling at 25°C with currents below 1C and in various SoC windows. Due to the low currents, the model errors of the 3C-cycles will not have a big impact. Most data for different SoC windows is at 45°C, such that the impact of SoC at 25°C is not known in as much detail, introducing larger uncertainties in the simulation from section 4.5. Even for the two cycles at 25°C for which there is data, the errors are a few percentage points, implying that the results from the simulations should not be taken for granted.

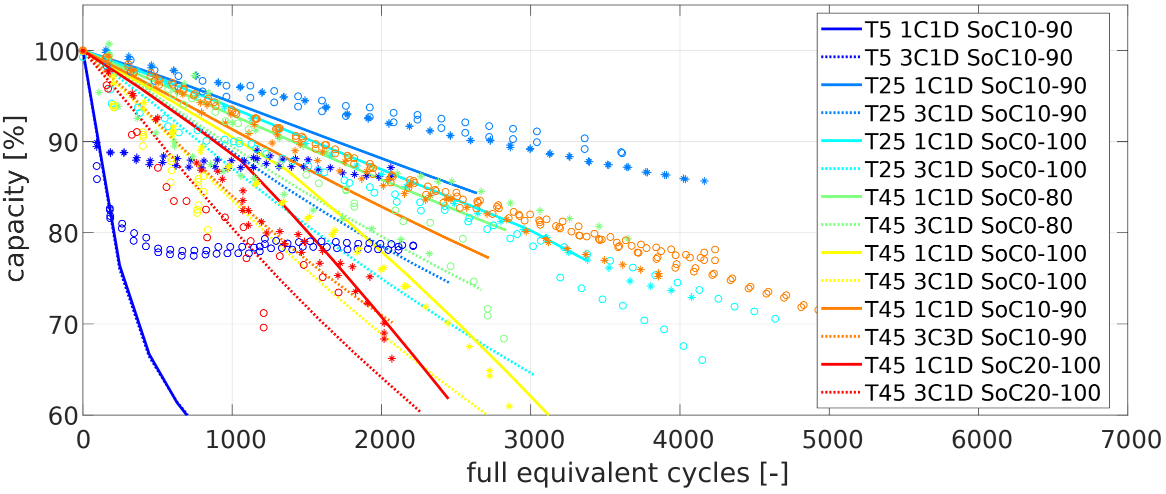

Fig. A.13 Comparison of the degradation simulations of the SPM with the generalised degradation model (lines) with the data (markers) for cycle ageing at various temperatures, currents, and SoC windows. C denotes the C-rate on charge, D the C-rate on discharge. For clarity, line styles and marker symbols indicate the charging current: solid lines and stars for 1C, and dotted lines and circles for 3C.

Appendix B

Simulation of the optimal usage profiles

This appendix shows the outcomes of the simulations with the optimal usage profiles as discussed in section 4.5. A cell simulated by the battery model with the ‘generalised degradation model’ (of which the fit is shown in section A.3.3) follows the optimal usage profiles from section 4.4.

As described in section 4.5, there are multiple ways in which the ‘usable capacity’ can be determined. This problem arises when the battery reaches a voltage limit while it is following the optimal usage profile. One option, shown in section B.1, is to immediately stop (dis)charging the cell and wait until the end of this step in the usage profile while the current is zero. A second option, shown in section B.2, is to keep the voltage constant at the voltage limit, doing a CV (dis)charge, for the remaining time of the present step. This means the battery does ‘the best it can’ to follow the original profile.

A third case, shown in section B.3, is where safety margins are introduced, and the bottom and top 10% of the SoC region cannot be used. In other words, the battery can only be used with a SoC between 10% and 90%. In reality, this can be enforced by the BMS, which estimates the SoC based on real-time data. Although this would be possible with the MTTB (see section 4.7), it was not possible with the experimental validation done in section 4.6 because those cells were connected directly to a battery tester, without BMS to estimate the SoC. Therefore, the experimental validation had to rely on voltage limits (but it can do a CV at those voltage limits). The SoC limitations can be translated to reduced voltage limits, with a CV phase at those limits. For example to limit the lower SoC to 10%, the battery tester can do a CV when the voltage would go below 3.42 V (which corresponds to 10% SoC on the OCV curve of the cell, see Fig. 1.2). Because the simulations should imitate the experiment, the same approach is followed here: the cell could only be used between 3.42 V and 4.08 V and when these voltage limits were reached, a CV (dis)charge was done for the remaining time of the present step in the profile.

In all three cases, the results are presented with three figures: the power from the battery to the grid, the SoC of the battery, and the economic performance and degradation of the battery. An important comment to be made is that the SoC was calculated by integrating the current to the battery. Therefore, there is a drift in the SoC due to the side current into the SEI growth and due to loss of active material. Both will change the lithium concentration in the particles, which determines the real SoC, independent of the total battery current, which determines the SoC as it is calculated here.

The results are discussed in section B.4.

B.1 CC only in the full SoC region

This section presents the results of the simulations where a cell tries to follow the optimal current profiles. When the minimum or maximum voltage limit, respectively 2.7 V and 4.2 V, is reached, the current is reduced to 0 A and the cell rests for the remaining time. For example, suppose the optimal profile instructs the cell to charge for 15 minutes at 1 A, but after 11 minutes the cell voltage becomes 4.2 V. Then for the remaining 4 minutes, the current is set to 0 A. Then, the cell tries to follow the next step of the optimal profile.

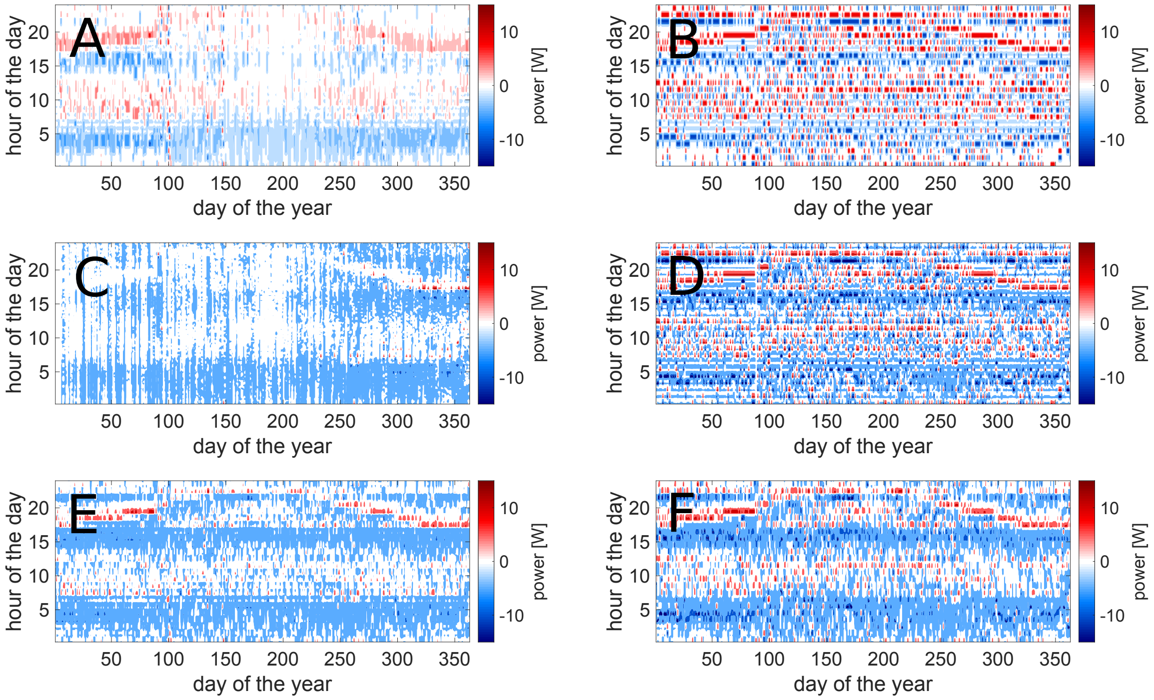

Fig. B.1 Optimal battery power for the six optimisations when only a CC phase is done. (A) BM maximising profit; (B) BM maximising revenue; (C) ECM maximising profit; (D) ECM maximising revenue; (E) SPM maximising profit; (F) SPM maximising revenue.

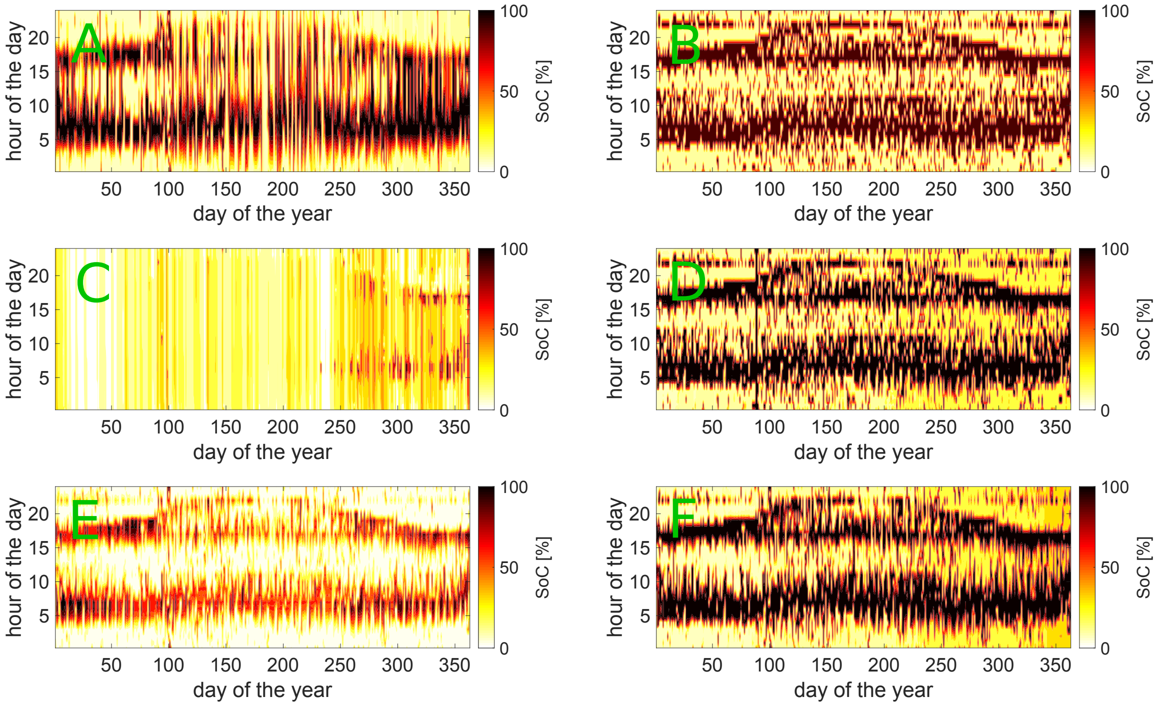

Fig. B.2 Optimal battery SoC for the six optimisations when only a CC phase is done. (A) BM maximising profit; (B) BM maximising revenue; (C) ECM maximising profit; (D) ECM maximising revenue; (E) SPM maximising profit; (F) SPM maximising revenue.

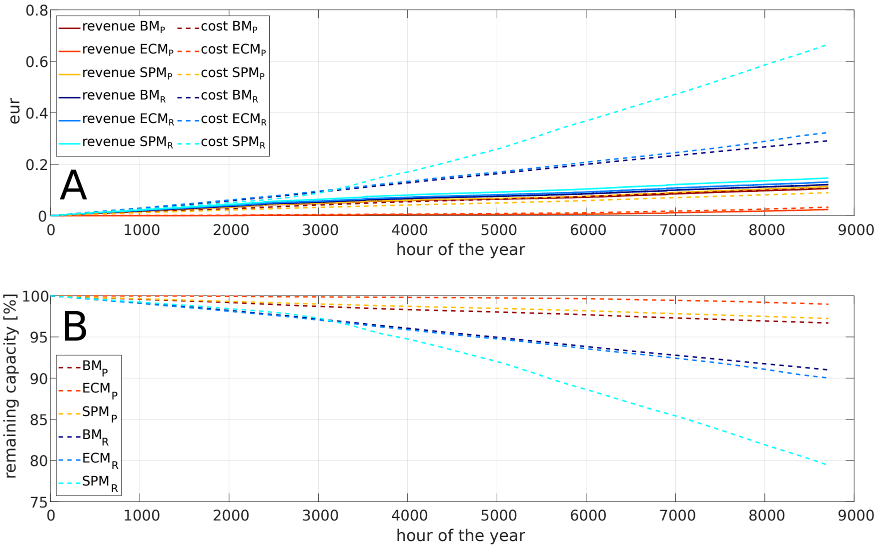

Fig. B.3 Overview of the battery performance when only a CC phase is done. (A) revenue and degradation cost of each of the six profiles; (B) relative remaining capacity for each of the six profiles.

B.2 CC and CV in the full SoC region

This section presents the results of the simulations where a cell tries to follow the optimal current profiles. When the minimum or maximum voltage limit, respectively 2.7 V and 4.2 V, is reached, the cell does a CV phase as the voltage limit for the remaining time. For example, suppose the optimal profile instructs the cell to charge for 15 minutes at 1 A, but after 11 minutes the cell voltage becomes 4.2 V. Then for the remaining 4 minutes, the cell is kept at 4.2 V and the current will decrease accordingly. Then, the cell tries to follow the next step of the optimal profile.

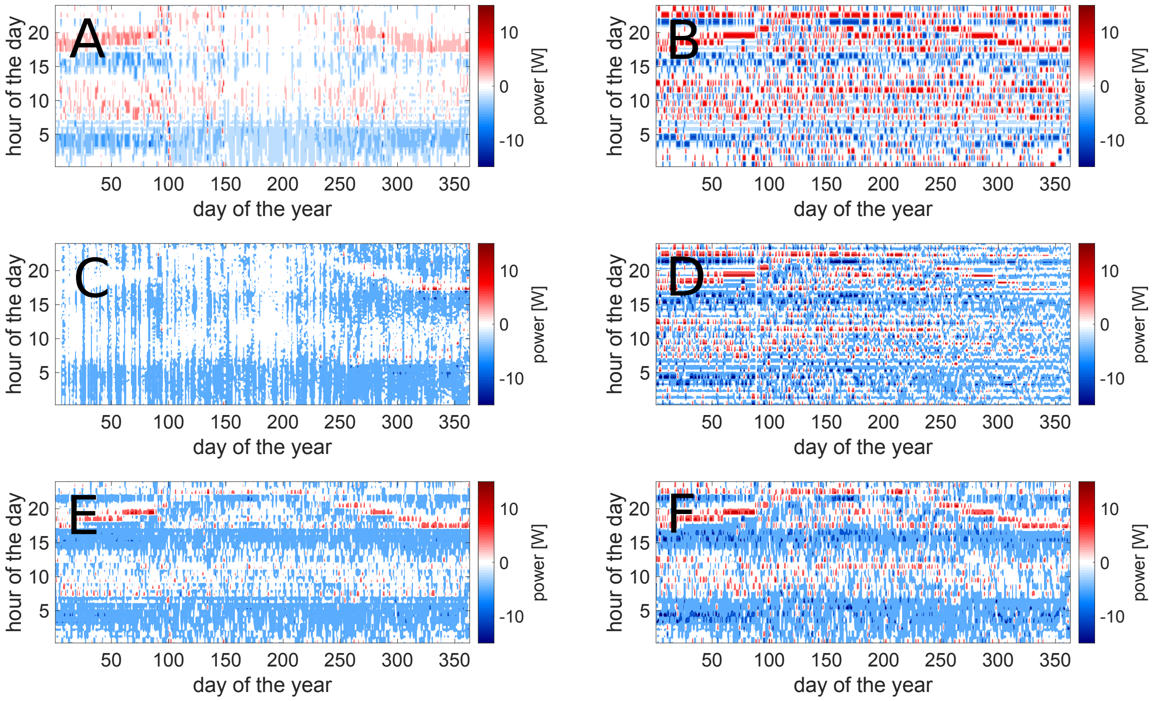

Fig. B.4 Optimal battery power for the six optimisations when a CV phase is done when the maximum or minimum voltage is reached. (A) BM maximising profit; (B) BM maximising revenue; (C) ECM maximising profit; (D) ECM maximising revenue; (E) SPM maximising profit; (F) SPM maximising revenue.

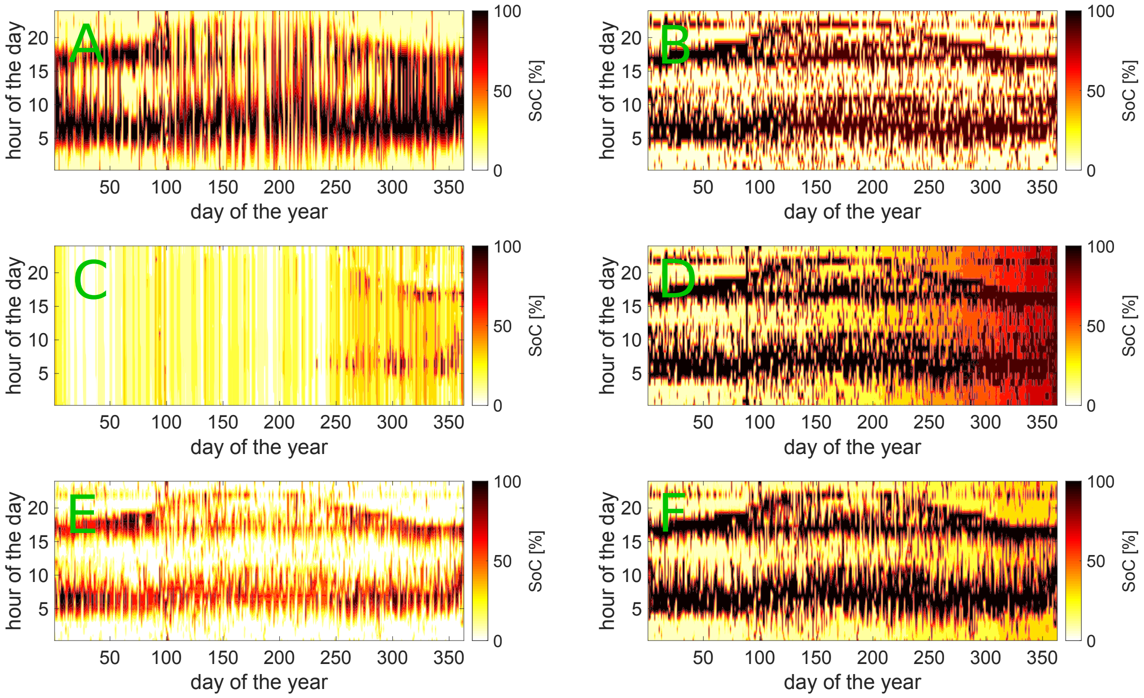

Fig. B.5 Optimal battery SoC for the six optimisations when a CV phase is done when the maximum or minimum voltage is reached. (A) BM maximising profit; (B) BM maximising revenue; (C) ECM maximising profit; (D) ECM maximising revenue; (E) SPM maximising profit; (F) SPM maximising revenue.

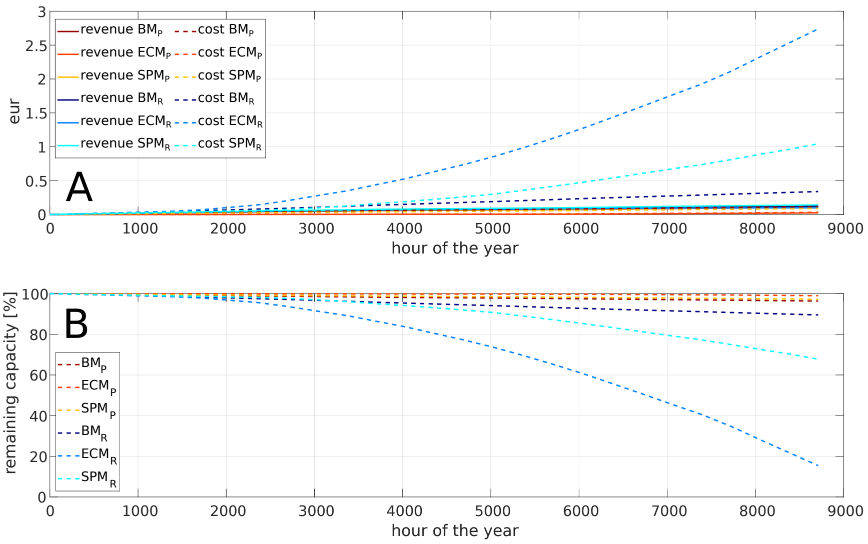

Fig. B.6 Overview of the battery performance when a CV phase is done when the maximum or minimum voltage is reached. (A) revenue and degradation cost of each of the six profiles; (B) relative remaining capacity for each of the six profiles.

B.3 CC and CV in the middle 80% of the voltage window

This section presents the results of the simulations where a cell tries to follow the optimal current profiles but is limited to the middle 80 % of its SoC window. As explained at the start of this appendix, this is translated to voltage limits: 3.42 V and 4.08 V corresponding to 10% and 90% on the OCV curve of the cell. When one of those limits is reached, the cell does a CV phase as the voltage limit for the remaining time. For example, suppose the optimal profile instructs the cell to charge for 15 minutes at 1 A, but after 9 minutes the cell voltage becomes 4.08 V. Then for the remaining 6 minutes, the cell is kept at 4.08 V and the current will decrease accordingly. Then, the cell tries to follow the next step of the optimal profile.

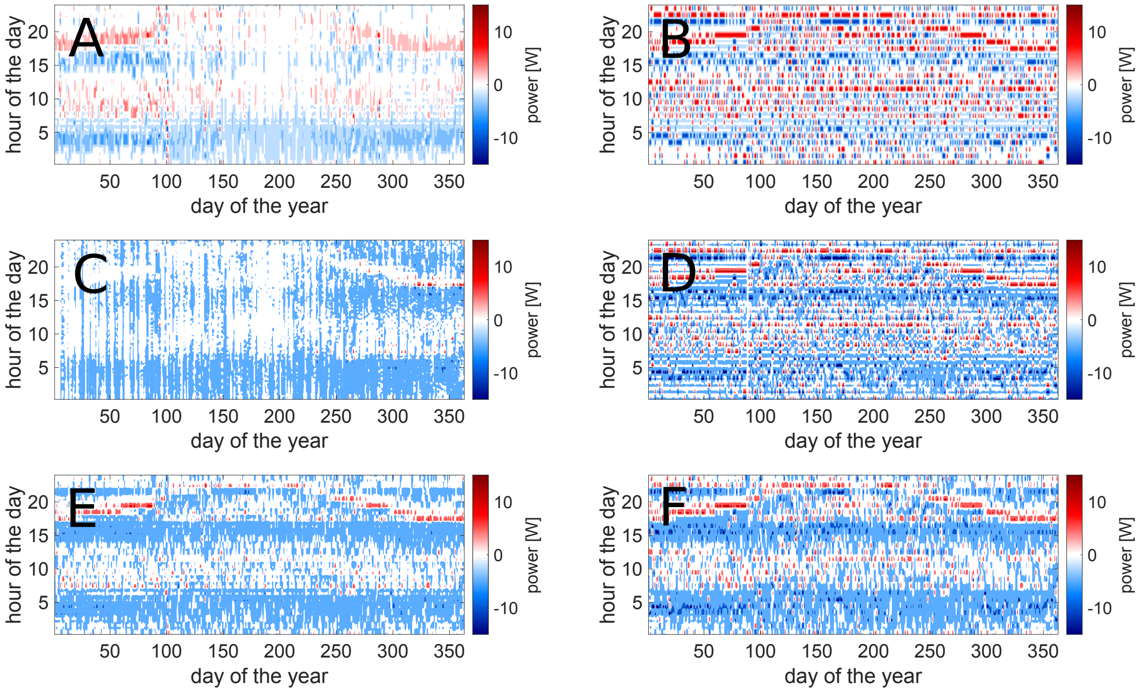

Fig. B.7 Optimal battery power for the six optimisations when the cell can only use the middle 80% of the SoC window and a CV phase is done the reduced voltage limits. (A) BM maximising profit; (B) BM maximising revenue; (C) ECM maximising profit; (D) ECM maximising revenue; (E) SPM maximising profit; (F) SPM maximising revenue.

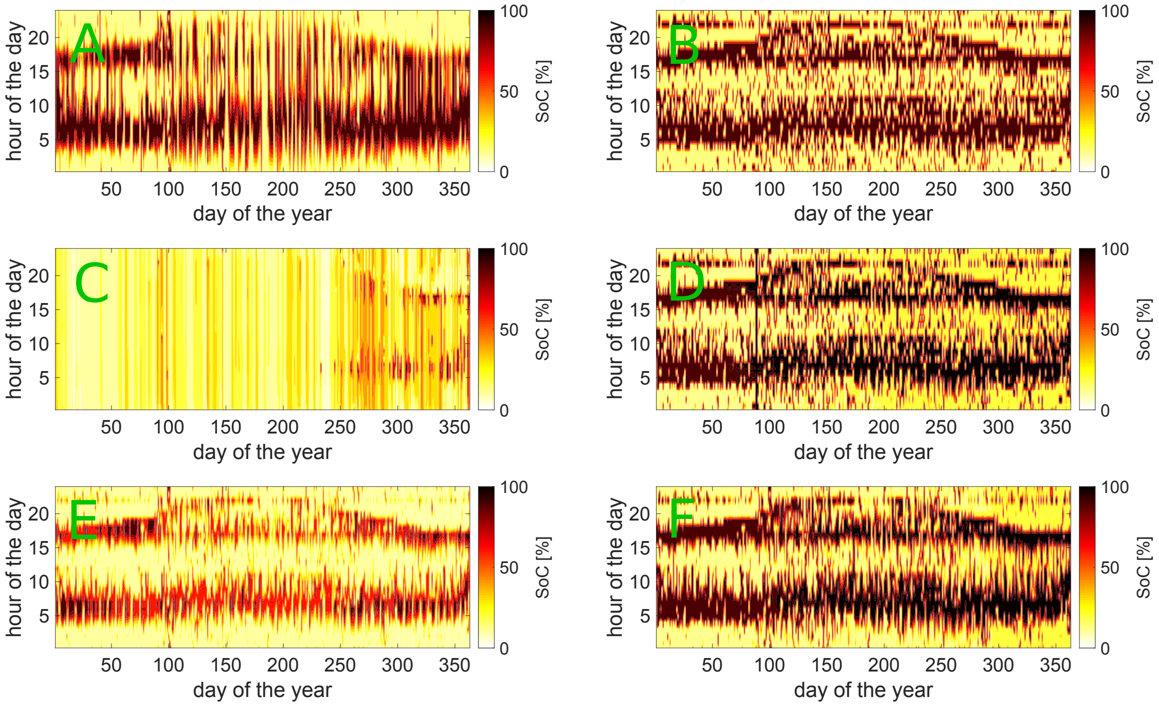

Fig. B.8 Optimal battery SoC for the six optimisations when the cell can only use the middle 80% of the SoC window and a CV phase is done the reduced voltage limits. (A) BM maximising profit; (B) BM maximising revenue; (C) ECM maximising profit; (D) ECM maximising revenue; (E) SPM maximising profit; (F) SPM maximising revenue.

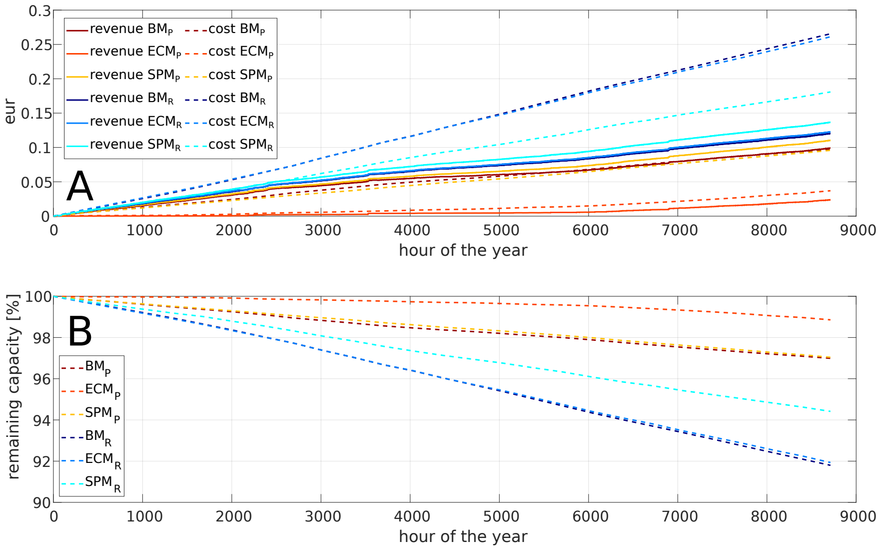

Fig. B.9 Overview of the battery performance when the cell can only use the middle 80% of the SoC window and a CV phase is done the reduced voltage limits. (A) revenue and degradation cost of each of the six profiles; (B) relative remaining capacity for each of the six profiles.

Table B.1 Comparison of the cumulative revenue and degradation of the three approaches at the end of the year. Full CCCV refers to cells doing both a CC and CV and can access the full SoC window as in section B.2. 80% CCCV refers refers to cells doing both a CC and CV but can only access the middle 80% of the SoC window as in section B.3.

	revenue [€]			degradation [%]		
	CC only	full CCCV	80% CCCV	CC only	full CCCV	80% CCCV
BM$_R$	0.1213	0.1246	0.1204	8.9958	10.4799	8.2019
BM$_P$	0.1063	0.1094	0.0992	3.3116	3.6628	3.0094
ECM$_R$	0.1313	0.0989	0.1229	9.9867	84.5951	8.0681
ECM$_P$	0.0245	0.0253	0.0239	1.0280	1.0239	1.1425
SPM$_R$	0.1467	0.1419	0.1368	20.5803	32.2592	5.5858
SPM$_P$	0.1141	0.1142	0.1105	2.7685	2.771	2.9603

B.4 Discussion

Table B.1 shows the results of the various models and approaches at the end of the year. For the profit-maximising ECM and SPM, there is little difference between the three approaches because they include a diffusion delay, and other voltage drops in the optimisation which includes a voltage limit, so voltage limit violations only occur due to model errors (when the voltage is higher or lower than expected). Since the models are fairly accurate, the limits are only exceeded very occasionally. The degradation of the revenue-maximising SPM and ECM is very different between all cases, because these usage profiles really use the cell to its full extend. Limiting the SoC region to the middle 80% reduces the damage these high-stress cycles cause, which is done to a smaller extend by setting the current to 0 once a voltage limit is reached. The CCCV in the full SoC regions causes excessive degradation due to the cathode dissolution at high SoC levels, which is only active when a current is running (and therefore is less present in the CC-only approach). Additionally, the more a cell degrades, the more time it spends at high SoC levels for the same current profile, which accelerates degradation even more. This positive feedback loop explains the excessive degradation for the revenue-maximising SPM and ECM with the CCCV in the full SoC window.

The BM does not have any diffusion limitation or resistive effects, such that the optimal profile produced by the BM-optimisation will reach the voltage limits frequently. Therefore, they cannot use the battery as much as the revenue-maximising SPM and ECM did. When only a CC phase is used as in section B.1, and the cell is rested for the remaining time of the step in the profile, this basically means that the cell only delivers the ‘usable capacity’ which can be accessed at the power levels demanded by the BM. Therefore, this is considered to be the most realistic approach.

The approach with a CCCV in the full SoC window causes most degradation for both BM models because it allows them to use a slightly larger part of the battery than the other approaches. The difference between the approach with only a CC and with a CC and CV limited to the middle 80% is small because both reduce the accessible capacity for the BM. In the former case, the voltage limit is reached well before the cell is fully (dis)charged due to the high current running in the cell, after which the cell is resting for the remaining time. Compared to the latter approach (CCCV in the middle 80%), this means a slightly higher power is maintained for a shorter amount of time but overall this makes little difference. For the BM_P cell the CC-only approach resulted in relatively more degradation compared to the case where the cell was constrained to the middle 80% due to the regularisation term from equation 4.5 which reduces the power. This allows the CC-only approach to use a larger part of the cell than the BM_R optimisation. The degradation from the revenue-maximising BM is much lower than the other revenue-maximising models when the full SoC window can be accessed because only those latter models succeed in reaching the very high SoC-regions, unlocking a slightly higher revenue but this is very detrimental for the battery life.

Although using only a CC phase would be the most realistic approach, its results would be difficult to reproduce because cells with a different diffusion behaviour (e.g. high-energy vs high-power cells, or cells operating at different temperatures due to non-perfect thermal management systems) would lead to a different ‘cut-off’ when the maximum voltage is reached. Therefore, the experimental validation from this work used both CC and CV phases. For the SPM, this did not make much difference. The profiles from the ECM could not be tested experimentally due to a shortage of test channels. For the BM, whether to use the full cell, or constrain it to the middle 80%, would have noticeable implications.

The BM maximising profit is supposed to represent how batteries are controlled today, i.e. with a simple model that still accounts for some degradation. Because the degradation behaviour was more similar when the cell was constrained to the middle 80%, and because in reality most BMS systems automatically limit the SoC region in which the battery can operate, the approach chosen for the BM maximising profit was to limit its SoC region (the approach from section B.3).

The BM maximising revenue is supposed to represent how a heavily used battery would behave, for example in a case where the battery operator does not care about degradation, which can have multiple reasons (ignorance, a guaranteed asset lifetime, inflation and discounting, etc.). Because the highest revenue was achieved when the full SoC region could be used, this approach was chosen for the BM maximising revenue (the approach from section B.2).